THE PREPARATION OF PYRIDYLIMINE MN(I) AND RU(II) COMPLEXES AS CATALYST PRECURSORS IN FORMIC ACID DEHYDROGENATION

by

Thabiso Isaac Mphuti

A dissertation submitted to the Faculty of Science, University of the Witwatersrand, Johannesburg, in fulfilment of the requirements for the degree of Master of Science.

Supervisor: Prof Andrew John Swarts

November 2024

Declaration

I declare that this dissertation, unless otherwise explicitly stated, is my own, unaided work. It is being submitted for the Degree of Master of Science in Chemistry at the University of the Witwatersrand, Johannesburg. It has not, in part or its entirety, been submitted before for any degree or examination at any other University.

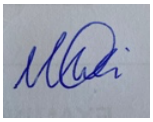

…….

Thabiso Mphuti

March 2025

Abstract

A series of known and new pyridylimine ligands **L1** – **L9** were synthesized in high yields (79 – 96%) from the condensation reaction between the appropriate pyridine-2-carboxaldehyde and amine derivatives. All the ligands were fully characterized by a range of analytical techniques. Reactions of ligands **L1** – **L9** with $MnBr(CO)_5$ yielded the new neutral manganese(I) complexes **C1** – **C9** in moderate to good yields (50 – 84%). The complexes were characterized by NMR and FT-IR spectroscopy, mass spectrometry, and elemental analysis. Single-crystal X-ray diffraction analysis confirmed the molecular connectivity for the targeted ligands and Mn(I) complexes. Evidence of light-induced Mn-CO bond dissociation accompanied by an increase in the Mn metal center's oxidation state (+1 to +2) was shown using FT-IR and SCXRD. The pyridylimine Mn(I) complexes **C1** – **C9** were evaluated and found to exhibit poor to no activity toward the dehydrogenation of FA. Varying several reaction parameters such as solvent, base, temperature, and catalyst loading, was futile. The poor activity of these complexes was attributed to their light-sensitive nature in solution and the generation of unproductive Mn(II) catalytic species during the reaction.

The reaction of ligands **L1** – **L9** with $[RuCl_2(p\text{-cymene})]_2$ generated cationic, half-sandwich ruthenium complexes **C10** – **C20** in good yields (73 – 87%). The complexes were characterized by FT-IR and NMR spectroscopy, mass spectrometry, elemental analysis, and single-crystal X-ray diffraction analysis. The cationic Ru(II) complexes were found to be active precatalysts for the base/additive-assisted dehydrogenation of FA. The performance of **C10** – **C18** was largely influenced by the pyridylimine ligand framework, as shown by catalyst screening studies. Varying the nature of the counterion on the cationic complexes did not affect FA dehydrogenation in DMSO. Complex **C1** displayed solvent-dependent catalytic activities in DMSO and water. The activation energies were estimated to be 84 and 108 kJ/mol for reactions performed in DMSO and water, respectively. The key Ru-monohydride species (δ = -11 ppm) in the catalytic cycle was identified using ^1H NMR spectroscopy. KIE experiments indicated decarboxylation as the rate-determining step in both DMSO and water. Based on the kinetic and spectroscopic investigations, plausible pathways for the dehydrogenation of FA over **C10** in DMSO and water were proposed. Catalyst recyclability studies indicated increased reusability of **C10** in water with TON = 6748 after six FA addition cycles compared to DMSO (TON ~ 3000).

Dedication

This MSc dissertation is dedicated to my mother

Francinah Mamokete Mphuti

for your love and support throughout my studies.

Acknowledgements

I want to express my heartfelt gratitude to all those who supported me throughout my dissertation journey.

First and foremost, I would like to thank my supervisor, Prof. Andrew Swarts, for his invaluable guidance, encouragement, and expertise. His insights and constructive feedback were instrumental in shaping this research project.

A special thanks to my colleagues and friends in the Swarts Research Group (SRG) at Wits University: Dr. Pamela Moyo, Rotondwa Mphephu, and Tshegofatso Molapo who provided a stimulating environment and shared their knowledge and camaraderie. Your support made the long hours in the lab more enjoyable.

I am also grateful to Drs Izak Kotzé, Juanita van Wyk, Monika Nowakowska, Sadhna Mathura, and the Inorganic Chemistry community at Wits University, for their thoughtful suggestions and support, which greatly enriched my work. I sincerely thank Prof. Manuel Fernandes at Wits University for timely assistance with SCXRD analyses. Special gratitude goes to Dr. Moegamat Joseph at Stellenbosch University for help with the ^{1}H NMR mechanistic investigations and for always being available to offer guidance during his time in the SRG. To Drs Tanya Hughes and Johann Fischer at Sasol Research and Technology, thank you for allowing me to tap into your experience and knowledge which have been very helpful in this journey.

To my family: Katleho, Zithobe, Ellen, Kagiso, and Omphile thank you for your unwavering love and encouragement. A special thanks to my mother Francinah Mphuti for her steadfast support and encouragement throughout my studies. Thank you all for being part of this important chapter of my life.

I wish to acknowledge the funding support from Sasol South Africa and the University of the Witwatersrand through the Postgraduate Merit Award (PMA), which made this research possible.

“I will give thanks to you, Lord, with all my heart; I will tell of all your wonderful deeds.” – Psalm 9:1.

Conference Contributions

Poster Presentations

Thabiso Mphuti and Andrew Swarts

Hydrogen Production from the Dehydrogenation of Formic Acid using a Water-soluble Pyridylimine Ru(II) Complex. Wits School of Chemistry Annual MSc Poster Conference, University of the Witwatersrand, Johannesburg, Gauteng, 2024.

Thabiso Mphuti and Andrew Swarts

Hydrogen Production from the Dehydrogenation of Formic Acid using a Water-soluble Pyridylimine Ru(II) Complex. 3rd Symposium on Organic and Inorganic Chemistry in Southern Africa (SOIC), Misty Hills Conference Centre, Muldersdrift, Gauteng, 2024.

Oral Presentation

Thabiso Mphuti and Andrew Swarts

The Preparation of Pyridylimine Mn(I) and Ru(II) Complexes as Catalyst Precursors in Formic Acid Dehydrogenation. Sasol Bi-Annual Virtual Postgraduate Research Seminar, 2024.

Contents

Chapter 2: Synthesis and Characterization of Neutral Pyridylimine Manganese(I) Complexes.

Chapter 3: Synthesis and Characterization of Cationic, Half-Sandwich Pyridylimine Ruthenium(II) Complexes.

List of Figures

Chapter 1: Fundamental and Catalytic Insights into Schiff-Base Transition Metal Complexes.

Chapter 2: Synthesis and Characterization of Neutral Pyridylimine Manganese(I) Complexes.

Chapter 3: Synthesis and Characterization of Cationic, Half-Sandwich Pyridylimine Ruthenium(II) Complexes.

List of Schemes

Chapter 1: Fundamental and Catalytic Insights into Schiff-Base Transition Metal Complexes.

Chapter 2: Synthesis and Characterization of Neutral Pyridylimine Manganese(I) Complexes.

Chapter 3: Synthesis and Characterization of Cationic, Half-Sandwich Pyridylimine Ruthenium(II) Complexes.

Chapter 4: Formic Acid Dehydrogenation Catalyzed by Cationic, Half-Sandwich Pyridylimine Ruthenium(II) Complexes.

List of Tables

Chapter 2: Synthesis and Characterization of Neutral Pyridylimine Manganese(I) Complexes.

Chapter 3: Synthesis and Characterization of Cationic, Half-Sandwich Pyridylimine Ruthenium(II) Complexes.

Chapter 4: Formic Acid Dehydrogenation Catalyzed by Cationic, Half-Sandwich Pyridylimine Ruthenium(II) Complexes.

List of Abbreviations and Symbols

δ	chemical shift
Å	Angstrom
ATR	Attenuated Total Reflectance
BPh_4	tetraphenylborate
br	broad
cm^{-1}	inverse centimetre
comp.	complex NMR pattern
DCM	dichloromethane
DMSO	dimethylsulfoxide
DMF	dimethylformamide
d	doublet
dd	doublet of doublets
ECE	electron-transfer chemical-reaction electron-transfer
ESI-MS	electrospray ionization mass spectrometry
Eq.	equivalents
FA	formic acid
FT-IR	Fourier transform infrared spectroscopy
GC-TCD	gas chromatography thermal coupled detector
hrs	hours
iPr	iso-propyl
J	coupling constant
HRMS	high-resolution mass spectrometry
m/z	mass to charge ratio
MHz	megahertz
M.p	melting point
MeOH	methanol
MeCN	acetonitrile
mins	minutes
mL	millilitres
mmol	millimoles
m	multiplet
NMR	nuclear magnetic resonance

PF_6	hexafluorophosphate
ppm	parts per million
PPh_3	triphenylphosphine
rt.	room temperature
s	singlet
sec	second
sept.	septet
SCXRD	single crystal X-ray diffraction
THF	tetrahydrofuran
t	triplet
TOF	turnover frequency
TON	turnover number

Chapter 1: Fundamental and Catalytic Insights into Schiff-Base Transition Metal Complexes

1.1 Introduction

Over the last three decades, the chemistry related to Schiff base ligands and their metallic complexation has gained significant traction amongst academics and industrial researchers. This increase may be pinned down to a growing interest in the field of coordination chemistry, some technological advancements and new analytical and/or spectroscopic techniques used to characterize inorganic compounds.[1] These compounds find application in various research areas. Examples include but are not limited to, nanomaterials in materials science, anti-therapeutics in medicinal chemistry, and catalyst precursors in homogeneous and heterogeneous catalysis.[1] Schiff base ligands are of particular interest due to their ease of synthesis through a condensation reaction and simple functionalization, allowing for inserting new functional groups with varying electronic and steric properties. The chemistry of Schiff bases and their related transition metal complexes is proliferating with nearly 7000 publications produced in 2018 – 2022 (**Figure 1.1**). This rampant interest in Schiff base metal complexes was spearheaded by the work of Temel and coworkers in 2002.[3] In this work, they detailed the synthesis and spectral characterization of a new set of Cu(II), Ni(II), Co(III) and Zn(II) Schiff base complexes indicating the variety of transition metal complexes that can be synthesized using these ligands.

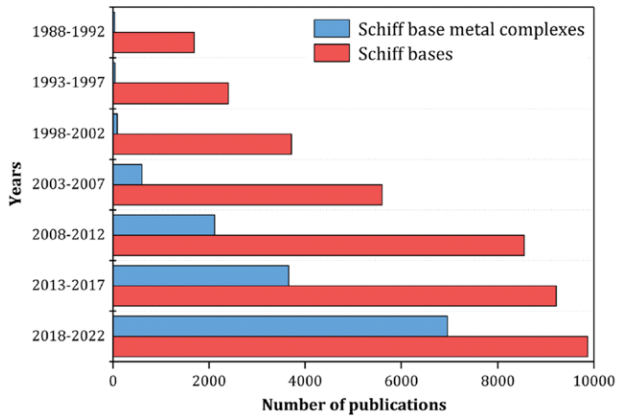

Figure 1.1: Number of scientific reports with the terms, Schiff base and Schiff base metal complexes, published from 1988 – 2022. **Source**: Scopus Database (Accessed 20-01-2024).

1.2 Brief historical overview and coordination modes of Schiff base ligands

Schiff bases are a type of organic compound that was first reported by German Scientist, Hugo Schiff in 1864.[2] In a follow-up publication in 1866, Schiff studied the interaction of a range of aldehyde-fuchsins which are compounds that contain two dye molecules and three aldehyde molecules with chemical reagent known as Fuchsine (**Figure 1.2**).[4] This resulted in Fuchsine being widely used for industrial dyes during the last years of the 19th century.[4] Over the last two decades, conjugated Schiff base polymers and oligomers have been extensively studied.[5] In this publication, Plesch and coworkers reflected on coordination geometries and cooperative ordering effects in copper(II) complexes bearing tridentate Schiff base dianions. Aliphatic Schiff bases, on the other hand, polymerize readily and are known to be unstable therefore, they are not widely explored in the literature.[5]

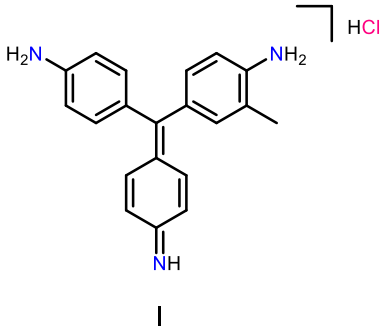

I

Figure 1.2: Chemical structure of Fuchsine.[4]

Jorgensen initiated the synthesis of metal-conjugated Schiff base complexes in the mid-1870s.[6] He studied metal ammine complexes, particularly those of cobalt. He relied on his mentors' chain theory to provide explanations for the many new series of compounds that he had synthesized for the first time. This was followed by the Nobel Prize-winning work of Swedish chemist Alfred Werner in 1893, where he studied a variety of these compounds as drugs for the treatment of cancers.[7] Werner is also famous for proposing the octahedral configuration of transition metal complexes which forms the basis for modern coordination chemistry.

Schiff bases are organic compounds containing the azomethine or imine (-HC=N-) functional group and occur due to a condensation reaction between carbonyl compounds, either ketones or aldehydes, with primary amines. Schiff bases commonly find use as intermediates in amino acid synthesis or as ligands for preparing metal complexes with tunable electronic and steric properties.[8]

The denticity in Schiff bases can vary from bidentate to tetradentate chelate ligands depending on the number of donor atoms in the ligand structure. The presence of more than one imine functional group increases the coordination versatility of these ligands due to increased coordination donor sites.[9] As shown in **Scheme 1.1**, the synthesis of Schiff bases is a reversible process and usually requires heat or acid/base catalysis. Most compounds of this nature can be hydrolyzed back to their carbonyl compounds and amines using an aqueous acid or base.[10]

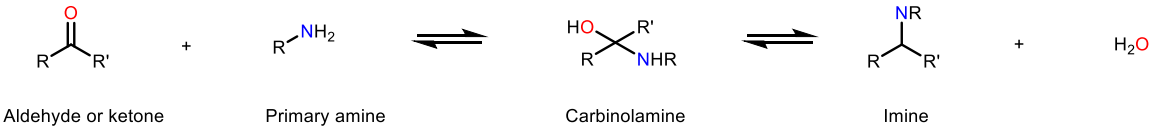

Scheme 1.1: Reaction scheme for the formation of Schiff bases.[10]

Coordination with these types of ligands occurs through the imine nitrogen and a group usually linked to the carbonyl moiety.[11] They are widely used due to their π acceptor properties on the imine nitrogen functional group as well as σ donor ability towards metal cations.[12] Notably, the double-bonded nitrogen in these ligands is never bonded to a hydrogen atom and is one of the sites where variations in the ligand structure can be implemented.[13] Various types of these ligands exist such as the salen-containing salicylaldehyde and ethylenediamine derivatives, salophen-bearing salicylaldehyde and *o*-phenylenediamine derivatives, hydrazone with carbonyl compounds and hydrazine derivatives, and semicarbazone containing carbonyl compounds with thiosemicarbazide variants (**Figure 1.3**).[14] This study focuses on a class of Schiff bases called pyridylimines, a subset of the hydrazone type. They can stabilize many transition metals in various oxidation states and influence the resulting complexes' performance in many useful applications.[15]

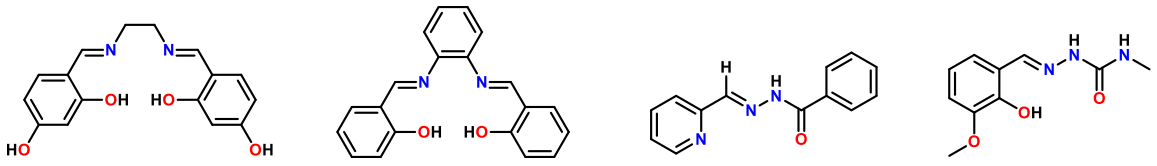

Figure 1.3: Chemical structures of different types of Schiff bases *viz*. (II) salen type, (III) salophen type, (IV) hydrazone type, and (V) semicarbazone type.[14]

The ligand design in pyridylimines is highly versatile and allows for the modulation of steric and electronic variation around the metal ion (**Figure 1.4**). The results are transition metal complexes with distinct coordination modes as required.[15]

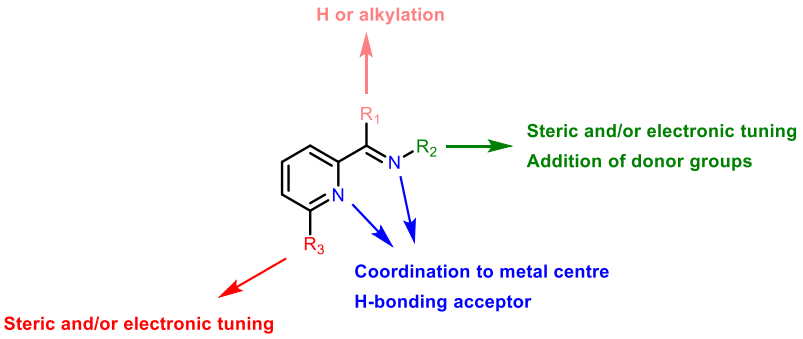

VI

Figure 1.4: Various functionalities of pyridylimine ligands.

Morales-Morales and coworkers showed that including a weakly electron-donating methyl group on the imine carbon influences whether an ionic or neutral complex is formed.[15] They prepared a series of Ni(II) complexes derived from pyridylimine ligands and observed that when the substituent on the imine carbon is hydrogen, the result is an ionic complex i.e. **VII** in **Scheme 1.2**. Conversely, a neutral complex **VIII** is formed when a methyl group is introduced to the imine carbon. This is evidenced by a slight increase in the bite angle of the seven-membered ring formed between the imine nitrogens and the Ni metal centre i.e. 89.87(7)° for **VII** and 92.50(6)° for **VIII**. Additionally, the presence of an aqua ligand in **VII** could offer potential hydrogen bonding with the chloride counter ion leading to the formation of the charged complex. It should be noted, however, that this variable coordination behaviour has not been established for pyridylimine complexes of other transition metals.

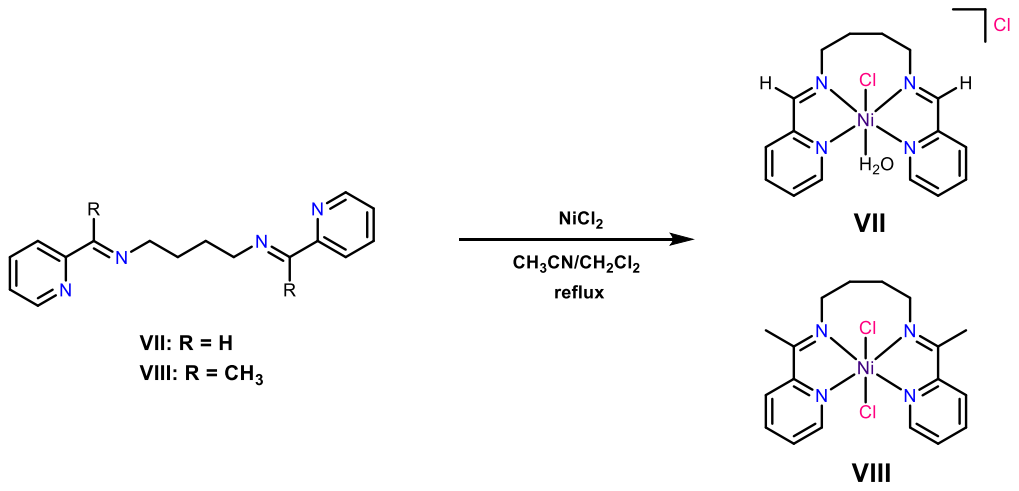

Scheme 1.2: Preparation of ionic, **VII** and neutral, **VIII** Ni(II) pyridylimine complex.[15]

1.3 Application of pyridylimine ligated metal complexes in catalysis

Pyridylimine ligands are quite adaptable and allow several variations in their ligand structure and hence, can support (pre)catalysts during a catalytic process. They can provide steric and electronic influence which in turn can improve catalyst stability, enhance reaction rates, and improve selectivity towards desired products. This section, to highlight the flexibility of pyridylimine ligands and their complexes, discusses the catalytic activity of reported manganese, ruthenium, nickel, and palladium transition metal complexes bearing these ligands. Other less explored pyridylimine transition metal complexes such as those derived from rhodium, molybdenum, and rhenium are discussed as additional examples. The discussion will exclude the more extensively studied PNP and PNN pincer ligand systems and their respective Mn, Ru, Ni, and Pd transition metal complexes.[16, 17]

1.3.1 Manganese complexes derived from pyridylimines

With some of the initial examples of Mn-based complexes as catalyst precursors only being reported in 2016, their application in catalytic processes is still in its infant stages and remains an active area of interest for many researchers in the field of organometallic chemistry. Before 2016, Mn catalysts were largely based on redox-active bis-pyridylimine ligands that acted as electron reservoirs which led to the metal center having higher, unproductive oxidation states and undergoing redox reactions usually observed with precious metal catalysts.[18] Hence, there is a need to incorporate ligands whose oxidation state in metal complexes is not well-defined, in particular, those bearing non-innocent N-H groups which have been shown to improve hydrogen bond breakage as well as facilitate hydrogen transfer to carbonyl groups without

interfering with the oxidation state of the metal center in the case of (de)hydrogenation reactions.[19] Concerning the application of manganese complexes in catalytic processes such as ketone hydrogenation and alcohol dehydrogenation, the existing chemical literature is flooded with reports based on PNP and PNN pincer-ligated Mn complexes which are beyond the scope of our discussion.[20, 21, 22]

Spall and co-workers detailed the first examples of manganese tricarbonyl complexes bearing asymmetric 2-iminopyridine ligands and their evaluation as electrocatalysts in CO_2 reduction.[23] The prepared Mn(I) complexes are shown in **Figure 1.5** below and contain various structural modifications that influence the catalytic process. For example, the introduction of the pyridine moiety allows for easy access to the desired reduction potential while the phenyl group attached to the imine functional group can be furnished with sterically demanding substituents with minimal effect on the electronic properties.

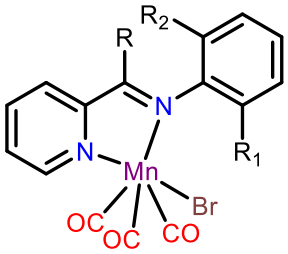

IX: R = R_1 = R_2 = H
X: R = R_2 = H, R_1 = iPr
XI: R = H, R_1 = R_2 = iPr
XII: R = R_2 = H, R_1 = tBu
XIII: R = CH_3, R_1 = H, R_2 = H

Figure 1.5: Mn(I) complexes bearing asymmetric α-diimine ligands with various alkyl substituents.[23]

A key observation from the testing of these Mn(I) complexes for CO_2 reduction was that the bulkier substituted complexes i.e. **XI** and **XIII**, were less prone to interact with the CO_2 substrate due to their rigidity and increased steric hindrance. Electrochemical studies conducted by cyclic voltammetry indicate notable differences between the cathodic pathways of complexes **IX** – **XII** and **XIII**. Under a N_2 atmosphere, complex **XIII** shows a reduction wave at $E_{p,c}$ = -1.53 V, and a distinguished anodic wave at $E_{p,a}$ = -1.3 V which is similar to other related Mn complexes reduced by an electron-transfer chemical-reaction electron-transfer (ECE) mechanism.[24] When **XIII** is exposed to CO_2, the anodic wave at -1.3 V disappears, accompanied by a change in the CV profile and a slight negative shift in the broad cathodic wave which is an indication of interaction with CO_2 (**Figure 1.6**, left). In the absence of a suitable Brønsted acid, no catalytic reduction of CO_2 was observed and similar observations have been reported in the literature for Mn-bpy complex systems.[25] The addition of 0.3 mL water led to significant

current enhancements at -2.18 V in all complexes, which is in agreement with related Mn(I) complexes in the literature.[24] This was attributed to the formation of a bicarbonate complex due to trace amounts of water in the CO_2 employed in this catalytic system. Most notably, CVs recorded under a N_2 environment in the presence of water did not show catalytic current enhancement, thus illustrating the need for both water and CO_2 in this system.

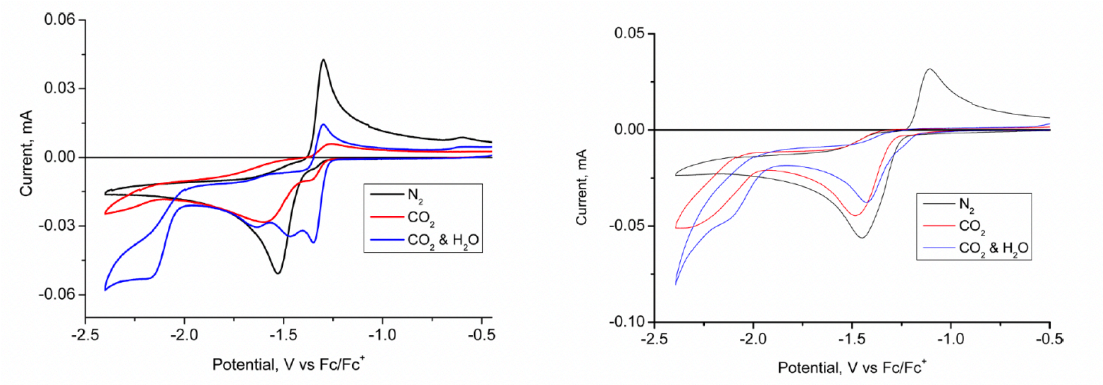

Figure 1.6: Cyclic voltammograms of 1 mM **XIII** (left) and 1 mM **XII** (right) in MeCN with 0.2 M $[Bu_4N][PF_6]$ at a scan rate of 0.1 V/s. Taken from reference.[23]

As illustrated in **Figure 1.7**, no anodic wave related to the reoxidation of the five-coordinate anion is observed for the least sterically challenged complex, **IX,** and the monosubstituted complex, **X**, a behavior which usually signals a fast reaction of the anion with CO_2. A similar observation was made in the case complex **XII** in **Figure 1.6** (right). A clear, yet diminished anodic wave was observed for complex, **XIII** under a CO_2 vs N_2 atmosphere, which signalled some degree of CO_2 interaction.

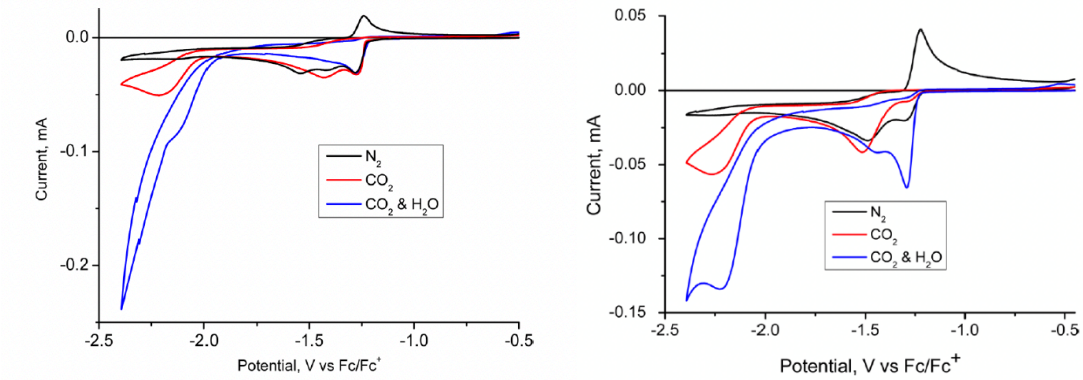

Figure 1.7: Cyclic voltammograms of 1 mM **IX** (left) and 1 mM **X** (right) in MeCN with 0.2 M $[Bu_4N][PF_6]$ at a scan rate of 0.1 V/s. Taken from reference.[23]

Regarding reactivity, the anodic wave of the anion reoxidation is observed for slower-reacting complexes, **XI** and **XIII,** and is absent in the CVs of **X** and **XII**. The cyclic voltammograms of **XI** (**Figure 1.8**), differ significantly in comparison to those of related Mn complexes **IX**, **X**, and **XII** i.e. no current enhancement below -2 V is observed upon saturation with CO_2. In addition, no intermediate bicarbonate complex reduction occurs which is an indication of a poor interaction between the complex and CO_2 due to steric influences emanating from the bulky isopropyl substituents. Additional characterization techniques such as FT-IR and UV-Vis Spectroelectrochemistry under inert and CO_2 atmospheres were also employed in this study to further understand the reactivity of the Mn(I) complexes towards CO_2.

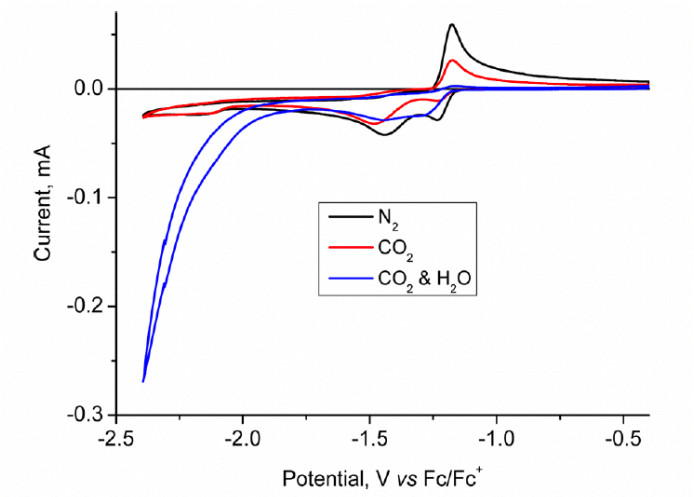

Figure 1.8: Cyclic voltammograms of 1 mM **XI** in MeCN with 0.2 M $[Bu_4N][PF_6]$ at a scan rate of 0.1 V/s. Taken from reference.[23]

The light-induced dissociation of CO ligands in $[Mn(CO)_3]$-type complexes is well documented in the chemical literature and complexes of this nature, called photo carbon monoxide releasing molecules (photoCORMs), find use in a variety of medicinal and catalytic applications.[26, 27] In a recent study, Henke and coworkers presented the ultrafast spectroscopic analysis of several Mn(I) complexes to tune the kinetics of light-induced CO release and solvent binding studies.[28] A series of $Mn(CO)_3(^{R}bpy)Br$ complexes bearing various electron-donating/withdrawing substituents were prepared and are shown in **Figure 1.9** below.

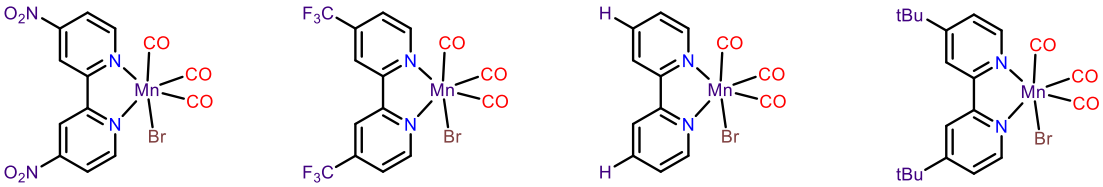

XIV **XV** **XVI** **XVII**

Figure 1.9: A series of Mn(I)-bpy complexes bearing electron donating/withdrawing substituents.[28]

With the aid of FT-IR spectroscopy, a series of photolysis experiments were carried out to monitor the *in-situ* generation of new species. The emergence of unique CO stretches as well as stretches synonymous with manganese complexes were noted between 2050 cm^{-1} and 1825 cm^{-1} upon irradiation of complex **XVI** with 415 nm light for 2 minutes. In addition, a stretch associated with free CO gas dissolved in MeCN was observed near 2143 cm^{-1} (**Figure 1.10**, left). Over time, the bands at 1924, 1934, and 2028 cm^{-1} associated with **XVI** became less intense accompanied by an increase in the intensity of bands at 1883, 1961, and 1976 cm^{-1} assigned to the manganese-containing photo products (**Figure 1.10**, right). Additionally, two less intense bands at 1856 cm^{-1} and 2050 cm^{-1} were observed and attributed to metastable intermediates due to little to no variation in intensity over 15 minutes.

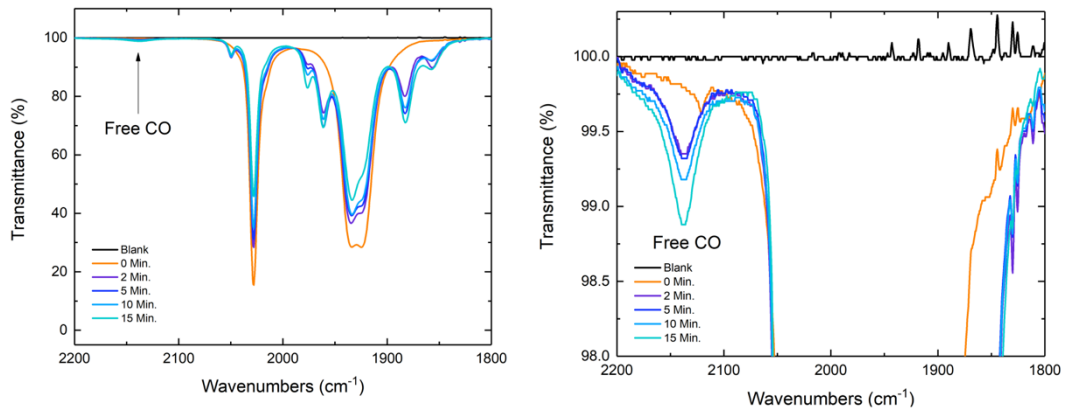

Figure 1.10: FT-IR spectroscopic monitoring of **XVI** in solution irradiated with 415 nm light over time. Taken from reference.[28]

Ultrafast transient absorption (TA) spectroscopy was employed to monitor the reaction following metal-to-ligand charge-transfer (MLCT) excitation of the Mn(I) complexes. The TA spectra of complexes, **XVII**, **XVI**, and **XIV** shown in **Figure 1.11** were observed to be similar at longer time delays with the initial excited state bands being double-

peaked and partially decaying in ≤1 picosecond. The initial excited state absorption bands followed a similar trend to the ground state MLCT bands of **XVII**, **XVI**, and **XIV** which supported the coordination of the bpy ligand to the Mn metal centre. For complex **XV**, the initial excited state absorption band is stronger, and decays slowly compared to the other complexes (**Figure 1.11**). In addition, there is no appearance of a secondary absorption feature at ~100 picoseconds on the TA spectrum that is observed for the other complexes in this study. This anomalous behavior of **XV** was attributed to the localization of the charge in the MLCT state due to the strongly electron-withdrawing nitro substituents, the result of which is a more stable and long-lived excited state for **XV**.

Using GC analyses, TA spectroscopy, and kinetics, a pathway for the speciation of complexes, **XVII**, **XVI**, and **XIV** that involves rapid CO ligand dissociation on the femtosecond scale followed by acetonitrile solvent coordination on the picosecond scale was proposed.

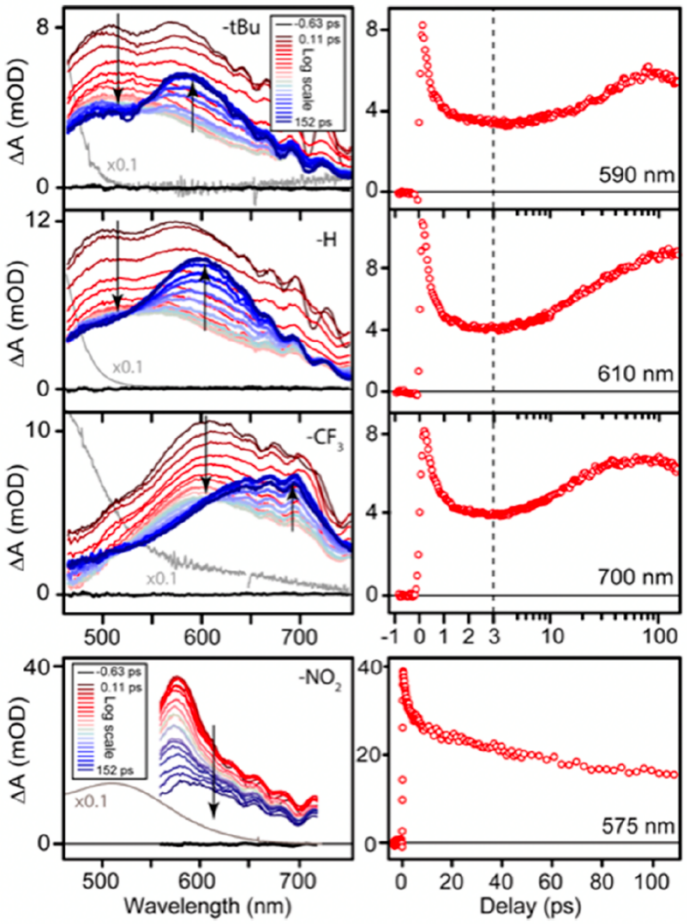

Figure 1.11: TA spectra of complexes **XVII**, **XVI**, **XV**, and **XIV** (top to bottom) in MeCN. Taken from reference.[28]

1.3.2 Ruthenium complexes derived from pyridylimines

The use and effectiveness of ruthenium complexes in catalysis are well-documented, in particular, ruthenium(II) complexes bearing pincer-type ligands. Examples include their application in transfer hydrogenation reactions,[29] dehydrogenative coupling reactions,[30] and acceptorless dehydrogenation of alcohols.[31] Zheng and co-workers prepared two Ru(II) complexes with tridentate Schiff base ligands for application as precatalysts in the acceptorless dehydrogenation of ethanol.[31] The structural variations for complexes, **XIX** and **XX** are represented in **Scheme 1.3** below. Both **XIX** and **XX** were found to be highly active for this transformation, reaching turnover numbers as high as 31 965 (equivalent to 387 mL of H_2 produced) in the case of complex **XX** under optimized reaction conditions. Both catalysts follow a similar reaction profile, yet **XX** is superior to **XIX** in terms of performance. This is evidenced by the fact that both catalysts reached peak performance at 150 °C, but **XX** reached TOF = 1526 hr^{-1} while **XIX** reached TOF = 1170 hr^{-1} after a reaction time of 5 hours. This catalytic behavior can be attributed to the presence of good leaving groups, for example, two CO ligands in **XX** as opposed to one CO ligand in **XIX**, which enhances the ethanol substrate coordination to the Ru metal centre.

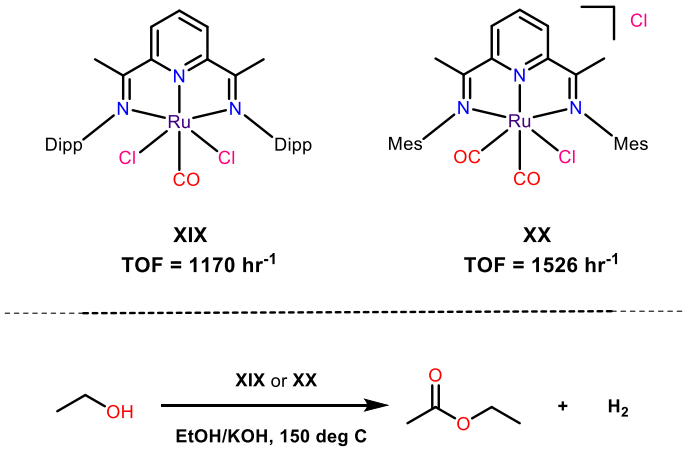

Scheme 1.3: Ru(II) Schiff base complexes for acceptorless dehydrogenation of ethanol.[31]

A small amount of methane gas was detected using gas chromatography measurements with no observable carbon monoxide content in the sample. Whilst the hydrogen generated from this reaction cannot be useful in applications that require clean hydrogen, the combination of hydrogen and methane is useful for solid oxide fuel cells (SOFCs) since CH_4 is known to prevent the formation of hotspots in these

technologies.[32] As a result, ethanol offers an interesting alternative for dehydrogenation reactions in comparison to the widely studied chemicals; methanol and formic acid.

Ramos and coworkers reported on the synthesis and spectroscopic characterization of ruthenium-cymene complexes bearing pyridine-derived aldimine ligands for use in transfer hydrogenation reactions of aryl ketones.[33] A total of six Ru(II) complexes were prepared with modifications being made on the aromatic ring directly linked to the imine nitrogen (**Scheme 1.4**). All the complexes displayed good catalytic activity when tested for the transfer hydrogenation of acetophenone, with complexes **XXI** and **XXIII** achieving the highest turnover frequencies of 300 and 291 hr^{-1} within 3 hours, respectively. In terms of product formation, this translates to about 90% of 1-phenylethanol for both complexes. Complexes **XXV** and **XXVI** yielded 64% and 63% 1-phenylethanol, respectively. This decrease in activity was attributed to the increased steric bulk brought on by the ethyl (**XXV**) and isopropyl (**XXVI**) substituents. Additionally, a negligible difference in the amount of the hydrogenated product suggests that the substituents do not have a significant role in the performance of both catalysts.

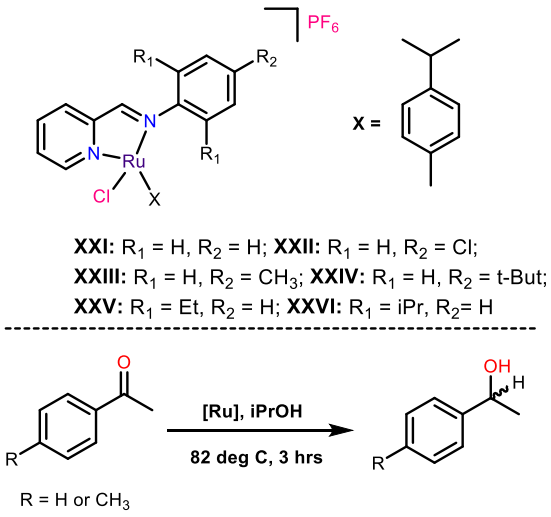

Scheme 1.4: Pyridine-derived aldimine Ru(II) complexes for transfer hydrogenation of aryl ketones.[33]

When the substrate was changed to 4-methylacetophenone, all complexes displayed good catalytic activities except for complex **XXIV** which only yielded 25% of the hydrogenated product(4-methyl-1-phenylethanol). The increased basicity of the substrate was mentioned to decrease the electrophilicity of the carbon atom of the

ketone functional group. This, as well as the steric hindrance caused by the tert-butyl substituent, accounted for the poor performance. Notably, the reduction of ketones was not observed when KOH was omitted from the reaction mixture, suggesting the formation of a ruthenium alkoxide intermediate is essential to produce the Ru hydride complex which is the catalytically active species.[34] Lastly, a kinetic study of the transfer hydrogenation of acetophenone was undertaken using complexes **XXII** and **XXVI** bearing chloride (electronic effect) and isopropyl (steric effect) substituents on the *ortho* and *para* positions of the imine ring, respectively. Interestingly, the activity of **XXII** was more affected by temperature variation than **XXVI**, as a result, the rate constant increased faster for the reaction catalyzed by **XXII** in comparison with the reaction catalyzed by **XXVI**. A less energy-demanding shift from the resting to the active state was proposed for **XXVI**, due to an outer-sphere reaction mechanism that the hydrogen donor aids.

1.3.3 Palladium complexes derived from pyridylimines

The seminal work by Brookhart and coworkers discovered that α-diimine palladium and nickel complexes are active catalyst precursors for ethylene polymerization/oligomerization reactions.[35] As a result, developing nitrogen-donor late transition metal catalyst precursors for these transformations has attracted much interest from many researchers. Darkwa and coworkers prepared several pyridylimine palladium complexes containing hemi-labile thiophene or furan groups for reactions with ethylene i.e. polymerization and/or oligomerization (**Figure 1.12**).[36] Coordination to the palladium metal centre occurred through the imine and pyridine nitrogen groups resulting in neutral complexes with a distorted square planar molecular geometry.

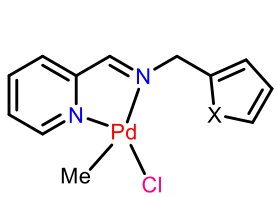

XXVII: X = O
XXVIII: X = S

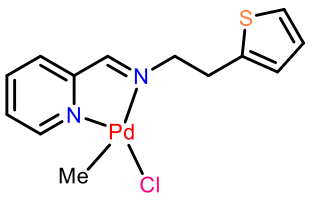

XXIX

Figure 1.12: Pyridylimine palladium complexes for ethylene reactions.[36]

Complexes **XXVII** - **XXIX** were tested for their ability to polymerize or oligomerize ethylene by employing NaBAr, where Ar = 3,5-$(CF_3)C_6H_3$, as the activating agent. This yielded cationic complexes **XXVIIa** – **XXIXa** (**Figure 1.13**). Although no decomposition of the catalysts was observed *via* the formation of palladium black, all the charged complexes displayed low activity for this transformation. The poor electrophilicity of the palladium metal centre and the strong binding affinity of the furan or thiophene groups were proposed to hinder ethylene coordination to account for the low activity of the Pd catalysts.

Using ^{1}H NMR studies, the half-lives were calculated to be 84, 96, and 72 hours for the cationic complexes **XXVIIa**, **XXVIIIa**, and **XXIXa**, respectively. This served as confirmation of the stability of the generated catalysts shown in **Figure 1.13**. DFT simulations determined the ethylene coordination barriers of ΔG = -5.48 kcal/mol; ΔH = -16.53 kcal/mol (**XXVIIa**), ΔG = -2.34 kcal/mol; ΔH = -13.18 kcal/mol (**XXVIIIa**), and ΔG = -8.26 kcal/mol; ΔH = -18.24 kcal/mol (**XXIXa**). When compared to ethylene coordination barriers of ΔG = -18.4 kcal/mol and ΔH = -29.4 kcal/mol for similar catalysts in a related study by Morokuma and coworkers,[37] it was concluded that the poor activity was due to the inability of ethylene to displace the coordinated furan and thiophene groups. Lastly, the ΔG values of -2.34 to -8.26 kcal/mol fall outside the -30 to -60 kcal/mol range for reported transition metal complexes that are active for ethylene polymerization or oligomerization reactions.[38]

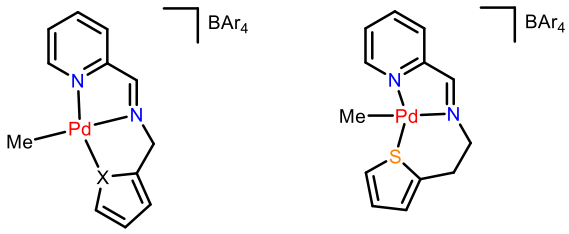

XXVIIa: X = O
XXVIIIa: X = S

XXIXa

Figure 1.13: Cationic pyridylimine palladium complexes for ethylene reactions.[36]

Ojwach and co-workers detailed the preparation of pyridylimine Pd(II) complexes as catalyst precursors for the methoxycarbonylation of higher olefins to produce a variety of linear and branched esters.[39] The efficiency of the catalytic process was found to be highly influenced by the olefin chain length as well as the structure of the palladium complex. A potentially hemi-labile donor arm was introduced to the ligand structure to

improve the activity of the catalysts shown in **Scheme 1.5**. A significant decrease (91% to 62%) in the catalytic methoxycarbonylation of 1-hexene was noted when changing from a Pd-Cl system in complex **XXX** to a Pd-Me variant in complex **XXXI**. This was assigned to the electron-withdrawing ability of the coordinated chloride ligand that increases the rate at which the substrate coordinates to the palladium metal centre.

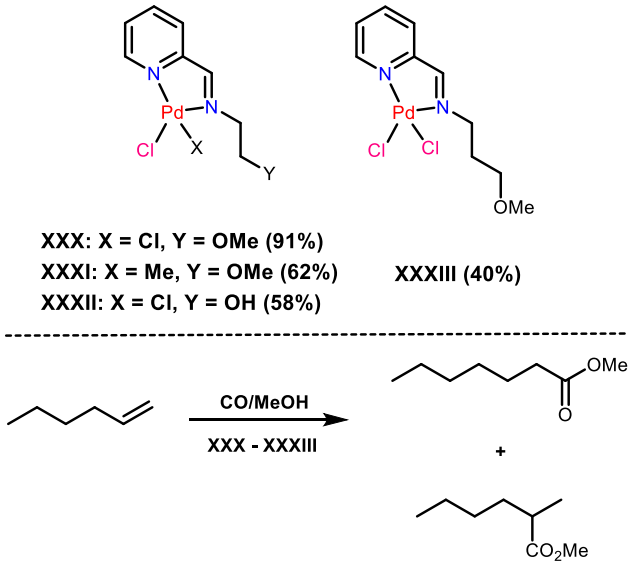

Scheme 1.5: Palladium(II) pyridylimine complexes for methoxycarbonylation of olefins.[39]

Careful examination of the structures of complexes **XXX** and **XXXII** revealed that the presence of the methoxy (OMe) functional group contributed significantly to **XXX** (91%) being catalytically superior to **XXXII** (58%) which contains a hydroxyl (OH) functional group. The OMe group is known to be hemi-labile which eases substrate coordination and stabilizes the active catalyst species.[40] The OH functional group strongly binds to the palladium metal centre; hence, a strong competing effect exists between OH and the 1-hexene substrate.[41] In all cases, the regioselectivity towards linear esters was not influenced by the structural modifications made to the complexes.

Increasing the substrate chain length i.e. from 1-hexene to 1-decene was observed to decrease the activity of complex **XXX** from 91% to 30%. This drastic decline was rationalized using the increased steric hindrance and electron density of 1-decene which hinders coordination to the palladium metal centre. This trend is consistent with observations made by the same research group when they studied palladium complexes chelated by N^O ligands for the same organic transformation.[42] Interestingly, increasing the olefin chain length was also found to affect the

regioselectivity of the ester products i.e. higher olefins favored the formation of branched esters. This was attributed to the possible isomerization of higher olefins to internal alkenes.

1.3.4 Nickel complexes derived from pyridylimines

Nickel(II) complexes bearing pyridylimine ligands were amongst the first transition metal complexes of this type to be prepared.[43] Amongst their advantages include their relatively low cost and stability under various reaction conditions. In this section, their application in the transfer hydrogenation of ketones and ethylene oligomerization and polymerization reactions is explored in detail.

Ojwach and co-workers prepared a series of chiral pyridylimine Ni(II) complexes for the transfer hydrogenation of a variety of ketones.[44] The complexes shown in **Scheme 1.6** displayed moderate to outstanding catalytic activity with conversions in the range of 54 – 98% in the asymmetric transfer hydrogenation of ketones but with a low enantiomeric excess (ee%) ranging from 11 – 16%. The formation of a major enantiomer is crucial in improving catalyst selectivity. From the kinetic studies, it was observed that complexes **XXXI** and **XXXII** containing a methyl substituent on the imine carbon recorded lower rate constants (k_{obs}) i.e. 4.00 x 10^{-5} s^{-1} and 5.52 x 10^{-5} s^{-1} respectively, compared to their analogous unsubstituted complexes, **XXXIII** (k_{obs} = 4.73 x 10^{-5} s^{-1}) and **XXXIV** (k_{obs} = 7.55 x 10^{-5} s^{-1}). The lower activity of **XXXII** in comparison with **XXXIV** was attributed to the poor electrophilicity of the Ni(II) metal ion due to the electron-donating methyl substituent and not necessarily to steric influences as the substituents are located away from the metal centre. These findings are consistent with those of Chirik and coworkers, who discovered that inserting a methyl group on the imine carbon of diamine Fe(II) complexes resulted in a decrease in the hydrosilylation of acetophenone.[45]

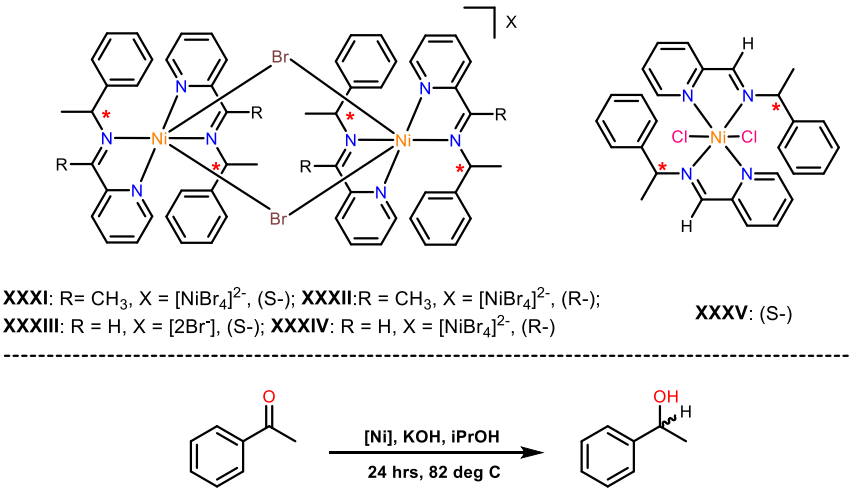

Scheme 1.6: Chiral pyridylimine Ni(II) complexes for transfer hydrogenation of ketones.[44]

Ojwach and coworkers attributed the low enantioselectivity of the complexes to two factors i.e. the remote location of the stereogenic centre being outside the metal coordination and the dissociation of the complexes into nickel(0) salts. The most active catalyst, **XXXIV** which converts 98% of acetophenone was tested for several ketone substrates and it was discovered that acetophenone derivatives bearing electron donating or withdrawing substituents on the *ortho* position resulted in lower catalytic activities. This finding contradicted numerous publications that reported that an increase in activity is observed when these groups are introduced into the structure of acetophenone.[46, 47, 48] This anomalous trend was attributed to steric influences since the substituents are closer to the carbonyl centre. Similar variations were made on the *para* position and were accompanied by a decrease in activity, a result largely attributed to electronic effects. Catalyst poisoning tests pointed to the possible formation of catalytically active Ni(0) nanoparticles as appreciable decreases in activity were observed when tricyclohexyl phosphine, triphenylphosphine, and carbon disulfide were added. This suggested that the catalytic mechanism is heterogeneous.

In another investigation, Tang and coworkers studied the behaviour of nickel(II) complexes containing 2-ethylcarboxylate-6-iminopyridyl ligands towards ethylene oligomerization and polymerization.[49] A total of six Ni(II) complexes were prepared, with the coordination sphere being completed by Cl ligands in complexes **XXXVI**, **XXXVII**, and **XXXIX** and Br ligands in the case of complexes **XXXVIII**, **XL**, and **XLI** as shown in **Figure 1.14**. All the complexes were found to be active for both ethylene oligomerization and polymerization i.e. 7.97 x 10^5 (Ni) hr^{-1} using **XL** and 1.37 x 10^4 (Ni) hr^{-1} with **XXXVIII**, respectively. The presence of PPh_3 as an auxiliary ligand was found

to be essential for improved activity in ethylene oligomerization reactions. This result is consistent with numerous existing literature reports on these types of reactions.[50, 51, 52] Butenes and hexenes were obtained as the main oligomeric products and no odd carbon number products were detected using gas chromatographic analyses, indicating that the oligomer distribution does not follow the Schulz-Flory probability.[49] For complexes, **XXXVI**, **XXXVII,** and **XXXIX**, small amounts of polyethylene were produced, and this result was attributed to steric influences caused by the bulky methyl, ethyl, and isopropyl substituents, respectively.

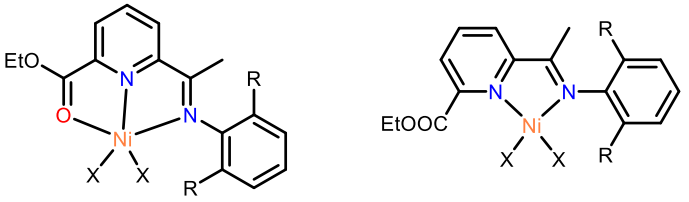

XXXVI: R = Me, X = Cl;
XXXVII: R = Et, X = Cl;
XXXVIII: R = F, X = Br

XXXIX: R = iPr, X = Cl;
XL: R = Cl, X = Br;
XLI: R = Br, X = Br

Figure 1.14: Ni(II) complexes bearing 2-ethylcarboxylate-6-iminopyridyl ligands for ethylene oligomerization and/or polymerization.[49]

The effects of the pyridylimine ligand environment on the catalytic activity can be observed for **XXXIX** which contains a bulky diisopropyl substituent produces long-chain oligomers, C≥8 over 40% oligomer distribution and an increased amount of polyethylene in comparison to complexes **XXXVI** and **XXXVII** which, under similar reaction conditions, produce C≥8 at 14% and 17% oligomer distribution, respectively. Consequently, the less bulky substituted complexes were observed to produce polyethylene in relatively small amounts. These results are consistent with the reasoning that bulky substituents in *ortho*-positions provide sufficient steric hindrance to retard the process of β-hydride elimination.[49]

Increasing the concentration of the co-catalyst, methyl aluminoxane (MAO), led to a diminished catalytic activity potentially due to the presence of impurities like alkyl aluminum in the commercially available MAO that deactivate the catalyst active sites.[49] Lastly, chain transfer to aluminum was observed when reaction temperatures were increased beyond 60 °C and when the Al/Ni ratio was increased beyond 2000. This is evidenced by a decrease in the production of polyethylene under these reaction conditions implying that the rate of chain transfer is greater than the rate of chain

propagation. In addition, this loss of activity can be attributed to lower ethylene solubility at higher temperatures as well as the decomposition of active catalytic sites.[49]

1.3.5 Other explored transition metal complexes derived from pyridylimines

In this section, pyridylimine complexes of rhodium(I), molybdenum(VI), and rhenium(I) transition metals and their use in catalytic applications such as epoxidation of olefins, hydroformylation and transfer hydrogenation reactions will be discussed. An example of a 'heterogenized' homogeneous system will also be discussed in detail for comparison with homogeneous catalyst systems. Although complexes based on platinum group metals (PGMs) like rhodium are generally considered expensive, the incorporation of ligand systems such as pyridylimines leads to the overall system being considered cost-effective and offering superior catalytic activity.

Makhubela and coworkers reported on pyridylimine Rh(I) complexes supported on a biopolymer called Chitosan as selective and recyclable hydroformylation catalysts.[53] Chitosan (**Figure 1.15**) is a biopolymer that can be obtained *via* the deacetylation of chitin, a substance that is found in the cell walls of algae.[54] It offers various advantages such as a high affinity for metal ions, high thermal stability, and contains amine groups that can be modified to create ligand donor sites.[55]

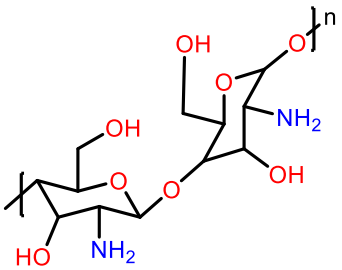

XLII

Figure 1.15: Chemical structure of Chitosan.[54]

A series of supported and unsupported mononuclear complexes shown in **Scheme 1.7** were prepared and evaluated as hydroformylation catalysts using 1-octene as the model substrate. The supported catalysts required an induction period of about 2 hours during which the diffusion of the synthetic gas into the solvent and Rh active sites on the Chitosan occurred. In contrast, the mononuclear monologues displayed high catalytic activity with no induction period required. This result agreed with observations made by Li and coworkers[56], where catalysts supported on SBA-15 required an

induction period before significant activities were observed. For all the catalysts (**XLIII** – **XLVI**), no hydrogenation products were observed and the formation of iso-octenes was favored at low temperatures (55 °C).

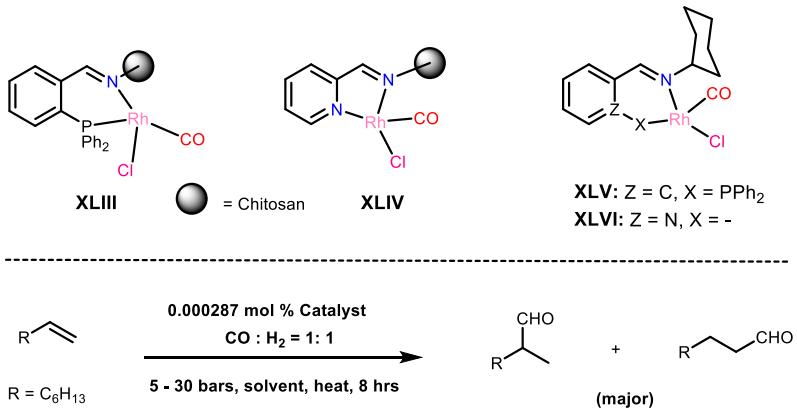

Scheme 1.7: Rh(I) complexes as catalyst precursors for hydroformylation reactions.[53]

Under optimized reaction conditions, all the catalysts (**XLIII** – **XLVI**) favored the formation of linear aldehydes, particularly nonanal. The iminophosphine-based catalysts, **XLIII** and **XLV**, were shown to be more selective, yielding 70 and 72% respectively towards the formation of nonanal compared to iminopyridyl-based catalysts, **XLIV** and **XLVI** which yielded 57% and 68%, respectively. This can be rationalized by assuming that the bulky phosphine ligand allows for a favorable bite angle for 1-octene and/or by the principles of the hard and soft acid-base rule.[57] Based on the n:iso ratios of aldehydes, it was concluded that the biopolymer support does not affect the activity of the rhodium complexes. Rather, the support plays a significant role in stabilizing the catalysts i.e. **XLIII** was recycled and reused four times while its model complex **XLV** decomposed into black particles during the reaction. Rh leaching tests were conducted, and it could be determined that the actual catalytic species are the Rh complexes supported on chitosan since the filtrates from these tests were not active for the hydroformylation of 1-octene. The small amount of Rh that leached into the solution was found to catalyze 1-octene polymerization. The authors suggested that a mixture of Rh complexes and colloidal particles is liable for the isomerization.

Oxomolybdenum(VI) complexes have been employed as catalysts for organic transformations such as the Arco and Halcon processes for propylene epoxidation and have been extensively studied over the last 30 – 40 years.[58,59,60] Balula and coworkers reported on the application of a dichlorodioxomolybdenum(VI) pyridylimine complex as a catalyst precursor for the epoxidation of olefins.[61] Complex **XLVII** (**Scheme 1.8**) was

tested for the epoxidation of cis-cyclooctene and exhibited high catalytic activity and selectivity with cyclooctene oxide being the only product formed in a 93% yield at only 10 minutes of the reaction. The complex was also shown to be highly active in the epoxidation of a variety of longer-chain olefins such as 1-octene, cyclododecene, and others. To improve the recyclability of the complex, **XLVII** was supported on a chemically modified micelle-templated silica support (**XLVIIa** in **Scheme 1.8**), and its catalytic activity was evaluated.

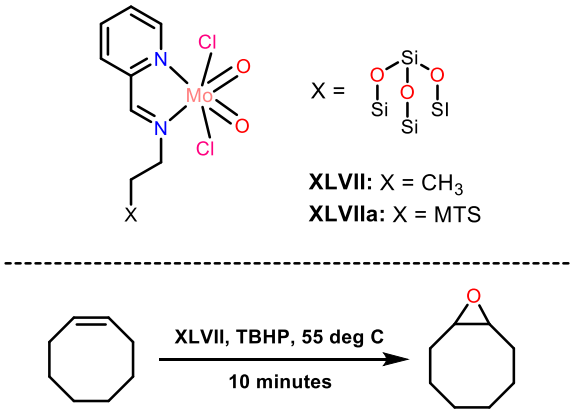

Scheme 1.8: Pyridylimine Mo(VI) complexes for olefin epoxidation reactions.[61]

When the epoxidation of cis-cyclooctene was evaluated using the immobilized catalyst **XLVIIa**, the product (cyclooctene oxide) was obtained at 85% yield only after a reaction time of 24 hours. This implied that the immobilized catalyst, **XLVIIa** performs slightly poorer than the unsupported homogeneous catalyst, **XLVII**. The authors also noted that the reaction rate remained the same over time and proposed that the cause could be deactivation or what they refer to as “non-productive decomposition” of the tert-butyl hydroperoxide (TBHP) oxidant. A series of iodometric titrations were performed and indicated negligible THBP decomposition and from the leaching tests it was concluded that the reaction was homogeneously catalyzed. As a result, the nature of the actual catalytic species could not be elucidated. An approach of using ionic liquids was also explored and yielded no improved results due to difficulties relating to mass transfer between the organic and ionic phases.

Higher oxidation state Re complexes, methyltrioxorhenium(VII), and several of its Lewis base adducts are active catalysts for the epoxidation of olefins.[62] Song and co-workers studied pyridylimine Re(I) carbonyl complexes and their application as olefin epoxidation catalysts.[63] The Re(I) complexes (**Scheme 1.9**) only yielded 30% of the epoxide after 24 hours, which indicated relatively poor activity for this transformation.

A structural variation from the imine N to amine N was made and led to little or no improvement in the catalytic activity. Decreasing the catalyst loading to 1 mol%, led to only 17% of the product being formed. This result is significantly lower than those reported by various researchers under similar reaction conditions.[64, 65, 66] The authors attributed the low activity to the *in-situ* formation of an unstable Re(VII) intermediate species during the reaction which tends to form perrhenate salts that are catalytically inactive. The structure of the unstable Re(VII) intermediate was not isolated and would provide further insights into the mechanism of deactivation of the catalysts. Most significantly, the formation of diols that are a result of the ring opening of epoxides was not observed using ^{1}H NMR and GC analyses, however, there were unidentified side products that formed. Other reported pyridylimine complexes for a range of catalytic reactions include those of iron[67], copper[68], and cobalt[69] and have been extensively reviewed in existing literature reports.

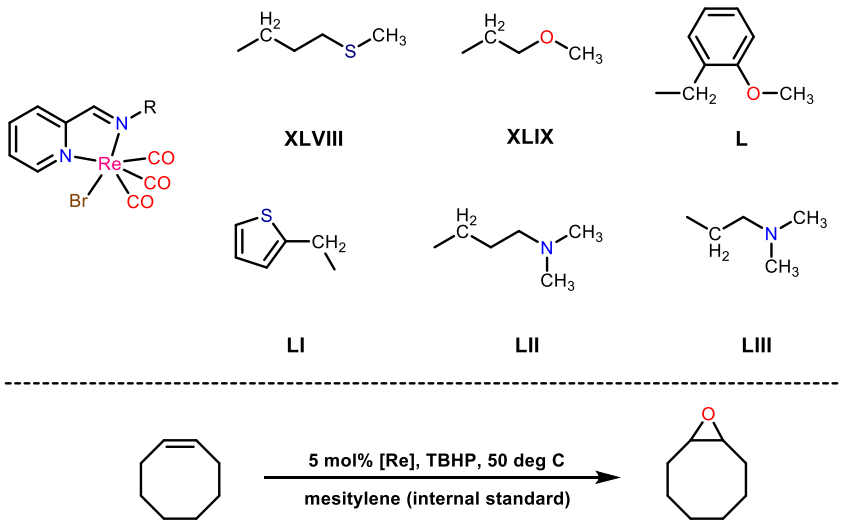

Scheme 1.9: Pyridylimine Re(I) complexes as catalyst precursors for olefin epoxidation.[63]

1.4 Liquid Organic Hydrogen Carriers: Overview & Applications

In this section, a class of compounds known as liquid organic hydrogen carriers (LOHCs) will be explored briefly. These compounds have been singled out as having the highest potential towards the implementation of the so-called 'hydrogen economy' and several aspects including but not limited to, their properties, advantages and/or disadvantages, examples, and feasibility to implement at a large scale, will be discussed in this section. To give context, the history and rationale behind the use of hydrogen as a source of clean energy will be provided.

The use of hydrogen as an energy vector is an idea that has been postulated as early as 1976.[70] This has led to many scientific developments toward a hydrogen economy and these were succinctly summarized by Bockris in 2013.[71] Hydrogen is desirable for several factors, most important being that its combustion usually liberates water (H_2O) as the only by-product and if the hydrogen can be sourced using techniques such as water electrolysis, an energy system that does not require carbon dioxide (CO_2) can be achieved.[72, 73] Of all the known energy vectors, hydrogen exhibits the highest gravimetric energy density (33.3 kWh/kg) as illustrated in **Figure 1.16** below.[74] The main barrier to the realization of a hydrogen economy has been attributed to the fact that it has to be produced from other forms of energy which often produce a lot of CO_2 as well as the high cost related to storing and transporting elemental hydrogen in large amounts.[74] The low volumetric energy density of H_2 is the main contributing factor to its difficulty in storage and delivery as indicated in **Figure 1.16**.

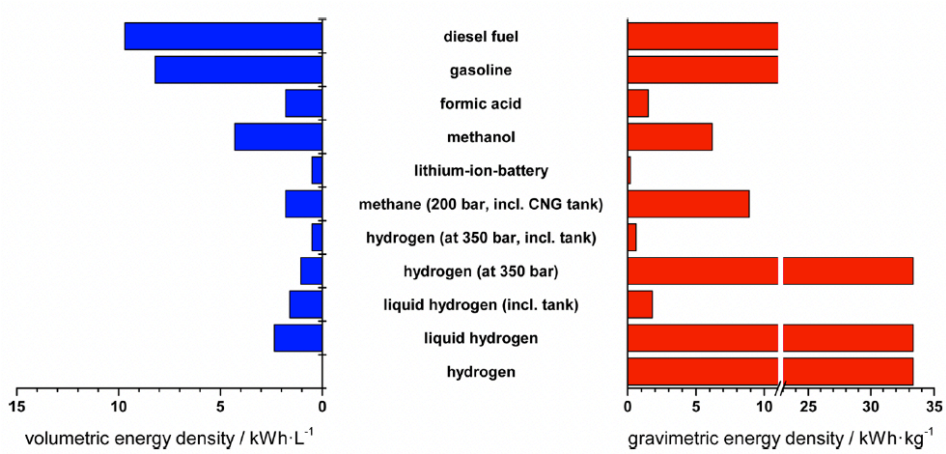

Figure 1.16: Comparison of the volumetric and gravimetric energy density of various energy carriers. Taken from reference.[74]

Several technological advancements such as the use of compressed and cryogenic hydrogen have been made to improve the volumetric energy content but are beyond the scope of our study.[75, 76] We will limit our discussion to LOHCs which are organic compounds that can store and release hydrogen through catalytic hydrogenation and dehydrogenation reactions, respectively.[74] LOHC systems should ideally possess several characteristic properties which include, a low melting point (< -30 °C) and a high boiling point (> 300 °C), a high hydrogen storage capacity (> 6 wt%), low production costs, toxicological safety during transportation, compatibility with modern infrastructure for fuels

and most importantly, low heat of desorption as this enables LOHCs to be dehydrogenated at relatively low temperatures (< 200 °C).[77, 78]

Well-studied examples of LOHC systems include those based on aromatic hydrocarbons such as toluene (TOL) and methylcyclohexane (MCH), N-heteroaromatics such as N-ethyl carbazole (H0-NEC), and perhydro-N-ethyl carbazole (H12-NEC) as shown in **Figure 1.17**. The drawbacks of the TOL/MCH system include the formation of side products *via* alkylation or coking when applied to Pt or Ni heterogeneous catalyst systems.[79, 80] On the other hand, the H0-NEC/H12-NEC system suffers from high dehydrogenation enthalpies (50 kJ/mol) and the dissociation of the N-alkyl substituent.[81] Other drawbacks include the use of high reaction temperatures and pressures. Modisha and coworkers have written an excellent review that details how the LOHC process can be integrated into the existing infrastructure networks, type of industrial reactors, key market participants, as well as opportunities that exist in South Africa concerning the mining, transportation, and electricity industries.[82]

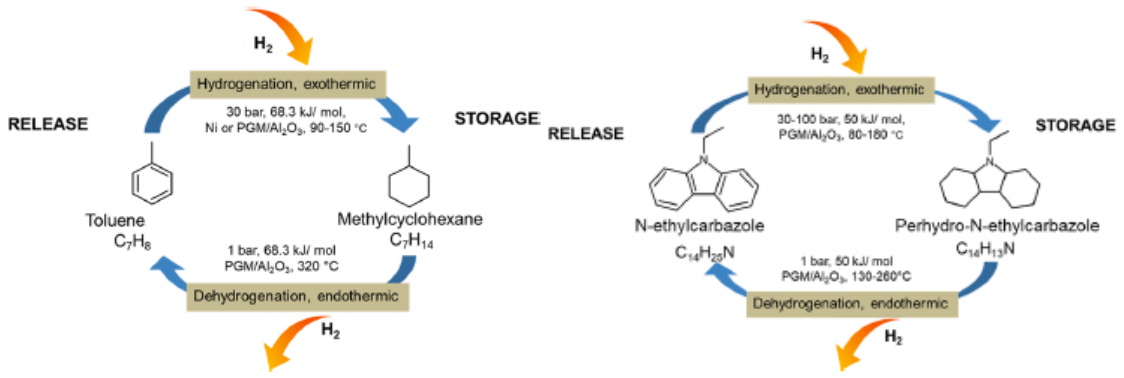

Figure 1.17: Schematic representation of the TOL/MCH (left) and H0-NEC/H12-NEC (right) LOHC systems. Taken from reference.[82]

The bulk chemicals, methanol and formic acid are the two most studied LOHCs largely due to their high volumetric energy densities and reasonably good gravimetric energy densities, which make them suitable candidates for catalytic hydrogenation and dehydrogenation at relatively low reaction temperatures and pressure. Our study delves into the dehydrogenation of formic acid using homogeneous Mn(I) and Ru(II) catalysts. The hydrogenation pathway necessary to complete a LOHC system falls outside the scope of our work and will not be discussed further. The use of manganese(I), ruthenium(II), and iridium(II) complexes toward formic acid dehydrogenation is discussed in the following section.

1.5 Homogeneous Catalysts for Formic Acid Dehydrogenation

The dehydrogenation of formic acid (HCOOH, FA) to selectively produce hydrogen using homogeneous catalysts was initiated by the seminal work of Beller and Laurenczy in 2008.[83, 84, 85] This section aims to provide insights into the various approaches to FA dehydrogenation that have been explored in the literature. The use of homogeneous catalysts based on ruthenium, manganese, and iridium metal centres toward FA dehydrogenation will form the basis of this discussion. Solid-supported heterogeneous catalyst systems for FA dehydrogenation remain an active area of interest for many researchers due to their high recovery.[86] However, they have consistently been outperformed by their analogous homogeneous catalyst systems which have achieved maximum turnover frequencies (TOF) of about 7000 hr^{-1}.[86] As a result, they will not form part of this discussion.

1.5.1 Ruthenium Catalyzed Formic Acid Dehydrogenation

Albrecht and co-workers reported on efficient additive-free formic acid dehydrogenation with a light-sensitive, NNN-ruthenium complex where the central amide functional group acts as an internal base.[87] Two moisture-stable Ru(II) complexes, **LIVa** and **LIVb** were prepared and found to be highly active for FA dehydrogenation (**Scheme 1.10**). Both complexes show similar reaction profiles and catalytic performance in DMSO, which suggests that the counter ion does not influence the catalytic cycle. Complex **LIVa** shows higher catalytic activity and outperforms many reported ruthenium-based systems i.e. Fischmeister's complex only reaches a TOF of 230 hr^{-1} compared to 10 000 hr^{-1} reached by **LIVa** under optimized reaction conditions i.e. **LIVa** (0.2 mol%), DMSO (1.2 mL), temperature (80 °C).[88]

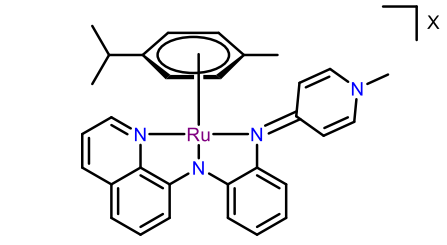

LIVa: X = OTf, **LIVb:** X = PF_6

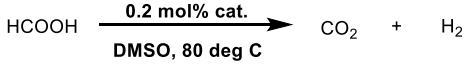

Scheme 1.10: Ru(II) complexes for additive-free formic acid dehydrogenation.[87]

Several solvents including dioxane, DMSO, water, propylene carbonate, and a mixture of toluene and tBuOH were screened, with no activity being observed when H_2O was used. The highest catalytic activities were seen when DMSO and dioxane were used, with initial TOFs around 2000 hr^{-1}. An interesting observation was made when propylene carbonate was employed as a solvent being that the gas evolution profile changes completely in comparison to that of other solvents as shown in **Figure 1.18**. This was rationalized by a slow catalyst activation in this solvent, the formation of a new co-solvent, or a gradual pH increase when FA is consumed. This result correlated with what has been reported previously with various carbonate solvents.[89] As expected, an increase in the reaction temperature was accompanied by an increase in catalytic activity due to a higher average kinetic energy of the molecules which leads to more effective collisions.

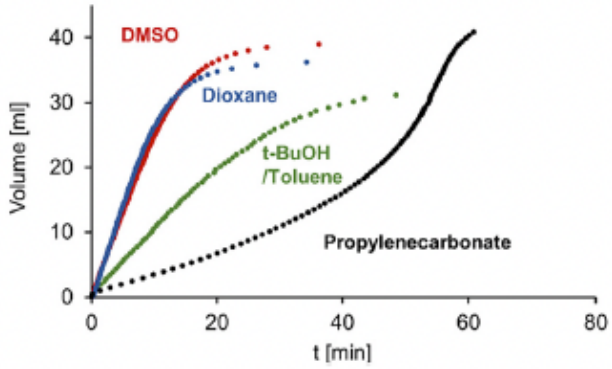

Figure 1.18: Gas evolution profiles for catalyst **LIVa** in different solvents towards FA dehydrogenation. Taken from reference.[87]

Based on the ^{1}H NMR, *in situ* UV-Vis, and kinetic studies of **LIVa** under catalytic conditions, a pathway for the activation of the complex for FA dehydrogenation was suggested as shown in **Scheme 1.11** below. This involves a fast protonation of the amide N which is understood to weaken the Ru – N bond thereby enhancing coordination by the formate. The Eyring analyses indicated $\Delta S^{\ddagger}$ = -177 ± 3 J/K/mol which does not support the proposition of β-hydrogen elimination but rather an associative turnover limiting step such as the interaction of Ru hydride and FA. The catalyst resting state was observed using UV-Vis as a purple solution (λ_{max} = 550 nm) that coincided with gas evolution. Most notably, the usually catalytically active Ru-H species was reported as inactive for this catalyst system, which is an observation that has not been made for similar or related catalyst systems.

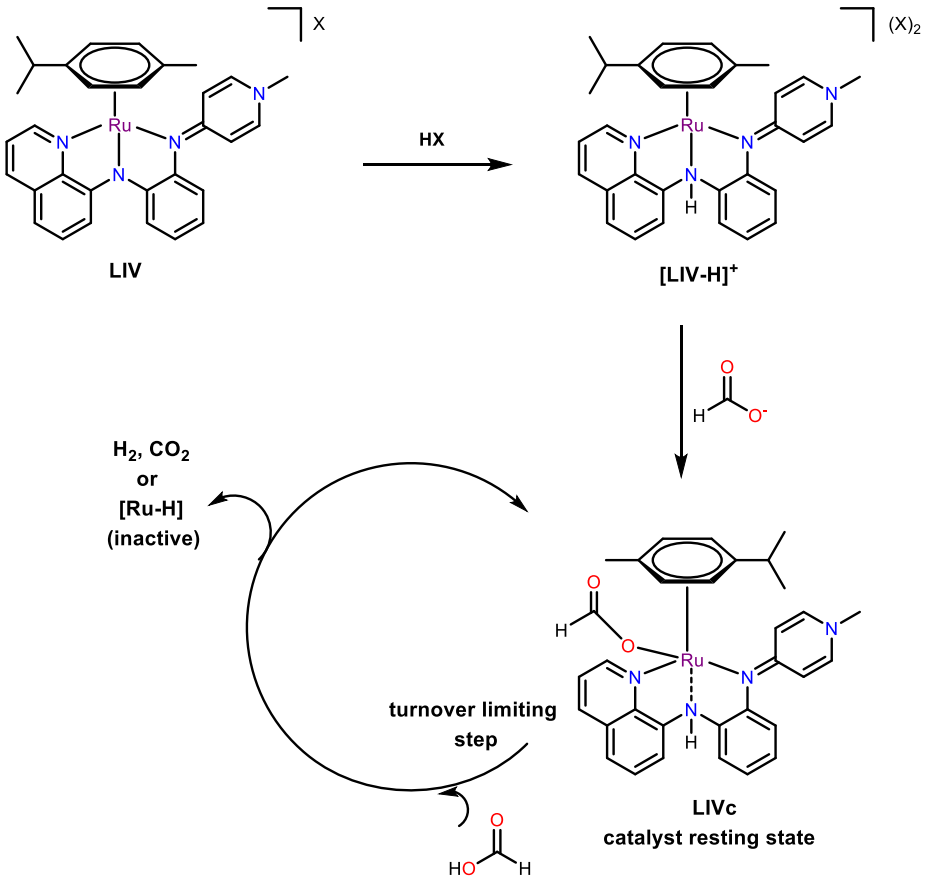

Scheme 1.11: A proposed pathway for activation of a Ru(II) catalyst, **LIVa** for FA dehydrogenation.[87]

In another literature report, Guan and co-workers reported on the dehydrogenation of FA over a ruthenium complex bearing an N,N'-diimine ligand.[90] Unlike other reported catalyst systems, complex **LV** shown in **Scheme 1.12** was able to catalyze the conversion of FA to hydrogen and carbon dioxide using water as a solvent without the addition of any organic additives with TOFs as high as 12 000 hr^{-1} and TONs of 350 000 at 90 °C. To rule out the possibility of the reaction being accelerated by the presence of a Lewis acidic Na^+, Na_2SO_4 was used as an additive and no remarkable changes in the TOF were observed in comparison to when sodium formate (HCOONa) was added. It was also noted that formate is not decomposed directly in this catalyst system, as little gas formation was seen when the aqueous HCOONa solution was heated in the presence of **LV** at 90 °C.[91] Importantly, no formation of carbon monoxide (CO) was observed in this system, which is essential for fuel cell applications as CO would poison the electrodes.[92] In this literature report, the authors have presented the first example of a Ru(II) catalyst system that operates using water as a solvent and can produce high-pressure hydrogen gas as indicated by their studies of FA dehydrogenation in an autoclave to generate a total of 25.8 MPa gases.

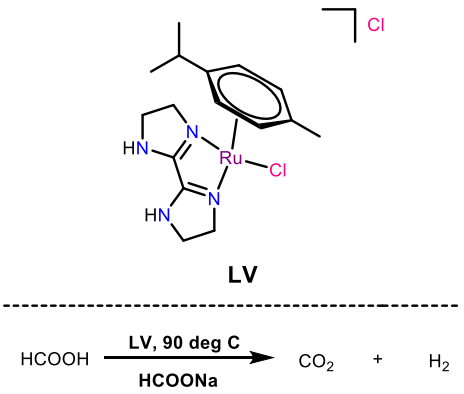

Scheme 1.12: N,N'-diimine ligated Ru(II) complex for FA dehydrogenation.[90]

Based on ESI-MS, ^{1}H NMR, and DFT studies, a plausible reaction mechanism toward FA dehydrogenation was proposed and is shown in **Scheme 1.13** below. This suggests that there may be two competitive reaction pathways for the key hydride transfer rate-determining step. This was supported by the presence of two hydride peaks at δ = -6.70 ppm and δ = -7.70 ppm in the ^{1}H NMR spectrum implying the formation of two Ru-H species. As a result, two reaction pathways were proposed (**Scheme 1.13**). When the reaction is performed in an aqueous FA medium, an energetically favorable (7.8 kcal/mol) water-coordinated Ru(II) complex, **LVa** is produced followed by the replacement of the aqua ligand by the formate to afford a stable intermediate species, **LVb** with -1.0 kcal/mol and a favorable Ru-N bond length of 2.101 Å. The decarboxylation of the formate results in the formation of the more energetically favourable key hydride complex, **LVc** with -1.9 kcal/mol, and the subsequent regeneration of the aqua Ru complex, **LVa** that coincides with H_2 gas production. Under more basic conditions, **LV** can be deprotonated with the loss of a chloride ligand to afford the singly charged species, **LVd**, in a reaction that has a low activation energy barrier (6.8 kcal/mol). This is followed by the coordination of formate on the Ru metal centre to form **LVe** which possesses shorter Ru-N bonds in comparison with **LVb** and subsequent decarboxylation of the formate to generate the active Ru-H complex, **LVf**. The formation of H_2 was investigated by studying two proton sources i.e. formic acid and the hydrated proton, presumed to be responsible for the protonation of the hydride intermediate, **LVc**. It was determined that the transition state with FA as the H^+ source had an activation energy barrier 13.7 kcal/mol higher than the transition state with the hydrated proton. In addition, the transition state with FA contained longer Ru-H (1.789 Å) bonds in comparison to the transition state resulting from the hydrated proton (1.700 Å). As a result, the hydrated proton was responsible for H_2 formation in the pathway that occurs without the presence of a base.

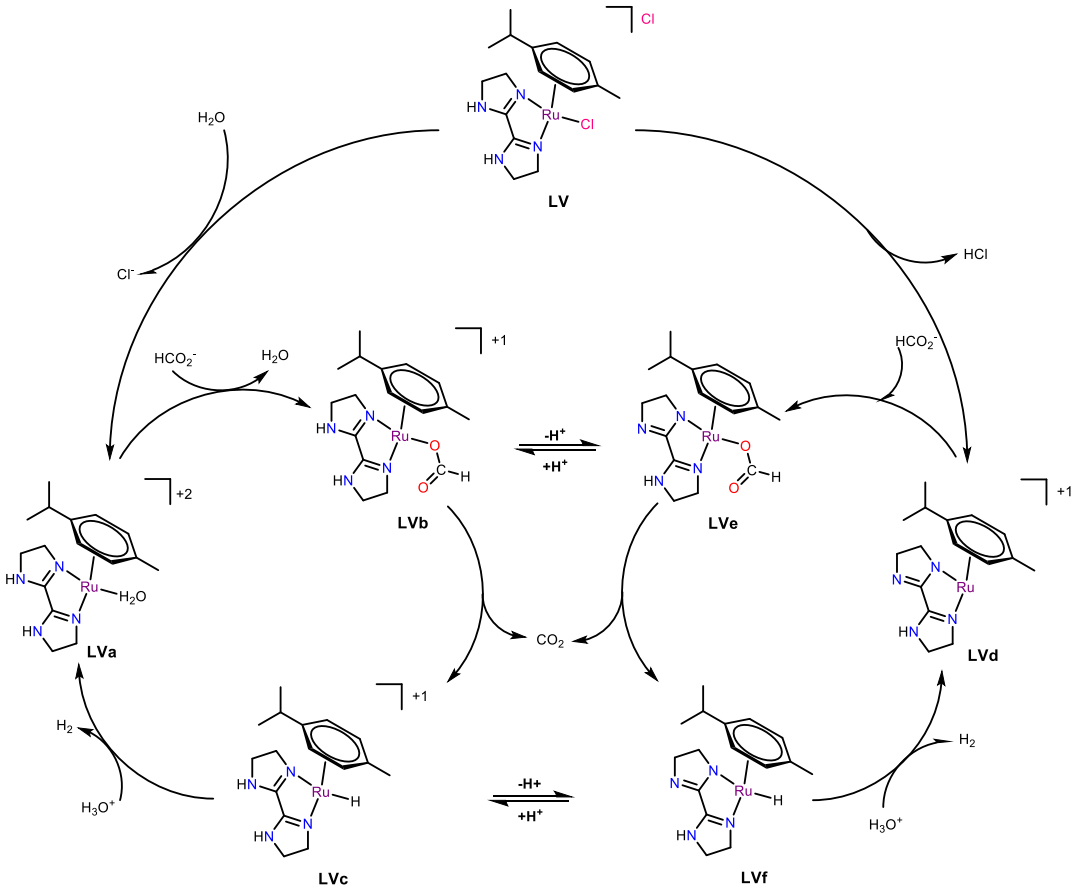

Scheme 1.13: Suggested reaction mechanism for FA dehydrogenation using a Ru(II) complex.[90]

Milstein and co-workers reported on a highly efficient ruthenium complex for additive-free dehydrogenation of neat formic acid.[93] A 9*H*-acridine Ru complex (**Scheme 1.14**) with remarkable solubility and stability in FA was prepared and found to be highly active towards FA dehydrogenation reaching TOFs as high as 3 067 hr^{-1} and TONs of about 1.7 million. Many catalysts often display poor solubility in FA, this factor coupled with the high acidity of FA renders many complexes ineffective toward the dehydrogenation of neat FA usually through the formation of unwanted catalytic species.[93] The difficulty in dehydrogenating neat FA at low temperatures is attributed to its endergonic nature (ΔG = 2.9 kcal/mol) as shown by Density Functional Theory (DFT) calculations.[93] Interestingly, **LVI** can dehydrogenate FA at room temperature as gas evolution is observed as soon as **LVI** and FA are mixed. A long-term experiment was carried out to test the robustness of the catalyst system and the activity was retained for over 50 days. Variations in the reaction conditions such as cooling down and heating the reaction solution during this reaction did not have a measurable impact on the activity of **LVI**. After 19 days of continuous operation, about 1.2 L of FA was dehydrogenated to produce more than 1 560 L of H_2/CO_2 gas with minimal CO gas content (< 20 ppm).

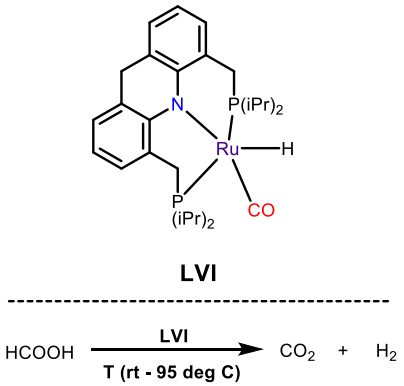

Scheme 1.14: Ru(II)-hydride complex for neat formic acid dehydrogenation.[93]

Most of the FA that is produced industrially, occurs *via* the hydrolysis of methyl formate, a process that requires large amounts of H_2O.[94] Hence, commercially available FA contains various amounts of water as dictated by the purity level of the acid. As a result, complex **LVI** was shown to survive the presence of water as similar dehydrogenation activities were observed when different grades of FA (98 – 100%, 97%, and 85%) were screened as illustrated in **Figure 1.19** below.

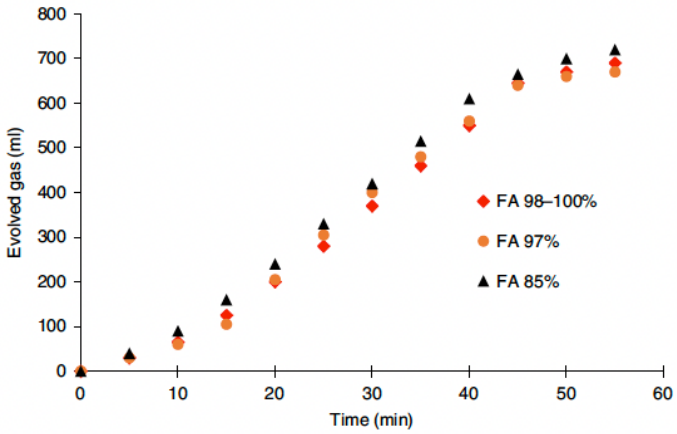

Figure 1.19: Catalytic dehydrogenation of different grades of FA using **LVI**. Taken from reference.[81]

Using ^{1}H NMR and DFT investigations, a plausible reaction mechanism using **LVI** was suggested and is shown below (**Scheme 1.15**). In this case, mixing FA and the Ru-acridine complex results in the formation of kinetically unstable *mer* isomers **LVIa** and **LVIb** that convert to a stable complex **LVIc** under ambient conditions. Intermediate species, **LVIc** and **LVId** exist in equilibrium and are stable under a CO_2 atmosphere. A similar reaction pathway was observed when **LVI** was reacted with acetic acid at room temperature. From the Eyring analyses, an activation energy barrier of 23.1 kcal/mol in close agreement with

DFT calculations was determined. A small kinetic isotope effect was observed when HCOOH was substituted with HCOOD and served as confirmation that H_2 generation precedes CO_2 formation during the catalytic cycle.

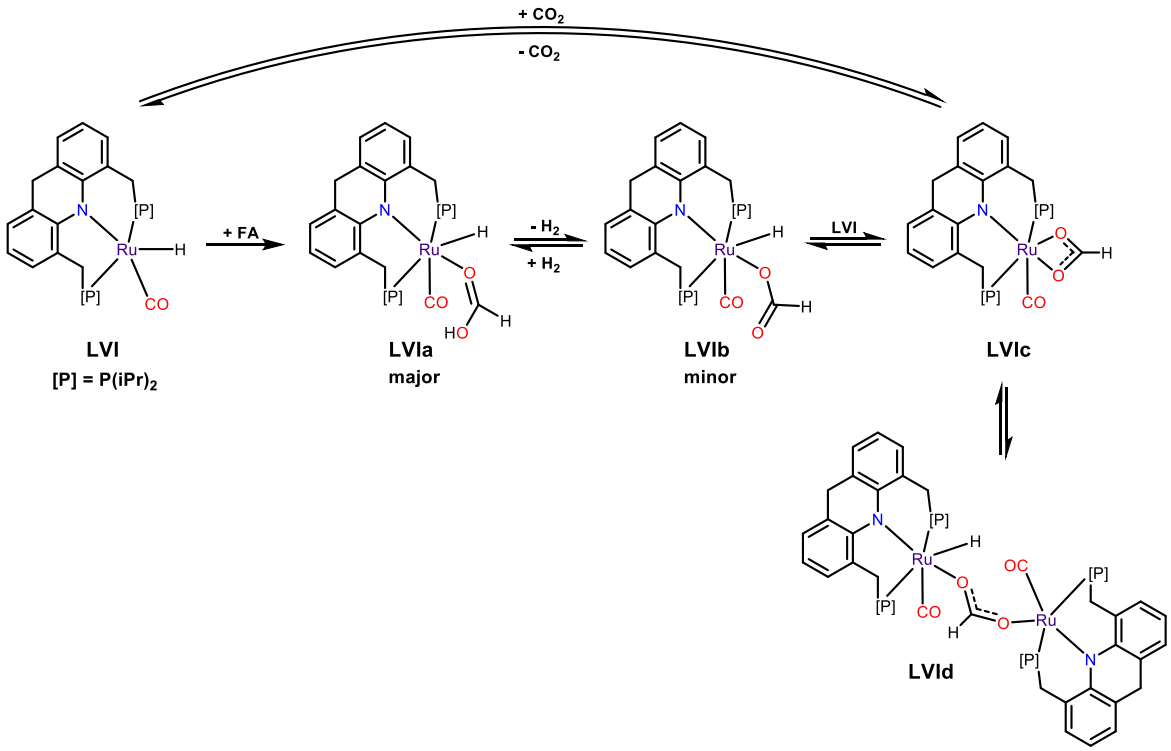

Scheme 1.15: A plausible reaction mechanism for FA dehydrogenation using a Ru(II) catalyst **LVI**.[92]

1.5.2 Manganese Catalyzed Formic Acid Dehydrogenation

The use of manganese in catalytic (de)hydrogenation reactions is rarely explored in the literature, largely due to the lack of suitable auxiliary ligands. Ligand systems that are rigid, and possess a strong field are known to avoid the unproductive high-spin states of Mn complexes and are necessary for dehydrogenation reactions.[95] It was not until 2016 that the first examples of Mn-catalyzed (de)hydrogenation reactions were reported by the groups of Milstein and Beller i.e. alcohol dehydrogenation and ketone hydrogenation, respectively.[20, 21] In this section, a few examples of Mn(I) complexes as catalyst precursors for FA dehydrogenation is discussed.

Beller and coworkers reported on the use of a manganese(I) κ^2-NN complex for FA dehydrogenation.[96] The catalyst system (**Scheme 1.16**) yielded improved gas evolution and better turnover numbers (TON = 7883 after 12 cycles of FA dosage) in comparison

to a similar and related catalyst system i.e. TON = 5746 under optimized conditions (HCOOH:DMOA = 11:10, catalyst loading of 57 μmol and reaction temperature of 95 °C) reported by the same group. Varying the reaction temperature from 75 – 95 °C resulted in not only improved gas evolution but also an increase in the CO content in the gas phase. Hence, FA dehydrogenation systems should not be heated at temperatures above 100 °C as the pathway toward FA dehydration or decarbonylation is favored. Unlike other Mn(I) complex systems, this Mn(I) catalyst system operates without the need for Lewis acid additives that have previously been shown to promote the dehydrogenation of FA.[97]

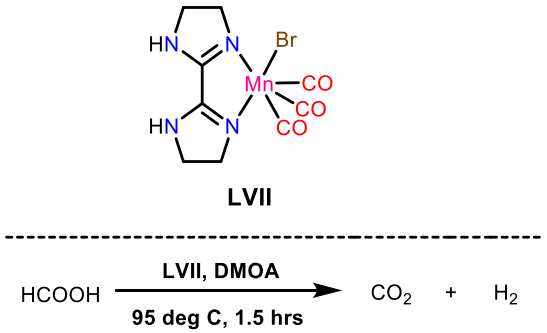

Scheme 1.16: Mn(I) complex for efficient formic acid dehydrogenation.[96]

Previous reports have suggested that the N-H functional group on imidazoline-based ligands is necessary for enhanced catalytic performance.[98, 99] An *in situ* catalytic system was developed to easily screen the ligands and was found to have similar catalytic activity as the discrete, isolated catalyst shown in **Scheme 1.16**. Several ligands were prepared and tested for FA dehydrogenation using the optimized *in situ* conditions (**Figure 1.20**). The benzoylated ligands, **LVIId**, **LVIIe,** and **LVIIf** showed a noticeable decrease in catalytic activity due to the absence of the N-H moiety. An increase in FA dehydrogenation was observed in the case of **LVIIf** due to the electron-withdrawing trifluoromethyl group that increases the electrophilicity of the Mn metal centre. The ligand bearing the methyl substituents, **LVIIc** was found to be poorly active largely due to the steric hindrance which inhibits ligand coordination to the metal centre. It can therefore be concluded that the structure of the ligand can negatively influence substrate coordination in an *in situ* system which results in poor catalytic performance.

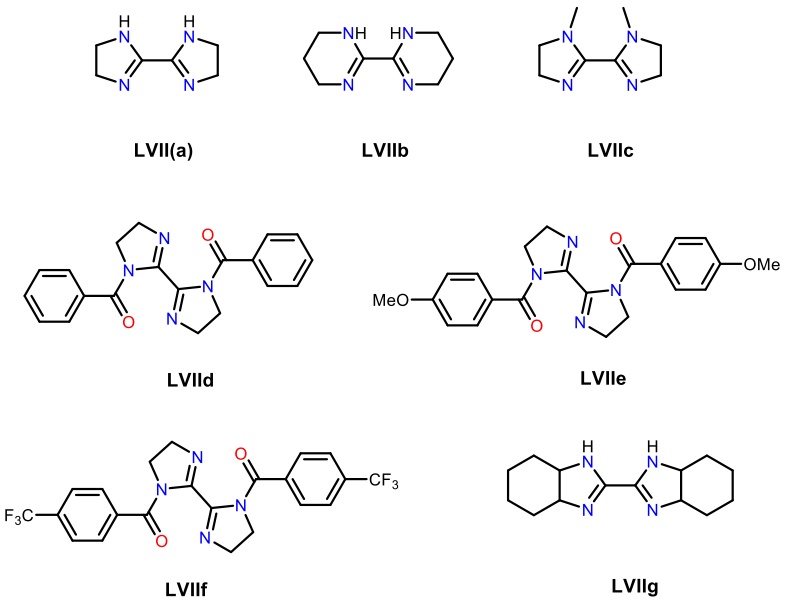

Figure 1.20: A series of bisimidazoline ligands tested for FA dehydrogenation.[96]

Dutta and coworkers detailed a FA dehydrogenation system catalyzed by a phosphorus-nitrogen PN^3P-manganese pincer complex that reaches a TON of 15 200 in about 49 hours under optimized reaction conditions i.e. 10 μmol of catalyst, acid-amine ratio of 1 and 90 °C reaction temperature.[100] This represents the highest TON achieved for a manganese-catalyzed FA dehydrogenation system. Aromatized and dearomatized versions of the Mn(I) complex were prepared and it was discovered that the latter has similar reactivity but yields a slightly lower turnover frequency (**Scheme 1.17**). Solvent screening studies indicate that the reaction does not occur in water, non-polar solvents such as toluene and moderately polar solvents such as THF result in no gas evolution when a reaction is conducted in these solvents. Mechanistically, this hints at the reaction proceeding through a polar intermediate that is stabilized by a polar solvent. No gas evolution was observed in the absence of a base and lowering the temperature led to an expected decrease in the conversion of the FA substrate.

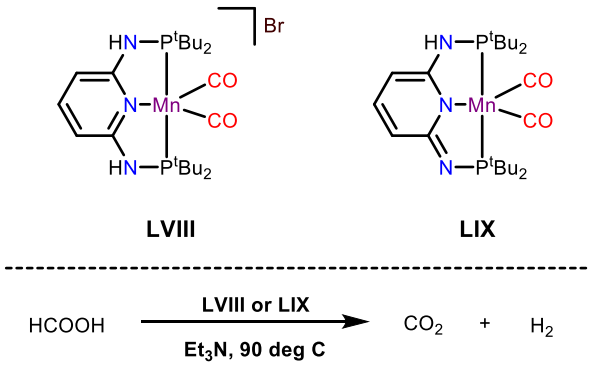

Scheme 1.17: Mn(I) catalysts for formic acid dehydrogenation.[100]

A plausible reaction mechanism based on ^{1}H NMR studies was suggested and is shown in **Scheme 1.18** below. In this instance, **LVIII** is dearomatized in the presence of triethylamine accompanied by a loss of the Br ligand to afford intermediate species **LVIIIa** followed by FA coordination to form the aromatized intermediate **LVIIIb** and subsequent decarboxylation of the formate to afford the catalytically active Mn-H complex, **LVIIIc** that allows for H_2 gas formation and the regeneration of the dearomatized intermediate **LVIIIa**.

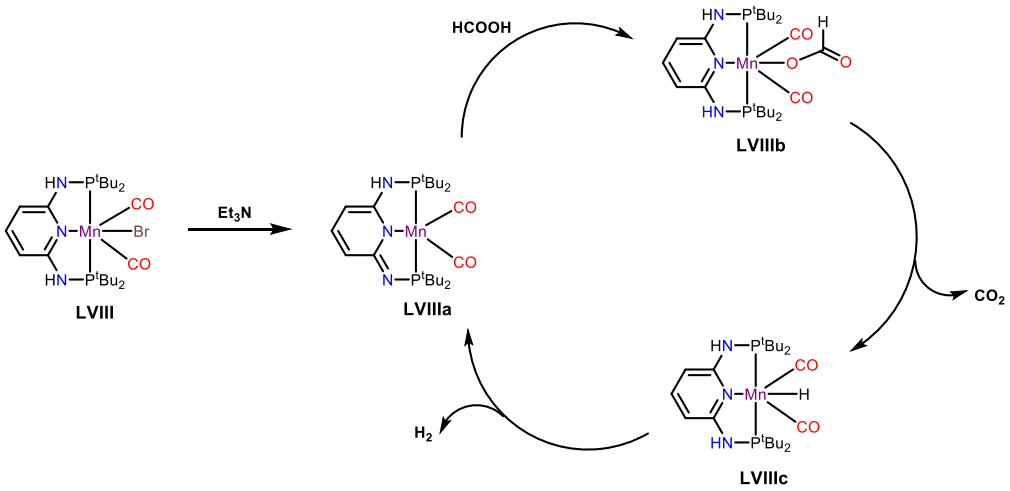

Scheme 1.18 A reaction mechanism for FA dehydrogenation using a Mn(I) complex **LVIII**.[100]

1.5.3 Iridium Catalyzed Formic Acid Dehydrogenation

Iridium-based complexes are highly effective for many catalytic processes and consistently outperform other complexes based on ruthenium and rhodium transition metals. However, the high cost of iridium has often led to researchers seeking cheaper alternative metal sources such as ruthenium (6x cheaper) and manganese (the third most abundant transition metal on Earth). This section will highlight the use of one iridium complex that does not obey the usual 18-electron rule for metal complexes in FA dehydrogenation.

Albrecht and coworkers reported on a low-coordinate iridium complex bearing a donor-flexible O,N-ligand for highly efficient FA dehydrogenation.[101] Under optimized reaction conditions i.e. 0.01 mol% of catalyst, 1 mL of DMSO, HCOOH, and HCOOLi in equimolar amounts (1 mmol) at 80 °C, complex **LX** in **Scheme 1.19** achieves TOFs of about 280 000 hr^{-1} with a 1:1 mixture of CO_2 and H_2 produced without any detectable amounts of H_2O or CO as determined by GC-TCD analyses.

When the alkali cation of the formate was varied, a trend (Li > Na > K) in the catalytic activity was observed with TOFs of 2900, 2000, and 1300 hr^{-1}, respectively. This was attributed to the Lewis acid activation of the substrate.[104] Upon FA consumption, a gradual decrease in activity attributable to pH changes is observed. Adding fresh batches of FA every 30 minutes led to maintained TOFs of 22 000 hr^{-1} over an extended period, reinforcing the role of formate as an additive and not a reactant in the system. The catalytic rate was maintained for over 60 hours at 60 °C and for over 8 hours at 100 °C indicating the robustness of the catalyst **LX**.

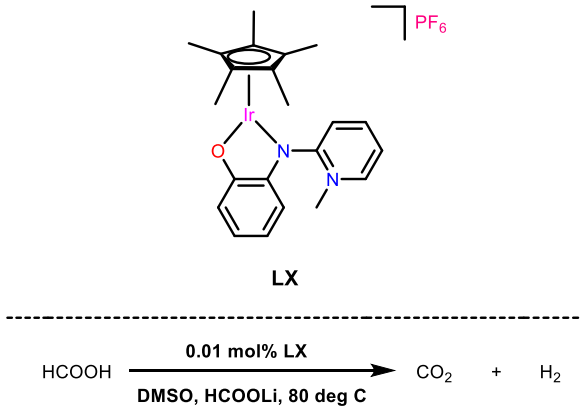

Scheme 1.19: A low coordinate, bidentate Ir complex for FA dehydrogenation.[101]

From the Eyring plot analyses, the activation parameters $\Delta H^{\ddagger}$ = 74 kJ/mol and $\Delta S^{\ddagger}$ = -146 J/K/mol were determined. A highly negative entropy value indicates an associative mechanism in the rate-determining step i.e. the reaction of the intermediate with formic acid.[105] Varying the catalyst concentration from 0.1 mol% to 0.3 mol% leads to increased gas evolution with a first-order rate dependence on the catalyst. A series of kinetic isotope experiments using HCOOH and its various isotopologues i.e. DCOOH, HCOOD, and DCOOD were conducted, and it was observed that the reaction rate decreases significantly when HCOOD is employed. This result implied the protonation of the Ir-H intermediate or an O-H bond cleavage as the rate-determining step. Lastly, a detailed cost and productivity analysis was presented to illustrate the cost efficiency of catalyst **LX** over many state-of-the-art catalysts, even those based on Earth-abundant metals such as Fe.

1.6 Conclusions

This brief review clearly outlines the reactivity and use of Schiff base complexes of transition metals such as manganese(I), palladium(II), ruthenium(II), and nickel(II) for a range of catalytic processes such as ethylene oligomerization/polymerization, transfer hydrogenation, methoxycarbonylation, and acceptorless dehydrogenation. Some less explored Schiff base complexes such as those of rhodium(I), molybdenum(VI), and rhenium(I) are discussed concerning their use as catalysts for transformations such as hydroformylation and epoxidation reactions. As far as the dehydrogenation of formic acid is concerned, complexes of ruthenium and iridium are amongst the most applied, with iridium exhibiting superior catalytic performance. However, the application of iridium complexes is limited by its high cost, and cheaper alternatives such as ruthenium and manganese are increasingly becoming more attractive. Although ruthenium(II) complexes bearing Schiff base ligands have been widely prepared and applied in various organic transformations, there exists no literature report, to the best of our knowledge, that details their use as catalyst precursors for FA dehydrogenation. To date, very few literature reports detail the use of manganese(I) complexes toward FA dehydrogenation with the existing reports focusing largely on the use of complexes bearing tridentate pincer-type ligands.[96, 100, 104, 105] It is in this context, that pyridylimine-ligated Mn(I) and Ru(II) complexes and their application as precatalysts in the dehydrogenation of FA will be investigated in this study. The aim and objectives of the study are outlined in the following section.

1.7 Aim and Objectives

This study aims to design stable nitrogen donor pyridylimine manganese(I) and ruthenium(II) complexes that are active for formic acid dehydrogenation, a common LOHC, as a route to the production of dihydrogen.

The objectives of this project are outlined below:

1. Synthesis and spectroscopic characterization of bidentate pyridylimine ligands with different aromatic and aliphatic substituents on the imine nitrogen. Various electron-donating alkyl functional groups will be introduced on the aromatic substituents to tune the electrophilicity of manganese and potentially improve the reactivity of the resulting complexes. Additionally, the incorporation of these groups increases the steric hindrance and allows for electronic modulation around the metal centre resulting in enhanced selectivity.

2. Synthesis and spectroscopic characterization of neutral, pyridylimine manganese(I) complexes obtained from the Schiff base ligands. The photostability of the complexes will be studied employing SCXRD and FT-IR spectroscopy.

3. Synthesis and spectroscopic characterization of cationic, half-sandwich ruthenium(II) complexes obtained from the Schiff base ligands.

4. Catalytic evaluation of pyridylimine Mn(I) and Ru(II) complexes as catalyst precursors for formic acid dehydrogenation en route to the production of dihydrogen. The influence of catalyst loading, formic acid concentration, reaction time, base or formate concentration, temperature, solvent effects, and pyridylimine variation will be investigated in detail. In addition, mechanistic details of FA dehydrogenation will be investigated using kinetic studies and ^{1}H NMR monitoring experiments.

1.8 Overview of the Dissertation by Chapter

Chapter 1 provides a brief overview of the history and coordination properties of pyridylimine ligands. An in-depth discussion of various pyridylimine-ligated transition metal complexes and their application as catalyst precursors in several organic transformations is provided. The concept of liquid organic hydrogen carriers (LOHCs) is briefly introduced and the key properties of a good LOHC system are discussed. The key benefits of using formic acid (FA) as a hydrogen storage medium are provided alongside several examples of transition metal-catalyzed FA dehydrogenation.

The preparation of nine neutral manganese(I) complexes derived from pyridylimine ligands is detailed in **Chapter 2**. Spectroscopic and crystallographic insights into the dissociation of Mn-CO bond under light exposure conditions are provided. This chapter also illustrates our attempts at FA dehydrogenation employing the synthesized Mn(I) complexes as catalyst precursors in this transformation.

Chapter 3 delves into the preparation and characterization of eleven cationic half-sandwich ruthenium(II) complexes. The application of the ruthenium complexes prepared in this chapter as catalyst precursors toward the dehydrogenation of FA is discussed in **Chapter 4**. Several reaction parameters such as temperature, catalyst loading, substrate loading, solvent effects, and the addition of various additives form a key part of this chapter. Based on evidence from ^{1}H NMR spectroscopy and kinetic studies, a reaction mechanism for the dehydrogenation of FA is proposed.

Chapter 5 provides a summary of the salient findings from each chapter, and concluding remarks based on the obtained data in the dissertation are discussed. Lastly, prospects concerning the research conducted in this project are outlined.

1.9 References

1. Boulechfar, C., Ferkous, H., Delimi, A., Djedouani, A., Kahlouche, A., Boublia, A., Darwish, A. S., Lemaoui, T., Verma, R., Benguerba, Y. *Inorg. Chem. Commun.,* **2023**, *150*, 110451.
2. Schiff, H. Mittheilungen aus dem Universitats-laboratorium in Pisa (A report from the University Laboratory in Pisa). *Justus Liebigs Ann. Chem.*, **1864**, *131,* 118 – 119.
3. Temel, H., İlhan, S., Şekerci, M., Ziyadanoğullari, R. *Spectrosc. Lett.*, **2002**, *35(2)*, 219 – 228.
4. Schiff, H. E. *Ann. Chem. Pharm.,* **1866**, *140*, 92 – 137.
5. Plesch, G., Kettman, V., Sivy, J., Švajlenova, O., Friebel, C. *Polyhedron*, **1998**, *17*, 539 – 545.
6. Kauffman, G. B., Jorgensen, S. M., A chapter in coordination chemistry history, **1959**.
7. Werner, A. *Zeitschr. Anorg. Chem.,* **1893**, *3*, 267.
8. Xavier, A., Srividhya, N. *IOSR J. Appl. Chem.,* **2014**, *7(11)*, 2278 – 5736.
9. Liu, X., Hamon, J. R. *Coord. Chem. Rev.*, **2019**, *389*, 94 – 118.
10. Solankee, A., Thakor, I. *Indian J. Chem.,* **2006**, *45(b)*, 517.
11. Dogaheh, S. G., Khanmohammadi, H., Sañudo, E. C. *Polyhedron*, **2017**, *133*, 48 – 53.
12. Bruns, H., Patil, M., Carreras, J., Vázquez, A., Thiel, W., Goddard, R., Alcarazo, M. *Angew. Chem. Int. Ed.,* **2010**, *49(21)*, 3680 – 3683.
13. Kostova, I., Saso, L. *Curr. Med. Chem.,* **2013**, *20(36)*, 4609 – 4632.
14. Malik, M. A., Dar, O. A., Gull, P., Wani, M. Y., Hashmi, A. A. *Med. Chem. Commun.,* **2018**, *9(3)*, 409 – 436.
15. Pioquinto-Mendoza, J. R., Rosas-Ortiz, J. A., Reyes-Martínez, R., Conelly-Espinosa, P., Toscano, R. A., Germán-Acacio, J. M., Avila-Sorrosa, A., Baldovino-Pantaleón, O., & Morales-Morales, D. *Inorg. Chim. Acta*, **2015**, *438*, 146 – 152.
16. Zhang, J., Xu, L., Wong, W. Y. *Coord. Chem. Rev.,* **2018**, *355*, 180 – 198.
17. Juyal, V. K., Pathak, A., Panwar, M., Thakuri, S. C., Prakash, O., Agrwal, A., Nand, V. *J. Organomet. Chem.,* **2023**, *999*, 122825.
18. Wang, Y., Wang, M., Li, Y., Liu, Q. *Chem.*, **2021**, *7*, 1180 – 1223.
19. Khusnutdinova, J. R., Milstein, D. *Angew. Chem. Int. Ed.,* **2015**, *54*, 12236 – 12273.
20. Elangovan, S., Topf, C., Fischer, S., Jiao, H., Spannenberg, A., Baumann, W., Ludwig, R., Junge, K., Beller, M. *J. Am. Chem. Soc.,* **2016**, *138*, 8809 – 8814.

21. Mukherjee, A., Nerush, A., Leitus, G., Shimon, L. J. W., Ben David, Y., Espinosa Jalapa, N. A., Milstein, D. *J. Am. Chem. Soc.*, **2016**, *138*, 4298 – 4301.
22. Bruneau-Voisine, A., Wang, D., Roisnel, T., Darcel, C., Sortais, J. *Catal. Commun.,* **2017**, *92*, 1 – 4.
23. Spall, S. J. P., Keane, T., Tory, J., Cocker, D. C., Adams, H., Fowler, H., Meijer, A. J. H. M., Hartl, F., Weinstein, J. A. *Inorg. Chem.,* **2016**, *55*, 12568 – 12582.
24. Zeng, Q., Tory, J., Hartl, F. *Organometallics,* **2014**, *33*, 5002 – 5008.
25. Bourrez, M., Molton, F., Chardon-Noblat, S., Deronzier, A. *Angew. Chem. Int. Ed.,* **2011**, *50*, 9903 – 9906.
26. Amorim, A. L., Guerreiro, A., Glitz, V. A., Coimbra, D. F., Bortoluzzi, A. J., Caramori, G. F., Braga, A. L., Neves, A., Bernardes, G. J. L., Peralta, R. A. *New. J. Chem.,* **2020**, *44*, 10892 – 10901.
27. Palominos, F., Mella, P., Guajardo, K. *Photochem. Photobiol. Sci.,* **2024**, *23*, 119 – 132.
28. Henke, W. C., Otolski, C. J., Moore, W. N. G., Elles, C. G., Blakemore, J. D. *Inorg. Chem.,* **2020**, *59*, 2178 – 2187.
29. Buldurun, K., Ozdemir, M. *J. Mol. Struct.*, **2020**, *1202*, 127266.
30. Spasyuk, D., Gusev, D. G. *Organometallics*, **2012**, *31*, 5239 – 5242.
31. Ma, C., Qin, L., Zheng, Z. *J. Organomet. Chem.,* **2024**, *1004*, 122950.
32. Mogensen, D., Grunwaldt, J. D., Hendriksen, P. V., Dam-Johansen, K., Nielsen, J. U. *J. Power Sources,* **2011**, *196*, 25 – 38.
33. Ramos, T. S., Luz, D. M., Nascimento, R. D., Silva, A. K., Lião, L. M., Miranda, V. M., Deflon, V. M., de Araujo, M. P., Ueno, L. T., Machado, F. B. C., Dinelli, L. R., Bogado, A. L. *J. Organomet. Chem.,* **2019**, *892*, 51 – 65.
34. Baratta, W., Chelucci, G., Gladialli, S., Siega, K., Toniutti, M., Zanette, M., Zangrandi, E., Rigo, P. *Angew. Chem. Int. Ed.*, **2005**, *44*, 6214 – 6219.
35. Johnson, L. K., Killian, C. M., Brookhart, M. *J. Am. Chem. Soc.*, **1995**, *117*, 6414.
36. Motswainyana, W. M., Ojwach, S. O., Onani, M. O., Iwuoha, E. I., Darkwa, J. *Polyhedron*, **2011**, *30*, 2574 – 2580.
37. Musaev, D. G., Svensson, M., Morokuma, K. *Organometallics,* **1997**, *16*, 1933.
38. Deng, L., Margl, P. T., Ziegler, T. *J. Am. Chem. Soc.,* **1997**, *119*, 1094.
39. Zulu, Z., Nyamato, G. S., Tshabalala, T. A., Ojwach, S. O. *Inorg. Chim. Acta*, **2020**, *501*, 119270.
40. Shi, P. Y., Liu, Y. H., Peng, S. M., Liu, S. T. *Organometallics*, **2002**, *21*, 3203 – 3207.
41. Ainooson, M. K., Guzei, I. A., Spencer, L. C., Darkwa, J. *Polyhedron,* **2013**, *53*, 295 – 303.
42. Akiri, S. O., Ojwach, S. O. *Inorg. Chim. Acta*, **2019**, *489*, 236 – 243.
43. Johnson, L. K., Killian, C. M., Brookhart, M. *J. Am. Chem. Soc.,* **1995**, *117*, 6414.

44. Kumah, R. T., Tsaulwayo, N., Xulu, B. A., Ojwach, S. O. *Dalton Trans.,* **2019**, *48*, 13630.
45. Tondreau, A. M., Lobkovsky, E., Chirik, P. J. *Org. Lett.,* **2008**, *10*, 2789 – 2792.
46. Dong, Z. R., Li, Y. Y., Yu, S. L., Sun, G. S., Gao, J. X. *Chin. Chem. Lett.,* **2012**, *23*, 533 – 536.
47. Bigler, R., Mezzetti, A. *Org. Process Res. Dev.,* **2016**, *20*, 253 – 261.
48. Bigler, R., Huber, R., Stöckli, M., Mezzetti, A. *ACS Catal.,* **2016**, *6*, 6455 – 6464.
49. Tang, X., Sun, W-H., Gao, T., Hou, J., Chen, J., Chen, W. *J. Organomet. Chem.,* **2005**, *690*, 1570 – 1580.
50. Carlini, C., Isola, M., Liuzzo, V., Galletti, A. M. P., Sbrana, G. *Appl. Catal. A Gen.,* **2002**, *231*, 307.
51. Hicks, F. A., Jenkins, J. C., Brookhart, M. *Organometallics*, **2003**, *22*, 3533.
52. Sun, W-H., Zhang, W., Gao, T., Tang, X., Li, Y., Jin, J. *Organomet. Chem.,* **2004**, *689*, 917.
53. Makhubela, B. C. E., Jardine, A., Smith, G. S. *Green Chem.,* **2012**, *14*, 338.
54. Peirano, B. F., Thierry, V., Quignard, F., Rabitzer, M., Guibal, E. *J. Memb. Sci.,* **2009**, *329*, 30.
55. Guibal. E. *Prog. Polym. Sci.,* **2005**, *30*, 71.
56. Li, P., Kawi, S. *J. Catal.*, **2008**, *257*, 23.
57. Pearson, R. G., *J. Am. Chem. Soc.,* **1963**, *85*, 3533.
58. Kollar, J. Halcon, US Patents 3350, 422 and 3351, 635, **1967**.
59. Kühn, F. E., Santos, A. M., Herrmann, W. A. *Dalton Trans.,* **2005**, 2483.
60. Freund, C., Abrantes, M., Kühn, F. E. *J. Organomet. Chem.,* **2006**, *691*, 3718.
61. Balula, S. S., Bruno, S. M., Gomes, A. C., Valente, A. A., Pillinger, M., Gonçalves, I. S., Macquarrie, D. J., Clark, J. H. *Inorg. Chim. Acta,* **2012**, *387*, 234 – 239.
62. Romão, C. C., Kühn, F. E., Herrmann, W. A. *Chem. Rev.,* **1997**, *97*, 3197 – 3246.
63. Song, X., Lim, M. H., Mohamed, D. K. B., Wong, S. M., Zhao, J., Hor, T. S. A., *J. Organomet. Chem.,* **2016**, *814*, 1 – 7.
64. Herrmann, W. A., Rauch, M. U., Artus, G. R. J. *Inorg. Chem.,* **1996**, *35*, 1988 – 1991.
65. Sachse, A., Mosch-Zanetti, N. C., Lyashenko, G., Wielandt, J. W., Most, K., Magull, J., Dall'Antonia, F., Pal, A., Herbst-Irmer, R. *Inorg. Chem.,* **2007**, *46*, 7129 – 7135.
66. Schrockeneder, A., Traar, P., Raber, G., Baumgartner, J., Belaj, F., Mosch-Zanetti, N. C. *Inorg. Chem.,* **2009**, *48*, 11608 – 11614.
67. Tsaulwayo, N., Kumar, R. T., Ojwach, S. O. *Polyhedron*, **2021**, *197*, 115034.
68. Tye, J. W., Weng, Z., Johns, A. M., Incarvito, C. D., Hartwig, J. F. *J. Am. Chem. Soc.*, **2008**, *130*, 9971 – 9983.
69. Alshehri, S. M., Ahamad, T., Aldalbahi, A., Alhokbany, N. *Adv. Polym. Tech.*, **2016**, *35*(1).

70. Jones, L. W. *Energy Commun.,* **1976**, *2*, 573 – 584.
71. Bockris, J. O. M., *Int. J. Hydrogen Energy,* **2013**, *38*, 2579 – 2588.
72. Singh, S., Jain, S., Tiwari, A. K., Nouni, M. R., Pandey, J. K., Goel, S., PS, V. *Renewable Sustainable Energy Rev.,* **2015**, *51*, 623 – 633.
73. Wang, M., Wang, Z., Gong, X., Guo, Z. *Renew. Sustain. Energy Rev.,* **2014**, *29*, 573 – 588.
74. Preuster, P., Papp, C., Wasserscheid, P. *Acc. Chem. Res.,* **2017**, *50*, 74 – 85.
75. Titze, V., Stolten, D. *Materials, Processes, Systems and Technology*, 1st Ed., Weinheim, Germany, **2016**, 659 – 692.
76. Alekseev, A., *Hydrogen Science and Engineering: Materials, Processes, Systems and Technology*, 1st Ed., Weinheim, Germany, **2016**, 733 – 762.
77. Cooper, A. C., Fowler, D. E., Scott, A. R., Abdourazak, A. H., Cheng, H., Wilhelm, F. C., Toseland, B. A., Campbell, K. M., Pez, G. P. *Pap. Am. Chem. Soc.,* **2005**, *50*, 271.
78. Markiewicz, M., Zhang, Y. Q., Bösmann, A., Brückner, N., Thöming, J., Wasserscheid, P., Stolte, S. *Energy Environ. Sci.,* **2015**, *8*, 1035 – 1045.
79. Okada, Y., Sasaki, E., Watanabe, E., Hyodo, S., Nishijima, H. *Int. J. of Hydrogen Energy,* **2006**, *31*, 1348 – 1356.
80. Yolcular, S., Olgun, O. *Catal. Today,* **2008**, *138*, 198 – 202.
81. Gleichweit, C., Amende, M., Schernich, S., Zhao, W., Lorenz, M. P. A., Höfert, O., Brückner, N., Wassersscheid, P., Libuda, J., Steinrück, H. P., Papp, C. *ChemSusChem,* **2013**, *6*, 974 – 977.
82. Modisha, P. M., Ouma, C. N. M., Garidzirai, R., Wassersscheid, P., Bessarabov, D. *Energy Fuels*, **2019**, *33*, 2778 – 2796.
83. Liu, C., Li, F., Ma, L. P., Cheng, H. M. *Adv. Mater.,* **2010**, *22*, E28 – E62.
84. Van Renssen, S. *Nat. Clim. Change,* **2020**, *10*, 799 – 801.
85. Armaroli, N., Balzani, V. *Energy Environ. Sci.,* **2011**, *4*, 3193.
86. Sun, Q., Chen, B. W. J., Wang, N., He, Q., Chang, A., Yang, C., Asakura, H., Tanaka, T., Hülsey, M. J., Wang, C., Yu, J., Yan, N. *Angew. Chem. Int. Ed.,* **2020**, *59*, 20183 – 20191.
87. Knörr, P., Lentz, N., Albrecht, M. *Catal. Sci. Technol.,* **2023**, *13*, 5625.
88. Verron, R., Puig, E., Sutra, P., Igau, A., Fischmeister, C. *ACS Catal.,* **2023**, *13*, 5787 – 5794.
89. Luque-Gómez, A., García-Albellán, S., Munarriz, J., Polo, V., Passarelli, V., Iglesias, M. *Inorg. Chem.,* **2021**, *60*, 15497 – 15508.
90. Guan, C., Zhang, D-D., Pan, Y., Iguchi, M., Ajitha, M. J., Hu, J., Li, H., Yao, C., Huang, M-H., Min, S., Zheng, J., Himeda, Y., Kawanami, H., Huang, K-W. *Inorg. Chem.,* **2017**, *56,* 438 – 445.

91. Sordakis, K., Dalebrook, A. F., Laurenczy, G. *ChemCatChem.,* **2015**, *7*, 2332 – 2339.
92. Bulushev, D. A., Beloshapkin, S., Ross, J. R., *Catal. Today,* **2010**, *154*, 7 – 12.
93. Kar, S., Rauch, M., Leitus, G., Ben-David, Y., Milstein, D. *Nature Catal.*, **2021**, *4*, 193 – 201.
94. Hietala, J. *et al*. *Ullmann's Encyclopedia of Industrial Chemistry*, 7th Edn., **2016**.
95. Alig, L., Fritz, M., Schneider, S. *Chem. Rev.,* **2019**, *119*, 2681 – 2751.
96. Léval, A., Junge, H., Beller, M. *Catal. Sci. Technol.,* **2020**, *10*, 3931.
97. Bielinski, E., Lagaditis, P. O., Zhang, Y., Mercado, B. Q., Würtele, C., Bernskoetter, W. H., Hazari, N., Schneider, S. *J. Am. Chem. Soc.,* **2014,** *136*, 10234 – 10237.
98. Onishi, N., Ertem, M. Z., Xu, S., Tsurusaki, A., Manaka, Y., Muckerman, J. T., Fujita, E., Himeda, Y. *Catal. Sci. Technol.,* **2016**, *6*, 988 – 992.
99. Li, J., Li, J., Zhang, D., Liu, C. *ACS Catal.,* **2016**, *6*, 4746 – 4754.
100. Dutta, I., Alobaid, N. A., Menicucci, F. L., Chakraborty, P., Guan, C., Han, D., Huang, K-W. *Int. J. of Hydrogen Energy,* **2023**, *48*, 26559 – 26567.
101. Lentz, N., Albrecht, M. *ACS Catal.,* **2022**, *12*, 12627 – 12631.
102. Heimann, J. E., Bernskoetter, W. H., Hazari, N. *J. Am. Chem. Soc.,* **2019**, *141*, 10520 – 10529.
103. Upadhyay, S. Temperature Effect on Reaction Rate. *In Chemical Kinetics and Reaction Dynamics*, Springer Netherlands, 2006, pp 46 – 54.
104. Léval, A., Agapova, A., Steinlechner, C., Alberico, E., Junge, H., Beller, M. *Green Chem.,* **2020**, *22*, 913.
105. Anderson, N. H., Boncella, J., Tondreau, A. M., *Chem. Eur. J.,* **2019**, *25*, 10557 – 10560.

Chapter 2: Synthesis and Characterization of Neutral Pyridylimine Manganese(I) Complexes

2.1 Introduction

2.1.1 Schiff base ligands and their transition metal complexes.

First described by German scientist Hugo Schiff, in 1864, Schiff base ligands are a product of a condensation reaction between an appropriate carbonyl and primary amine, as shown in **Scheme 2.1**.[1] They are described by the general formula $R_1N{=}CR_2R_3$. Spectroscopic evidence from literature reports suggests that Schiff bases generated from aromatic aldehydes are more stable than those derived from aliphatic aldehydes due to the effective conjugation present in the aromatic aldehydes. Aliphatic aldehydes are reported to readily polymerize and thus are less stable.[2,3] Hence, 2-pyridinecarboxaldehyde, an aromatic aldehyde, and its substituted derivatives 6-methyl-2-pyridinecarboxaldehyde and 6-trifluoromethyl-2-pyridinecarboxaldehyde will be employed in the ligand synthesis for our investigation.

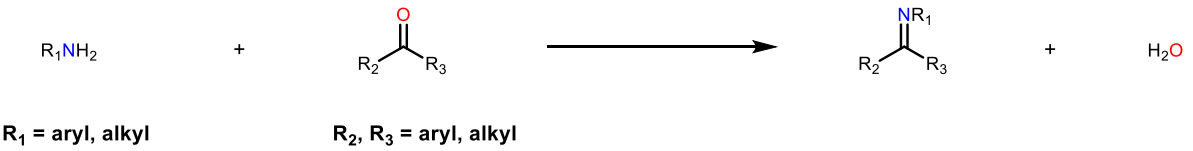

Scheme 2.1: General condensation reaction between a primary amine and an aldehyde or ketone.

The utilization of Schiff base ligands in organometallic chemistry in academia and industry has gained significant traction over the past century. Their preparation is relatively facile, and they can coordinate a wide range of transition metals in various oxidation states and effectively control their performance in catalytic applications.[4] The ligand design is versatile and allows for easy variation of the electronic and steric characteristics around the metal ion *via* the insertion of functional groups that promote coordination or complex formation.[5] The reversibility of the imine formation has also proved useful in synthesizing large structures such as ring systems and macromolecules.[6] The literature contains many reports detailing the preparation and application of transition metal complexes bearing Schiff base ligands for various organic transformations. Examples include nickel,[5] palladium,[7,8] and ruthenium[9] complexes as shown in **Figure 2.1**.

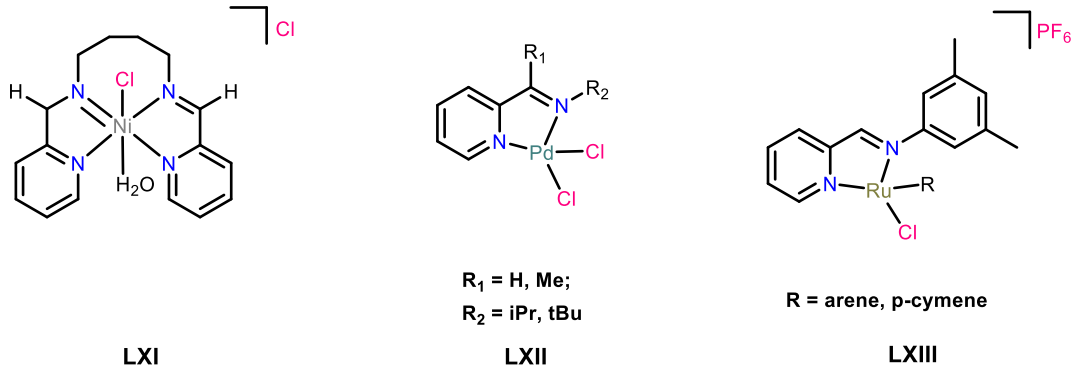

LXI **LXII** **LXIII**

Figure 2.1: Examples of transition metal complexes bearing Schiff base ligands; **LXI**) nickel,[5] **LXII**) palladium,[7, 8] and **LXIII**) ruthenium.[9]

Regarding the preparation and application of manganese complexes, existing literature reports focus mainly on the use of often expensive, tridentate phosphine-amine-phosphine (PNP) or amine-amine-amine (NNN) pincer-type ligands such as those developed by the research groups of Gambarotta[10] and Milstein[11] as shown in **Figure 2.2** below.

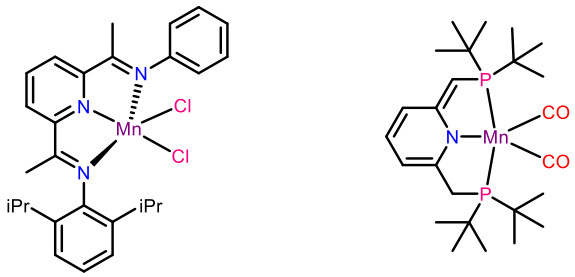

LXIV **LXV**

Figure 2.2: Examples of manganese complexes bearing tridentate pincer-type ligands.[10, 11]

To our knowledge, manganese complexes bearing the proposed pyridylimine ligands except **C1** and **C3** have not been reported. In this context, we herein detail the preparation and spectroscopic characterization of a range of pyridylimine-ligated Mn(I) complexes containing different alkyl substituents on the aromatic and/or pyridine ring(s) as well as Mn(I) complexes bearing various aliphatic substituents. Additionally, we report on a crystallographic and spectroscopic investigation into the photosensitivity of these Mn(I) complexes.

2.2 Results and Discussion

2.2.1 Synthesis and characterization of pyridylimine ligands, L1 – L9.

A series of reported and one novel pyridylimine ligands were prepared by the Schiff base condensation of 2-pyridinecarboxaldehyde or its substituted derivatives with various aromatic and aliphatic amines in a 1:1 molar ratio as illustrated in **Scheme 2.2.**

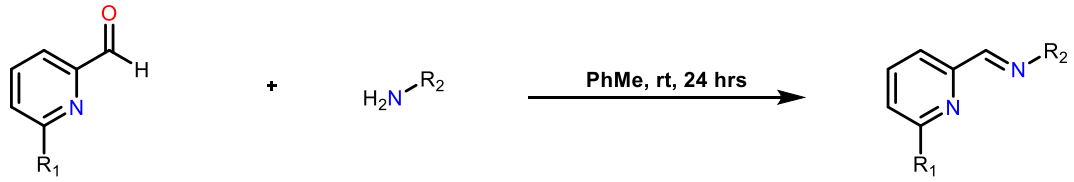

L1: R_1 = H, R_2 = Phenyl; L2: R_1 = H, R_2 = 2,6-dimethylphenyl; L3: R_1 = H, R_2 = 2,6-diisopropylphenyl; L4: R_1 = H, R_2 = Mesityl; L5: R_1 = H, R_2 = Benzyl; L6: R_1 = H, R_2 = Cyclohexyl; L7: R_1 = H, R_2 = Propyl; L8: R_1 = CH_3, R_2 = Phenyl; L9: R_1 = CF_3, R_2 = Phenyl

Scheme 2.2: Synthetic route to bidentate pyridylimine ligands **L1 – L9.**

All the ligands, **L1**[12], **L2** and **L4**[13], **L3**[14], **L5**[15], **L6**[16], **L7**[17], and **L8**[18] except for **L9** were previously reported and fully characterized. The ligands were isolated in high yields (79 – 96%) as yellow-orange oils (**L1**, **L4**, **L5**, **L6**, **L7**, and **L8**) and yellow-orange crystalline solids (**L2**, **L3**, and **L9**). All the ligands displayed good solubility in most polar and non-polar organic solvents at room temperature. The ligands were also observed to be stable in solution and a solid state over six months. The variations in the ligand structure such as the introduction of electron-donating methyl groups or bulky isopropyl groups on an aromatic ring, were introduced to study the effects of both steric and electronic properties on the stability of the ligands as well as to potentially enhance the catalytic activity of the complexes obtained from these ligand systems. In addition, pyridylimine ligands where the R_2 group (**Scheme 2.2**) is an aliphatic electron-donating substituent were prepared to further study the electronic effects through comparison with aromatic substituents.

2.2.1.1 FT-IR and ^{1}H NMR Spectroscopy

The FT-IR spectra of all ligands (**L1** – **L9**) showed a strong absorption band in the region 1627 – 1649 cm^{-1} which was assigned to the imine ($\nu_{C=N}$) absorption. This indicated that the condensation reaction had occurred. The FT-IR spectra also indicated a strong absorption band in the region 1584 – 1589 cm^{-1}, which was assigned to the pyridylimine ($\nu_{pyr-C=N}$) absorption.

The imine proton resonance (**Figure 2.3, H[6]**) in the ^{1}H NMR spectra of the ligands **L1 – L9** was observed as a singlet downfield in the region 8.31 – 8.61 ppm (**Tables 2.1 & 2.2**). For ligand **L2**, the chemical equivalence of the methyl groups on the aromatic ring was observed as a strong, intense singlet that integrates for a total of six protons in the most upfield region of the spectrum (**Figure 2.4**). This is evidence for free rotation along the N-C bond (**Figure 2.3, N-C[7]**).

The imine proton and carbon resonances, its absorption band, and the pyridylimine absorption band are crucial since they reveal significant insights into the coordination sphere around the metal center for the manganese complexes obtained from these ligands. Hence, the relative position in the wavenumber of the pyridylimine and imine absorptions, the relative chemical shift, the splitting pattern, and the shape of the imine resonance are examined in detail throughout this study.

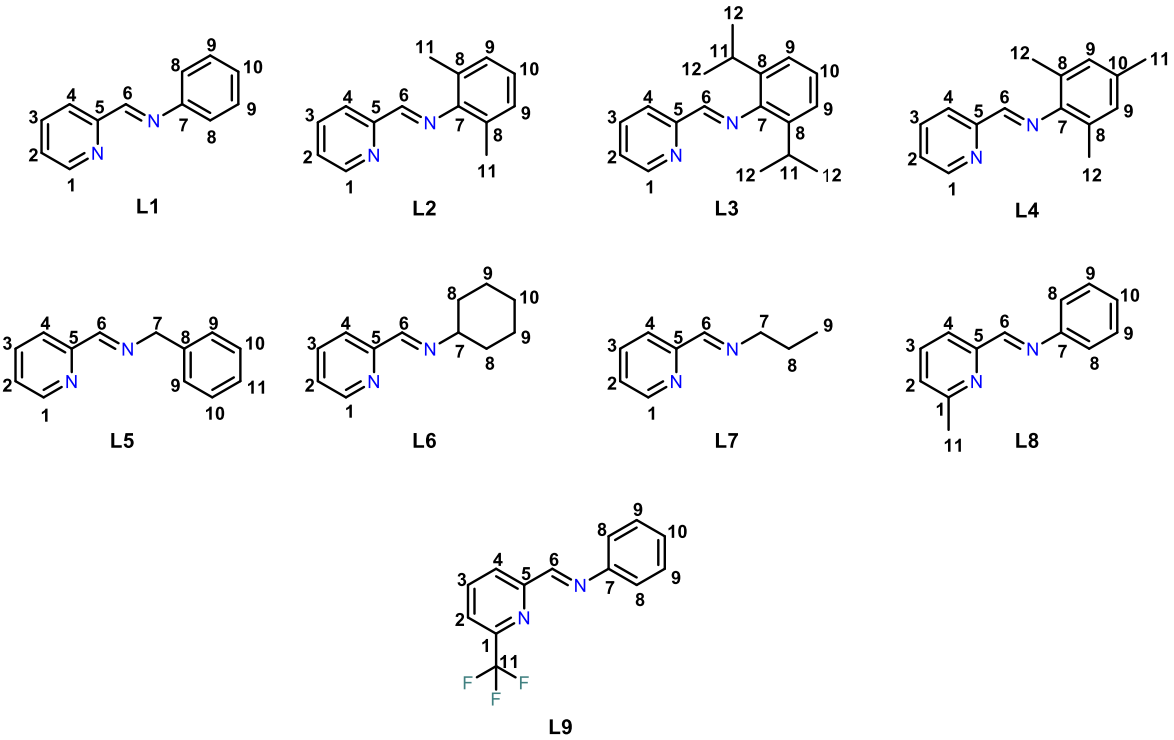

Figure 2.3: Molecular structures of pyridylimine ligands, **L1** – **L9** showing numbering for NMR assignment.

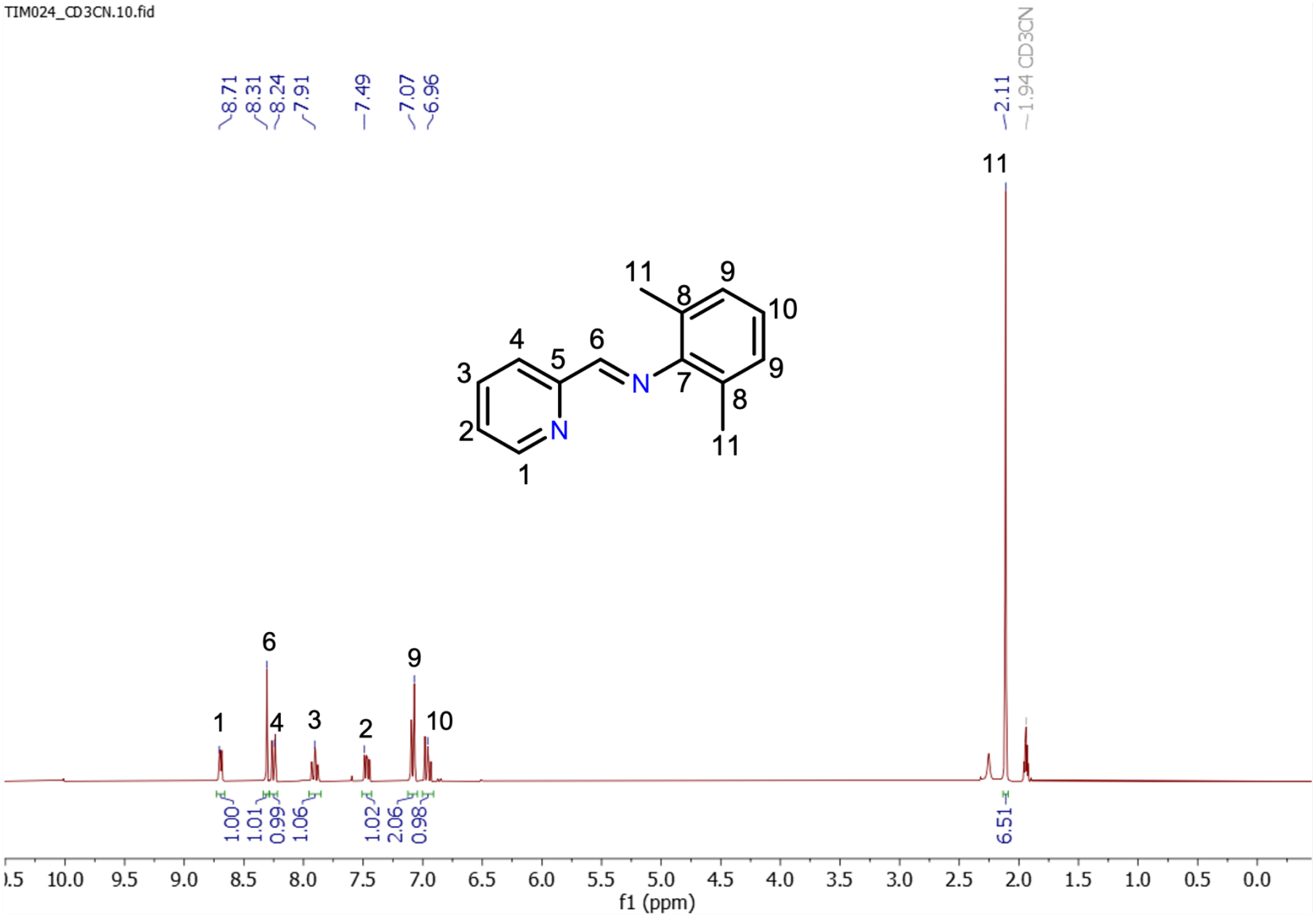

Figure 2.4: ^{1}H NMR spectrum of pyridylimine ligand, **L2** recorded in CD_3CN-d_3 at 300 K.

Table 2.1: ^{1}H NMR spectral data of pyridylimine ligands, **L1** – **L4**.[a]

Ligand	C=N***H***	Aromatic region	Aliphatic region		
			C***H*₃**	C***H***$(CH_3)_2$	C***H*₂**
L1	δ 8.59 (s, 1H, H^6)	δ 8.69 (d, *J* = 3.3 Hz, 1H, H^1) δ 8.16 (d, *J* = 7.9 Hz, 1H, H^4) δ 7.87 (t, *J* = 7.6 Hz, 1H, H^3) δ 7.43 – 7.31 (m, 6H, $H^{2, 8, 9, 10}$)	-	-	-
L2	δ 8.31 (s, 1H, H^6)	δ 8.71 (d, *J* = 4.0 Hz, 1H, H^1) δ 8.24 (d, *J* = 7.9 Hz, 1H, H^4) δ 7.91 (t, *J* = 7.9 Hz, 1H, H^3) δ 7.49 (t, *J* = 6.3 Hz, 1H, H^2) δ 7.07 (d, *J* = 7.7 Hz, 2H, H^9) δ 6.96 (t, *J* = 7.8 Hz, 1H, H^{10})	δ 2.11 (s, 6H, H^{11})	-	-
L3	δ 8.27 (s, 1H, H^6)	δ 8.70 (d, *J* = 3.6 Hz, 1H, H^1) δ 8.20 (d, *J* = 8.1 Hz, 1H, H^4) δ 7.92 (t, *J* = 8.0 Hz, 1H, H^3) δ 7.50 (t, *J* = 6.3 Hz, 1H, H^2) δ 7.17 (m, 3H, $H^{9, 10}$)	-	δ 2.93 (sept, *J* = 7.1 Hz, 2H, H^{11}) δ 1.14 (d, *J* = 6.8 Hz, 12H, H^{12})	-
L4	δ 8.33 (s, 1H, H^6)	δ 8.71 (d, *J* = 3.7 Hz, 1H, H^1) δ 8.27 (d, *J* = 8.1 Hz, 1H, H^4) δ 7.84 (t, *J* = 7.6 Hz, 1H, H^3) δ 7.40 (t, *J* = 6.0 Hz, 1H, H^2) δ 6.91 (s, 2H, H^9)	δ 2.29 (s, 3H, H^{11}) δ 2.14 (s, 6H, H^{12})	-	-

[a] Spectra recorded in CD_3CN at 300 K; chemical shifts (δ) are reported in ppm values, referenced relative to the residual CD_3CN resonance; superscripts indicate protons as per numbering scheme in **Figure 2.3**; s = singlet, d = doublet, t = triplet, sept = septet, m = multiplet.

Table 2.2: ^{1}H NMR spectral data of pyridylimine ligands, **L5** – **L9**.[a]

Ligand	CN=***H***	Aromatic region	Aliphatic region		
			C***H₃***	C***H₂***	C***H***
L5	δ 8.48 (s, 1H, H^{6})	δ 8.64 (d, *J* = 4.1 Hz, 1H, H^{1}) δ 7.95 (d, *J* = 7.9 Hz, 1H, H^{4}) δ 7.79 (t, *J* = 7.7 Hz, 1H, H^{3}) δ 7.37 (m, 6H, $H^{2, 9, 10, 11}$)	-	δ 4.84 (s, 2H, H^{7})	-
L6	δ 8.35 (s, 1H, H^{6})	δ 8.58 (d, *J* = 4.7 Hz, 1H, H^{1}) δ 7.91 (d, *J* = 7.9 Hz, 1H, H^{4}) δ 7.77 (t, *J* = 7.7 Hz, 1H, H^{3}) δ 7.35 (t, *J* = 6.2 Hz, 1H, H^{2})	-	δ 1.81 – 1.24 (m, 10H, $H^{8, 9, 10}$)	δ 3.29 (m, 1H, H^{7})
L7	δ 8.34 (s, 1H, H^{6})	δ 8.62 (d, *J* = 3.7 Hz, 1H, H^{1}) δ 7.94 (d, *J* = 7.9 Hz, 1H, H^{4}) δ 7.78 (t, *J* = 7.7 Hz, 1H, H^{3}) δ 7.37 (t, *J* = 6.1 Hz, 1H, H^{2})	δ 0.94 (t, *J* = 7.3 Hz, 3H, H^{9})	δ 3.60 (t, *J* = 6.9 Hz, 2H, H^{7}) δ 1.68 (m, 2H, H^{8})	-
L8	δ 8.51 (s, 1H, H^{6})	δ 7.95 (d, *J* = 7.7 Hz, 1H, H^{4}) δ 7.74 (t, *J* = 7.6 Hz, 1H, H^{3}) δ 7.40 – 7.31 (m, 6H, $H^{2, 8, 9, 10}$)	δ 2.56 (s, 3H, H^{11})	-	-
L9	δ 8.61 (s, 1H, H^{6})	δ 8.38 (d, *J* = 7.6 Hz, 1H, H^{4}) δ 8.11 (t, *J* = 7.5 Hz, 1H, H^{3}) δ 7.88 (d, *J* = 6.4 Hz, 1H, H^{2}) δ 7.43 – 7.35 (m, 5H, $H^{8, 9, 10}$)	-	-	-

[a] Spectra recorded in CD_3CN at 300 K; chemical shifts (δ) are reported in ppm values, referenced relative to the residual CD_3CN resonance; superscripts indicate protons as per numbering system in **Figure 2.3**; s = singlet, d = doublet, t = triplet, sept = septet, m = multiplet.

2.2.1.2 Mass Spectrometry and Elemental Analysis

ESI-MS recorded in the positive ion mode were in accordance with the suggested pyridylimine ligands. The base peak for all the ligands corresponds with the $[M+H]^+$ fragment ion and is reported in **Table 2.3**. The theoretical or calculated fragmentation pattern corresponds to the experimental fragmentation pattern and is represented in **Figure 2.5.** CHN analysis confirmed the overall purity of the new pyridylimine ligand **L9**.

Table 2.3: Mass spectrometry data of pyridylimine ligands **L1** – **L9**.

Ligand	Fragment ion (m/z)	
	Experimental $[M+H]^+$	**Calculated $[M+H]^+$**
L1	183.0917	183.0922
L2	211.1215	211.1235
L3	267.1810	267.1861
L4	225.1372	225.1392
L5	197.1064	197.1079
L6	189.1371	189.1392
L7	149.1068	149.1079
L8	197.1080	197.1079
L9	251.0796	251.0796

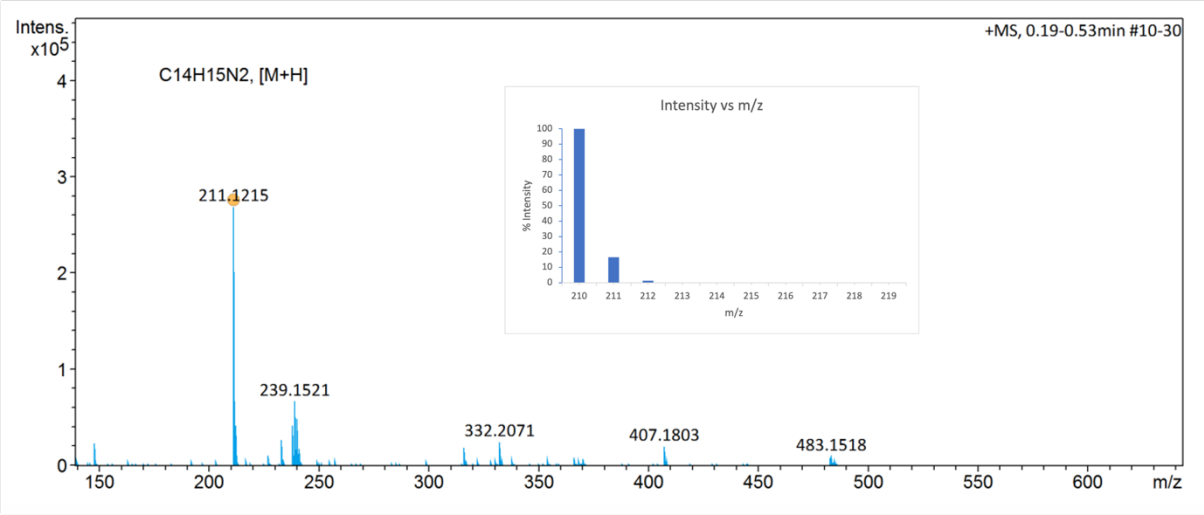

Figure 2.5: ESI-MS spectrum of pyridylimine ligand, **L2** recorded in the positive ion mode. The peak located at 211.1215 represents the $[M+H]^+$ fragment ion. Inset shows the calculated isotopic pattern for the $[M+H]^+$ fragment ion.

2.2.2 Synthesis and characterization of pyridylimine-ligated Mn(I) complexes, C1 – C9.

The neutral pyridylimine-ligated Mn(I) complexes, **C1 – C9**, were obtained by the reaction of the prepared Schiff base ligands with commercially available manganese pentacarbonyl bromide, $MnBr(CO)_5$ in the presence of tetrahydrofuran (THF) as solvent of choice (**Scheme 2.3**). They were isolated as light-sensitive solids confirmed by various analytical techniques (**See Section 2.4**) in moderate to good yields (50 – 84%) and stored away from direct sunlight at low temperatures. All the complexes displayed good solubility in most organic solvents but were observed to be unstable in strong coordinating solvents such as acetonitrile (MeCN), dimethyl sulfoxide (DMSO), and dimethyl formamide (DMF) when exposed to light. All the complexes, except **C1** and **C3**, have not been reported in the literature and were fully characterized using various analytical and spectroscopic techniques. The general characterization data for complexes **C1** – **C9** are summarized in **Table 2.4** – **Table 2.9**.

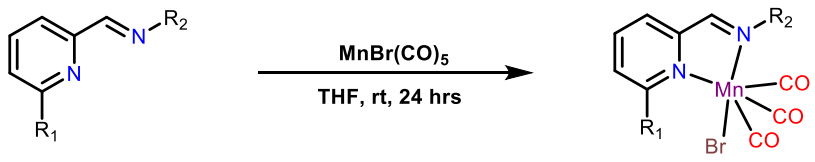

C1: R_1 = H, R_2 = Phenyl; C2: R_1 = H, R_2 = 2,6-dimethylphenyl; C3: R_1 = H, R_2 = 2,6-diisopropylphenyl; C4: R_1 = H, R_2 = Mesityl; C5: R_1 = H, R_2 = Benzyl; C6: R_1 = H, R_2 = Cyclohexyl; C7: R_1 = H, R_2 = Propyl; C8: R_1 = CH_3, R_2 = Phenyl; C9: R_1 = CF_3, R_2 = Phenyl

Scheme 2.3: Synthetic protocol to pyridylimine Mn(I) complexes, **C1** – **C9**.

2.2.2.1 FT-IR Spectroscopy and Thermal Stability

The FT-IR spectra of the pyridylimine Mn(I) complexes provided evidence of a successful complexation reaction. The coordination of the imine nitrogen to the manganese metal center was confirmed by a bathochromic shift (13 cm^{-1} for **C1**, 27 cm^{-1} for **C2**, 7 cm^{-1} for **C3**, 8 cm^{-1} for **C4**, 17 cm^{-1} for **C5**, 24 cm^{-1} for **C6**, 22 cm^{-1} for **C7**, 2 cm^{-1} for **C8**, and 27 cm^{-1} for **C9**) of the imine ($\nu_{C=N}$) absorption which appears in the region 1601 – 1632 cm^{-1} compared to that of the pyridylimine ligands, **L1 – L9**. Upon complexation, this resulted in a decreased double bond character of the imine functional group.[19] Coordination through the pyridylimine nitrogen was indicated by a blue shift (2 cm^{-1} for **C1**, 4 cm^{-1} for **C3**, 4 cm^{-1} for **C4**, 10 cm^{-1} for **C5**, 4 cm^{-1} for **C6**, 7 cm^{-1} for **C7**, 8 cm^{-1} for **C8**, and 3 cm^{-1} for **C9**) of the pyridylimine ($\nu_{pyr\text{-}C=N}$) absorption which appears in the region 1582 – 1596 cm^{-1} compared to that of the uncoordinated Schiff base ligands, **L1 – L9** (**Table 2.5**). This indicates an increased double bond character of the pyridylimine functional group upon coordination.[19]

In the case of complex **C2**, a red shift of 1 cm^{-1} in the pyridylimine absorption was observed, suggesting an alternative bonding mechanism such as coordination of the nitrogen to the manganese metal centre *via* the π electrons of the pyridylimine double bond instead of the lone pair and consequently, a decreased double bond character.[19] Two strong absorption bands characteristic of the symmetric and asymmetric carbonyl (CO) functional groups were observed in the regions 1896 cm^{-1} – 1940 cm^{-1} and 2016 cm^{-1} – 2028 cm^{-1}. Similar carbonyl stretches were reported in the literature for related Mn(I) complexes and suggest the formation of the *fac* isomer of the complexes.[20]

Table 2.4: FT-IR spectral data and decomposition temperatures for pyridylimine Mn(I) complexes **C1 – C9** and Schiff base ligands **L1 – L9**.

Complex	Decomposition Temperature (°C)[a]	FT-IR[b]		Ligand	FT-IR[b]
		($\nu_{C=N}$, cm^{-1})	(ν_{CO}, cm^{-1})		($\nu_{C=N}$, cm^{-1})
C1	169 – 174	1614	1896; 2020	**L1**	1627
C2	169 – 174	1611	1908; 2022	**L2**	1637
C3	169 – 174	1632	1904; 2020	**L3**	1639
C4	205 – 207	1631	1912; 2021	**L4**	1639
C5	156 – 158	1628	1904; 2019	**L5**	1645
C6	188 – 190	1623	1903; 2016	**L6**	1647
C7	138 - 141	1627	1906; 2016	**L7**	1649
C8	177 - 179	1626	1900; 2020	**L8**	1628
C9	169 - 171	1601	1922; 2028	**L9**	1628

[a] Decomposition temperatures are reported as uncorrected. Decomposition was observed without melting. [b] Recorded as neat solids or oils using an ATR accessory.

All the complexes turned black upon decomposition which occurred without melting. Additionally, decomposition temperatures for **C1**, **C2**, **C3**, and **C9** were significantly higher than the melting points determined for the corresponding ligands **L1**, **L2**, **L3**, and **L9** which indicates increased stability of the synthesized pyridylimine Mn(I) complexes (**Table 2.4**). The higher stability is caused by the change in intermolecular forces as a result of complex formation which produces a much larger molecule. Ligands **L4** – **L8** are liquids hence no comment can be made regarding stability upon their coordination with the manganese metal centre.

Table 2.5: FT-IR spectral data for the pyridylimine absorption band in Mn(I) complexes (**C1** – **C9**) and free Schiff base ligands (**L1** – **L9**).

Complex	FT-IR[a] ($\nu_{pyr\text{-}C=N}$, cm^{-1})	Ligand	FT-IR[a] ($\nu_{pyr\text{-}C=N}$, cm^{-1})
C1	1586	**L1**	1584
C2	1582	**L2**	1584
C3	1589	**L3**	1585
C4	1589	**L4**	1585
C5	1596	**L5**	1586
C6	1592	**L6**	1587
C7	1594	**L7**	1586
C8	1594	**L8**	1586
C9	1592	**L9**	1589

[a] Recorded as neat solids and oils using an ATR accessory.

2.2.2.2 ^{1}H – and ^{13}C NMR Spectroscopy

The ^{1}H- and $^{13}C\{^{1}H\}$ NMR spectra of the neutral pyridylimine Mn(I) complexes, **C1 – C9** indicated the formation of a five-membered ring between the manganese metal centre and the bidentate Schiff base ligands. The ^{1}H NMR spectra of complexes **C1 – C9** illustrated a downfield shift of the imine proton resonance in the region δ = 8.53 – 8.82 ppm (**Tables 2.7** and **2.8**) compared to the imine proton resonance of the free Schiff base ligands. Coordination through the π-electrons of the imine double bond often leads to chemical shifts as large as 2 ppm.[21] Hence, the observed chemical shift in the range of δ = 0.04 – 0.28 ppm provides evidence of the imine moiety coordinating with the manganese metal centre *via* the nitrogen lone pair.

Notable peak broadening in the ^{1}H NMR spectrum of complex **C2** in deuterated acetonitrile (CD_3CN-d_3) (**Figure 2.7**) reveals further information regarding decomposition or instability as well as CO ligand dissociation in strongly coordinating organic solvents under light exposure conditions. Additional information to substantiate this observation is provided in **Section 2.4**. Further ^{1}H NMR spectral analysis reveals the absence of free rotation of the 2,6-dimethylaniline moiety for the pyridylimine Mn(I) complex, **C2**. Upon complexation, rotation along the C-N bond (**N-C^{7}**) was limited (**Figure 2.6, C2**). As a result, the symmetry of the 2,6-dimethylphenyl moiety that is observed for the free pyridylimine ligand, **L2** is not present.

In the aliphatic region, a significant downfield shift in the methyl proton resonances (H^{11}) was observed (**Figure 2.7**). The singlet which integrates for six protons in the ligand **L2** appeared as two separate singlets each integrating for three protons for the pyridylimine Mn(I) complex, **C2**. Hence, protons H^{11} are chemically inequivalent (**Figure 2.7**) in complex **C2**, and there exists no free rotation.

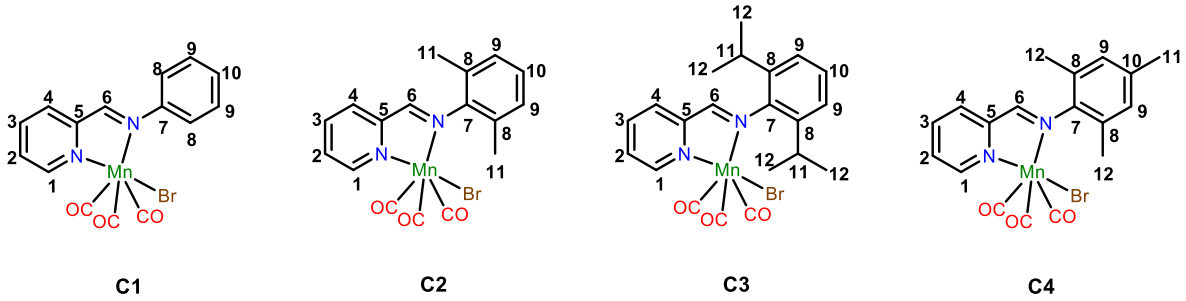

Figure 2.6: Molecular structures of pyridylimine Mn(I) complexes, **C1** – **C4** showing numbering for NMR assignment.

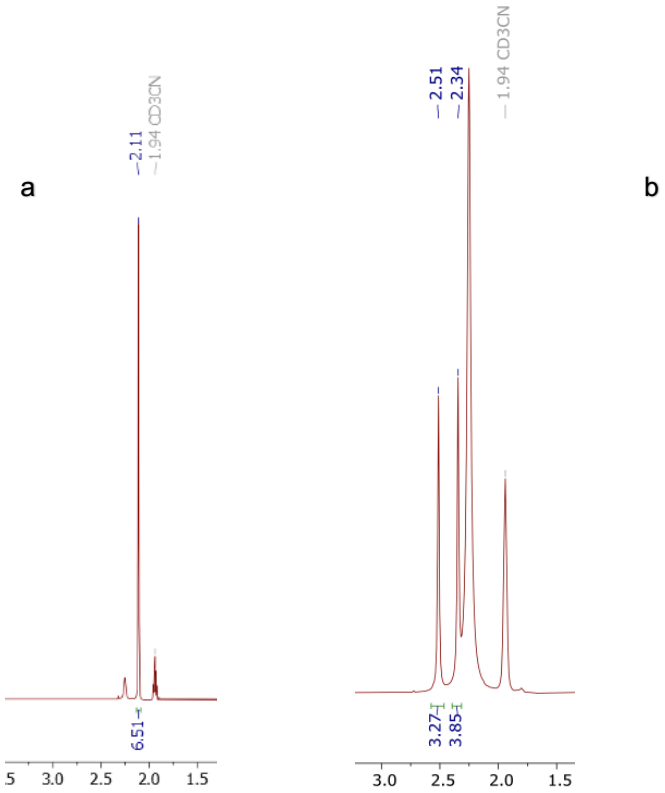

Figure 2.7: ^{1}H NMR spectrum showing the methyl resonances of the dimethyl moiety for (a) free Schiff base ligand, **L2,** and (b) pyridylimine Mn(I) complex, **C2**.

The $^{13}C\{^{1}H\}$ NMR spectra of pyridylimine Mn(I) complexes, **C1** – **C9** indicated the desired number of carbon resonances. Coordination of the imine nitrogen to the manganese metal centre was indicated by the downfield shifts of the imine carbon resonance (**C^{6}**) in the region 160.1 – 176.9 ppm relative to that of the Schiff base ligands (**Table 2.6**). The resonances corresponding to the CO functional groups were not observed in the $^{13}C\{^{1}H\}$ NMR spectra owing to their photolability in solution.

Table 2.6: ^{13}C $\{^{1}H\}$ NMR spectral data for pyridylimine Mn(I) complexes (**C1** – **C9**) and Schiff base ligands (**L1** – **L9**) indicating the imine carbon resonance.

Complex	^{13}C $\{^{1}H\}$ NMR[a] ($\delta_{C=N}$, ppm)	Ligand	^{13}C $\{^{1}H\}$ NMR[a] ($\delta_{C=N}$, ppm)
C1	175.9	**L1**	160.5
C2	176.9	**L2**	163.5
C3	171.3	**L3**	163.0
C4	171.5	**L4**	163.6
C5	175.0	**L5**	161.8
C6	160.1	**L6**	159.6
C7	166.9	**L7**	161.9
C8	169.8	**L8**	161.1
C9	169.3	**L9**	160.2

[a] Spectra recorded in CD_3CN-d_3 at 300 K. Chemical shifts reported as δ in ppm values, referenced relative to the residual CD_3CN resonance.

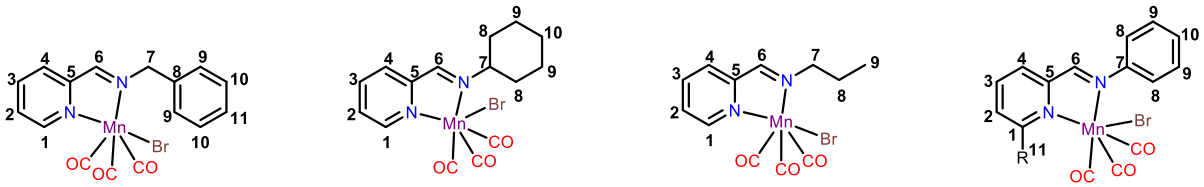

Figure 2.8: Molecular structures of pyridylimine Mn(I) complexes, **C5** – **C9** showing numbering for NMR assignment.

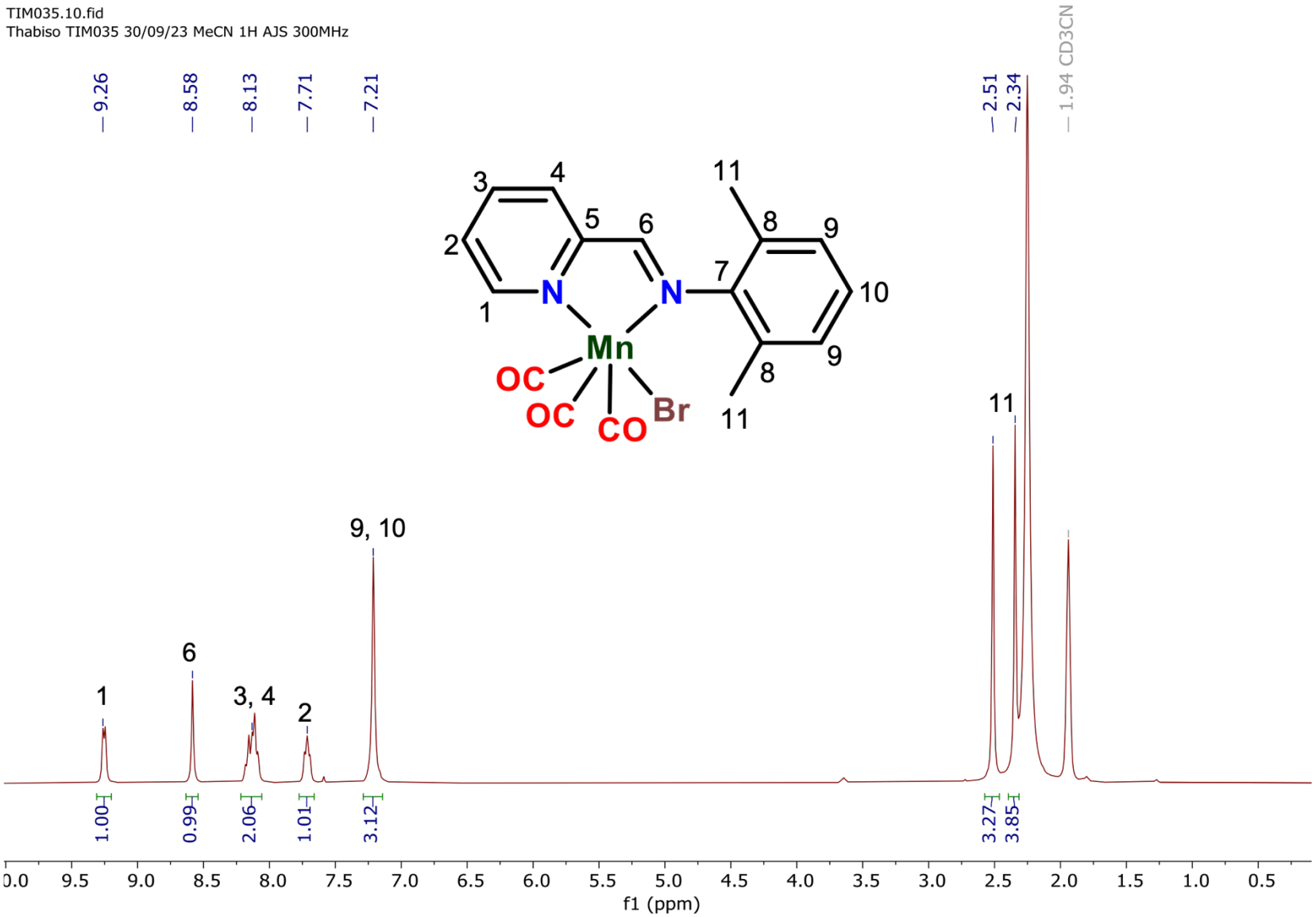

Figure 2.9: ^{1}H NMR spectrum of pyridylimine Mn(I) complex, **C2** recorded in CD_3CN-d_3 at 300 K.

Table 2.7: ^{1}H NMR spectral data of pyridylimine Mn(I) complexes, **C1** – **C4**.[a]

Complex	C=N***H***	Aromatic region	Aliphatic region		
			C***H*₃**	C***H***$(CH_3)_2$	C***H*₂**
C1	δ 8.61 (s, 1H, H^6)	δ 9.23 (d, *J* = 3.3 Hz, 1H, H^1) δ 8.12 (d, *J* = 4.9 Hz, 2H, $H^{3, 4}$) δ 7.56 – 7.68 (m, 6H, $H^{2, 8, 9, 10}$)	-	-	-
C2	δ 8.58 (s, 1H, H^6)	δ 9.25 (d, *J* = 3.3 Hz, 1H, H^1) δ 8.13 (d, *J* = 6.1 Hz, 2H, $H^{3, 4}$) δ 7.71 (t, *J* = 3.4 Hz, 1H, H^2) δ 7.21 (s, 3H, $H^{9, 10}$)	δ 2.51 (s, 6H, H^{11})	-	-
C3	δ 8.79 (s, 1H, H^6)	δ 9.44 (d, *J* = 3.8 Hz, 1H, H^1) δ 8.33 (d, *J* = 5.1 Hz, 2H, $H^{3, 4}$) δ 7.90 (d, *J* = 5.9 Hz, 1H, H^2) δ 7.54 (m, 3H, $H^{9, 10}$)	δ 1.46 – 1.19 (m, 12H, H^{12})	δ 3.19 (s, 2H, H^{11})	-
C4	δ 8.53 (s, 1H, H^6)	δ 9.23 (d, *J* = 3.7 Hz, 1H, H^1) δ 8.13 (d, *J* = 8.0 Hz, 2H, $H^{3, 4}$) δ 7.69 (t, *J* = 6.0 Hz, 1H, H^2) δ 7.02 (s, 2H, H^9)	δ 2.45 (s, 3H, H^{11}) δ 2.29 (s, 6H, H^{12})	-	-

[a] ^{1}H NMR spectra recorded in CD_3CN at 300 K; chemical shifts (δ) are reported in ppm values, referenced relative to the residual CD_3CN resonance; superscripts indicate protons as per numbering system in **Figure 2.6**; s = singlet, d = doublet, t = triplet, sept = septet, m = multiplet.

Table 2.8: ^{1}H NMR spectral data of pyridylimine Mn(I) complexes, **C5** – **C9**.[a]

Complex	C=N***H***	Aromatic region	Aliphatic region		
			C***H*$_3$**	C***H*$_2$**	C***H***
C5	δ 8.59 (s, 1H, H^{6})	δ 9.16 (d, *J* = 4.1 Hz, 1H, H^{1}) δ 8.07 (d, *J* = 7.9 Hz, 2H, H$^{3, 4}$) δ 7.60 (s, 1H, H^{2}) δ 7.45 (s, 5H, H$^{9, 10, 11}$)	-	δ 5.35 (s, 2H, H^{7})	-
C6	δ 8.58 (s, 1H, H^{6})	δ 9.15 (d, *J* = 3.9 Hz, 1H, H^{1}) δ 8.06 (d, *J* = 7.3 Hz, 2H, H$^{3, 4}$) δ 7.59 (s, 1H, H^{2})	-	δ 1.79 – 1.27 (m, 10H, H$^{8, 9, 10}$)	δ 4.07 (pent., *J* = 4.1 Hz, 1H, H^{7})
C7	δ 8.54 (s, 1H, H^{6})	δ 9.16 (d, *J* = 6.7 Hz, 1H, H^{1}) δ 8.07 (d, *J* = 4.1 Hz, 2H, H$^{3, 4}$) δ 7.60 (s, 1H, H^{2})	δ 1.00 (t, *J* = 2.2 Hz, 3H, H^{9})	δ 4.21 (d, *J* = 6.5 Hz, 2H, H^{7}) δ 2.10 (m, 2H, H^{8})	-
C8	δ 8.60 (s, 1H, H^{6})	δ 7.97 (t, *J* = 5.0 Hz, 1H, H^{4}) δ 7.87 (d, *J* = 4.8 Hz, 1H, H^{3}) δ 7.60 – 7.45 (m, 6H, H$^{2, 8, 9, 10}$)	δ 3.05 (s, 3H, H^{11})	-	-
C9	δ 8.82 (s, 1H, H^{6})	δ 8.37 – 8.21 (m, 3H, H$^{2, 3, 4}$) δ 7.54 (m, 5H, H$^{8, 9, 10}$)	-	-	-

[a] ^{1}H NMR spectra recorded in CD_3CN at 300 K; chemical shifts (δ) are reported in ppm values, referenced relative to the residual CD_3CN resonance; superscripts indicate protons as per numbering system in **Figure 2.8**; s = singlet, d = doublet, t = triplet, sept = septet, m = multiplet.

2.2.2.3 Mass Spectrometry and Elemental Analysis

ESI-MS recorded in the positive ion mode were consistent with the proposed pyridylimine Mn(I) complexes. The base peak for complexes **C1** – **C7** corresponds with the $[M\text{-}Br]^+$ fragment ion and is reported in **Table 2.9**. For complexes **C8** and **C9**, the base peak corresponds with the $[M\text{-}Br\text{-}3CO+MeOH]^+$ fragment ion. Additionally, the peaks corresponding to the fragment ions due to solvent exchange and CO ligand dissociation are reported in **Table 2.9**. The exchange of ligands with solvent molecules used in the analysis such as the observed methanol exchange is common and is often observed in ESI-MS.[22] The protonated molecular ion $[M+H]^+$ and dimeric fragment ions were not observed in the mass spectra for all complexes. The calculated fragmentation pattern[23] for each assigned fragment is the same as the experimentally observed pattern (**Figures 2.10**). CHN analysis confirmed the overall purity of the neutral manganese complexes **C1** – **C9**. The experimental elemental percentages were accordant with the calculated values.

Table 2.9: Mass spectrometry data of pyridylimine Mn(I) complexes **C1** – **C9**.

Complex	Fragment ion (m/z)		
	$[M\text{-}Br]^+$	$[M\text{-}Br\text{-}3CO+MeOH]^+$	$[M\text{-}Br\text{-}3CO]^+$
C1	321.0674 (321.0072)	269.0654 (269.0487)	237.0710 (237.0224)
C2	349.1064 (349.0385)	297.1037 (297.0799)	265.1091 (265.0537)
C3	405.1785 (405.1011)	353.1748 (353.1425)	321.1272 (321.1163)
C4	363.1248 (363.0541)	311.1218 (311.0956)	279.1272 (279.0694)
C5	335.0884 (335.0228)	283.0860 (283.0643)	251.0911 (251.0381)
C6	327.1186 (327.0541)	278.2230 (275.0956)	243.1213 (243.0694)
C7	287.0824 (287.0228)	235.0792 (235.0643)	203.0842 (203.0381)
C8	335.0224 (335.0228)	283.0275 (283.0643)	251.0091 (251.0381)
C9	-	336.9994 (337.0360)	-

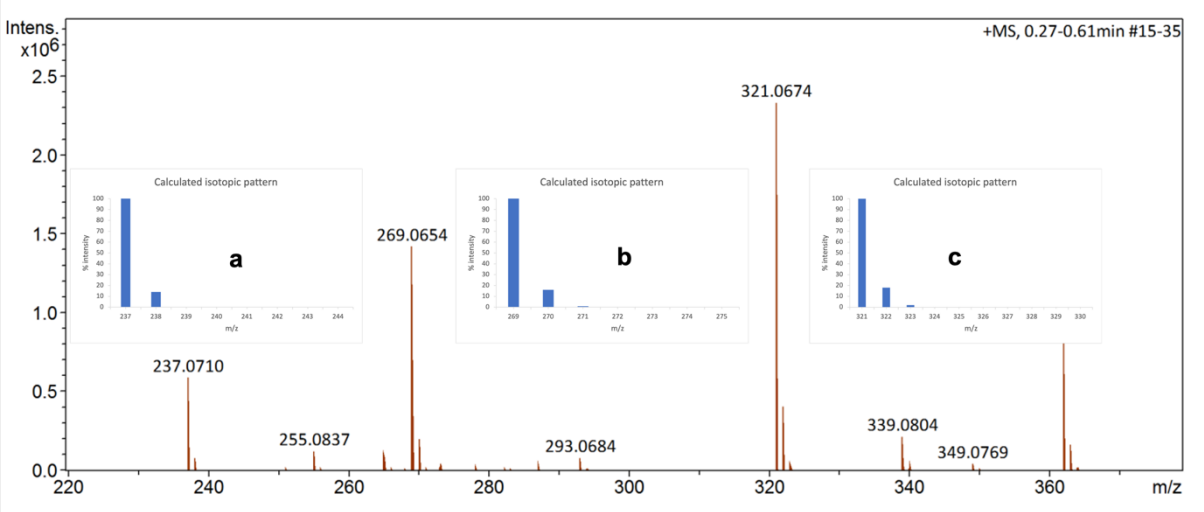

Figure 2.10: ESI-MS spectrum of pyridylimine Mn(I) complex **C1** recorded in the positive ion mode. Peaks located at 321.0674 m/z, 269.0654 m/z, and 237.0710 m/z correspond to the $[M\text{-}Br]^+$, $[M\text{-}Br\text{-}3CO+MeOH]^+$ and $[M\text{-}Br\text{-}3CO]^+$ fragment ions respectively. Inset shows the calculated isotopic patterns for the different fragmentations.

2.3 Single Crystal X-ray Diffraction (SCXRD)

Suitable single crystals of complexes **C1** - **C7** were isolated from a 1:1 THF-hexane solution placed in the dark, using liquid-liquid diffusion at room temperature to afford maroon and orange needle-like crystals for 7 days. Single-crystal X-ray diffraction analyses successfully determined the molecular structures. All atomic labels are given in the ORTEP pictures depicted in **Figure 2.11** – **Figure 2.14**. Crystallographic data and selected metric parameters such as bond lengths, bond angles, and torsion angles are shown in **Table 2.10** - **Table 2.13**.

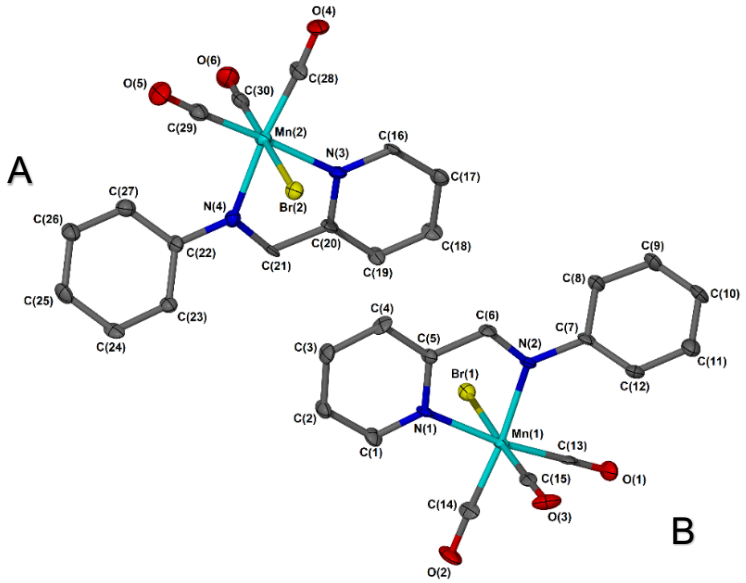

Figure 2.11: Molecular structures of complex **C1** with atomic numbering illustrated with 30% probability ellipsoids. All hydrogen atoms are omitted for clarity. The complex crystallizes as two independent molecules in the asymmetric unit labelled **A** and **B**.

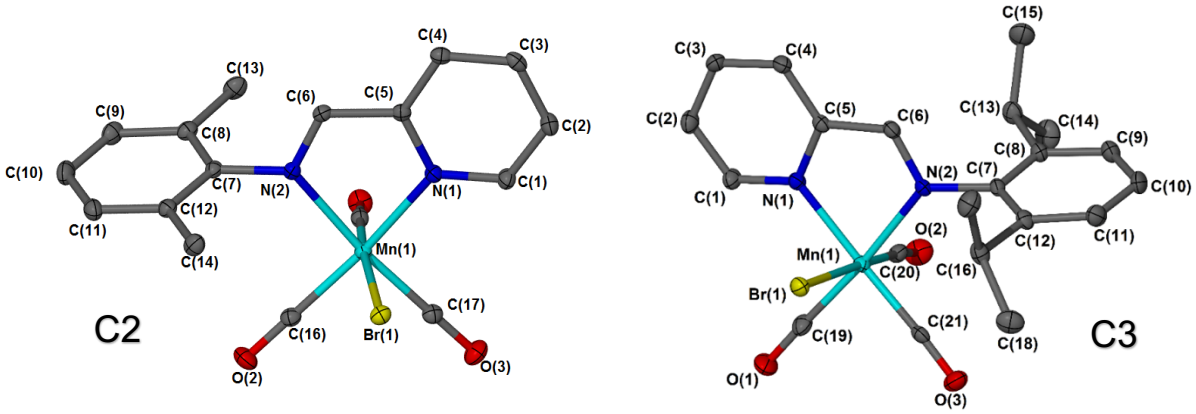

Figure 2.12: Molecular structures of complexes **C2** and **C3** with atomic numbering illustrated with 30% probability ellipsoids. All hydrogen atoms are omitted for clarity.

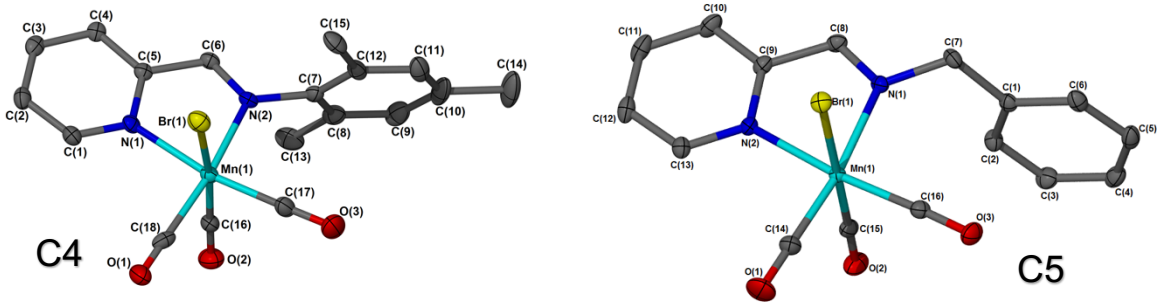

Figure 2.13: Molecular structures of complexes **C4** and **C5** with atomic numbering illustrated with 30% probability ellipsoids. All hydrogen atoms are omitted for clarity.

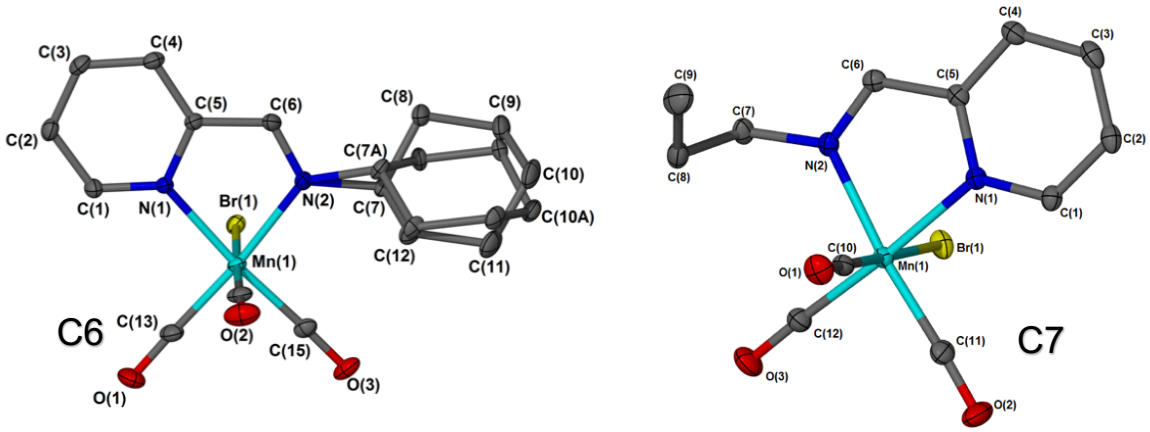

Figure 2.14: Molecular structures of complexes **C6** and **C7** with atomic numbering illustrated with 30% probability ellipsoids. All hydrogen atoms are omitted for clarity.

In all the complexes, the coordination sphere of manganese has a slightly distorted octahedral geometry. The pyridylimine ligand is situated in the equatorial position while the bromine ligand is located axially. Two of the carbonyl ligands are located equatorially with the third one situated axially confirming the formation of the *fac* isomer for all the complexes as indicated by FT-IR data. For complex **C1**, the distortion of the octahedral geometry is described by the bond angles N(3) - Mn(2) - N(4) and N(1) - Mn(1) - N(2) in **C1(A)** and **C1(B)** of 79.3(4)° and 78.4(4)° respectively (**Table 2.11**), while in **C2** it is evidenced by the bond angles N(1) - Mn(1) - N(2) and N(2) - Mn(1) - Br(1) of 78.28(6)° and 97.39(4)° respectively (**Table 2.11**). In complex **C3,** it is clearly described by the bond angles N(1) - Mn(1) - N(2) and N(2) - Mn(1) - C(21) of 79.05(14)° and 95.91(17)° respectively (**Table 2.11**). Similar deviations from the ideal bond angles of 90° for octahedral complexes can be observed in complexes **C4**, **C5**, **C6**, and **C7** (**Table 2.12**).

The distortion is because of the coordination of the rigid bidentate ligand to the manganese metal centre which leads to increased strain in the five-membered ring that forms.[24] The crystal structure of complex **C1** contains two discrete molecules (labelled **A** and **B**) with different geometries within the asymmetric unit cell. The C(21) - N(4) - C(22) - C(23) and C(6) - N(2) - C(7) - C(8) torsion angles (**Figure 2.11**) of 37.4(18)° and -49.2(17)° for **C1(A)** and **C1(B)** respectively, illustrate the structural differences between the two molecules. In complex **C6**, the cyclohexyl substituent adopts a chair conformation which is the thermodynamically stable conformation. Additionally, the cyclohexyl moiety is disordered due to the fluxional motion of the saturated ring with carbon atoms C(7) – C(12) and C(7)A – C(12)A having site occupancy factors of 0.782(4) and 0.218(4) at position *X*, respectively. The Mn – N, Mn – Br, and Mn –

CO bond lengths are approximately 2 Å, 2.5 Å and 1.8 Å, respectively. These bond lengths are within the range of related manganese(I) tricarbonyl complexes.[25] Complexes **C1**, **C3**, **C6,** and **C7** crystallized in the monoclinic crystal system with the $P2_1/c$, $P2_1/n$, $P2_1/c$, and $P2_1/c$ space groups, respectively. Manganese complexes **C2** and **C4** crystallized in the orthorhombic crystal system with the *Pbca* space group. Lastly, complex **C5** crystallized in the triclinic crystal system with the *P-1* space group.

Table 2.10: Crystallographic data and structure refinement parameters of manganese complexes **C1, C2, C3** and **C4.**

Parameter	Complexes			
	C1	**C2**	**C3**	**C4**
Empirical formula	$C_{30}H_{20}Br_2Mn_2N_4O_6$	$C_{17}H_{14}N_2O_3MnBr$	$C_{21}H_{22}BrMnN_2O$	$C_{18}H_{16}N_2O_3MnBr$
Mr (g/mol)	802.20	429.15	485.25	443.18
Crystal system	Monoclinic	Orthorhombic	Monoclinic	Orthorhombic
Space group	*P2₁/c*	*Pbca*	*P2₁/n*	*Pbca*
a (Å)	21.682(3)	14.1107(5)	8.7623(9)	14.0851(10)
b (Å)	8.7963(13)	7.5377(3)	23.178(3)	7.5882(6)
c (Å)	16.639(3)	31.2873(11)	10.8884(15)	33.875(3)
α (deg)	90	90	90	90
β (deg)	105.767(5)	90	103.242(5)	90
γ (deg)	90	90	90	90
Crystal size (mm^3)	0.02 x 0.22 x 0.22	0.221 x 0.163 x 0.068	0.03 x 0.05 x 0.14	0.329 x 0.224 x 0.018
Volume ($Å^3$)	3054.0(8)	3327.8(2)	2152.6(4)	3620.6(5)
Z	4	8	4	8
D_{calc} (g/cm^3)	1.7444	1.713	1.497	1.626
F(000)	1584	1712.0	984	1776.0
λ (MoK_a) (Å)	0.71073	0.71073	0.71073	0.71073
Temperature (K)	173.00	173.00	173.00	173.00
2*θ* min (deg)	2.0	3.888	1.8	3.76
2*θ* max (deg)	26.5	56.61	26.0	51.998
μ (mm^{-1})	3.493	3.212	2.492	2.955
Goodness-of-fit on F^2	1.16	1.051	1.09	1.131
Final R_1 indices [$I>2\sigma(I)$]	0.10624	0.0263	0.0490	0.0702
wR_2 (all reflections)	0.2480	0.0627	0.1419	0.1761
Flack x parameter	-	-	-	-

Table 2.11: Crystallographic data and structure refinement parameters of manganese complexes, **C5**, **C6** and **C7**.

Parameter	Complexes		
	C5	**C6**	**C7**
Empirical formula	$C_{16}H_{12}BrMnN_2O_3$	$C_{15}H_{16}N_2O_3MnBr$	$C_{12}H_{12}N_2O_3MnBr$
Mr (g/mol)	415.13	407.15	367.09
Crystal system	Triclinic	Monoclinic	Monoclinic
Space group	*P-1*	$P2_1/c$	$P2_1/c$
a (Å)	7.3726(3)	11.3875(4)	14.8437(5)
b (Å)	10.5909(4)	8.8972(3)	8.2151(3)
c (Å)	11.5986(4)	16.8270(6)	12.0167(5)
α (deg)	75.6230(10)	90	90
β (deg)	81.851(2)	107.6920(10)	102.738(2)
γ (deg)	71.997(2)	90	90
Crystal size (mm^3)	0.264 x 0.136 x 0.09	0.242 x 0.091 x 0.072	0.183 x 0.157 x 0.067
Volume ($Å^3$)	832.25(6)	1624.23(10)	1429.28(9)
Z	2	4	4
D_{calc} (g/cm^3)	1.657	1.665	1.706
F(000)	412.0	816.0	728.0
λ (MoK_a) (Å)	0.71073	0.71073	0.71073
Temperature (K)	173.00	173.00	173.00
2*θ* min (deg)	3.634	5.082	5.628
2*θ* max (deg)	56.892	56.904	56.78
μ (mm^{-1})	3.208	3.285	3.723
Goodness-of-fit on F^2	1.106	1.051	1.046
Final R_1 indices [$I>2\sigma(I)$]	0.0250	0.0235	0.0250
wR_2 (all reflections)	0.0769	0.0571	0.0614
Flack x parameter	-	-	-

Table 2.12: Selected bond lengths (Å), bond angles (°), and torsion angles (°) of manganese complexes **C1(A), C1(B), C2,** and **C3**.[a]

Bond Lengths	Bond Angles	Torsion Angles	Complexes			
			C1(A)	C1(B)	C2	C3
Mn(1) – N(1)	-	-	-	2.049(10)	2.0437(15)	2.036(4)
Mn(1) – N(2)	-	-	-	2.053(9)	2.0645(15)	2.067(4)
Mn(1) – Br(1)	-	-	-	2.521(2)	2.5536(3)	2.5308(8)
Mn(2) – N(3)	-	-	2.041(10)	-	-	-
Mn(2) – N(4)	-	-	2.051(11)	-	-	-
Mn(2) – Br(2)	-	-	2.502(2)	-	-	-
Mn(1) – C(19)	-	-	-	-	-	1.797(5)
Mn(1) – C(20)	-	-	-	-	-	1.813(5)
Mn(1) – C(21)	-	-	-	-	-	1.811(5)
Mn(1) – C(13)	-	-	-	1.827(13)	-	-
Mn(1) – C(14)	-	-	-	1.779(12)	-	-
Mn(1) – C(15)	-	-	-	1.818(16)	1.797(2)	-
Mn(1) – C(16)	-	-	-	-	1.821(2)	-
Mn(1) – C(17)	-	-	-	-	1.809(2)	-
Mn(2) – C(28)	-	-	1.813(14)	-	-	-
Mn(2) – C(29)	-	-	1.815(13)	-	-	-
Mn(2) – C(30)	-	-	1.842(16)	-	-	-
-	N(1) - Mn(1) – N(2)	-	-	78.4(4)	78.28(6)	79.05(14)
-	N(1) - Mn(1) – Br(1)	-	-	85.6(3)	86.02(4)	83.12(9)
-	N(3) - Mn(2) – N(4)	-	79.3(4)	-	-	-
-	N(3) - Mn(2) – Br(2)	-	86.3(3)	-	-	-
-	N(1) - Mn(1) – C(19)	-	-	-	-	95.93(18)
-	N(1) - Mn(1) – C(14)	-	-	95.0(5)	-	-
-	N(1) - Mn(1) – C(17)	-	-	-	96.25	-
-	N(3) - Mn(2) – C(28)	-	94.7(5)	-	-	-
-	-	C(6) - N(2) - C(7) - C(8)	-	-49.2(17)	-	-69.9(5)
-	-	C(21) - N(4) - C(22) - C(23)	+37.4(18)	-	-	-
-	-	Mn(1) – N(2) – C(6) – C(5)	-	-	-3.0(2)	-

[a] Atoms are labelled as per numbering given in **Figure 2.11** – **Figure 2.12**.

Table 2.13: Selected bond lengths (Å), bond angles (°), and torsion angles (°) of manganese complexes **C4**, **C5**, **C6**, and **C7**.[a]

Bond Lengths	Bond Angles	Torsion Angles	Complexes			
			C4	C5	C6	C7
Mn(1) – N(1)	-	-	2.052(5)	2.0405(16)	2.0436(13)	2.0392(16)
Mn(1) – N(2)	-	-	2.055(5)	2.0529(16)	2.0509(16)	2.0389(17)
Mn(1) – Br(1)	-	-	2.5508(13)	2.5115(4)	2.5186(3)	2.5275(4)
Mn(1) – C(16)	-	-	1.795(8)	1.814(2)	-	-
Mn(1) – C(15)	-	-	-	1.798(2)	1.8169(18)	-
Mn(1) – C(14)	-	-	-	1.799(2)	1.799(2)	-
Mn(1) – C(10)	-	-	-	-	-	1.796(2)
Mn(1) – C(11)	-	-	-	-	-	1.802(2)
Mn(1) – C(12)	-	-	-	-	-	1.812(2)
Mn(1) – C(13)	-	-	-	-	1.798(2)	-
Mn(1) – C(17)	-	-	1.815(8)	-	-	-
Mn(1) – C(18)	-	-	1.894(9)	-	-	-
-	N(1) - Mn(1) – N(2)	-	77.9(2)	78.57(6)	78.94(6)	78.81(6)
-	N(1) - Mn(1) – Br(1)	-	86.55(15)	85.23(5)	86.62(4)	87.07(4)
-	N(2) – Mn(1) – Br(1)	-	97.39(15)	88.66(5)	88.29(5)	86.83(5)
-	C(7A) – N(2) – Mn(1)	-	-	-	138.1(4)	-
-	C(14) - Mn(1) – C(16)	-	-	89.42(10)	-	-
-	C(13) - Mn(1) – C(15)	-	-	-	88.06(4)	-
-	C(11) - Mn(1) – C(12)	-	-	-	-	88.47(10)
-	N(1) – Mn(1) – C(16)	-	95.1(3)	95.97(8)	-	-
-	N(2) – Mn(1) – C(14)	-	-	-	91.45(8)	-
-	N(2) – Mn(1) – C(10)	-	-	-	-	92.83(8)
-	-	C(8) - C(9) – N(2) – Mn(1)	-	-4.5(2)	-	-
-	-	C(9) – C(8) – N(1) – Mn(1)	-	0.1(2)	-	-
-	-	Mn(1) - N(2) - C(6) - C(5)	-0.1(7)	-	-0.3(2)	-2.2(2)
-	-	Mn(1) – N(1) – C(5) – C(6)	3.8(7)	-	-2.2(2)	1.87(19)

[a] Atoms are labelled as per numbering given in **Figure 2.13** – **Figure 2.14**.

2.4 Investigations into the photolability of Mn-CO in pyridylimine Mn(I) complexes.

2.4.1 Introduction

Several literature reports have highlighted the potential photosensitivity and decomposition of manganese tricarbonyl systems when exposed to light. An example is a study where Blakemore and his colleagues studied the photosensitivity of [$Mn(CO)_3$] complexes using transient absorption spectroscopy which revealed ultrafast CO ligand dissociation from the manganese metal centre which occurs on the femtosecond scale.[26] Furthermore, they discovered that the rate of CO ligand loss is greater when catalyst systems contain electron-donating substituents than electron-withdrawing substituents (**Figure 2.15**). They also illustrated the rate of solvent coordination to the manganese metal centre to be on the picosecond scale.

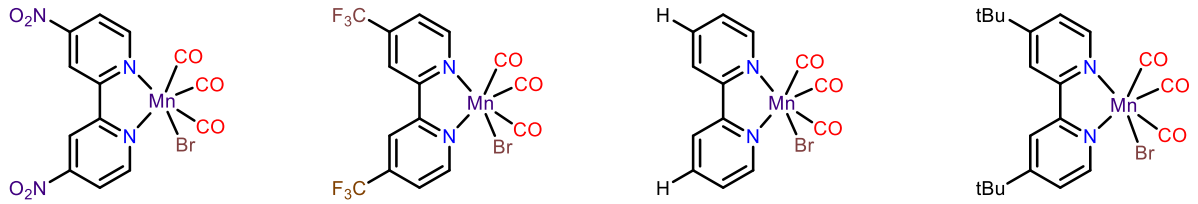

LXVI **LXVII** **LXVIII** **LXIX**

Figure 2.15: A series of manganese complexes bearing varying electron donating and withdrawing substituents prepared by Blakemore and co-workers.[26]

Prompted by these findings, we studied our manganese complexes, **C1** and **C5** for potential photosensitivity using Fourier Transform Infrared Spectroscopy (FT-IR) and Single Crystal X-ray Diffraction (SCXRD). Complexes **C1** and **C5** were chosen to illustrate that CO ligand dissociation occurs in both aromatic and aliphatic substituted pyridylimine Mn(I) complexes.

2.4.1.1 FT-IR Spectroscopy

Manganese complexes, **C1a** and **C5a** were exposed to direct sunlight for 5 hours in their solid state and solution i.e. dissolved in acetonitrile. Similarly, **C1** and **C5** were placed in the dark both in their solid state and dissolved in acetonitrile. After 5 hours, the acetonitrile was evaporated, and the complexes were recorded as neat solids on an FT-IR instrument. For complexes placed in direct sunlight in their solid state, the peaks assigned to CO ligands were observed at (ν_{CO}: 1898.88 cm^{-1}, 2020.43 cm^{-1} for **C1a** and ν_{CO}: 1898.74 cm^{-1}, 2021.53 cm^{-1} for **C5a**). Similar data was obtained when **C1** and **C5** were placed away from sunlight in the solid state (**Figure 2.17**). No shifts in the imine ($\nu_{C=N}$) absorption bands were observed for the

complexes under this set of conditions (**Table 2.14**). Hence, it can be deduced that there is no CO ligand dissociation when the complexes are in their solid state.

A disappearance of the carbonyl (ν_{CO}) absorption bands was noted in the FT-IR spectra obtained for both **C1a** and **C5a** dissolved in acetonitrile when exposed to direct sunlight (**Figure 2.16**). Additionally, a shift (37 cm^{-1} for **C1a** and 18 cm^{-1} for **C5a**) to higher wavenumbers for the imine ($\nu_{C=N}$) absorption band is observed for the complexes exposed to sunlight in solution state in comparison to the complexes stored in their solid state under the same conditions (**Table 2.14**). Similar blue shifts are observed for the pyridylimine ($\nu_{pyr\text{-}C=N}$) absorption band and are an indication of an increased double bond character for both the imine and pyridylimine functional groups under visible light conditions.[19]

The FT-IR spectra obtained from **C1** and **C5** dissolved in acetonitrile and placed in the dark also indicate blue shifts (36 cm^{-1} for **C1** and 27 cm^{-1} for **C5**) compared to the complexes stored in the solid state under the same conditions (**Table 2.14**). As expected, the carbonyl (ν_{CO}) absorption bands were still present in the FTIR spectral region 1800 – 2100 cm^{-1} for both complexes in solution and in the dark (**Figure 2.17**). Hence, it can be deduced that **C1** and **C5** remain stable in solution when visible light is excluded.

Table 2.14: FT-IR data for complexes **C1a** and **C5a** placed in direct sunlight in their solid and solution states.

Complex	FT-IR (light)[a]		FT-IR (dark)[a]	
	($\nu_{C=N}$, cm^{-1}), solution	**($\nu_{C=N}$, cm^{-1}), solid state**	**($\nu_{C=N}$, cm^{-1}), solution**	**($\nu_{C=N}$, cm^{-1}), solid state**
C1a	1652	1615	1650	1614
C5a	1646	1628	1655	1628

[a] Recorded as neat solids using an ATR accessory.

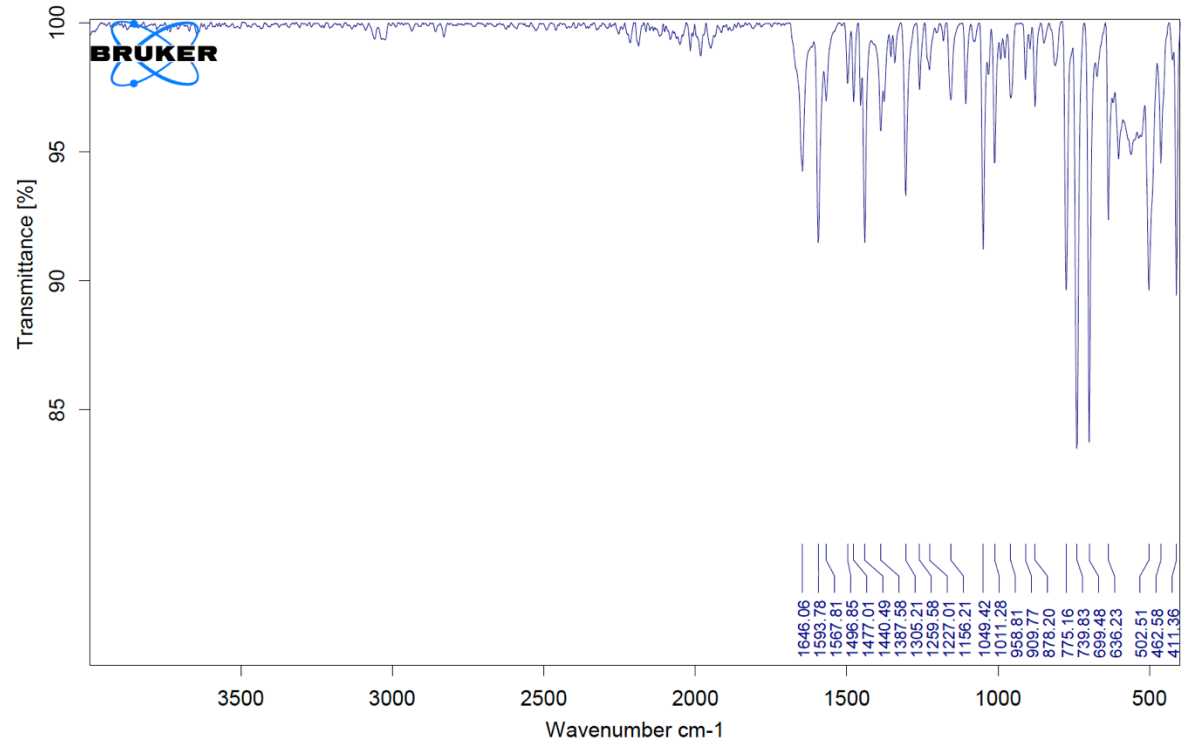

Figure 2.16: FT-IR spectra of complex **C5a** dissolved in MeCN with light exposure.

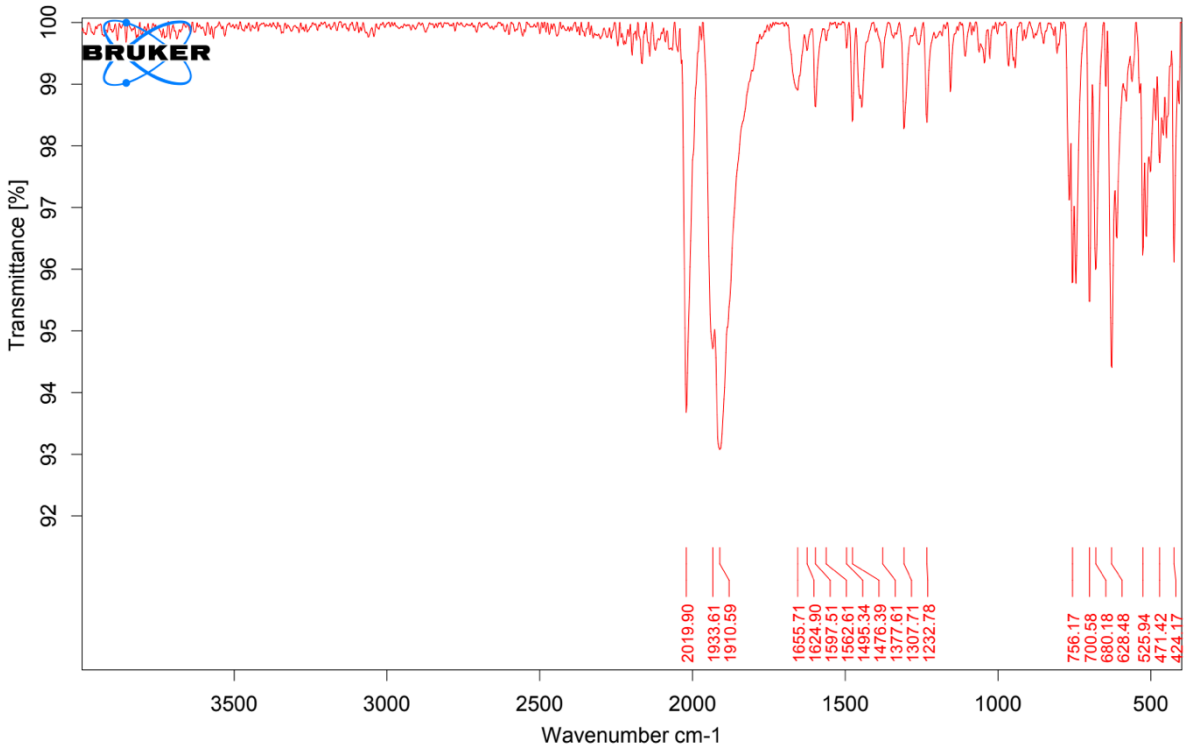

Figure 2.17: FT-IR spectra of complex **C5** dissolved in MeCN with light exclusion.

2.4.1.2 Single Crystal X-Ray Diffraction (SCXRD)

Suitable single crystals of complexes, **C1a** and **C5a,** were grown using two crystallization methods i.e., vapour diffusion of hexane into a solution of **C1a** dissolved in THF and slow evaporation of a solution of **C5a** in THF for 7 days. The maroon single crystals were grown while exposed to visible light over an extended period. The molecular structures were successfully elucidated using single-crystal diffraction analyses. All atomic labels are given in the ORTEP pictures depicted in **Figures 2.18** and **2.19**. Crystallographic data and selected metric parameters such as bond lengths, bond angles, and torsion angles are shown in **Table 2.14** and **Table 2.15**.

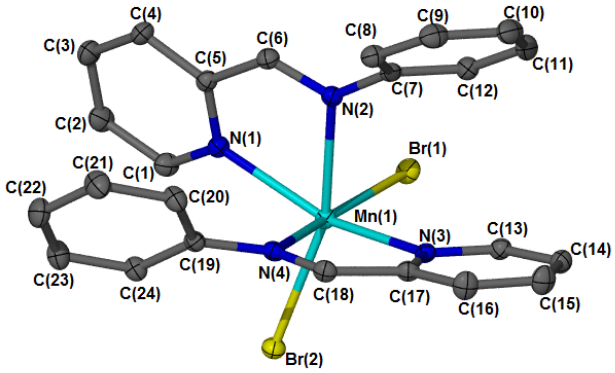

Figure 2.18: Molecular structure of complex **C1a** grown under visible light conditions with atomic numbering illustrated with 30% probability ellipsoids. All hydrogen atoms are omitted for clarity.

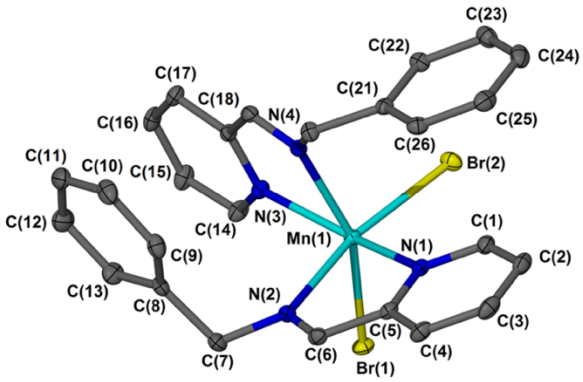

Figure 2.19: Molecular structure of complex **C5a** grown under visible light conditions with atomic numbering illustrated with 30% probability ellipsoids. All hydrogen atoms are omitted for clarity.

The molecular structures of **C1a** and **C5a** grown under visible light exposure conditions indicate a more distorted octahedral geometry around the manganese metal center than the slightly distorted octahedral geometry of the same complexes grown under visible light exclusion (**Figures 2.18** and **2.19**). This is evidenced by the N(1) – Mn(1) – N(2) bond angles of 70.86(6)° and 72.19(4)° for **C1a** and **C5a**, respectively (**Table 2.16**). Complexes **C1a** grown under visible light exposure and exclusion conditions have a monoclinic crystal system. In contrast, a triclinic to monoclinic change in the crystal system is observed for complexes **C5a** grown under visible light exclusion and exposure conditions (**Table 2.15**).

The Mn(1) – N(1) and Mn(1) – N(2) bond lengths of 2.2583(17) Å and 2.2938(11) Å for **C1a** and **C5a** respectively, are greater than similar bond lengths for **C1a** and **C5a** grown under visible light exclusion conditions. This reduced bond strength because of an increased bond length implies less strain in the five-membered ring formed between the pyridylimine ligands and the manganese metal centre. The deviation from the ideal bond angles of 90° for octahedral complexes is due to the chelation to the manganese metal centre by the rigid, bidentate pyridylimine ligands.

The coordination sphere around the metal centre is completed by two pyridylimine ligands, in axial and equatorial positions, and two bromine ligands also in axial and equatorial positions. The crystal structures grown in direct sunlight indicate a +2 oxidation state of the metal compared to the +1 oxidation state of the crystal structures grown in the dark (**Figures 2.18** and **2.19**). Most importantly, the crystal structures do not have any carbonyl (CO) ligands present which provides further evidence of CO ligand loss under visible light exposure conditions.

Table 2.15: Crystallographic and structure refinement parameters of complexes **C1a** and **C5a**.

Parameter	Complexes	
	C1a	**C5a**
Empirical formula	$C_{24}H_{20}N_4MnBr_2$	$C_{26}H_{24}Br_2MnN_4$
Mr (g/mol)	579.20	607.25
Crystal system	Monoclinic	Monoclinic
Space group	*C2/c*	$P2_1/n$
a (Å)	24.9932(9)	8.8312(3)
b (Å)	15.1263(5)	13.3514(4)
c (Å)	14.3324(6)	20.9441(7)
α (deg)	90	90
β (deg)	118.2220(10)	90.3230(10)
γ (deg)	90	90
Crystal size (mm^3)	0.189 x 0.135 x 0.052	0.322 x 0.25 x 0.164
Volume ($Å^3$)	4774.3(3)	2469.46(14)
Z	8	4
D_{calc} (g/cm^3)	1.612	1.633
F(000)	2296.0	1212.0
λ (MoK_a) (Å)	0.71073	0.71073
Temperature (K)	173.00	173.00
2*θ* min (deg)	3.928	4.944
2*θ* max (deg)	56.722	57.226
μ (mm^{-1})	3.919	3.792
Goodness-of-fit on F^2	1.074	1.037
Final R_1 indices [$I>2\sigma(I)$]	0.0251	0.0211
wR_2 (all reflections)	0.0619	0.0524
Flack x parameter	-	-

Table 2.16: Selected bond lengths (Å), bond angles (°), and torsion angles (°) of light-exposed manganese complexes, **C1a** and **C5a**.[a]

Bond Lengths	Bond Angles	Torsion Angles	Complexes	
			C1a	C5a
Mn(1) – N(1)	-	-	2.2583(17)	2.2938(11)
Mn(1) – N(2)	-	-	2.4314(16)	2.3025(12)
Mn(1) – N(3)	-	-	2.2418(16)	2.2900(12)
Mn(1) – N(4)	-	-	2.3427(16)	2.3636(12)
Mn(1) – Br(1)	-	-	2.5474(4)	2.6527(3)
Mn(1) – Br(2)	-	-	2.6089(3)	2.5917(3)
-	N(1) - Mn(1) – N(2)	-	70.86(6)	72.19(4)
-	N(1) - Mn(1) – Br(1)	-	96.57(4)	88.86(4)
-	N(2) - Mn(1) – N(3)	-	83.85(5)	97.80(4)
-	N(3) - Mn(1) – Br(2)	-	106.00(4)	96.64(3)
-	N(3) - Mn(1) – N(4)	-	72.34(6)	71.46(4)
-	N(2) – Mn(1) – Br(2)	-	162.22(4)	165.42(3)
-	-	C(5) – C(6) – N(2) – Mn(1)	-13.2(2)	3.50(17)
-	-	C(6) – C(5) – N(1) – Mn(1)	5.0(2)	4.80(15)
-	-	N(1) – C(5) – C(6) – N(2)	6.4(3)	-5.7(2)

[a] Atoms are labelled as per numbering in **Figure 2.18** and **Figure 2.19**.

2.5 Attempts at Formic Acid dehydrogenation using Mn(I) complexes.

Manganese complexes have experienced a recent surge in attention for their ability to operate as catalyst precursors in organic transformations such as the hydrogenation and dehydrogenation of carbon dioxide and formic acid, respectively. Tondreau and coworkers reported a rapid and robust manganese(I) catalyst for efficient FA dehydrogenation (**Scheme 2.4**).[27] Manganese complex **LXX** catalyzed the dehydrogenation of FA over several cycles without loss of activity reaching turnover frequencies (TOFs) above 8500 hr^{-1}.

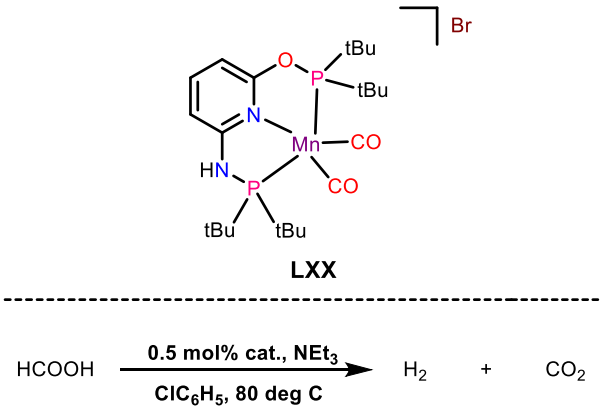

Scheme 2.4: Manganese(I) catalyst for efficient FA dehydrogenation.[27]

Based on these observations and sufficient evidence of efficient H_2 production from the dehydrogenation of FA over manganese catalysts as presented in **Chapter 1**, we evaluated the activity of the manganese complexes prepared in this study. The reaction conditions used were modified from a literature catalytic procedure by Albrecht and coworkers.[28] A summary of all the catalytic experiments toward Mn-catalyzed FA dehydrogenation is provided in **Table 2.17**.

Table 2.17: Evaluation of Mn(I) complexes for FA dehydrogenation.[a]

Entry	Catalyst	$CO_2 + H_2$ (mL)	Conversion (%)
1	**$MnBr(CO)_5$**	0	-
2	**C1**	20	8
3	**C2**	26	10
4	**C3**	15	6
5	**C4**	20	8
6	**C5**	0	-
7	**C6**	0	-
8	**C7**	0	-
9	**C8**	0	-
10	**C9**	0	-
11[b]	**C1**	5	2
12[c]	**C1**	0	-

[a] **Conditions**: FA (5 mmol, 0.2 mL), Mn catalyst (0.2 mol%, 0.01 mmol), KOH (5 mmol), H_2O (1 mL) dioxane (2 mL), temperature (90 °C), total reaction volume (2.2 mL).[b] Performed using HCOONa as additive. [c] Performed in neat FA. Maximum theoretical volume ($CO_2 + H_2$): 259 mL.

No gas evolution was observed when the reaction was conducted using the manganese pentacarbonyl bromide, $MnBr(CO)_5$ precursor (**Table 2.17**, entry 1). Similarly, no gas evolution was noted when the reaction was performed without a catalyst. Complexes **C1** – **C4** displayed some activity towards FA dehydrogenation with conversions up to 14% (**Table 2.17**, entries 2 – 5). However, gas evolution ceased within 15 minutes accompanied by a colour change from the usual yellow-orange solution to a brown-colored reaction mixture indicative of catalyst decomposition. No gas evolution was observed for the dehydrogenation of FA over complexes **C5** – **C7** that possess aliphatic substituents on the imine nitrogen (**Table 2.17**, entries 6 – 8). Attempts at FA dehydrogenation using complexes **C8** and **C9** also resulted in no gas evolution (**Table 2.17**, entries 9 – 10). Lastly, efforts to employ HCOONa instead of KOH yielded some

activity while conducting the reaction under neat FA conditions was futile (**Table 2.17**, entries 11 and 12).

2.6 Conclusions

A series of manganese(I) complexes bearing pyridylimine ligands with different electronic and steric properties were successfully prepared and characterized using a range of analytical and spectroscopic techniques. Single crystal X-ray diffraction analysis indicates unambiguously that the geometry around the metal center is a distorted octahedron. FT-IR and SCXRD analyses obtained from selected light-exposed complexes indicate the 'photo-lability' of the Mn-CO bond in solution that is accompanied by an increase in the oxidation state (I $\rightarrow$ II) of the manganese metal centre. The prepared pyridylimine Mn(I) complexes were found to be inactive towards the dehydrogenation of FA due to their unstable nature when exposed to light and in solution.

2.7 Materials and Methods

All reactions involving air- and/or moisture-sensitive compounds were performed under purified dry nitrogen using normal Schlenk techniques. All reagents were obtained from Sigma-Aldrich and used as purchased. Solvents were purchased from Promark Chemicals and Sigma Aldrich and used without further purification. IR spectra were recorded as neat oils or solids on a Bruker Tensor 27 FTIR spectrometer fitted with an Attenuated Total Reflectance (ATR) accessory. NMR spectra were recorded on a Bruker Avance NMR spectrometer (^{1}H at 300 MHz and 400 MHz, ^{13}C at 75 MHz and 101 MHz). The chemical shifts are reported in ppm and referenced to the residual protons of the deuterated solvents with tetramethylsilane (TMS) as an internal standard. ESI-MS analyses were recorded on a Thermo Scientific Dionex Ultimate 3000 UHPLC coupled to a Bruker Compact QqTOF HRMS in the positive mode using the Loop method. Melting point measurements were recorded using a Stuart SMP30 instrument and were reported as obtained. Single X-ray diffraction data was collected on a Bruker APEX-II CCD diffractometer. The crystal was kept at 173.00 K during data collection. Using Olex2,[29] the structure was solved with the SHELX[30] structure solution program using Intrinsic Phasing and refined with the SHELXL[31] refinement package using Least Squares minimization. All non-hydrogen atoms were refined anisotropically. Molecular diagrams were drawn using the POV-Ray program.[32] Elemental analysis was recorded using a Thermo Scientific Flash 2000 Series CHNS-O Analyzer (UJ).

2.7.1 Synthesis of pyridylimine ligands, L1 – L9.

2.7.1.1 N-Phenyl-1-(2-pyridinyl)methanimine (L1)

Aniline (1306.6 mg, 14.03 mmol) was added to a stirred solution of 2-pyridinecarboxaldehyde (1502.9 mg, 14.03 mmol) in toluene (5 mL) under a N_2 atmosphere. Following the complete addition of the amine, the mixture was reacted at room temperature for 24 hours. After the reaction, the mixture was concentrated under reduced pressure and the residue was dried under a high vacuum to obtain the ligand as a yellow oil. **Yield**: 2298.5 mg (90%). **^{1}H NMR** (300 MHz, CD_3CN-d_3): δ (in ppm) = 8.69 (d, *J* = 3.25 Hz, 1H, H^1), 8.59 (s, 1H, H^6), 8.16 (d, *J* = 7.86 Hz, 1H, H^4), 7.87 (t, *J* = 7.63 Hz, 1H, H^3), 7.43 (t, *J* = 7.53 Hz, 3H, $H^{2, 8}$), 7.31 (t, *J* = 8.14 Hz, 3H, $H^{9, 10}$). **^{13}C NMR** (75 MHz, CD_3CN-d_3): δ (in ppm) = 160.5, 154.4, 150.8, 149.5, 136.5, 129.0, 126.5, 125.0, 121.7, 120.9. **FTIR** (ATR, neat): 1627.14 cm^{-1} ($\nu_{C=N}$), 1584.38 cm^{-1} ($\nu_{pyr\text{-}C=N}$). **ESI-MS** (+ve, m/z): Calcd. for $[M+H]^+$ 183.0922, found 183.0917.

2.7.1.2 N-(2,6-Dimethylphenyl)-1-(2-pyridinyl)methanimine (L2)

Synthesized using the synthetic procedure described for **L1** by employing 2,6-dimethylaniline (1711.6 mg, 14.12 mmol) as a reagent. The ligand was isolated as a yellow crystalline solid. **Yield**: 2631.8 mg (89%). **^{1}H NMR** (300 MHz, CD_3CN-d_3): δ (in ppm) = 8.71 (d, *J* = 3.98 Hz, 1H, H^1), 8.31 (s, 1H, H^6), 8.24 (d, *J* = 7.93 Hz, 1H, H^4), 7.91 (t, *J* = 7.86 Hz, 1H, H^3), 7.49 (t, *J* = 6.34 Hz, 1H, H^2), 7.07 (d, *J* = 7.72 Hz, 2H, H^9), 6.96 (t, *J* = 7.76 Hz, 1H, H^{10}), 2.11 (s, 6H, H^{11}). **^{13}C NMR** (75 MHz, CD_3CN-d_3): δ (in ppm) = 163.5, 154.4, 150.3, 149.7, 136.7, 128.3, 126.9, 125.4, 124.1, 121.3, 18.3. **FTIR** (ATR, neat): 1637.36 cm^{-1} ($\nu_{C=N}$), 1584.57 cm^{-1} ($\nu_{pyr\text{-}C=N}$). **ESI-MS** (+ve, m/z): Calcd. for $[M+H]^+$ 211.1235, found 211.1215.

2.7.1.3 N-(2,6-Diisopropylphenyl)-1-(2-pyridinyl)methanimine (L3)

Synthesized using the synthetic procedure described for **L1** by employing 2,6-diisopropylaniline (1044.8 mg, 5.89 mmol) as a reagent. The ligand was isolated as a yellow crystalline solid. **Yield**: 1232.8 mg (79%). **^{1}H NMR** (300 MHz, CD_3CN-d_3): δ (in ppm) = 8.70 (d, *J* = 3.62 Hz, 1H, H^1), 8.27 (s, 1H, H^6), 8.20 (d, *J* = 8.11 Hz, 1H, H^4), 7.92 (t, *J* = 7.97 Hz, 1H, H^3), 7.50 (t, *J* = 6.33 Hz, 1H, H^2), 7.17 (s, 3H, $H^{9, 10}$), 2.93 (q, *J* = 7.12 Hz, 2H, H^{11}), 1.14 (d, *J* = 6.84 Hz, 12H, H^{12}). **^{13}C NMR** (75 MHz, CD_3CN-d_3): δ (in ppm) = 163.0, 154.4, 149.7, 148.4, 137.3, 136.8, 125.4, 124.5, 123.1, 121.4, 28.0, 23.5, 22.5. **FTIR** (ATR, neat): 1639.09 cm^{-1} ($\nu_{C=N}$), 1585.08 cm^{-1} ($\nu_{pyr\text{-}C=N}$). **ESI-MS** (+ve, m/z): Calcd. for $[M+H]^+$ 267.1861, found 267.1810.

2.7.1.4 N-Mesityl-1-(2-pyridinyl)methanimine (L4)

Synthesized using the synthetic procedure described for **L1** by employing 2,4,6-trimethylaniline (1897.1 mg, 14.03 mmol) as a reagent. The ligand was isolated as a dark orange oil. **Yield**: 2788.5 mg (89%). **^{1}H NMR** (300 MHz, CD_3CN-d_3): δ (in ppm) = 8.71 (d, *J* = 3.71 Hz, 1H, H^1), 8.33 (s, 1H, H^6), 8.27 (d, *J* = 8.06 Hz, 1H, H^4), 7.84 (t, *J* = 7.64 Hz, 1H, H^3), 7.40 (t, *J* = 5.95 Hz, 1H, H^2), 6.91 (s, 2H, H^9), 2.29 (s, 3H, H^{11}), 2.14 (s, 6H, H^{12}). **^{13}C NMR** (75 MHz, CD_3CN-d_3): δ (in ppm) = 163.6, 154.7, 149.7, 148.0, 136.8, 133.6, 129.0, 127.0, 125.4, 121.3, 20.9, 18.4. **FTIR** (ATR, neat): 1639.64 cm^{-1} ($\nu_{C=N}$), 1585.40 cm^{-1} ($\nu_{pyr\text{-}C=N}$). **ESI-MS** (+ve, m/z): Calcd. for $[M+H]^+$ 225.1392, found 225.1372.

2.7.1.5 N-Benzyl-1-(2-pyridinyl)methanimine (L5)

Synthesized using the synthetic procedure described for **L1** by employing benzylamine (1501.2 mg, 14.01 mmol) as a reagent. The ligand was isolated as an orange oil. **Yield**: 2630.2 mg (96%). **^{1}H NMR** (300 MHz, CD_3CN-d_3): δ (in ppm) = 8.64 (d, *J* = 4.08 Hz, 1H, H^1), 8.48 (s, 1H, H^6), 7.95 (d, *J* = 7.93 Hz, 1H, H^4), 7.79 (t, *J* = 7.68 Hz, 1H, H^3), 7.37 (m, 6H, $H^{2, 9, 10, 11}$), 4.84 (s, 2H, H^7). **^{13}C NMR** (75 MHz, CD_3CN-d_3): δ (in ppm) = 161.8, 153.5, 148.4, 137.6, 135.5, 127.5, 127.2, 126.1, 123.8, 120.3. **FTIR** (ATR, neat): 1645.60 cm^{-1} ($\nu_{C=N}$), 1586.13 cm^{-1} ($\nu_{pyr\text{-}C=N}$). **ESI-MS** (+ve, m/z): Calcd. for $[M+H]^+$ 197.1079, found 197.1064.

2.7.1.6 N-Cyclohexyl-1-(2-pyridinyl)methanimine (L6)

Synthesized using the synthetic procedure described for **L1** by employing cyclohexylamine (1396.9 mg, 14.08 mmol) as a reagent. The ligand was isolated as a dark orange oil. **Yield**: 2296.0 mg (87%). **^{1}H NMR** (300 MHz, CD_3CN-d_3): δ (in ppm) = 8.58 (d, *J* = 4.68 Hz, 1H, H^1), 8.35 (s, 1H, H^6), 7.91 (d, *J* = 7.90 Hz, 1H, H^4), 7.77 (td, ^3J = 7.65 Hz, ^4J = 1.50 Hz, 1H, H^3), 7.35 (d, *J* = 6.19 Hz, 1H, H^2), 3.29 (m, 1H, H^7), 1.81 – 1.24 (m, 10H, H). **^{13}C NMR** (75 MHz, CD_3CN-d_3): δ (in ppm) = 159.6, 155.0, 149.5, 136.6, 124.6, 121.5, 69.8, 34.3, 25.7, 24.8. **FTIR** (ATR, neat): 1647.40 cm^{-1} ($\nu_{C=N}$), 1587.55 cm^{-1} ($\nu_{pyr\text{-}C=N}$). **ESI-MS** (+ve, m/z): Calcd. for $[M+H]^+$ 189.1392, found 189.1371.

2.7.1.7 N-Propyl-1-(2-pyridinyl)methanimine (L7)

Synthesized using the synthetic procedure described for **L1** by employing propylamine (844.0 mg, 14.28 mmol) as a reagent. The ligand was isolated as a dark orange oil. **Yield**: 1870.2 mg

(88%). **^{1}H NMR** (300 MHz, CD_3CN-d_3): δ (in ppm) = 8.62 (d, *J* = 3.65 Hz, 1H, H^1), 8.34 (s, 1H, H^6), 7.94 (d, *J* = 7.85 Hz, 1H, H^4), 7.78 (t, *J* = 7.71 Hz, 1H, H^3), 7.37 (t, *J* = 6.08 Hz, 1H, H^2), 3.60 (t, *J* = 6.87 Hz, 2H, H^7), 1.68 (s, *J* = 7.20 Hz, 2H, H^8), 0.94 (t, *J* = 7.31 Hz, 3H, H^9). **^{13}C NMR** (75 MHz, CD_3CN-d_3): δ (in ppm) = 161.9, 154.8, 149.5, 136.7, 124.7, 121.3, 63.5, 24.0, 12.0. **FTIR** (ATR, neat): 1646.57 cm^{-1} ($\nu_{C=N}$), 1586.80 cm^{-1} ($\nu_{pyr\text{-}C=N}$). **ESI-MS** (+ve, m/z): Calcd. for $[M+H]^+$ 149.1079, found 149.1068.

2.7.1.8 N-Phenyl-1-(6-methyl-2pyridinyl)methanimine (L8)

Synthesized using the synthetic procedure described for **L1** by employing 6-methyl-2-pyridinecarboxaldehyde (358.4 mg, 2.96 mmol) as a reagent. The ligand was isolated as a yellow oil. **Yield**: 410.0 mg (71%). **^{1}H NMR** (300 MHz, CD_3CN-d_3): δ (in ppm) = 8.51 (s, 1H, H^6), 7.95 (d, *J* = 7.7 Hz, 1H, H^4), 7.74 (t, *J* = 7.6 Hz, 1H, H^3), 7.40 – 7.31 (m, 6H, $H^{2, 8, 9, 10}$), 2.56 (s, 3H, H^{11}). **^{13}C NMR** (75 MHz, CD_3CN-d_3): δ (in ppm) = 161.1, 158.5, 153.9, 151.1, 137.3, 129.1, 126.4, 124.7, 120.9, 117.2, 22.3. **FTIR** (ATR, neat): 1627.99 cm^{-1} ($\nu_{C=N}$), 1586.28 cm^{-1} ($\nu_{pyr\text{-}C=N}$). **ESI-MS** (+ve, m/z): Calcd. for $[M+H]^+$ 197.1079, found 197.1080.

2.7.1.9 N-Phenyl-1-(6-trifluoromethyl-2-pyridinyl)methanimine (L9)

Synthesized using the synthetic procedure described for **L1** by employing 6-trifluoromethyl-2-pyridinecarboxaldehyde (297.6 mg, 1.70 mmol) as a reagent. The ligand was isolated as a yellow crystalline solid. **Yield**: 356.6 mg (84%). **^{1}H NMR** (300MHz, CD_3CN-d_3): δ (in ppm) = 8.61 (s, 1H, H^6), 8.38 (d, *J* = 7.6Hz, 1H, H^4), 8.11 (t, *J* = 7.5 Hz, 1H, H^3), 7.88 (t, *J* = 6.4 Hz, 1H, H^2), 7.43 – 7.35 (m, 5H, $H^{8, 9, 10}$). **^{13}C NMR** (75 MHz, CD_3CN-d_3): δ (in ppm) = 160.2, 156.1, 151.4, 148.6, 148.2, 140.0, 130.3, 128.2, 125.2, 124.5, 123.1, 122.2, 120.9. **FTIR** (ATR, neat): 1628.22 cm^{-1} ($\nu_{C=N}$), 1589.26 cm^{-1} ($\nu_{pyr\text{-}C=N}$). **ESI-MS** (+ve, m/z): Calcd. for $[M+H]^+$ 251.0796, found 251.0796. Anal. Calcd. for $C_{13}H_9F_3N_2$: C 62.40; H 3.63; N 11.20. Found: C 61.80; H 3.77; N 11.26.

2.7.2 Synthesis of neutral pyridylimine Mn(I) complexes, C1 – C9.

2.7.2.1 [MnBr(CO)$_3$(L1)]

A solution of ligand **L1** (69.2 mg, 0.380 mmol) in tetrahydrofuran (3 mL) was added to a stirred solution of manganese pentacarbonyl bromide (104.4 mg, 0.380 mmol) in tetrahydrofuran (3 mL) under a N_2 atmosphere. The resulting dark orange solution was reacted at room temperature for 24 hours. After the reaction, the solution was layered with hexane to afford a

dark red crystalline solid. The excess solvent was removed, and the solid was dried *in vacuo* overnight. **Yield**: 185.0 mg (50%). Decomposition temperature: 169 – 174 °C (without melting). **^{1}H NMR** (300 MHz, CD_3CN-d_3): δ (in ppm) = 9.23 (d, *J* = 4.23 Hz, 1H, H^{1}), 8.61 (s, 1H, H^{6}), 8.12 (d, *J* = 4.89 Hz, 2H, $H^{3, 4}$), 7.68 – 7.56 (m, 6H, $H^{2, 8, 9, 10}$). **^{13}C NMR** (75 MHz, CD_3CN-d_3): δ (in ppm) = 188.8, 175.9, 165.4, 154.5, 148.2, 140.4, 129.9, 122.4, 108.7. **FTIR** (ATR, neat): 1614.37 cm^{-1} ($\nu_{C=N}$), 1586.83 cm^{-1} ($\nu_{pyr\text{-}C=N}$), 1896.46 cm^{-1}, 2020.56 cm^{-1} (ν_{CO}). **ESI-MS** (+ve, m/z): Calcd. for $[M\text{-}Br]^+$ 321.0072, found 321.0674. Calcd. for $[M\text{-}Br\text{-}3CO\text{+}MeOH]^+$ 269.0487, found 269.0654. Calcd. for $[M\text{-}Br\text{-}3CO]^+$ 237.0224, found 237.0710. Anal. Calcd for $C_{15}H_{10}BrMnN_2O_3$: C 44.92; H 2.51; N 6.98. Found: C 44.94; H 2.61; N 7.06.

2.7.2.2 [MnBr(CO)$_3$(L2)]

Synthesized using the synthetic procedure described for complex **C1**, using ligand **L2** (195.4 mg, 0.93 mmol) as a reagent. Complex was isolated as a dark red crystalline solid. **Yield**: 333.3 mg (84%). Decomposition temperature: 169 – 174 °C (without melting). **^{1}H NMR** (300 MHz, CD_3CN-d_3): δ (in ppm) = 9.25 (d, *J* = 3.30 Hz, 1H, H^{1}), 8.58 (s, 1H, H^{6}), 8.13 (d, *J* = 6.10 Hz, 2H, $H^{3, 4}$), 7.71 (t, *J* = 3.44 Hz, 1H, H^{2}), 7.21 (m, 3H, $H^{9, 10}$), 2.51 (s, 6H, H^{11}). **^{13}C NMR** (75 MHz, CD_3CN-d_3): δ (in ppm) = 176.9, 172.2, 160.6, 155.1, 151.7, 147.9, 140.3, 131.2, 129.9, 129.31, 128.2, 21.2, 19.6. **FTIR** (ATR, neat): 1611.85 cm^{-1} ($\nu_{C=N}$), 1582.75 cm^{-1} ($\nu_{pyr\text{-}C=N}$), 1908.53 cm^{-1}, 2022.92 cm^{-1} (ν_{CO}). **ESI-MS** (+ve, m/z): Calcd. for $[M\text{-}Br]^+$ 349.0385, found 349.1064. Calcd. for $[M\text{-}Br\text{-}3CO\text{+}MeOH]^+$ 297.0799, found 297.1037. Calcd. for $[M\text{-}Br\text{-}3CO]^+$ 265.0537, found 265.1091. Anal. Calcd for $C_{17}H_{14}BrMnN_2O_3$: C 47.58; H 3.29; N 6.53. Found: C 46.38; H 3.28; N 6.50.

2.7.2.3 [MnBr(CO)$_3$(L3)]

Synthesized using the synthetic procedure described for complex **C1**, using ligand **L3** 251.9 mg, 0.95 mmol) as a reagent. Complex was isolated as a dark red crystalline solid. **Yield**: 295.1 mg (64%). Decomposition temperature: 169 – 174 °C (without melting). **^{1}H NMR** (400 MHz, CD_3CN-d_3): δ (in ppm) = 9.44 (d, *J* = 3.83 Hz, 1H, H^{1}), 8.79 (s, 1H, H^{6}), 8.33 (d, *J* = 5.08 Hz, 2H, $H^{3, 4}$), 7.90 (d, *J* = 5.93 Hz, 1H, H^{2}), 7.54 (m, 3H, $H^{9, 10}$), 3.19 (s, 2H, H^{11}), 1.46 - 1.19 (m, 12H, H^{12}). **^{13}C NMR** (75 MHz, CD_3CN-d_3): δ (in ppm) = 171.3, 155.0, 148.5, 141.5, 139.9, 137.5, 131.8, 130.0, 128.9, 124.9, 99.1, 89.3, 28.5, 26.1, 25.7, 23.2, 22.7, 8.4. **FTIR** (ATR, neat): 1632.27 cm^{-1} ($\nu_{C=N}$), 1589.92 cm^{-1} ($\nu_{pyr\text{-}C=N}$), 1904.16 cm^{-1}, 2020.55 cm^{-1} (ν_{CO}). **ESI-MS** (+ve, m/z): Calcd. for $[M\text{-}Br]^+$ 405.1011, found 405.1785. Calcd. for $[M\text{-}Br\text{-}3CO\text{+}MeOH]^+$

353.1425, found 353.1748. Calcd. for $[M\text{-}Br\text{-}3CO]^+$ 321.1163, found 321.1272. Anal. Calcd for $C_{21}H_{22}BrMnN_2O_3$: C 51.98; H 4.57; N 5.77. Found: C 51.64; H 4.62; N 5.79.

2.7.2.4 [MnBr(CO)$_3$(L4)]

Synthesized using the synthetic procedure described for complex **C1**, using ligand **L4** (194,3 mg, 0.92 mmol) as a reagent. Complex was isolated as a brown crystalline solid. **Yield**: 244.1 mg (60%). Decomposition temperature: 205 – 207 °C (without melting). **^{1}H NMR** (400 MHz, CD_3CN-d_3): δ (in ppm) = 9.23 (d, *J* = 3.32 Hz, 1H, H^1), 8.53 (s, 1H, H^6), 8.13 (d, *J* = 8.11 Hz, 2H, $H^{3,4}$), 7.69 (t, *J* = 4.80 Hz, 1H, H^2), 7.02 (s, 2H, H^9), 2.45 (s, 3H, H^{11}), 2.29 (s, 6H, H^{12}). **^{13}C NMR** (101 MHz, CD_3CN-d_3): δ (in ppm) = 171.5, 155.0, 154.4, 149.0, 139.6, 137.3, 130.4, 130.1, 129.8, 129.2, 128.6, 20.5, 20.2, 18.9. **FTIR** (ATR, neat): 1631.68 cm^{-1} ($\nu_{C=N}$), 1589.87 cm^{-1} ($\nu_{pyr\text{-}C=N}$), 1912.37 cm^{-1}, 2021.82 cm^{-1} (ν_{CO}). **ESI-MS** (+ve, m/z): Calcd. for $[M\text{-}Br]^+$ 363.0541, found 363.1248. Calcd. for $[M\text{-}Br\text{-}3CO\text{+}MeOH]^+$ 311.0956, found 311.1218. Calcd. for $[M\text{-}Br\text{-}3CO]^+$ 279.0694, found 279.1272. Anal. Calcd for $C_{18}H_{16}BrMnN_2O_3$: C 48.78; H 3.64; N 6.32. Found: C 48.24; H 3.76; N 6.36.

2.7.2.5 [MnBr(CO)$_3$(L5)]

Synthesized using the synthetic procedure described for complex **C1**, using **L5** (183.2 mg, 0.93 mmol) as the reagent. Complex was isolated as a light brown crystalline solid. **Yield**: 325.7 mg (84%). Decomposition temperature: 156 – 158 °C (without melting). **^{1}H NMR** (300 MHz, CD_3CN-d_3): δ (in ppm) = 9.16 (d, *J* = 4.36 Hz, 1H, H^1), 8.59 (s, 1H, H^6), 8.07 (d, *J* = 7.9 Hz, 2H, $H^{3,4}$), 7.60 (t, *J* = 5.26 Hz, 1H, H^2), 7.45 (s, 5H, $H^{9,10,11}$), 5.35 (s, 2H, H^7). **^{13}C NMR** (75 MHz, CD_3CN-d_3): δ (in ppm) = 175.0, 167.9, 165.3, 161.0, 156.0, 154.8, 149.4, 142.7, 140.1, 136.1, 130.5, 129.8, 128.4, 68.2. **FTIR** (ATR, neat): 1645.44 cm^{-1} ($\nu_{C=N}$), 1596.39 cm^{-1} ($\nu_{pyr\text{-}C=N}$), 1904.15 cm^{-1}, 2019.88 cm^{-1} (ν_{CO}). **ESI-MS** (+ve, m/z): Calcd. for $[M\text{-}Br]^+$ 335.0228, found 335.0884. Calcd. for $[M\text{-}Br\text{-}3CO\text{+}MeOH]^+$ 283.0643, found 283.0860. Calcd. for $[M\text{-}Br\text{-}3CO]^+$ 251.0381, found 251.0911. Anal. Calcd for $C_{16}H_{12}BrMnN_2O_3$: C 46.29; H 2.91; N 6.75. Found: C 46.22; H 3.10; N 6.98.

2.7.2.6 [MnBr(CO)$_3$(L6)]

Synthesized using the synthetic procedure described for complex **C1**, using ligand **L6** (182.2 mg, 0.96 mmol) as a reagent. Complex was isolated as an orange amorphous powder. **Yield**: 248.1 mg (64%). Decomposition temperature: 188 – 190 °C (without melting). **^{1}H NMR** (300

MHz, CD_3CN-d_3): δ (in ppm) = 9.15 (d, *J* = 3.89 Hz, 1H, H^1), 8.58 (s, 1H, H^6), 8.06 (d, *J* = 7.29 Hz, 2H, $H^{3, 4}$), 7.59 (s, 1H, H^2), 4.07 (pent., *J* = 4.06 Hz, 1H, H^7), 1.79 – 1.27 (m, 10H, $H^{8, 9, 10}$). **^{13}C NMR** (75 MHz, CD_3CN-d_3): δ (in ppm) = 160.1, 157.6, 150.8, 138.6, 125.8, 71.6, 35.9, 25.8, 23.9. **FTIR** (ATR, neat): 1623.92 cm^{-1} ($\nu_{C=N}$), 1592.36 cm^{-1} ($\nu_{pyr\text{-}C=N}$), 1903.78 cm^{-1}, 2016.85 cm^{-1} (ν_{CO}). **ESI-MS** (+ve, m/z): Calcd. for $[M\text{-}Br]^+$ 327.0541, found 327.1186. Calcd. for $[M\text{-}Br\text{-}3CO+MeOH]^+$ 275.0956, found 278.2230. Calcd. for $[M\text{-}Br\text{-}3CO]^+$ 243.0694, found 243.1213. Anal. Calcd for $C_{15}H_{16}BrMnN_2O_3$: C 44.25; H 3.96; N 6.88. Found: C 44.22; H 4.26; N 7.07.

2.7.2.7 [MnBr(CO)$_3$(L7)]

Synthesized using the synthetic procedure described for complex **C1**, using ligand **L7** (142.8 mg, 0.96 mmol) as a reagent. Complex was isolated as a light brown crystalline solid. **Yield**: 208.6 mg (59%). Decomposition temperature: 138 – 141 °C (without melting). **^{1}H NMR** (400 MHz, CD_3CN-d_3): δ (in ppm) = 9.16 (d, *J* = 6.7 Hz, 1H, H^1), 8.54 (s, 1H, H^6), 8.07 (t, *J* = 4.1 Hz, 2H, $H^{3, 4}$), 7.60 (s, 1H, H^2), 4.21 (d, *J* = 6.5 Hz, 2H, H^7), 2.10 (m, 2H, H^8), 1.00 (t, *J* = 2.2 Hz, 3H, H^9). **^{13}C NMR** (101 MHz, CD_3CN-d_3): δ (in ppm) = 166.9, 156.0, 154.6, 139.9, 128.8, 128.2, 66.7, 23.8, 11.4. **FTIR** (ATR, neat): 1649.84 cm^{-1} ($\nu_{C=N}$), 1594.30 cm^{-1} ($\nu_{pyr\text{-}C=N}$), 1906.48 cm^{-1}, 2016.34 cm^{-1} (ν_{CO}). **ESI-MS** (+ve, m/z): Calcd. for $[M\text{-}Br]^+$ 287.0228, found 287.0824. Calcd. for $[M\text{-}Br\text{-}3CO+MeOH]^+$ 235.0643, found 235.0792. Calcd. for $[M\text{-}Br\text{-}3CO]^+$ 203.0381, found 203.0842. Anal. Calcd for $C_{12}H_{12}BrMnN_2O_3$: C 39.26; H 3.30; N 7.63. Found: C 38.52; H 3.25; N 7.53.

2.7.2.8 [MnBr(CO)$_3$(L8)]

Synthesized using the synthetic procedure described for complex **C1**, using ligand **L8** (72.7 mg, 0.37 mmol) as a reagent. Complex was isolated as a dark red crystalline solid. **Yield**: 133.8 mg (87%). Decomposition temperature: 177 – 179 °C (without melting). **^{1}H NMR** (300 MHz, CD_3CN-d_3): δ (in ppm) = 8.60 (s, 1H, H^6), 7.97 (t, *J* = 5.0 Hz, 1H, H^4), 7.87 (d, *J* = 4.8 Hz, 1H, H^3), 7.60 – 7.45 (m, 6H, $H^{2, 8, 9, 10}$), 3.05 (s, 3H, H^{11}). **^{13}C NMR** (75 MHz, CD_3CN-d_3): δ (in ppm) = 169.8, 165.1, 156.2, 153.3, 139.7, 130.3, 129.7, 128.0, 122.7, 66.2, 50.0, 29.1, 15.6. **FTIR** (ATR, neat): 1625.60 cm^{-1} ($\nu_{C=N}$), 1594.59 cm^{-1} ($\nu_{pyr\text{-}C=N}$), 1899.94 cm^{-1}, 1940.93 cm^{-1}, 2020.50 cm^{-1} (ν_{CO}). **ESI-MS** (+ve, m/z): Calcd. for $[M\text{-}Br]^+$ 335.0228, found 335.0224. Calcd. for $[M\text{-}Br\text{-}3CO+MeOH]^+$ 283.0643, found 283.0275. Calcd. for $[M\text{-}Br\text{-}3CO]^+$ 251.0381, found 251.0091. Anal. Calcd for $C_{16}H_{12}BrMnN_2O_3$: C 46.29; H 2.91; N 6.75. Found: C 45.78; H 2.96; N 6.77.

2.7.2.9 [MnBr(CO)$_3$(L9)]

Synthesized using the synthetic procedure described for complex **C1**, using ligand **L9** (141.7 mg, 0.57 mmol) as a reagent. Complex was isolated as a maroon crystalline solid. **Yield**: 188.7 mg (71%). Decomposition temperature: 169 – 171 °C (without melting). **^{1}H NMR** (300 MHz, CD_3CN-d_3): δ (in ppm) = 8.82 (s, 1H, H^6), 8.37 – 8.21 (m, 3H, $H^{2, 3, 4}$), 7.54 (m, 5H, $H^{8, 9, 10}$). **^{13}C NMR** (75 MHz, CD_3CN-d_3): δ (in ppm) = 169.3, 157.9, 153.2, 142.1, 132.9, 130.4, 129.6, 126.7, 122.5. **FTIR** (ATR, neat): 1601.67 cm^{-1} ($\nu_{C=N}$), 1592.24 cm^{-1} ($\nu_{pyr\text{-}C=N}$), 1921.64 cm^{-1}, 2028.48 cm^{-1} (ν_{CO}). **ESI-MS** (+ve, m/z): Calcd. for $[M\text{-}Br\text{-}3CO+MeOH]^+$ 337.0360, found 336.9994. Anal. Calcd for $C_{16}H_9BrF_3MnN_2O_3$: C 40.97; H 1.93; N 5.97. Found: C 40.75; H 2.08; N 6.02.

2.8 References

1. Schiff, H. *Ann. Suppl.,* **1864**, *3*, 343.
2. Campbell, K., Sommers, A. H., Campbell, B. *J. Am. Chem. Soc.,* **1944**, *66*, 82.
3. Brewster, C. *J. Am. Chem. Soc.,* **1964**, *46*, 2463.
4. Yoon, T. P., Jacobsen, E. N. *Science,* **2003**, *299*, 1691.
5. Pioquinto-Mendoza, J. R., Rosas-Ortiz, J. A., Reyes-Martínez, R., Conelly-Espinosa, P., Toscano, R. A., Germán-Acacio, J. M., Avila-Sorrosa, A., Baldovino-Pantaleón, O., Morales-Morales, D. *Inorg. Chim. Acta*, **2015**, *438*, 146 – 152.
6. Frischmann, P. D., MacLachlan, M. J. *Chem. Soc. Rev.,* **2013**, *42*, 871.
7. Zulu, Z., Nyamato, G. S., Tshabalala, T. A., Ojwach, S. O. *Inorg. Chim. Acta*, **2020**, *501*, 119270.
8. Pelagatti, P., Carcelli, M., Costa, M., Ianelli, S., Pelizzi, C., Rogolino, D. *J. Mol. Cat. A. Chem.*, **2005**, *226*, 107 – 110.
9. Gichumbi, J. M., Friedrich, H. B., Omondi, B. *Transit. Met. Chem.,* **2016**, *41*, 867 – 877.
10. Reardon, D., Aharonian, G., Gambarotta, S., Yap, G. P. A. *Organometallics*, **2002**, *21*, 786 – 788.
11. Mukherjee, A., Nerush, A., Leitus, G., Shimon, L. J. W., Ben David, Y., Espinosa Jalapa, N. A., Milstein, D. *J. Am. Chem. Soc.,* **2016**, *138*, 4298 – 4301.
12. Chien, C-H., Fujita, S., Yamoto, S., Hara, T., Yagamata, T., Watanabe, M., Mashima, K. *Dalton Trans.,* **2008**, *8*, 916 – 923.
13. Biewer, C., Hamacher, C., Kaiser, A., Vogt, N., Sandleben, A., Chin, M. T., Yu, S., Vicic, D. A., Klein, A. *Inorg. Chem.*, **2016**, *55*, 12716 – 12727.
14. Wu, J. Y., Moreau, B., Ritter, T. *J. Am. Chem. Soc.,* **2009**, *131*, 12915 – 12917.
15. Regnier, T., Lavastre, O. *Tetrahedron*, **2006**, *62*, 155 – 159.

16. Kim, S., Kim, E., Lee, H-J., Lee, H. *Polyhedron,* **2014**, *69*, 149 – 155.
17. Wilhelms, N., Kulchat, S., Lehn, J-M. *Helv. Chim. Acta*, **2012**, *95*, 2635 – 2651.
18. Gellrich, U., Diskin-Posner, Y., Shimon, L. J. W., Milstein, D. *J. Am. Chem. Soc.,* **2016**, *138(40)*, 13307 – 13313.
19. Onoue, H., Moritani, I. *J. Organomet. Chem.,* **1972**, *43*, 431.
20. Twala, T. N., Schutte-Smith, M., Roodt, A., Visser, H. G. *Dalton Trans.,* **2013**, *00*, 1 – 3.
21. Chertkov, V. A., Ustynyuk, Y., Barinov, I. *J. Organomet. Chem.,* **1971**, *29*, 53.
22. Tjosaas, F., Fiksdahl, A. *J. Organomet. Chem.,* **2007**, *692*, 5429.
23. Antolasic, F. *Mol. Weight Calc.,* **2005**, www.wsearch.com.au.
24. Adrio, L., Antelo, J. M, Ortigueira, J. M, Fernandez, J. J., Fernandez, A., Teresa-Pereira, M., Vila, J. M. *J. Organomet. Chem.,* **2009**, *694*, 1273.
25. Spall, S. J. P., Keane, T., Tory, J., Cocker, D. C., Adams, H., Hannah, F., Meijer, A. J. H., Hartl, F., Weinstein, J. A. *Inorg. Chem.,* **2016**, *55*, 12568 – 12582.
26. Henke, W. C., Otolski, C. J., Moore, W. N. G., Elles, C. G., Blakemore, J. D. *Inorg. Chem.,* **2020**, *59*, 2178 – 2187.
27. Anderson, N. H., Boncella, J., Tondreau, A. M. *Chem. Eur. J.,* **2019**, *25*, 10557 – 10560.
28. Lentz, N., Albrecht, M. *ACS Catal.,* **2022**, *12*, 12627 – 12631.
29. Dolomanov, O. V., Bourhis, L. J., Gildea, R. J., Howard, J. A. K., Puschmann, H. *J. Appl. Cryst.,* **2009**, *42*, 339 – 341.
30. Sheldrick, G. M. *Acta Cryst.,* **2015**, *A71*, 3 – 8.
31. Sheldrick, G. M. *Acta Cryst.,* **2015**, *C71*, 3 – 8.
32. POV-Ray, *Version 3.6,* Williamstown, Australia, Persistence of vision ray.

Chapter 3: Synthesis and Characterization of Cationic, Half-Sandwich Pyridylimine Ruthenium(II) Complexes

3.1 Introduction

As a result of the poor stability under light exposure and inactivity of the pyridylimine manganese(I) complexes prepared in **Chapter 2** towards FA dehydrogenation, a series of analogous ruthenium(II) complexes were prepared and are discussed in this chapter. Over half a century ago, Coffey discovered the dehydrogenation of FA using an iridium phosphine complex (TOF = 1187 hr^{-1}).[1] This seminal work has led to significant research efforts concerning applying late-transition metal complexes as catalyst precursors in FA dehydrogenation. Consequently, Ru(II) complexes have received much interest due to their high activity and selectivity when applied to FA dehydrogenation and relatively low cost compared to iridium catalyst systems.[2] The following literature example, highlighting the versatility and activity of N-donor ligated complexes, presents a recent application of bidentate, nitrogen-donor ligated iridium, and ruthenium complexes toward FA dehydrogenation.

He and coworkers reported the dehydrogenation of aqueous FA by iridium and ruthenium complexes with a diamino-bis-(1*H*-1,2,4-triazole) ligand.[3] Unlike many reported catalyst systems, complexes **LXX** and **LXXI** (**Scheme 3.1**) were able to catalyze the dehydrogenation of FA in water without the production of CO as confirmed by GC analyses. The concentrations of FA and **LXX** were found to affect the overall efficiency of the system with a maximum TOF of 12468 hr^{-1} being reached when [FA] = 4 mol/L with a catalyst loading of 0.002 mol%. Often a delicate pH balance is necessary for efficient FA dehydrogenation, which was investigated by varying the ratio of FA to sodium formate (HCOONa). The activity of **LXX** decreased with an increasing pH with optimal catalytic performance (TON = 7042, TOF = 12468 hr^{-1}) being reached at pH = 1.34. This result is significantly different from the usual pH range of 3.5 – 4 reported for similar iridium and ruthenium catalyst systems and implies that **LXX** and **LXXI** can be used in additive-free FA dehydrogenation as the diamine portion of the ligand can act as an internal base.[4] Overall, the iridium complex **LXX** had better catalytic activity (TOF = 8756 hr^{-1}) than the ruthenium complex **LXXI** (TOF = 570 hr^{-1}) when evaluated at 0.01 mol% catalyst loading, 20 mmol of FA, and a reaction temperature of 90 °C. The superior catalytic performance of iridium complexes is usually attributed to their ease of decarboxylation to form the metal hydride intermediate.[5]

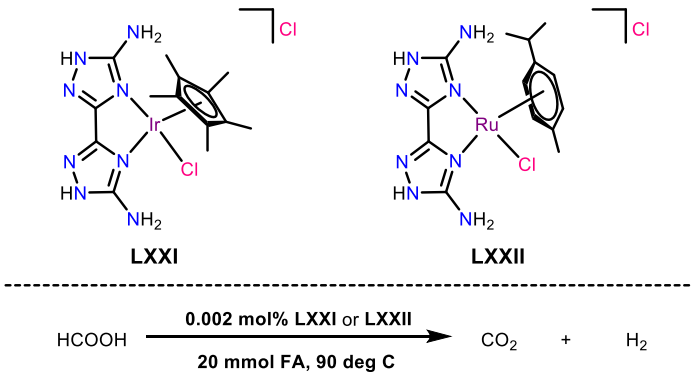

Scheme 3.1: Iridium and ruthenium complexes with a diamino-bis-(1*H*-1,2,4-triazole) ligand for FA dehydrogenation.[3]

Based on these observations and the successful preparation of a set of pyridylimine ligands in **Chapter 2**, it was anticipated that this ligand framework could be used to prepare cationic, half-sandwich Ru(II) catalyst precursors that could be active and selective towards FA dehydrogenation. The choice of a ruthenium metal centre was motivated by its cost efficiency and ability to display similar reactivity to iridium. Herein, we report the preparation and spectroscopic characterization of a wide range of cationic, half-sandwich pyridylimine Ru(II) complexes.

3.2 Results and Discussion

3.2.1 Synthesis and Characterization of Pyridylimine-ligated Ru(II) Complexes

The pyridylimine ligands, **L1** – **L9** discussed in **Chapter 2** were reacted with $[RuCl_2(p\text{-cymene})]_2$ in MeOH for 24 hours at room temperature under inert conditions (N_2) to afford complexes **C10** – **C18** with a Cl counterion (**Scheme 3.2**). For **C19** and **C20**, the cationic complexes, [(**L**)RuCl(*p*-cymene)]Cl, generated in solution were treated with excess sodium tetraphenylborate ($NaBPh_4$) and potassium hexafluorophosphate (KPF_6), respectively to afford complexes **C19** and **C20** with BPh_4 and PF_6 counterions respectively. Salt metathesis between large counterions such as PF_6 and BPh_4 and small counterions such as Cl is well documented in the literature and is usually used to isolate more stable cationic complexes.[6] The pyridylimine Ru(II) complexes, except for **C10**, **C14**, **C15**, and, **C16**, were isolated as air- and moisture-stable solids that displayed good solubility in solvents such as dimethylsulfoxide, dimethylformamide, dichloromethane, and water and poor to no solubility in diethyl ether, toluene, hexane, and tetrahydrofuran. The moisture-sensitive complexes were stored under inert conditions. Only complex **C20**,[7] to the best of our knowledge, has been previously reported while complexes **C10** – **C19** are all unreported in the literature.

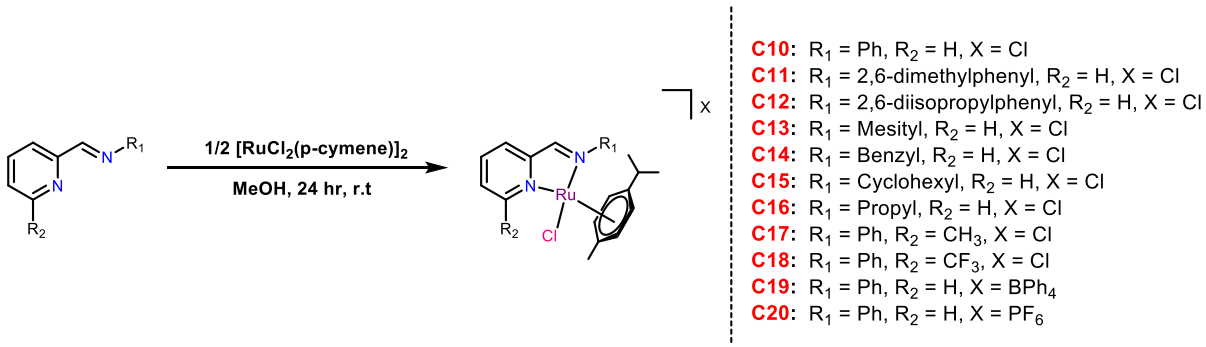

Scheme 3.2: Synthetic protocol towards the preparation of cationic, half-sandwich complexes ruthenium(II) complexes, **C10** – **C20**.

3.2.1.1 FT-IR and Thermal Stability

The FT-IR spectra of the cationic half-sandwich pyridylimine Ru(II) complexes confirmed the coordination of the ligands to the ruthenium metal centre (**Table 3.1**). Upon complexation, the imine ($\nu_{C=N}$) band of the ligands in the region 1627 – 1649 cm^{-1} shifted towards lower wavenumbers i.e. 1611 – 1626 cm^{-1} and provides evidence of a decreased double bond character of the imine functional group.[8] The $\nu_{C=N}$ band of the pyridine ring for the ligands shifted towards higher wavenumbers for complexes, **C10**, **C11**, **C14**, **C15**, **C16**, **C17**, **C18**, and **C20**. This shift indicates an increase in the double bond character of pyridine ring imine due to coordination with the metal centre using the lone pair on the nitrogen.[8] In the case of **C12**, **C13**, and **C19**, a shift of the pyridine ring ($\nu_{C=N}$) band towards lower wavenumbers was observed and is an indication of coordination to the ruthenium metal centre *via* the π electrons which leads to a decreased double bond character.[8] For complexes **C19** and **C20**, intense absorption bands in the region 705 – 733 cm^{-1} and 828 cm^{-1} are observed and ascribed to the stretching vibration modes of the BPh_4 and PF_6 counterions, respectively. The appearance of these absorption bands illustrated the anion exchange of the chloride anion with the BPh_4 and PF_6 anions.

Table 3.1: FT-IR spectral data and decomposition temperatures for pyridylimine Ru(II) complexes, **C10** – **C20**.

Complex	Decomposition temperature [a]	C=N bond stretch [b]	Pyr-C=N bond stretch [b]	BPh_4 bond stretch [b]	PF_6 bond stretch [b]
	(°C)	($\nu_{C=N}$, cm^{-1})	($\nu_{C=N}$, cm^{-1})	(ν_{B-C}, cm^{-1})	(ν_{P-F}, cm^{-1})
C10	110 – 112	1612	1588	-	-
C11	216 – 217	1615	1589	-	-
C12	210 – 211	1611	1582	-	-
C13	242 – 243	1613	1583	-	-
C14	130 – 133	1619	1594	-	-
C15	140 – 141	1618	1594	-	-
C16	120 – 122	1621	1596	-	-
C17	136 – 137	1615	1588	-	-
C18	133 – 134	1617	1600	-	-
C19	162 – 164	1626	1579	705, 733	-
C20	134 – 135	1614	1590	-	828

[a] Decomposition temperatures are reported as uncorrected. [b] Recorded as neat spectra at room temperature using an ATR accessory.

3.2.1.2 NMR Spectroscopy (^1H, ^{13}C and ^{31}P)

The ^1H and $^{13}C\{^1H\}$ NMR spectra of the cationic half-sandwich pyridylimine Ru(II) complexes, **C10** – **C20** provided additional evidence of coordination of the Schiff base ligands to the ruthenium metal centre. The ^1H NMR spectra of the complexes **C10** – **C20** display a singlet for the imine proton in the region δ = 8.49 – 9.09 ppm which is considerably downfield compared to the imine proton of the free ligand, δ = 8.31 – 8.61 ppm. Coordination of the imine nitrogen to the Ru metal centre weakens the C=N bond, resulting in the deshielding of the proton of the azomethine group.[9] Spectral analysis of the ^{13}C NMR for **C10** – **C20** revealed a downfield chemical shift of the methine moiety in the region δ = 165.68 – 173.87 ppm compared to that of the uncoordinated pyridylimine ligands observed in the region δ = 157.56 – 163.57 ppm. For complex **C19**, broad resonances assigned to the protons of the BPh_4 counter ion were observed in the region δ = 6.79 – 7.18 ppm. The ^{31}P NMR spectrum of **C20** shows a septet at δ = -143.1 ppm, which is evidence of the presence of the PF_6 counterion. The aromatic ^1H resonances for the coordinated p-cymene are typically found in the range δ = 4 – 6 ppm.[10] However, the coordination of the pyridylimine ligand to the Ru metal centre

leads to a loss of the p-cymene two-fold symmetry, resulting in the aromatic proton resonances being observed as a set of four doublets in the region δ = 5.32 – 6.31 ppm. This result is consistent with observations made for similar Ru(II) complexes in the literature.[11]

Further analysis of the ^{1}H NMR spectra for complexes **C19** and **C20** reveals that the counterions had a negligible effect on the chemical shifts of the protons of the pyridylimine ligand framework in DMSO-d_6. For example, the imine resonances appear as a singlet at ~ 8.92 ppm for **C19** and **C20** containing BPh_4 and PF_6 counterions respectively. A similar observation was made for the resonances of the pyridine proton which appear as doublets at 9.57 ppm. This phenomenon was also observed and expertly studied by our research group using a combination of Nuclear Overhauser Effect (NOE) NMR spectroscopy, Pulsed Gradient Spin Echo (PGSE) spectroscopy, and conductivity measurements.[12] This behavior was attributed to the formation of different ion pairs depending on the nature of the solvent. **Figure 3.1** illustrates the prepared cationic half-sandwich ruthenium(II) complexes with numbering used for NMR data. The ^{1}H NMR spectrum of ruthenium complex **C11** is shown in **Figure 3.2** as a representative example. A summary of all the ^{1}H NMR chemical shifts observed in complexes **C10** – **C20** is given in **Tables 3.2** – **3.4**.

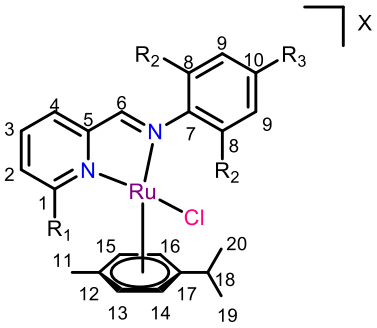

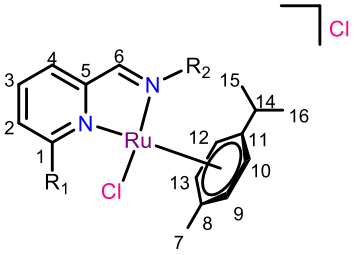

C10: R_1 = H, R_2 = R_3 = H, X = Cl
C11: R_1 = H, R_2 = Me, R_3 = H, X = Cl
C12: R_1 = H, R_2 = iPr, R_3 = H, X = Cl
C13: R_1 = H, R_2 = R_3 = Me, X = Cl
C17: R_1 = CH_3, R_2 = R_3 = H, X = Cl
C18: R_1 = CF_3, R_2 = R_3 = H, X = Cl
C19: R_1 = H, R_2 = R_3 = H, X = BPh_4
C20: R_1 = H, R_2 = R_3 = H, X = PF_6

C14: R_1 = H, R_2 = Benzyl
C15: R_1 = H, R_2 = Cyclohexyl
C16: R_1 = H, R_2 = Propyl

Figure 3.1: Cationic pyridylimine ruthenium(II) complexes with various substituents on the imine nitrogen and the pyridine ring, illustrating a numbering system for NMR data.

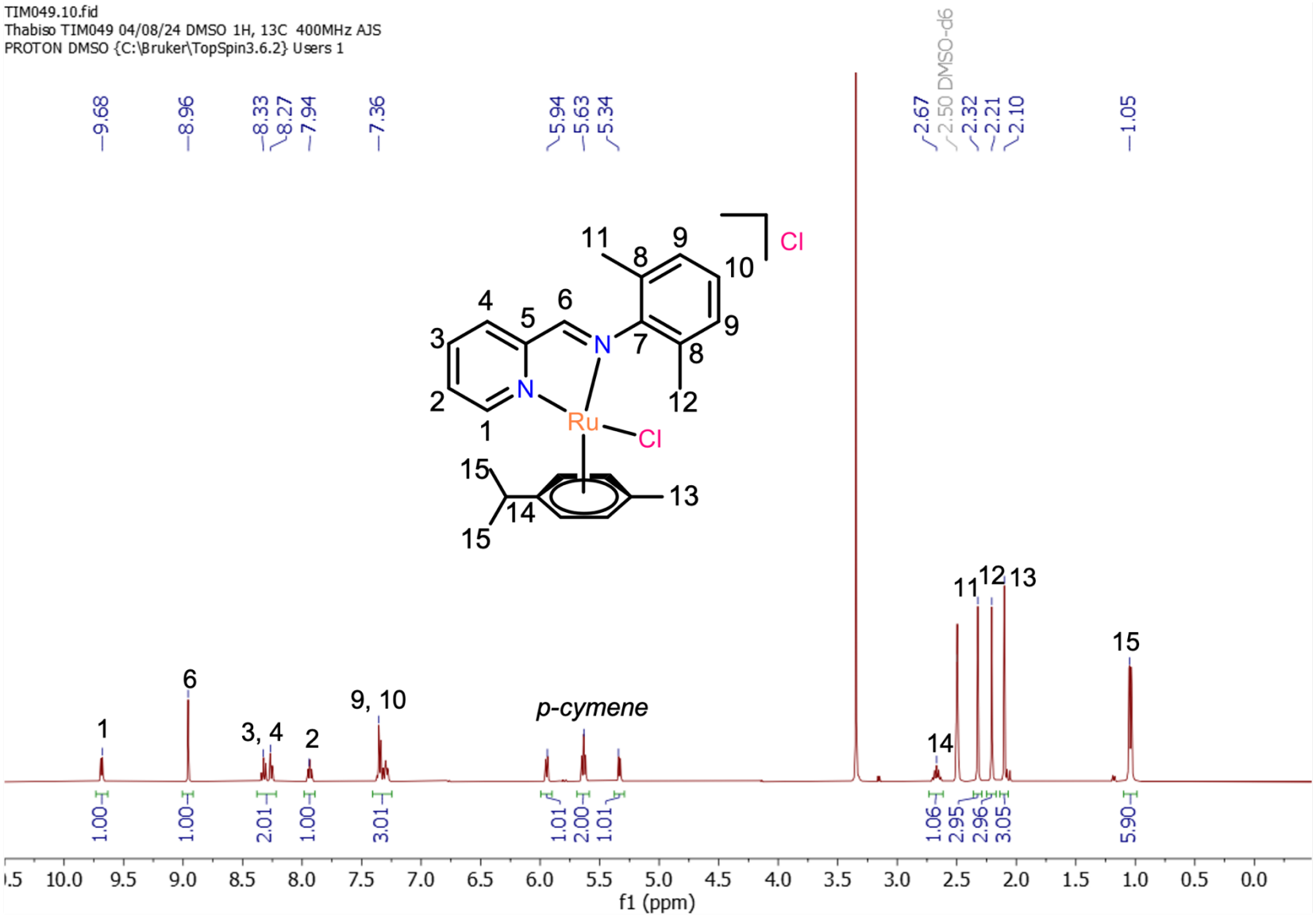

Figure 3.2: ^{1}H NMR spectrum of complex **C11**, recorded in DMSO-d_6 at 300 K.

Table 3.2: ^{1}H NMR spectral data for cationic half-sandwich pyridylimine Ru(II) complexes, **C10** – **C13**.[a]

Complex	Imine proton (C=N***H***)	Pyridine imine proton (C=N***H***)	Aromatic region	Aromatic p-cymene
C10	δ 9.08 (s, 1H, H^6)	δ 9.69 (d, 1H, *J* = 5.7 Hz, H^1)	δ 8.37 – 8.32 (comp., 2H, H^{Ar}) δ 7.88 – 7.81 (comp., 3H, H^{Ar}) δ 7.63 (comp., 3H, H^{Ar})	δ 6.12 (d, 1H, *J* = 6.2 Hz, $H^{p\text{-}cy}$) δ 5.82 (d, 1H, *J* = 6.2 Hz, $H^{p\text{-}cy}$) δ 5.64 (dd, 2H, J^3 = 6.2 Hz, J^4 = 6.0 Hz, $H^{p\text{-}cy}$)
C11	δ 8.96 (s, 1H, H^6)	δ 9.68 (d, 1H, *J* = 5.7 Hz, H^1)	δ 8.33 – 8.27 (comp., 2H, H^{Ar}) δ 7.94 (t, 1H, *J* = 6.9 Hz, H^{Ar}) δ 7.36 (comp., 3H, H^{Ar})	δ 5.94 (d, 1H, *J* = 6.4 Hz, $H^{p\text{-}cy}$) δ 5.63 (dd, 2H, J^3 = 6.4 Hz, J^4 = 6.3 Hz, $H^{p\text{-}cy}$) δ 5.34 (d, 1H, *J* = 6.4 Hz, $H^{p\text{-}cy}$)
C12	δ 9.09 (s, 1H, H^6)	δ 9.75 (d, 1H, *J* = 5.8 Hz, H^1)	δ 8.36 (comp., 2H, H^{Ar}) δ 7.96 (t, 1H, *J* = 6.1 Hz, H^{Ar}) δ 7.49 – 7.38 (comp., 3H, H^{Ar})	δ 6.09 (d, 1H, *J* = 6.3 Hz, $H^{p\text{-}cy}$) δ 5.65 (d, 1H, *J* = 6.3 Hz, $H^{p\text{-}cy}$) δ 5.47 (d, 1H, *J* = 6.3 Hz, $H^{p\text{-}cy}$) δ 5.34 (d, 1H, *J* = 6.3 Hz, $H^{p\text{-}cy}$)
C13	δ 8.91 (s, 1H, H^6)	δ 9.67 (d, 1H, *J* = 5.6 Hz, H^1)	δ 8.32 – 8.27 (comp., 2H, H^{Ar}) δ 7.93 (t, 1H, *J* = 7.1 Hz, H^{Ar}) δ 7.16 (s, 1H, H^{Ar}) δ 7.11 (s, 1H, H^{Ar})	δ 5.99 (d, 1H, *J* = 6.0 Hz, $H^{p\text{-}cy}$) δ 5.64 (dd, 2H, J^3 = 6.0 Hz, J^4 = 6.1 Hz, $H^{p\text{-}cy}$) δ 5.32 (d, 1H, *J* = 6.0 Hz, $H^{p\text{-}cy}$)

[a] ^{1}H NMR spectra recorded in DMSO-d_6 at 300 K; chemical shifts (δ) reported in ppm values, referenced relative to the residual DMSO resonance; superscripts indicate protons as per numbering in **Figure 3.1**; s = singlet, d = doublet, t = triplet, m = multiplet, comp. = complex.

Table 3.3: ^{1}H NMR spectral data for cationic half-sandwich pyridylimine Ru(II) complexes, **C14** – **C17**.[a]

Complex	Imine proton (C=N***H***)	Pyridine imine proton (C=N***H***)	Aromatic region	Aromatic p-cymene
C14	δ 8.49 (s, 1H, H^{6})	δ 9.61 (d, 1H, *J* = 5.7 Hz, H^{1})	δ 8.22 (s, 2H, H^{Ar}) δ 7.80 (t, 1H, *J* = 7.1 Hz, H^{Ar}) δ 7.61 – 7.51 (comp., 5H, H^{Ar})	δ 6.29 (d, 1H, *J* = 6.3 Hz, $H^{p\text{-}cy}$) δ 6.01 (d, 1H, *J* = 6.3 Hz, $H^{p\text{-}cy}$) δ 5.89 (dd, 2H, J^{3} = 6.3 Hz, J^{4} = 6.2 Hz, $H^{p\text{-}cy}$)
C15	δ 8.89 (s, 1H, H^{6})	δ 9.55 (d, 1H, *J* = 5.7 Hz, H^{1})	δ 8.25 – 8.19 (comp., 2H, H^{Ar}) δ 7.80 (t, 1H, *J* = 7.2 Hz, H^{Ar})	δ 6.31 (d, 1H, *J* = 6.5 Hz, $H^{p\text{-}cy}$) δ 6.21 (d, 1H, *J* = 6.5 Hz, $H^{p\text{-}cy}$) δ 5.92 (dd, 2H, J^{3} = 6.5 Hz, J^{4} = 6.3 Hz, $H^{p\text{-}cy}$)
C16	δ 8.83 (s, 1H, H^{6})	δ 9.58 (d, 1H, *J* = 5.7 Hz, H^{1})	δ 8.21 (comp., 2H, H^{Ar}) δ 7.80 (t, 1H, *J* = 6.7 Hz, H^{Ar})	δ 6.31 (d, 1H, *J* = 6.5 Hz, $H^{p\text{-}cy}$) δ 6.22 (d, 1H, *J* = 6.5 Hz, $H^{p\text{-}cy}$) δ 5.93 (dd, 2H, J^{3} = 6.5 Hz, J^{4} = 6.3 Hz, $H^{p\text{-}cy}$)
C17	δ 8.98 (s, 1H, H^{6})	-	δ 8.18 – 8.14 (comp., 2H, H^{Ar}) δ 7.87 (comp., 3H, H^{Ar}) δ 7.65 (comp., 3H, H^{Ar})	δ 6.18 (d, 1H, *J* = 6.6 Hz, $H^{p\text{-}cy}$) δ 5.75 (d, 1H, *J* = 6.6 Hz, $H^{p\text{-}cy}$) δ 5.50 (d, 1H, *J* = 6.6 Hz, $H^{p\text{-}cy}$) δ 5.44 (d, 1H, *J* = 6.6 Hz, $H^{p\text{-}cy}$)

[a] ^{1}H NMR spectra recorded in DMSO-d_6 at 300 K; chemical shifts (δ) are reported in ppm values, referenced relative to the residual DMSO resonance; superscripts indicate protons as per numbering in **Figure 3.1**; s = singlet, d = doublet, t = triplet, m = multiplet, comp. = complex.

Table 3.4: ^{1}H NMR spectral data for cationic half-sandwich pyridylimine Ru(II) complexes, **C18** – **C20**.[a]

Complex	Imine proton (C=N***H***)	Pyridine imine proton (C=N***H***)	Aromatic region	Aromatic p-cymene
C18	δ 9.22 (s, 1H, H^{6})	-	δ 8.63 – 8.56 (comp., 3H, H^{Ar}) δ 7.92 (comp., 2H, H^{Ar}) δ 7.68 (comp., 3H, H^{Ar})	δ 5.92 (d, 1H, *J* = 6.3 Hz, $H^{p\text{-}cy}$) δ 5.59 (dd, 2H, J^{3} = 6.3 Hz, J^{4} = 6.2 Hz, $H^{p\text{-}cy}$) δ 5.40 (d, 1H, *J* = 6.3 Hz, $H^{p\text{-}cy}$)
C19	δ 8.91 (s, 1H, H^{6})	δ 9.57 (d, 1H, *J* = 5.7 Hz, H^{1})	δ 8.27 (comp., 2H, H^{Ar}) δ 7.87 (t, 1H, *J* = 7.1 Hz, H^{Ar}) δ 7.79 (comp., 2H, H^{Ar}) δ 7.64 (comp., 3H, H^{Ar}) δ 7.18 (comp., 8H, H^{Ar}) δ 6.92 (comp., 8H, H^{Ar}) δ 6.79 (comp., 4H, H^{Ar})	δ 6.06 (d, 1H, *J* = 6.2 Hz, $H^{p\text{-}cy}$) δ 5.76 (d, 1H, *J* = 6.2 Hz, $H^{p\text{-}cy}$) δ 5.61 (d, 1H, *J* = 6.2 Hz, $H^{p\text{-}cy}$) δ 5.57 (d, 1H, *J* = 6.2 Hz, $H^{p\text{-}cy}$)
C20	δ 8.93 (s, 1H, H^{6})	δ 9.57 (d, 1H, *J* = 5.9 Hz, H^{1})	δ 8.28 (comp., 2H, H^{Ar}) δ 7.89 (t, 1H, *J* = 7.2 Hz, H^{Ar}) δ 7.80 (comp., 2H, H^{Ar}) δ 7.64 (comp., 3H, H^{Ar})	δ 6.08 (d, 1H, *J* = 6.1 Hz, $H^{p\text{-}cy}$) δ 5.75 (d, 1H, *J* = 6.1 Hz, $H^{p\text{-}cy}$) δ 5.62 (dd, 2H, J^{3} = 6.1 Hz, J^{4} = 6.0 Hz, $H^{p\text{-}cy}$)

[a] ^{1}H NMR spectra recorded in DMSO-d_6 at 300 K; chemical shifts (δ) are reported in ppm values, referenced relative to the residual DMSO resonance; superscripts indicate protons as per numbering in **Figure 3.1**; s = singlet, d = doublet, t = triplet, m = multiplet, comp. = complex.

3.2.1.3 Mass Spectrometry and Elemental Analysis

ESI-MS recorded in the positive ion mode were in accordance with the proposed cationic, half-sandwich pyridylimine Ru(II) complexes. The base peak for all the complexes **C10** – **C20** corresponds with the $[M]^+$ fragment ion and is reported in **Table 3.5**. **Figure 3.3** shows the spectrum obtained for complex **C11** and the calculated isotopic cluster for the base peak. Dimeric fragment ions were not observed in the mass spectra for all the complexes. The experimental isotopic clusters agreed with the theoretical isotopic clusters.[13] CHNS analysis confirmed the overall purity of the half-sandwich pyridylimine ruthenium(II) complexes **C10** – **C20**. The experimental elemental percentages were in close agreement with the theoretical values.

Table 3.5: Mass spectrometry data for cationic pyridylimine Ru(II) complexes **C10** – **C20**.

Complex	Fragment ion (m/z)	
	Experimental $[M]^+$	**Calculated $[M]^+$**
C10	453.0669	453.0671
C11	481.0984	481.0984
C12	537.1612	537.1610
C13	495.1140	495.1141
C14	467.0824	467.0828
C15	459.1122	459.1141
C16	419.0809	419.0828
C17	467.0811	467.0828
C18	520.1395	521.0545
C19	453.0654	453.0671
C20	453.0652	453.0671

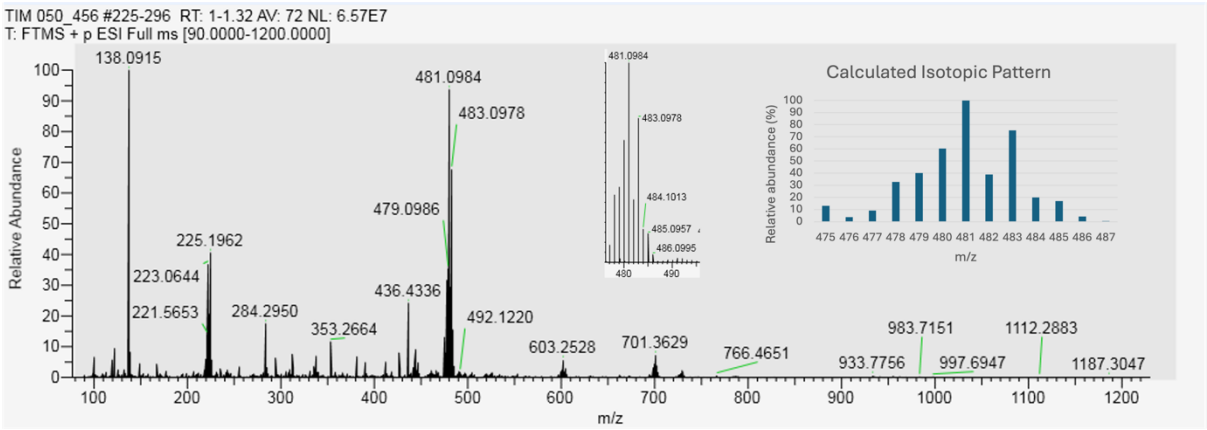

Figure 3.3: ESI-MS spectrum of pyridylimine Ru(II) complex **C11** recorded in the positive ion mode. Peak located at 481.0984 m/z correlates with the $[M]^+$ fragment ion. Inset shows the calculated isotopic cluster for the fragment at 481.0984 m/z.

3.2.1.4 Single Crystal X-ray Diffraction (SCXRD)

Suitable single crystals of Ru(II) complexes **C10**, **C19**, and **C20** were obtained from a 1:1 DCM-diethyl ether solution placed in direct sunlight, using liquid-liquid diffusion at room temperature to afford orange-colored crystals. Single crystal X-ray analyses successfully determined the molecular structures of the complexes. All atomic labels are given in the ORTEP pictures outlined in **Figures 3.4 – 3.6**. Crystallographic data and selected metric parameters such as bond lengths, bond angles, and torsion angles are shown in **Table 3.6** and **3.7**, respectively.

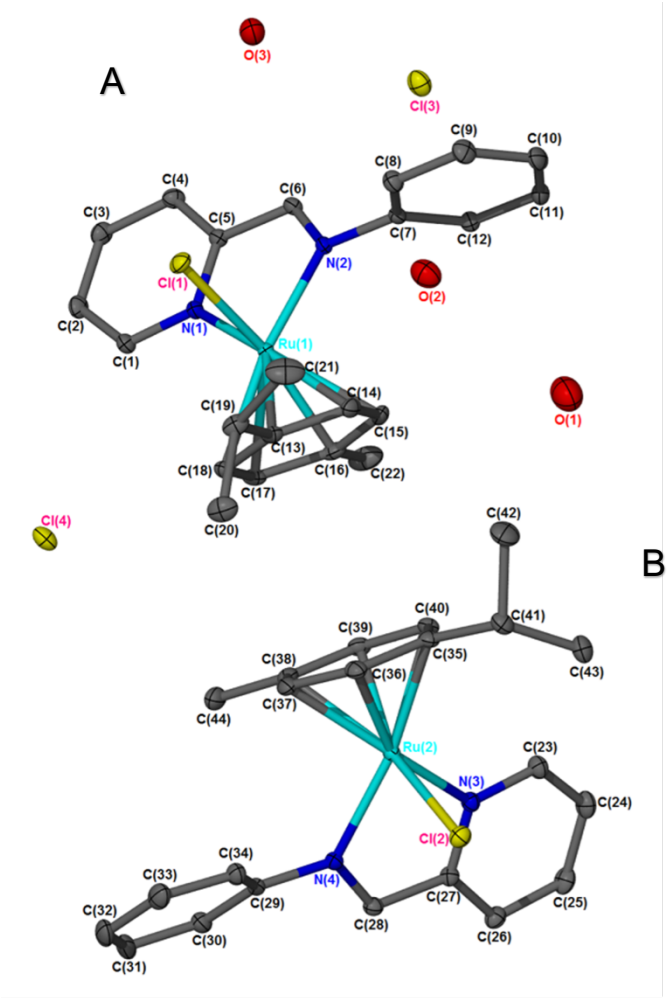

Figure 3.4: Molecular structures of complexes **C10(A)** and **C10(B)** with atomic numbering illustrated with 30% probability ellipsoids. All hydrogen atoms are omitted for clarity. The complex crystallizes as two independent molecules in the asymmetric unit labelled **A** and **B**.

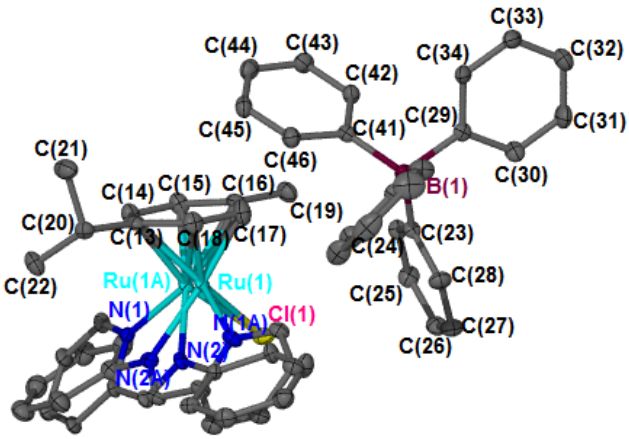

Figure 3.5: Molecular structure of complex **C19** with atomic numbering illustrated with 30% probability ellipsoids. All hydrogen atoms are omitted for clarity.

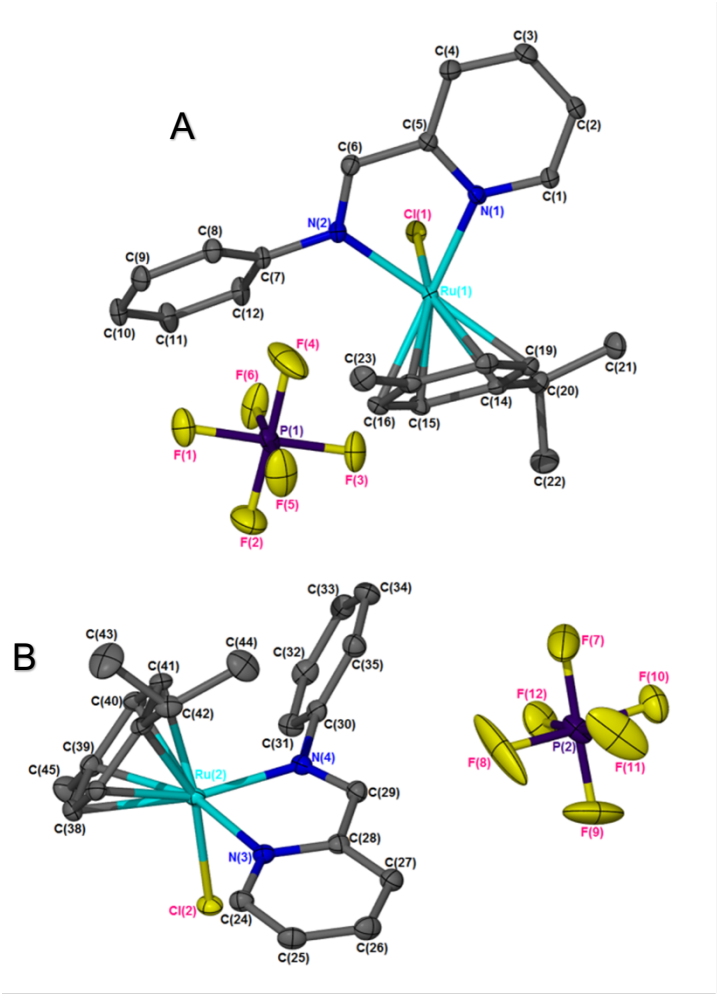

Figure 3.6: Molecular structures of complexes **C20(A)** and **C20(B)** with atomic numbering illustrated with 30% probability ellipsoids. All hydrogen atoms are omitted for clarity. The complex crystallizes as two independent molecules in the asymmetric unit labelled **A** and **B**.

All the complexes adopt a three-legged piano stool arrangement in which the Ru(II) metal centre has a pseudo-octahedral molecular geometry. The coordination sphere around ruthenium is completed by the pyridylimine ligand which coordinates to the Ru metal centre through the N atoms of the imine and the pyridine ring, p-cymene ring at the top of the stool, and a Cl atom at the bottom of the stool. The crystal structures of **C10** and **C20** (**Figures 3.4** and **3.6**) contain two discrete molecules labelled **A** and **B** with different geometries within the asymmetric unit cell. The crystal structure of **C10** contains three water molecules in its asymmetric unit. The crystal structure of **C19** (**Figure 3.5**) is highly disordered but indicates the presence and location of the BPh_4 anion in relation to the cation. Complexes **C10** and **C20** crystallized in the triclinic crystal system with the *P-1* space group. Complex **C19** crystallized in the monoclinic crystal system with the $P2_1/n$ space group. Interestingly, for complex **C10** (**A** and **B**), the isopropyl portion of the p-cymene ring is located on the same side as the Cl atom whereas in complex **C20**, they are oriented on the same side in **C20(A)** and on different sides

in **C20(B)**. The arrangement in **C20(B)** is the most common conformation, however, the arrangements in complexes **C10** (**A** and **B**) and **C20(A)** have also been reported.[14,15] In addition, the relative position of the PF_6 anion to the cation in complex **C20** exhibited an interesting arrangement such that the anion is located below the phenyl substituent and on the same side as the p-cymene ring in **C20(A)** and above the phenyl substituent and on the opposite side as the p-cymene ring in **C20(B)**.

The Ru-N_{py} bond lengths i.e. Ru(1)-N(1) equals 2.0961(15) Å, 2.059(9) Å, and 2.083(2) Å for **C10(A)**, **C19,** and **C20(A)**, respectively, and Ru(2)-N(3) equals 2.0865(15) Å and 2.095(2) Å for **C10(B)** and **C20(B)**, respectively, are all comparable with similar bond lengths observed for related ruthenium complexes.[16,17] Similar bond lengths are observed for the Ru-N_{imine} bond. The N(2)-Ru(1)-N(1) bond angles of 76.43(6)°, 78.0(4)°, and 76.75(9)° for **C10(A)**, **C19**, and **C20(A)** deviate from the ideal 90° bond angles expected for molecules with an octahedral geometry. Similar deviations are observed for complexes **C10(B)** and **C20(B)** with N(3)-Ru(2)-N(4) bond angles of 76.86(6)° and 76.63(9)°, respectively. These deviations are an indication of increased rigidity in the complexes due to coordination. The planar nature, with slight distortion, of the pyridylimine ligands in the complexes is reflected by the Ru(1)-N(1)-C(1)-C(2) torsion angles of 171.98(4)°, 179.9(11)°, and 175.1(2)° for **C10(A)**, **C19**, and **C20(A)** respectively. Similar ligand planarity is indicated by Ru(2)-N(3)-C(27)-C(28) torsion angles of 3.0(2)° and -0.2(4)° for **C10(B)** and **C20(B)**, respectively.

Table 3.6: Crystallographic data and structure refinement parameters of ruthenium complexes **C10**, **C19**, and **C20**.

Parameters	Complexes		
	C10	**C19**	**C20**
Empirical formula	$C_{44}H_{54}N_4O_3Cl_4Ru_2$	$C_{46}H_{44}BClN_2Ru$	$C_{22}H_{24}N_2F_6PClRu$
Mr (g/mol)	1030.85	772.16	597.92
Crystal system	Triclinic	Monoclinic	Triclinic
Space group	*P-1*	$P2_1/n$	*P-1*
a (Å)	9.0233(2)	9.9561(4)	9.4087(3)
b (Å)	15.1561(4)	28.3627(12)	11.5327(4)
c (Å)	16.8106(5)	13.2348(6)	22.1496(8)
α (deg)	81.2230(10)	90	81.8520(10)
β (deg)	75.7230(10)	90.100(2)	83.0070(10)
γ (deg)	84.0900(10)	90	87.1900(10)
Crystal size (mm^3)	0.213 x 0.16 x 0.081	0.153 x 0.082 x 0.061	0.217 x 0.076 x 0.063
Volume ($Å^3$)	2196.76(10)	3737.3(3)	2360.21(14)
Z	2	4	4
D_{calc} (g/cm^3)	1.558	1.372	1.683
F(000)	1052.0	1600.0	1200.0
λ (MoK_a) (Å)	0.71073	0.71073	0.71073
Temperature (K)	173.00	173.00	173.00
2*θ* min (deg)	2.522	4.21	3.74
2*θ* max (deg)	57.144	52.786	57.18
μ (mm^{-1})	0.975	0.527	0.906
Goodness-of-fit on F^2	1.040	1.347	1.035
Final R_1 indices [$I>2\sigma(I)$]	0.0257	0.1037	0.0376
wR_2 (all reflections)	0.0671	0.2339	0.0990
Flack x parameter	-	-	-

Table 3.7: Selected bond lengths (Å), bond angles (°), and torsion angles (°) of ruthenium complexes **C10**, **C19**, and **C20**.[a]

Bond Lengths	Bond Angles	Torsion Angles	Complexes				
			C10A	C10B	C19	C20A	C20B
Ru(1) – Cl(1)	-	-	2.3885(5)	-	2.390(2)	2.3863(7)	-
Ru(1) – N(1)	-	-	2.0961(15)	-	2.059(9)	2.083(2)	-
Ru(1) – N(2)	-	-	2.0711(14)	-	2.099(10)	2.079(2)	-
Ru(1) – C(13)	-	-	2.2407(17)	-	2.235(7)	-	-
Ru(2) – Cl(2)	-	-	-	2.4053(5)	-	-	2.3835(7)
Ru(2) – N(3)	-	-	-	2.0865(15)	-	-	2.095(2)
Ru(2) – N(4)	-	-	-	2.0915(15)	-	-	2.070(2)
Ru(2) – C(35)	-	-	-	2.2124(17)	-	-	-
Ru(1A) – Cl(1)	-	-	-	-	2.421(3)	-	-
Ru(1A) – N(1A)	-	-	-	-	2.106(16)	-	-
Ru(1A) – N(2A)	-	-	-	-	2.139(15)	-	-
-	N(2) – Ru(1) – N(1)	-	76.43(6)	-	78.0(4)	76.75(9)	-
-	N(1) – Ru(1) – Cl(1)	-	83.69(4)	-	89.1(3)	84.92(6)	-
-	N(1) – Ru(1) – C(13)	-	145.78(6)	-	108.0(3)	-	-
-	N(3) – Ru(2) – Cl(2)	-	-	86.54(4)	-	-	84.57(7)
-	N(3) – Ru(2) – N(4)	-	-	76.86(6)	-	-	76.63(9)
-	N(1A) – Ru(1A) – N(2A)	-	-	-	76.4(5)	-	-
-	N(1A) – Ru(1A) – Cl(1)	-	-	-	88.9(5)	-	-
-	-	Ru(1) – N(1) – C(1) – C(2)	171.98(14)	-	179.9(11)	175.1(2)	-
-	-	Ru(2) – N(3) – C(27) – C(28)	-	3.0(2)	-	-	-0.2(4)
-	-	Ru(1A) – N(1A) – C(1A) – C(2A)	-	-	176(2)	-	-
-	-	Ru(2) – N(4) – C(28) – C(29)	-	-	-	-	2.3(2)
-	-	Ru(1) – N(2) – C(7) – C(8)	-72.83(19)	-	148.1(10)	132.2(2)	-
-	-	Ru(2) – N(4) – C(28) – C(27)	-	-3.8(2)	-	-	-

[a] Atoms are labelled as per numbering given in **Figure 3.4** – **Figure 3.6**.

3.3 Conclusions

A series of cationic half-sandwich ruthenium complexes with various aromatic and aliphatic substituents on the imine nitrogen were successfully synthesized and characterized using various analytical and spectroscopic techniques. ^{1}H and ^{13}C NMR indicated the expected number of proton and carbon resonances, respectively. ESI-MS indicated the base peak as the $[M]^{+}$ fragment ion for all the complexes. SCXRD analysis of the complexes revealed molecular structures that corresponded with what was obtained in the solution. The complexes adopted the usual piano-stool conformation in which the ruthenium metal centre has a pseudo-octahedral geometry.

3.4 Experimental Methods

All reactions involving air- and/or moisture-sensitive compounds were performed under purified dry nitrogen using normal Schlenk techniques. All reagents were obtained from Sigma-Aldrich and used as received. Solvents were purchased from Promark Chemicals and Sigma Aldrich and used without further purification. IR spectra were recorded as neat oils or solids on a Bruker Tensor 27 FTIR spectrometer fitted with an Attenuated Total Reflectance (ATR) accessory. NMR spectra were recorded on a Bruker Avance NMR spectrometer (^{1}H at 400 MHz, ^{13}C at 101 MHz, and ^{31}P at 121 MHz). The chemical shifts (in ppm) are referenced to the residual protons of the deuterated solvents with tetramethylsilane (TMS) as an internal standard. ESI-MS analyses were recorded on a Thermo Scientific Dionex Ultimate 3000 UHPLC coupled to a Bruker Compact QqTOF HRMS in the positive mode using the Loop method. Melting point measurements were recorded using a Stuart SMP30 instrument and were reported as obtained. Single X-ray diffraction data was collected on a Bruker APEX-II CCD diffractometer. The crystal was kept at 173.00 K during data collection. Using Olex2,[18] the structure was solved with the SHELXT[19] structure solution program using Intrinsic Phasing and refined with the SHELXL[20] refinement package using Least Squares minimization. All non-hydrogen atoms were refined anisotropically. Molecular diagrams were produced using the POV-Ray program.[21] Elemental analysis was recorded using a Thermo Scientific Flash 2000 Series CHNS-O Analyzer (UJ).

3.4.1 Synthesis of Cationic Pyridylimine Ru(II) Complexes C10 – C20.

3.4.1.1 [(L1)RuCl(p-cymene)]Cl, C10

Ligand **L1** (47.8 mg, 0.26 mmol) was added to a stirring solution of $[RuCl_2(p\text{-cymene})]_2$ (80.4 mg, 0.13 mmol) in MeOH (10 mL), and the resulting solution was reacted for 24 hours at room temperature under a N_2 atmosphere. After the reaction, the solution was concentrated to 1 mL, redissolved in DCM (10 mL), and layered with excess diethyl ether to afford the product as a yellow crystalline solid (145.1 mg, 87%). **^{1}H NMR** (400 MHz, DMSO-d_6): δ (jn ppm) = 9.69 (d, J = 5.7 Hz, 1H, H^1), 9.08 (s, 1H, H^6), 8.37 - 8.32 (m, 2H, H^{Ar}), 7.88 – 7.81 (m, 3H, H^{Ar}), 7.63 (m, 3H, H^{Ar}), 6.12 (d, J = 6.2 Hz, 1H, $H^{p\text{-}cy}$), 5.82 (d, J = 6.2 Hz, 1H, $H^{p\text{-}cy}$), 5.64 (dd, J = 6.2 Hz, 2H, $H^{p\text{-}cy}$), 2.15 (s, 3H, H^{11}), 0.98 (d, J = 7.1 Hz, 6H, $H^{19, 20}$). **^{13}C NMR** (101 MHz, DMSO-d_6): δ (in ppm) = 168.0, 156.2, 154.6, 151.7, 139.9, 130.2, 129.7, 129.5, 128.9, 122.5, 105.1, 103.3, 86.6, 86.1, 85.1, 85.0, 30.5, 21.7, 21.6, 18.3. **FT-IR** (ATR, neat): 1612.64 cm^{-1} ($\nu_{C=N}$), 1587.62 cm^{-1} ($\nu_{pyr\text{-}C=N}$). **ESI-MS** (+ve, m/z): Calcd. for $[M]^+$ 453.0671, found 453.0669. Anal. Calcd for $C_{22}H_{24}Cl_2N_2Ru$: C 54.10; H 4.95; N 5.74. Found: C 54.03; H 5.16; N 5.63.

3.4.1.2 [(L2)RuCl(p-cymene)]Cl, C11

Synthesized using the same synthetic protocol described for complex **C10**, using ligand **L2** (43.8 mg, 0.21 mmol) as a reagent. Complex **11** was obtained as a yellow crystalline solid (108.2 mg, 84%). **^{1}H NMR** (400 MHz, DMSO-d_6): δ (in ppm) = 9.68 (d, J = 5.7 Hz, 1H, H^1), 8.96 (s, 1H, H^6), 8.33 – 8.27 (m, 2H, H^{Ar}), 7.94 (t, J = 6.9 Hz, 1H, H^{Ar}), 7.36 (m, 3H, H^{Ar}), 5.94 (d, J = 6.4 Hz, 1H, $H^{p\text{-}cy}$), 5.63 (dd, J = 6.4 Hz, 2H, $H^{p\text{-}cy}$), 5.34 (d, J = 6.4 Hz, 1H, $H^{p\text{-}cy}$), 2.67 (m, 1H, H^{14}), 2.32 (s, 3H, H^{11}), 2.21 (s, 3H, H^{Al}), 2.10 (s, 3H, H^{Al}), 1.05 (d, J = 7.2 Hz, 6H, $H^{19, 20}$). **^{13}C NMR** (101 MHz, DMSO-d_6): δ (in ppm) = 173.4, 156.1, 154.1, 150.7, 140.1, 131.1, 130.0, 129.3, 129.3, 128.8, 128.6, 128.1, 106.3, 100.4, 87.1, 86.6, 85.9, 84.9, 30.5, 22.1, 21.6, 19.7, 18.7, 17.9. **FT-IR** (ATR, neat): 1614.98 cm^{-1} ($\nu_{C=N}$), 1589.15 cm^{-1} ($\nu_{pyr\text{-}C=N}$). **ESI-MS** (+ve, m/z): Calcd. for $[M]^+$ 481.0984, found 481.0984. Anal. Calcd for $C_{24}H_{28}Cl_2N_2Ru$: C 55.81; H 5.46; N 5.42. Found: C 55.67; H 5.82; N 5.30.

3.4.1.3 [(L3)RuCl(p-cymene)]Cl, C12

Synthesized using the same synthetic protocol described for complex **C10**, using ligand **L3** (44.9 mg, 0.17 mmol) as a reagent. Complex **12** was obtained as a yellow crystalline solid (87.3 mg, 80%). **^{1}H NMR** (400 MHz, DMSO-d_6): δ (jn ppm) = 9.75 (d, J = 5.8 Hz, 1H, H^1), 9.09 (s, 1H, H^6), 8.36 (m , 2H, H^{Ar}), 7.96 (t, J = 6.1 Hz, 1H, H^{Ar}), 7.49 – 7.38 (m, 3H, H^{Ar}), 6.09 (d,

J = 6.3 Hz, 1H, $H^{p\text{-}cy}$), 5.65 (d, *J* = 6.3 Hz, 1H, $H^{p\text{-}cy}$), 5.47 (d, *J* = 6.3 Hz, 1H, $H^{p\text{-}cy}$), 5.34 (d, *J* = 6.3 Hz, 1H, $H^{p\text{-}cy}$), 3.73 (m, 1H, H^{18}), 2.63 (m, 2H, H^{Al}), 2.13 (s, 3H, H^{11}), 1.45 (d, *J* = 6.5 Hz, 3H, H^{Al}), 1.26 (d, *J* = 6.7 Hz, 3H, H^{Al}), 1.15 (d, *J* = 6.5 Hz, 3H, H^{Al}), 1.05 (d, *J* = 6.8 Hz, 3H, H^{19}), 0.84 (d, *J* = 7.2 Hz, 3H, H^{20}). **^{13}C NMR** (101 MHz, DMSO-d_6): δ (in ppm) = 173.9, 156.9, 154.4, 148.6, 141.6, 140.8, 140.0, 130.4, 129.9, 129.5, 124.8, 106.0, 101.6, 87.3, 86.4, 85.1, 30.8, 28.1, 27.6, 27.0, 26.2, 23.5, 22.7, 22.0, 21.7, 18.4. **FT-IR** (ATR, neat): 1611.29 cm^{-1} ($\nu_{C=N}$), 1582.05 cm^{-1} ($\nu_{pyr\text{-}C=N}$). **ESI-MS** (+ve, m/z): Calcd. for $[M]^+$ 537.1610, found 537.1612. Anal. Calcd for $C_{28}H_{36}Cl_2N_2Ru$: C 58.74; H 6.34; N 4.89. Found: C 58.65; H 6.54; N 4.70.

3.4.1.4 [(L4)RuCl(p-cymene)]Cl, C13

Synthesized using the same synthetic protocol described for complex **C10**, using ligand **L4** (41.4 mg, 0.20 mmol) as a reagent. Complex **13** was obtained as a yellow crystalline solid (96.6 mg, 85%). **^{1}H NMR** (400 MHz, DMSO-d_6): δ (in ppm) = 9.67 (d, *J* = 5.6 Hz, 1H, H^1), 8.91 (s, 1H, H^6), 8.32 - 8.27 (m, 2H, H^{Ar}), 7.93 (t, *J* = 7.1 Hz, 1H, H^{Ar}), 7.16 – 7.11 (d, *J* = 7.4 Hz, 2H, H^{Ar}), 5.99 (d, *J* = 6.0 Hz, 1H, $H^{p\text{-}cy}$), 5.64 (m, 2H, $H^{p\text{-}cy}$), 5.32 (d, *J* = 6.0 Hz, 1H, $H^{p\text{-}cy}$), 2.68 (m, 1H, H^{18}), 2.36 (s, 3H, H^{Al}), 2.30 (s, 3H, H^{Al}), 2.17 (s, 3H, H^{Al}), 2.11 (s, 3H, H^{11}), 1.05 (d, *J* = 7.1 Hz, 6H, $H^{19, 20}$). **^{13}C NMR** (101 MHz, DMSO-d_6): δ (in ppm) = 173.3, 156.1, 154.1, 148.6, 140.1, 137.3, 130.9, 129.9, 129.8, 129.3, 128.3, 106.4, 100.5, 87.2, 86.7, 85.8, 84.6, 30.6, 22.1, 21.6, 20.5, 19.6, 18.1, 18.0. **FT-IR** (ATR, neat): 1613.47 cm^{-1} ($\nu_{C=N}$), 1583.29 cm^{-1} ($\nu_{pyr\text{-}C=N}$). **ESI-MS** (+ve, m/z): Calcd. for $[M]^+$ 495.1141, found 495.1140. Anal. Calcd for $C_{25}H_{30}Cl_2N_2Ru$: C 56.60; H 5.70; N 5.28. Found: C 56.31; H 5.61; N 5.30.

3.4.1.5 [(L5)RuCl(p-cymene)]Cl, C14

Synthesized using the same synthetic protocol described for complex **C10**, using ligand **L5** (49.9 mg, 0.25 mmol) as a reagent. Complex **14** was obtained as a brown oil (121.9 mg, 82%). **^{1}H NMR** (400 MHz, DMSO-d_6): δ (in ppm) = 9.61 (d, *J* = 5.7 Hz, 1H, H^1), 8.49 (s, 1H, H^6), 8.22 (m, 2H, H^{Ar}), 7.80 (t, *J* = 7.1 Hz, 1H, H^{Ar}), 7.61 – 7.51 (m, 5H, H^{Ar}), 6.29 (d, *J* = 6.3 Hz, 1H, $H^{p\text{-}cy}$), 6.01 (d, *J* = 6.3 Hz, 1H, $H^{p\text{-}cy}$), 5.89 (dd, *J* = 6.3 Hz, 2H, $H^{p\text{-}cy}$), 5.72 (d, *J* = 6.3 Hz, 1H, H^{Al}), 5.51 (d, *J* = 6.8 Hz, 1H, H^{Al}), 2.11 (s, 3H, H^{11}), 0.99 – 0.90 (d, *J* = 7.1 Hz, 6H, $H^{19, 20}$). **^{13}C NMR** (101 MHz, DMSO-d_6): δ (in ppm) = 167.2, 156.0, 154.5, 139.7, 134.4, 129.9, 129.3, 129.0, 128.8, 128.2, 104.4, 103.6, 87.7, 84.4, 84.2, 83.9, 68.7, 30.4, 22.0, 21.5, 18.4. **FT-IR** (ATR, neat): 1619.18 cm^{-1} ($\nu_{C=N}$), 1594.42 cm^{-1} ($\nu_{pyr\text{-}C=N}$). **ESI-MS** (+ve, m/z): Calcd. for $[M]^+$ 467.0828, found 467.0824.

3.4.1.6 [(L6)RuCl(p-cymene)]Cl, C15

Synthesized using the same synthetic protocol described for complex **C10**, using ligand **L6** (43.9 mg, 0.23 mmol) as a reagent. Complex **15** was obtained as a yellow oil (148.3 mg, 73%). **^{1}H NMR** (400 MHz, DMSO-d_6): δ (in ppm) = 9.55 (d, *J* = 5.7 Hz, 1H, H^{1}), 8.89 (s, 1H, H^{6}), 8.25 – 8.19 (m, 2H, H^{Ar}), 7.80 (t, *J* = 7.2 Hz, 1H, H^{Ar}), 6.31 – 6.21 (dd, *J* = 6.5 Hz, 2H, $H^{p\text{-}cy}$), 5.92 (d, *J* = 6.5 Hz, 2H, $H^{p\text{-}cy}$), 4.44 (t, *J* = 7.6 Hz, 1H, H^{Al}), 2.60 (m, 1H, H^{14}), 2.40 (d, *J* = 6.6 Hz, 1H, H^{Al}), 2.26 (d, *J* = 7.2 Hz, 1H, H^{Al}), 2.16 (s, 3H, H^{7}), 1.89 – 1.55 (m, 7H, H^{Al}), 1.18 (m, 2H, H^{Al}), 1.03 – 0.93 (d, *J* = 7.3 Hz, 6H, $H^{15, 16}$). **^{13}C NMR** (101 MHz, DMSO-d_6): δ (in ppm) = 165.7, 155.7, 155.1, 139.7, 128.8, 128.2, 104.2, 103.4, 87.7, 84.5, 84.2, 73.3, 34.6, 32.6, 30.5, 25.1, 24.7, 21.9, 21.6, 18.4. **FT-IR** (ATR, neat): 1618.38 cm^{-1} ($\nu_{C=N}$), 1593.89 cm^{-1} ($\nu_{pyr\text{-}C=N}$). **ESI-MS** (+ve, m/z): Calcd. for $[M]^+$ 459.1141, found 459.1122.

3.4.1.7 [(L7)RuCl(p-cymene)]Cl, C16

Synthesized using the same synthetic protocol described for complex **C10**, using ligand **L7** (32.1 mg, 0.22 mmol) as a reagent. Complex **16** was obtained as a yellow crystalline solid (101.3 mg, 75%). **^{1}H NMR** (300 MHz, DMSO-d_6): δ (in ppm) = 9.58 (d, *J* = 5.7 Hz, 1H, H^{1}), 8.83 (s, 1H, H^{6}), 8.21 (m, 2H, H^{Ar}), 7.80 (t, *J* = 6.7 Hz, 1H, H^{Ar}), 6.31 (d, *J* = 6.5 Hz, 1H, $H^{p\text{-}cy}$), 6.22 (d, *J* = 6.5 Hz, 1H, $H^{p\text{-}cy}$), 5.93 (d, *J* = 6.5 Hz, 2H, $H^{p\text{-}cy}$), 4.49 - 4.27 (m, 2H, H^{Al}), 2.60 (m, 1H, H^{14}), 2.16 (s, 3H, H^{7}), 1.94 – 1.82 (m, 2H, H^{Al}), 1.03 (m, 3H, H^{Al}), 0.93 (m, 6H, $H^{15, 16}$). **^{13}C NMR** (101 MHz, DMSO-d_6): δ (in ppm) = 167.2, 155.9, 154.3, 139.6, 128.6, 128.0, 104.1, 102.8, 87.2, 84.8, 84.6, 84.1, 67.6, 30.2, 22.2, 21.9, 21.1, 18.1, 11.1. **FT-IR** (ATR, neat): 1621.28 cm^{-1} ($\nu_{C=N}$), 1595.70 cm^{-1} ($\nu_{pyr\text{-}C=N}$). **ESI-MS** (+ve, m/z): Calcd. for $[M]^+$ 419.0828, found 419.0809. Anal. Calcd for $C_{19}H_{26}Cl_2N_2Ru$: C 50.22; H 5.77; N 6.17. Found: C 50.05; H 6.13; N 6.26.

3.4.1.8 [(L8)RuCl(p-cymene)]Cl, C17

Synthesized using the same synthetic protocol described for complex **C10**, using ligand **L8** (48.5 mg, 0.25 mmol) as a reagent. Complex **17** was obtained as a yellow crystalline solid (129.2 mg, 81%). **^{1}H NMR** (400 MHz, DMSO-d_6): δ (in ppm) = 8.98 (s, 1H, H^{6}), 8.18 - 8.14 (m, 2H, H^{Ar}), 7.87 (m, 3H, H^{Ar}), 7.65 (m, 3H, H^{Ar}), 6.18 (d, *J* = 6.6 Hz, 1H, $H^{p\text{-}cy}$), 5.75 (d, *J* = 6.6 Hz, 1H, $H^{p\text{-}cy}$), 5.50 (d, *J* = 6.6 Hz, 1H, $H^{p\text{-}cy}$), 5.44 (d, *J* = 6.6 Hz, 2H, $H^{p\text{-}cy}$), 3.16 (s, 3H, H^{Al}), 2.21 (s, 3H, H^{11}), 1.02 (d, *J* = 7.0 Hz, 3H, H^{19}), 0.92 (d, *J* = 7.0 Hz, 3H, H^{20}). **^{13}C NMR** (101 MHz, DMSO-d_6): δ (in ppm) = 168.6, 165.0, 154.8, 151.8, 139.4, 129.8, 129.6, 129.5, 128.3,

122.3, 87.4, 85.4, 84.2, 82.9, 30.6, 28.2, 22.2, 21.3, 18.4. **FT-IR** (ATR, neat): 1615.21 cm^{-1} ($\nu_{C=N}$), 1588.01 cm^{-1} ($\nu_{pyr\text{-}C=N}$). **ESI-MS** (+ve, m/z): Calcd. for $[M]^+$ 467.0828, found 467.0811. Anal. Calcd for $C_{23}H_{26}Cl_2N_2Ru$: C 54.98; H 5.22; N 5.58. Found: C 54.29; H 5.47; N 5.57.

3.4.1.9 [(L9)RuCl(p-cymene)]Cl, C18

Synthesized using the same synthetic protocol described for complex **C10**, using ligand **L9** (66.8 mg, 0.27 mmol) as a reagent. Complex **18** was obtained as a yellow crystalline solid (143.9 mg, 74%). **^{1}H NMR** (300 MHz, DMSO-d_6): δ (in ppm) = 9.22 (s, 1H, H^6), 8.63 – 8.56 (m, 3H, H^{Ar}), 7.92 (m, 2H, H^{Ar}), 7.68 (m, 3H, H^{Ar}), 5.92 (d, *J* = 6.3 Hz, 1H, $H^{p\text{-}cy}$), 5.59 (dd, *J* = 6.3 Hz, 2H, $H^{p\text{-}cy}$), 5.40 (d, *J* = 6.3 Hz, 1H, $H^{p\text{-}cy}$), 2.59 (m, 1H, H^{18}), 2.22 (s, 3H, H^{11}), 1.05 (d, *J* = 6.9 Hz, 3H, H^{19}), 0.97 (d, *J* = 7.2 Hz, 3H, H^{20}). **^{13}C NMR** (75 MHz, DMSO-d_6): δ (in ppm) = 159.0, 154.5, 149.7, 139.6, 129.3, 127.3, 124.5, 122.4, 121.4, 106.3, 100.0, 86.3, 85.5, 29.9, 21.5, 17.8. **FT-IR** (ATR, neat): 1617.06 cm^{-1} ($\nu_{C=N}$), 1600.42 cm^{-1} ($\nu_{pyr\text{-}C=N}$). **ESI-MS** (+ve, m/z): Calcd. for $[M]^+$ 521.0545, found 520.1395. Anal. Calcd for $C_{23}H_{23}Cl_2F_3N_2Ru$: C 49.65; H 4.17; N 5.03. Found: C 49.37; H 4.06; N 5.26.

3.4.1.10 [(L1)RuCl(p-cymene)]BPh$_4$, C19

Ligand **L1** (38.9 mg, 0.21 mmol) and excess $NaBPh_4$ (85.6 mg, 0.25 mmol) were added to a stirring solution of $[RuCl_2(p\text{-cymene})]_2$ (65.4 mg, 0.11 mmol) in MeOH (10 mL) and the resulting solution was reacted for 24 hours at room temperature under a N_2 atmosphere. After the reaction, the solution was concentrated to 1 mL, redissolved in DCM (3 mL), and filtered through celite. The solvent evaporated overnight; then, the residue was dried under a high vacuum to afford **C19** as a yellow solid (60.2 mg, 83%). **^{1}H NMR** (400 MHz, DMSO-d_6): δ (in ppm) = 9.57 (d, *J* = 5.7 Hz, 1H, H^1), 8.91 (s, 1H, H^6), 8.27 (m, 2H, H^{Ar}), 7.87 (t, *J* = 7.1 Hz, 1H, H^{Ar}), 7.79 (m, 2H, H^{Ar}), 7.64 (m, 3H, H^{Ar}), 7.18 (m, 8H, H^{Ar}), 6.92 (m, 8H, H^{Ar}), 6.79 (m, 4H, H^{Ar}), 6.06 (d, *J* = 6.2 Hz, 1H, $H^{p\text{-}cy}$), 5.76 (d, *J* = 6.2 Hz, 1H, $H^{p\text{-}cy}$), 5.61 – 5.57 (d, *J* = 6.2 Hz, 2H, $H^{p\text{-}cy}$), 2.15 (s, 3H, H^{11}), 0.99 (d, *J* = 7.1 Hz, 6H, $H^{19, 20}$). **^{13}C NMR** (101 MHz, DMSO-d_6): δ (in ppm) = 167.9, 164.1, 163.6, 163.1, 162.6, 156.0, 154.5, 151.7, 139.9, 135.5, 130.1, 129.8, 129.5, 128.9, 125.3, 122.5, 121.5, 105.1, 103.4, 86.5, 86.1, 85.1, 84.9, 30.5, 21.7, 21.6, 18.3. **FT-IR** (ATR, neat): 1626.40 cm^{-1} ($\nu_{C=N}$), 1579.44 cm^{-1} ($\nu_{pyr\text{-}C=N}$), 704.73 cm^{-1}, 733.36 cm^{-1} ($\nu_{B\text{-}C}$). **ESI-MS** (+ve, m/z): Calcd. for $[M]^+$ 453.0671, found 453.0654. Anal. Calcd for $C_{46}H_{44}BClN_2Ru$: C 71.55; H 5.74; N 3.63. Found: C 71.34; H 5.56; N 3.66.

3.4.1.11 [(L1)RuCl(p-cymene)]PF_6, C20

Ligand **L1** (47.9 mg, 0.26 mmol) and excess KPF_6 (55.2 mg, 0.30 mmol) were added to a stirring solution of $[RuCl_2(p\text{-cymene})]_2$ (80.5 mg, 0.13 mmol) in MeOH (10 mL) and the resulting solution was reacted for 24 hours at room temperature under a N_2 atmosphere. After the reaction, the solution was concentrated to 1 mL, redissolved in DCM (3 mL), and filtered through celite. The solvent was allowed to evaporate overnight followed by drying the residue under a high vacuum to afford **C20** as a brown solid (156.8 mg, 85%). **^{1}H NMR** (400 MHz, DMSO-d_6): δ (in ppm) = 9.57 (d, J = 5.9 Hz, 1H, H^1), 8.93 (s, 1H, H^6), 8.28 (m, 2H, H^{Ar}), 7.89 (t, J = 7.2 Hz, 1H, H^{Ar}), 7.80 (m, 2H, H^{Ar}), 7.64 (m, 3H, H^{Ar}), 6.08 (d, J = 6.1 Hz, 1H, $H^{p\text{-}cy}$), 5.75 (d, J = 6.1 Hz, 2H, $H^{p\text{-}cy}$), 5.62 (dd, J = 6.1 Hz, 2H, $H^{p\text{-}cy}$), 2.16 (s, 3H, H^{11}), 0.99 (d, J = 7.1 Hz, 6H, $H^{19, 20}$). **^{13}C NMR** (101 MHz, DMSO-d_6): δ (in ppm) = 167.7, 155.8, 154.3, 151.5, 139.7, 129.9, 129.6, 129.3, 128.7, 122.3, 104.9, 103.2, 86.3, 85.9, 84.9, 84.7, 30.3, 21.5, 21.4, 18.1. **^{31}P NMR** (121 MHz, DMSO-d_6): δ (in ppm) = -143.1 (sept., J = 709.1 Hz). **FT-IR** (ATR, neat): 1613.64 cm^{-1} ($\nu_{C=N}$), 1589.84 cm^{-1} ($\nu_{pyr\text{-}C=N}$), 828.16 cm^{-1} ($\nu_{P\text{-}F}$). **ESI-MS** (+ve, m/z): Calcd. for $[M]^+$ 453.0671, found 453.0652. Anal. Calcd for $C_{22}H_{24}ClF_6N_2PRu$: C 44.19; H 4.05; N 4.69. Found: C 44.01; H 4.53; N 4.82.

3.5 References

1. Coffey, R. S. *Chem. Commun.,* **1967**, 923 – 924.
2. Guan, C., Zhang, D-D., Pan, Y., Iguchi, M., Ajitha, M. J., Hu, J., Li, H., Yao, C., Huang, M-H., Min, S., Zheng, J., Himeda, Y., Kawanami, H., Huang, K-W. *Inorg. Chem.,* **2017**, *56*, 438 – 445.
3. Ge, S., Liu, J-H., Gong, L., Mo. X-F., Liu, C., Yi, X-Y., He, P. *Eur. J. Inorg. Chem.,* **2024**, *27*, e202300509.
4. Onishi, N., Kanega, R., Fujita, E., Himeda, Y. *Adv. Synth. Catal.,* **2019**, *361*, 289 – 296.
5. Wang, W. H., Himeda, Y., Muckerman, J. T., Manbeck, G. F., Fujita, E. *Chem. Rev.,* **2015**, *115*, 12936 – 12973.
6. Joseph, M. C., Swarts, A. J., Mapolie, S. F. *Polyhedron*, **2022**, *212*, 115579.
7. Ramos, T. S., Luz, D. M., Nascimento, R. D., Silva, A. K., Lião, L. M., Miranda, V. M., Deflon, V. M., de Araujo, M. P., Ueno, L. T., Machado, F. B. C., Dinelli, L. R., Bogado, A. L. *J. Organomet. Chem.,* **2019**, *892*, 51 – 65.
8. Onoue, H., Moritani, I. *J. Organomet. Chem.,* **1972**, *43*, 431.
9. Gichumbi, J. M., Friedrich, H. B., Omondi, B. *Inorg. Chim. Acta*, **2017**, *456*, 55 – 63.

10. Pregosin, P. S., NMR in Organometallic Chemistry, 1st ed., WILEY-VCH Verlag, Weinheim, **2012**.
11. Prasad, K., Therrien, B., Rao, K. *J. Organomet. Chem.,* **2008**, *693*, 3049.
12. Joseph, M. C., Kotźe, I. A., Nnaji, N. J., Swarts, A. J., Mapolie, S. F. *Organometallics*, **2022**, *41*, 3546 – 3556.
13. Lenntech, *Mol. Weight Calc.,* www.lenntech.com. (accessed 04 October 2024).
14. Gichumbi, J. M., Friedrich, H. B., Omondi, B. *J. Organomet. Chem.,* **2016**, *808*, 87 – 96.
15. Ruzziconi, R., Bellachioma, G., Giancaleoni, G., Lepri, S., Superchi, S., Zanasi, R., Monaco, G. *Dalton Trans.,* **2014**, *43*, 1636 – 1650.
16. Hohloch, S., Suntrup, L., Sarkar, B. *Organometallics,* **2013**, *32*, 7376.
17. Scattergood, P. A., Khushnood, U., Tariq, A., Cooke, D. J., Rice, C. R., Elliott, P. I. P. *Inorg. Chem.,* **2016**, *55*, 7787.
18. Dolomanov, O. V., Bourhis, L. J., Gildea, R. J., Howard, J. A. K., Puschmann, H. *J. Appl. Cryst.,* **2009**, *42*, 339 – 341.
19. Sheldrick, G. M. *Acta Cryst.,* **2015**, *A71*, 3 – 8.
20. Sheldrick, G. M. *Acta Cryst.,* **2015**, *C71*, 3 – 8.
21. POV-Ray, *Version 3.6*, Williamstown, Australia, Persistence of vision ray.

Chapter 4: Formic Acid Dehydrogenation Catalyzed by Cationic, Half-Sandwich Pyridylimine Ruthenium(II) Complexes

4.1 Introduction

The catalytic dehydrogenation of formic acid (HCOOH, FA) was first reported by Coffey in 1967 and is one of the increasingly important organic transformations as the world seeks to move away from fossil fuels that have significant environmental implications.[1] FA is considered an attractive chemical hydrogen carrier due to its favorable chemical properties which are expertly summarized by He and coworkers.[2] Most importantly, the hydrogenation of CO_2 can yield FA and this interconversion between CO_2 + H_2 and FA makes FA a sustainable hydrogen storage and release medium.[3] The commonly employed approaches towards FA dehydrogenation include dehydrogenation in the presence or absence of base or additives in an organic solvent medium (**Scheme 4.1,** top) and neat FA dehydrogenation (**Scheme 4.1,** bottom). The latter is rarely explored due to the poor solubility of many transition metal complexes in FA and the low pH of the reaction solution which could lead to catalyst deactivation.[4] As a result, the addition of bases such as triethylamine (NEt_3) and alkali metal hydroxides such as potassium hydroxide (KOH) has commonly been applied to address the delicate pH balance required for efficient FA dehydrogenation.[5] It should be noted, however, that the presence of bases and/or organic solvents can pose significant operational risks in applications such as proton exchange membrane (PEM) fuel cells. As a result, hydrogen produced from such systems should be subjected to a purification step.[6]

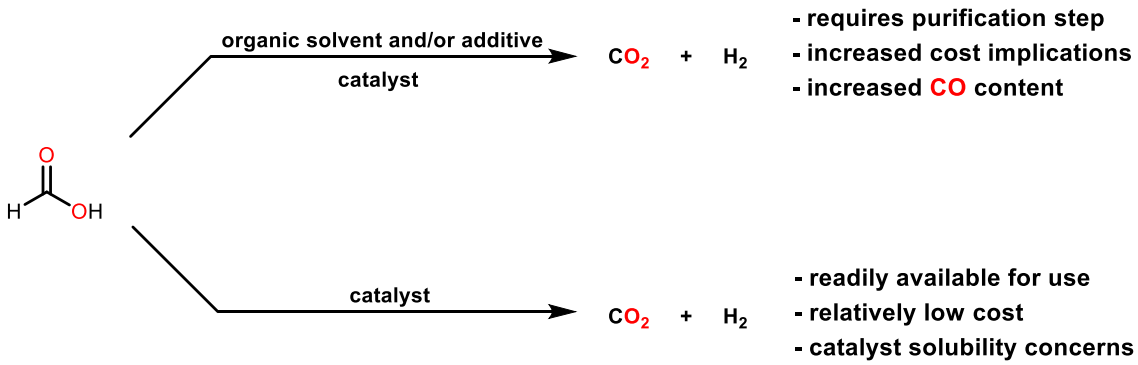

Scheme 4.1: Differences between FA dehydrogenation in the presence of organic solvent and/or additive (top) and neat FA dehydrogenation (bottom).

Williams and coworkers reported on the catalytic dehydrogenation of neat FA using 5 mol% HCOONa as an additive and a high concentration of the usually undesired CO (~ 500 ppm) was observed under such reaction conditions.[7] Fischmeister, Himeda, and their coworkers reported more examples of neat FA dehydrogenation in the absence of additives, but their systems required high concentrations (4 – 8 mol/L) of the substrate (FA) for efficient gas generation.[8,9] To date, one of the most efficient neat FA dehydrogenation systems with a total turnover number of 1 701 150 and the generation of H_2/CO_2 at pressures up to 100 bars was reported by Milstein and coworkers.[4]

Transition metal complexes commonly applied towards the dehydrogenation of FA include those of iridium,[10,11] ruthenium,[12,13] iron,[14,15] and most recently manganese due to its relatively cheap cost and abundance.[16,17] Although pyridylimine ligands and their Ru(II)-arene complexes have been extensively studied and reported in the chemical literature, there are no existing reports, to the best of our knowledge, detailing their application towards the dehydrogenation of FA to produce H_2. Herein, we report the application of the cationic, half-sandwich pyridylimine ruthenium(II) complexes reported in **Chapter 3** as catalyst precursors in FA dehydrogenation.

4.2 Optimization of catalytic reaction conditions

The pyridylimine ruthenium(II) complexes **C10** – **C18** were assessed as catalyst precursors in the dehydrogenation of FA (**Scheme 4.2**). For complexes **C10** – **C16**, several aromatic and aliphatic substituents were introduced on the imine nitrogen to investigate steric influences. In the case of complexes **C17** and **C18**, a methyl and a trifluoromethyl substituent were introduced on the pyridine ring to study the electronic effects. Herein, the nature and amount of formate cation and solvent and the effects of reaction temperature, catalyst loading, counterion, and FA concentration were studied in detail. In addition, mechanistic insights and prospects toward sustainable FA dehydrogenation through water-mediated reactions are presented.

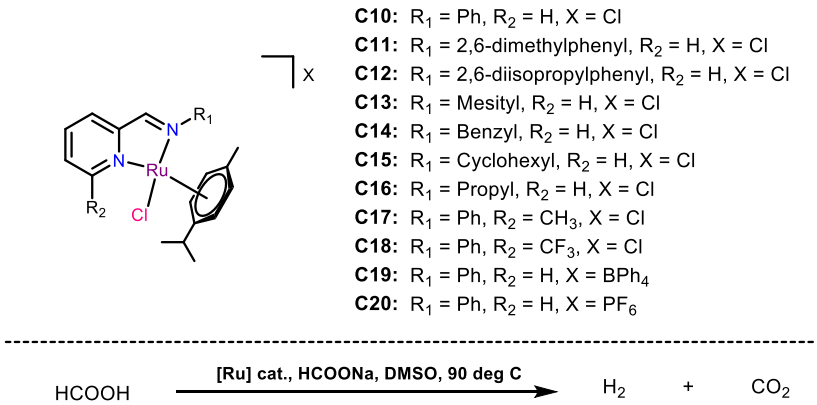

Scheme 4.2: Cationic half-sandwich pyridylimine Ru(II) complexes for FA dehydrogenation.

4.2.1 Initial testing of cationic Ru(II) complexes, C10 – C18

The reaction conditions utilized were modified from a literature procedure by Albrecht and coworkers.[10] The reactions were performed at 90 °C using 0.2 mol% of Ru catalyst, 1 mmol of sodium formate (HCOONa) as the additive, and 2 mL of dimethyl sulfoxide (DMSO) as the solvent for 2 hours. The catalytic activities of all ruthenium complexes tested under the abovementioned conditions are summarized in **Table 4.1**.

Table 4.1: Initial screening of pyridylimine Ru(II) complexes **C10** – **C18**.[a]

Entry	Catalyst	$CO_2 + H_2$ (mL)	TON	TOF (hr^{-1})	Conversion (%)
1	**Precursor**	-	-	-	-
2	**C10**	236	483	281	91
3	**C11**	64	130	46	25
4	**C12**	25	51	21	10
5	**C13**	72	147	54	28
6	**C14**	217	444	191	84
7	**C15**	4	7	5	2
8	**C16**	36	73	27	14
9	**C17**	117	238	85	45
10	**C18**	144	294	123	56

[a]**Conditions**: FA (5 mmol, 0.2 mL), **C10** – **C18** (0.2 mol%, 0.01 mmol), HCOONa (1 mmol), DMSO (2 mL), temperature (90 °C), total reaction volume (2.2 mL). TOF estimated based on gas evolution at 90 mins. TONs and conversion determined at 120 mins. Each reaction was repeated twice with an error of less than 5%. Maximum theoretical volume ($CO_2 + H_2$): 259 mL.

No gas evolution was observed when the reaction was conducted without a catalyst. Similarly, no gas was generated when the dichloro(p-cymene)ruthenium(II) dimer used to prepare the complexes was used as a catalyst (**Table 4.1**, entry 1). The Ru(II) complexes were active for the dehydrogenation of FA with the activity being highly correlated to the nature of the substituent on the imine nitrogen. For complexes **C10** – **C13**, the imine nitrogen is bonded to aromatic substituents bearing different alkyl moieties. The reaction performed with **C10**, bearing the unsubstituted phenyl ring, yielded the highest amount of CO_2 + H_2 i.e. 236 mL, reaching TONs of 483 (**Table 4.1**, entry 2). A drastic decrease in activity was observed when varying the alkyl substitution from **C10** to **C11** (TON = 130) and **C12** (TON = 51) owing to the introduction of successively bulkier alkyl (dimethyl and diisopropyl) substituents on the aromatic ring that hinder substrate coordination to the Ru metal center (**Table 4.1**, entries 3 and 4). Complex **C13** containing mesityl substituents on the aromatic ring displayed similar catalytic activity as the 2,6-dimethyl substituted version, **C11** (**Table 4.1**, entries 3 and 5). Overall, introducing alkyl substituents on the aromatic ring bound to the imine nitrogen undermined FA dehydrogenation.

For complexes **C14** – **C16**, the imine nitrogen is bound to a range of aliphatic substituents. Complex **C14** bearing a benzyl substituent exhibited good catalytic activity i.e. TON = 444 compared to **C15** (TON = 7) and **C16** (TON = 73) bearing cyclohexyl and propyl substituents, respectively (**Table 4.1**, entries 6 – 8). The high activity of **C14** is attributed to the flexibility of the benzyl ring which enables easy substrate coordination to the metal center. In addition, **C14** possesses a combination of inductive and resonance effects that help stabilize the complex during the reaction. Complexes **C17** and **C18** possess a methyl and a trifluoromethyl substituent on the α carbon of the pyridine ring, respectively. In both cases, introducing these substituents led to decreased catalytic activity, i.e. TON = 238 for **C17** and TON = 294 for **C18**, compared to the analogous unsubstituted complex **C10** with TONs of 483 (**Table 4.1**, entries 9 and 10). **C18** exhibits slightly higher catalytic performance than **C17** due to the electron-withdrawing trifluoromethyl substituent that increases the electron deficiency of the Ru metal center and thus, allows efficient FA coordination.

The formation of H_2 gas was confirmed by a series of ^{1}H NMR monitoring studies in DMSO-d_6 as a singlet at δ = 4.61 ppm (**Figure S1**). Fulmer and coworkers reported a similar chemical shift for hydrogen gas in DMSO-d_6.[18] The production of CO_2 with negligible CO formation and the absence of H_2O was confirmed by GC-TCD analyses using helium as the carrier gas (**Figure S2**).

4.2.2 Effect of the nature and amount of formate cation on FA dehydrogenation

The use of alkali metal hydroxides such as KOH and alkali metal formates as additives in transition metal complex-catalyzed FA dehydrogenation has previously been shown to affect catalytic performance.[10, 16] The additive plays several crucial roles in FA dehydrogenation i.e. increasing the pH of the reaction medium to avoid possible catalyst deactivation, generating the catalytically active metal hydride species, and/or activating the FA substrate during the reaction.

In this study, HCOOM (where M = Na, Li, or K) and KOH were varied under the reaction conditions shown in **Figure 4.1**. No gas evolution was observed when the reaction was conducted without any organic additives or base. This result was ascribed to the low pH of the reaction medium that deactivates the catalyst **C10**. When 1 mmol of KOH was added, a maximum TON of 427 was achieved within 2 hours. Under similar reaction conditions, the nature of the formate alkali cation was varied, and a reactivity trend K (TON = 499) > Na (TON = 483) > Li (TON = 332) was established. To the best of our knowledge, an analysis of the formate cation reactivity has not been reported for FA dehydrogenation catalyzed by Ru(II) complexes in the literature. However, the superior catalytic activity of **C10** in the presence of HCOOK is assigned to the relative ease with which it interacts with the catalyst precursor to afford the usually catalytically active Ru-hydride species. In addition, K^+ due to its relatively large size compared to Na^+ and Li^+ has a greater affinity towards the Cl ligand of the Ru(II) complex as dictated by the Hard and Soft Acid and Base (HSAB) principle. Interestingly, Albrecht and coworkers observed an increase in reactivity along the series Li > Na > K in a report that details FA dehydrogenation using an iridium complex and assigned this behavior to the Lewis acid activation of the FA substrate.[10] Hence, the performance of the alkali metal formates in aiding FA dehydrogenation is highly catalyst-specific.

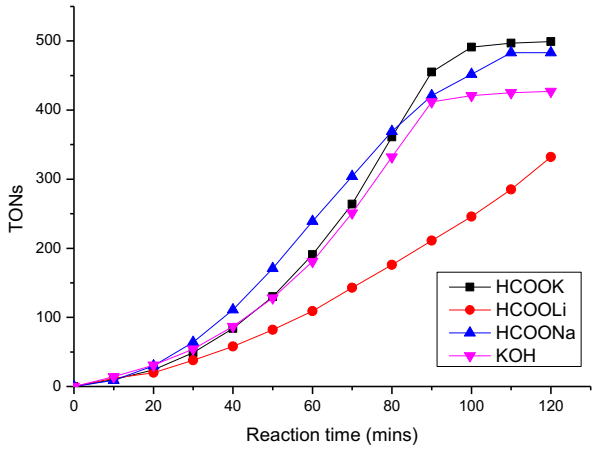

Figure 4.1: Influence of the nature of the formate alkali cation on FA dehydrogenation. **Conditions**: FA (5 mmol, 0.2 mL), **C10** (0.2 mol%, 0.01 mmol), formate salt or KOH (1 mmol), DMSO (2 mL), temperature (90 °C), total reaction volume (2.2 mL).

Under the reaction conditions shown in **Figure 4.2**, the amount of HCOOK added to the reaction was varied and affected the overall catalytic performance as increasing its quantity led to improved catalytic performance i.e. shorter reaction times. Increasing the HCOOK amount led to a TON of 521 for 3 mmol compared to TON = 130 for 1 mmol after 50 minutes of gas evolution. Increasing the HCOOK amount to 5 mmol led to a slight decrease in catalytic activity i.e. TON = 486 after 50 minutes. This result illustrates the often delicate pH balance required for efficient FA dehydrogenation. Interestingly, when 7 mmol equivalents of HCOOK were used, TONs greater than the maximum theoretical TON = 530 achievable were observed. This result was attributed to the dehydrogenation of formate ($HCOO^-$) upon full consumption of the available FA (5 mmol).

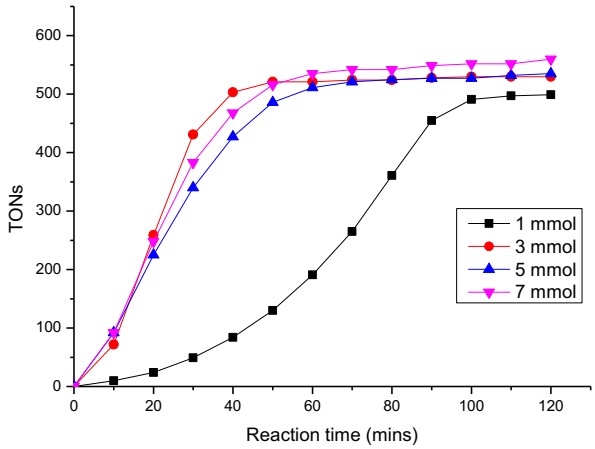

Figure 4.2: Influence of the equivalents of HCOOK on the activity of **C10** in FA dehydrogenation. **Conditions**: FA (5 mmol, 0.2 mL), **C10** (0.2 mol%, 0.01 mmol), HCOOK (as indicated), DMSO (2 mL), temperature (90 °C), total reaction volume (2.2 mL).

4.2.3 Effect of the nature and amount of solvent on FA dehydrogenation

Various organic solvent media such as tetrahydrofuran (THF), dioxane, and propylene carbonate usually affect the rate and extent of FA dehydrogenation.[19] Although the complex **C10** displayed good solubility in neat FA, no gas evolution was observed when the reaction mixture was heated from room temperature to 90 °C. **C10** was insoluble in some high boiling point solvents such as THF, 1,4-dioxane, and toluene and had good solubility in DMSO, DMF, and water. The catalytic activity of **C10** in various organic solvents was evaluated under the reaction conditions shown in **Figure 4.3**. The reaction performed in dry DMSO displayed the highest activity (TON = 521) compared to water (TON = 208) and dry DMF (TON = 36) after 50 minutes of gas evolution. The better catalytic activity of **C10** in DMSO was attributed to the solvent's strong coordinating nature, which plays a role in stabilizing the key intermediate species during the reaction.

A colour change of the reaction solution from orange to purple was observed when the reaction was performed in DMF and hinted at possible catalyst deactivation through the generation of off-cycle species which explains the poor activity of **C10** in DMF. Kawanami and coworkers studied the effects of different solvents on H_2 gas generation using ruthenium complexes.[19] They found that 1,4-dioxane was the best solvent for FA dehydrogenation followed closely by DMSO. Hence, the dehydrogenation of FA and its efficiency in various solvent media is highly catalyst-specific.

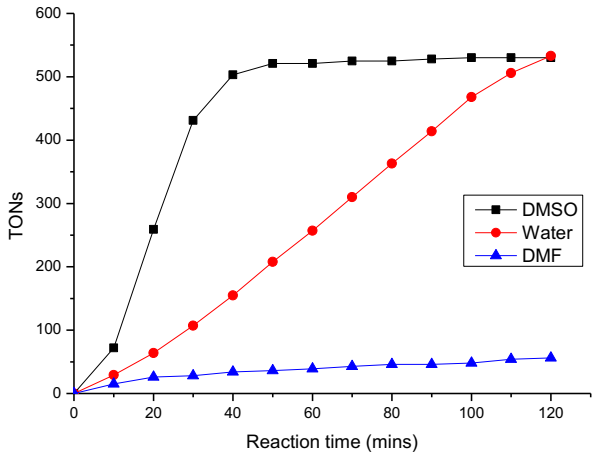

Figure 4.3: Influence of different solvents on the activity of **C10** in FA dehydrogenation. **Conditions**: FA (5 mmol, 0.2 mL), **C10** (0.2 mol%, 0.01 mmol), HCOOK (3 mmol), solvent (2 mL), temperature (90 °C), total reaction volume (2.2 mL).

The volume of the solvent in which **C10** exhibits good catalytic performance i.e. DMSO, was varied using the reaction conditions shown in **Figure 4.4**. Doubling the volume from 2 mL to 4 mL led to a noticeable decrease in activity with TON = 382 at 50 minutes compared to TON of 506 achieved with 2 mL of DMSO at the same time interval. This decrease in activity is attributed to concentration effects as increasing the overall reaction volume leads to fewer catalyst molecules interacting with the FA substrate. Hence, fewer effective collisions between the active catalytic species and FA occur per unit of time leading to a decreased reaction rate. In addition, a slightly longer induction period was observed for the reaction performed in 4 mL DMSO. Halving the solvent volume from 2 mL to 1 mL also decreased the catalytic activity as TON = 288 at 30 minutes of the reaction compared to TON = 394 for the reaction conducted in 2 mL DMSO. The decreased activity of **C10** was attributed to the poor solubility of the HCOOK additive in 1 mL DMSO even at 90 °C which resulted in a slightly longer time to convert the catalyst precursor to the active catalytic species. Like the reaction performed in 4 mL DMSO, a slightly longer induction period was observed for the reaction conducted in 1 mL DMSO owing to the poor homogeneity of the system. Hence, 2 mL of DMSO is necessary for optimal FA dehydrogenation using this ruthenium catalytic system.

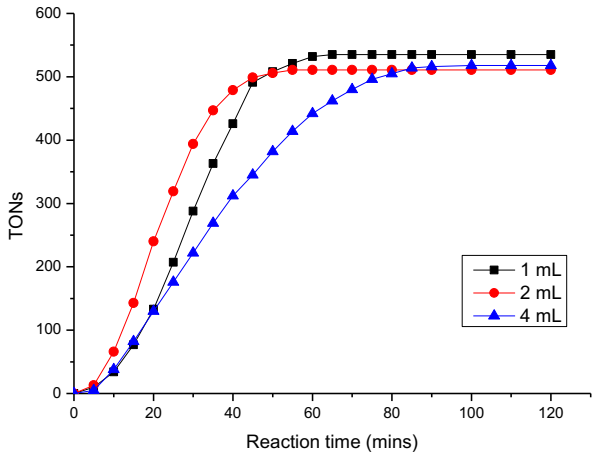

Figure 4.4: Influence of different DMSO volumes on the activity of **C10** in FA dehydrogenation. **Conditions**: FA (5 mmol, 0.2 mL), **C10** (0.2 mol%, 0.01 mmol), HCOOK (3 mmol), DMSO volume (as indicated), temperature (90 °C), total reaction volume (varies).

4.2.4 Effect of reaction temperature on FA dehydrogenation

Using catalyst **C10**, the dependence of our catalytic system on temperature was evaluated under the reaction conditions specified in **Figure 4.5**. No gas evolution was observed when the reaction was conducted at room temperature. Increasing the reaction temperature by 10 °C increments from 70 to 100 °C led to improved gas evolution rates. For example, at 70 °C, the TOF estimated using the first 20 minutes of the reaction increases to 34 hr^{-1} and increases to 181 hr^{-1}, 721 hr^{-1}, and 1220 hr^{-1} for reactions performed at 80 °C, 90 °C, and 100 °C, respectively. This observation was attributed to the increased kinetic energy of the molecules in the system at elevated temperatures, which led to more effective collisions between the molecules of the catalyst and FA thus, increasing the overall reaction rate. The system was not heated beyond 100 °C as this would favour the dehydration of FA leading to the formation of H_2O and unwanted CO, which is detrimental in fuel cell applications.[17]

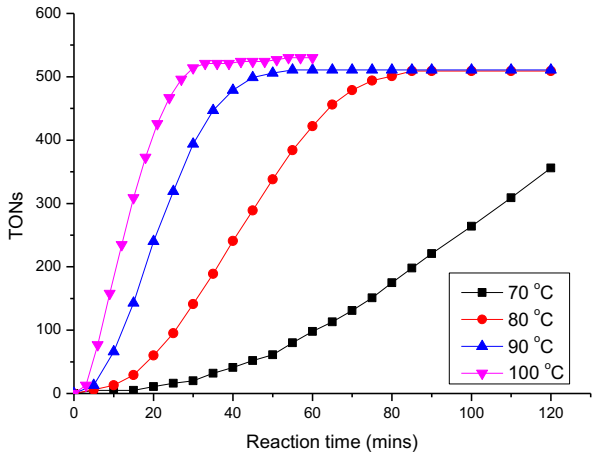

Figure 4.5: Influence of reaction temperature on the activity of **C10** in FA dehydrogenation. **Conditions**: FA (5 mmol, 0.2 mL), **C10** (0.2 mol%, 0.01 mmol), HCOOK (3 mmol), DMSO (2 mL), temperature (as indicated), total reaction volume (2.2 mL).

The activation energy (E_A) was obtained by measuring the initial rates of FA consumption from 70 to 100 °C under the reaction conditions shown in **Figure 4.5** above. A plot of the initial rates of FA consumption at different temperatures is provided in **Section 4.8.4**, **Figure S3**. Using the slope of the Arrhenius plot in **Figure 4.6** (a), the apparent activation energy was estimated to be 84 kJ/mol, within the range of FA dehydrogenation reactions catalyzed by other noble metals. The activation parameters $\Delta H^{\ddagger}$ = 81 kJ/mol and $\Delta S^{\ddagger}$ = -134 J/K/mol were calculated from the slope and y-intercept of the Eyring plot, respectively (**Figure 4.6** (b)). The highly negative entropy of activation value points towards an associative rate-determining step after corrections for electrostriction effects i.e. the interaction of a reaction intermediate with a molecule of FA.[20]

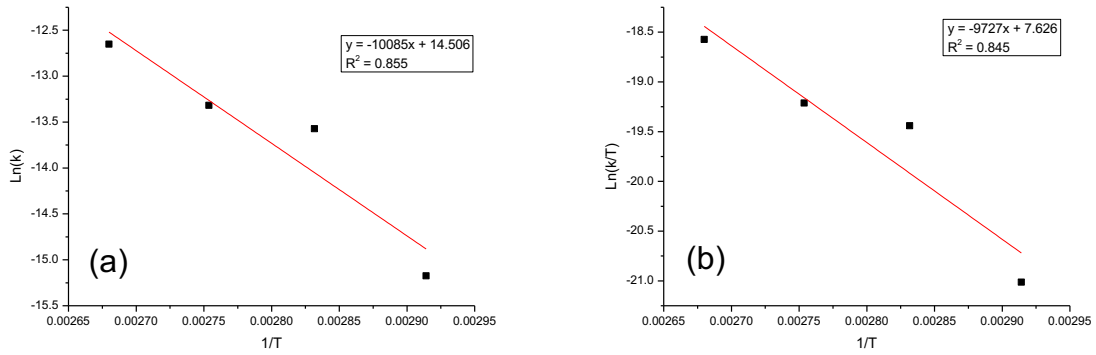

Figure 4.6: (a) Arrhenius plot and (b) Eyring plot based on FA consumption during the first 60 minutes of the reaction using **C10**.

4.2.5 Effect of catalyst and substrate concentration on FA dehydrogenation

Increasing the concentration of catalyst **C10** under the reaction conditions shown in **Figure 4.7** led to an expected increase in the rate of gas evolution. At elevated catalyst concentrations, more catalyst molecules per unit volume exist, leading to more effective collisions with the substrate molecules. Rate saturation is a phenomenon that is observed when increasing the catalyst concentration does not lead to improved reaction rates. This phenomenon will be examined in some detail in this section.

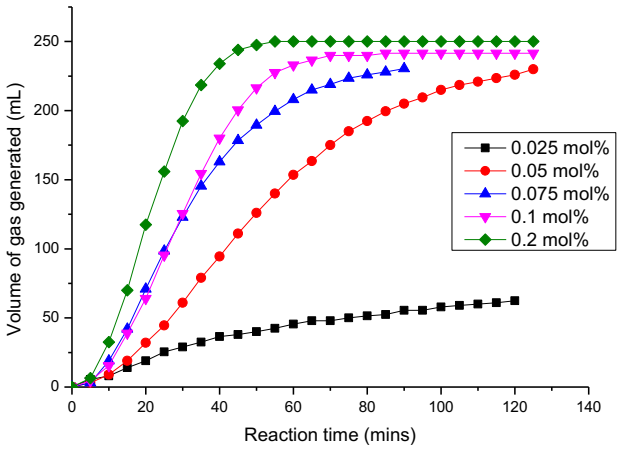

Figure 4.7: Influence of catalyst **C10** concentration on FA dehydrogenation. **Conditions**: FA (5 mmol, 0.2 mL), **C10** (as indicated), HCOOK (3 mmol), DMSO (2 mL), temperature (90 °C), total reaction volume (2.2 mL).

The double logarithmic plots of the initial rates of FA dehydrogenation (2.5 M, 0.2 mL) with the concentration of **C10** (0.025 – 0.1 mol%) illustrated a linear or first-order regime at low concentrations of **C10** (**Figure 4.8**). At higher catalyst concentrations, i.e. 0.2 mol%, the dehydrogenation of FA follows zero-order kinetics indicating possible rate saturation. The attained reaction order of 1.30 for the catalyst loading implies that the monomeric species of **C10** generated during the initial reaction period are the most active species involved in FA dehydrogenation and that dimeric catalyst species are not involved in the reaction.[21] In addition, it is accordant with the possible involvement of Ru-formato species in the catalytic cycle for the dehydrogenation of FA.[22] A plot of the initial rates of FA dehydrogenation at different catalyst concentrations is supplied in **Section 4.8.4**, **Figure S4**.

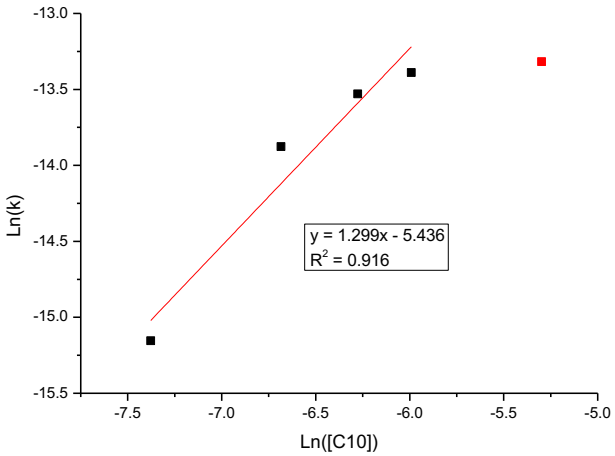

Figure 4.8: Rate order determination from the plot of Ln(k) vs Ln([**C10**]). **Conditions**: FA (5 mmol, 0.2 mL), **C10** (0.025 – 0.2 mol%), HCOOK (3 mmol), DMSO (2 mL), temperature (90 °C), total reaction volume (2.2 mL).

The effect of changing the substrate concentration on FA dehydrogenation was studied by varying the amount of FA added into the catalyst system using the reaction conditions shown in **Figure 4.9**. As shown, increasing the volume of FA added into the system undermined the efficiency of FA dehydrogenation. This indicates dilution effects as increasing the volume of FA effectively decreases concentration in the reaction solution. As a result, fewer molecules interact with the per unit of time leading to slower reaction rates.

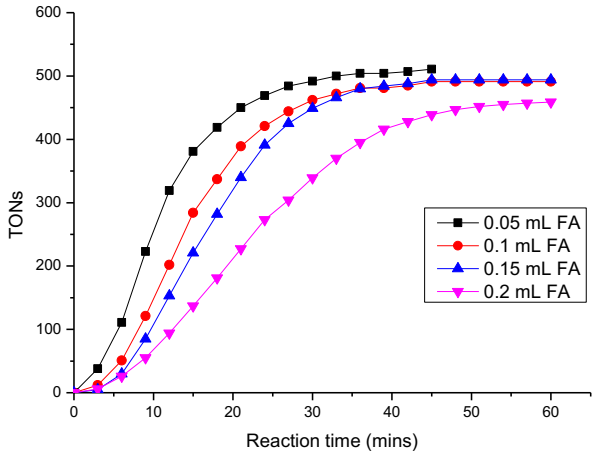

Figure 4.9: Influence of FA concentration on the activity of **C10** in FA dehydrogenation. **Conditions**: FA (as indicated), **C10** (0.2 mol%), HCOOK (3 mmol), DMSO (2 mL), temperature (90 °C), total reaction volume (2.05 – 2.2 mL).

From the double logarithmic plot of the initial rates of FA dehydrogenation to FA concentration in **Figure 4.10**, a linear or first-order dependence was deduced, i.e., increasing FA concentration leads to improved FA dehydrogenation. A plot of the initial rates of FA consumption at different FA concentrations is provided in **Section 4.8.4**, **Figure S5**. Beller and coworkers examined the influence of FA concentration on FA dehydrogenation catalyzed by an iron catalyst.[21] A positive broken reaction order of 0.44 was attained and it was concluded that only one FA molecule interacts with the iron catalyst. In addition, it was established that an equilibrium exists between the Fe catalyst + HCOOH and the [Fe-COOH] species. Based on the observed reaction order of 0.963 for our system, it can be concluded that no preequilibrium exists between catalyst **C10** and FA/formate *viz*. instant coordination of a molecule of FA/formate to the Ru metal center to afford [HCOO-Ru] species.

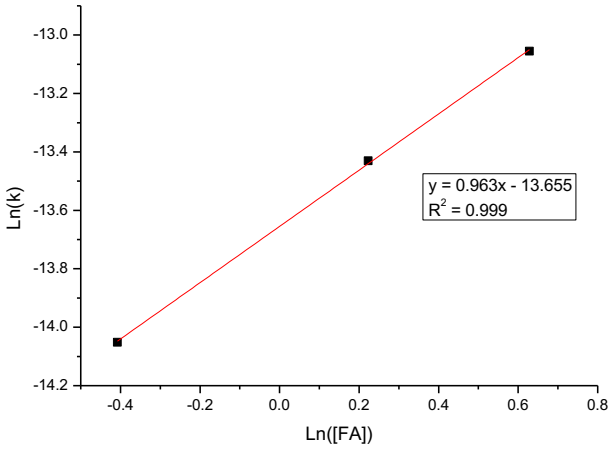

Figure 4.10: Rate order determination from the plot of Ln(k) vs Ln([FA]). **Conditions**: FA (0.05 – 0.15 mL), **C10** (0.2 mol%), HCOOK (3 mmol), DMSO (2 mL), temperature (90 °C), total reaction volume (2.05 – 2.2 mL).

4.2.6 Effect of Ru complex counterion on FA dehydrogenation

Slight modifications were introduced to the most active complex **C10** by exchanging the Cl anion to yield complexes **C19** and **C20** bearing BPh_4 and PF_6 anions, respectively. Under the reaction conditions shown in **Figure 4.11**, the introduction of these anions surprisingly did not affect the performance of the complexes toward FA dehydrogenation. It would be expected that the larger anion i.e. BPh_4 would exert a significant steric influence which results in poor interaction between the substrate and the Ru metal centre, reflected in diminished catalytic activity compared to the complexes bearing the smaller Cl and PF_6 anions. This result is attributed to the high dielectric constant, ε = 46.83 of DMSO that often leads to the formation

of either solvent-separated or solvent-shared ion pairs between the complexes cation and anion.[23] It is anticipated that the effect of the different Ru(II) complex counterions towards FA dehydrogenation will be more pronounced for reactions conducted in low dielectric constant (ε < 10) solvents due to the formation of contact ion pairs (CIPs). Investigations into the different types of ion pairs formed in different solvent media are beyond the scope of this study.

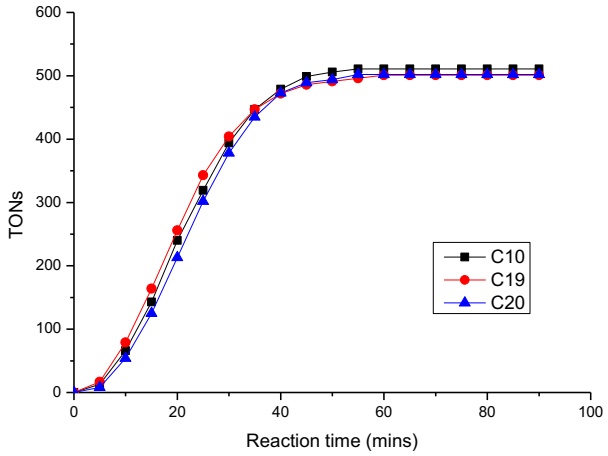

Figure 4.11: Influence of nature of complex counterion on FA dehydrogenation using complexes **C10**, **C19**, and **C20**. **Conditions**: FA (5 mmol, 0.2 mL), **C10**, **C19**, and **C20** (0.2 mol%, 0.01 mmol), HCOOK (3 mmol), DMSO (2 mL), temperature (90 °C), total reaction volume (2.2 mL).

4.3 Long-term catalyst performance under optimized reaction conditions

To determine the reusability and long-term stability of catalyst **C10** for large-scale H_2 production, fresh batches of 0.1 mL FA were added to the reaction solution in 30-minute intervals, i.e., time taken to consume the initial amount of FA added into the system. Under the optimized reaction conditions shown in **Figure 4.12**, the total volume of gas generated decreased with each FA refill. During the reaction, the TOFs of about 1636 hr^{-1} were attained at the end of the initial addition and halved to 837 hr^{-1} at the end of the sixth refill. This drastic reduction in activity can be attributed to possible catalyst deactivation due to pH changes associated with the consumption of the substrate and further drastic pH changes during FA refills. **Figure 4.12**(b) illustrates the stepwise addition of 0.1 mL FA batches as a plot of TONs versus total reaction time. From this plot, a plateau of the rate of generated TONs with an increase in reaction time indicates the deactivation of **C10** with each addition of fresh FA.

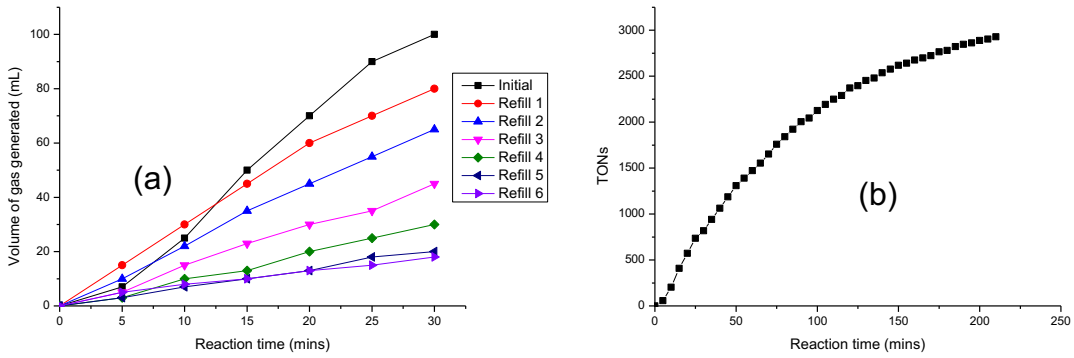

Figure 4.12: (a) Stacked plots of the gas evolution upon repetitive FA addition with t = 0 mins for each addition (b) Influence of repeated FA injections on FA dehydrogenation. **Conditions**: FA (2.5 mmol, 0.1 mL), **C10** (0.1 mol%, 0.0025 mmol), HCOOK (3 mmol), DMSO (2 mL), temperature (90 °C), total reaction volume (2.1 mL).

To further explore the robustness of catalyst **C10**, FA was continually introduced using an automatic syringe pump at the rate of its consumption i.e. 0.01 mL/min. Under these reaction conditions, the catalytic rate decreased with time with TOFs of 540 hr^{-1} reached in the first hour of the reaction decreasing to 199 hr^{-1} after 5 hours. **Figure 4.13** indicates the plateau in the generated turnover numbers as a function of time with maximum TONs of 1009 after 5 hours under the optimized reaction conditions. These results further reinforce the pH sensitivity of catalyst **C10** when DMSO is employed as a solvent medium.

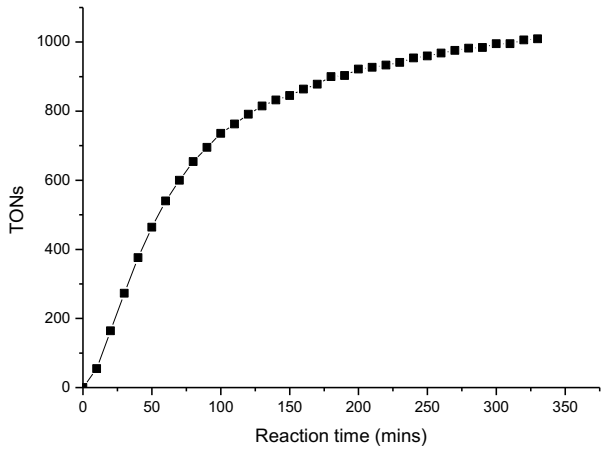

Figure 4.13: FA dehydrogenation with **C10** (0.1 mol%, 0.0075 mmol) in DMSO (6 mL) starting from a mixture of FA (7.5 mmol) and HCOOK (9 mmol) at 90 °C under continuous FA addition conditions. FA addition at 0.01 mL/min.

4.4 Mechanistic considerations in DMSO: ^{1}H NMR Spectroscopy and KIE

The elucidation of reaction mechanisms for catalytic processes is crucial in the research and development of new catalyst systems. The identification of key intermediate species in a catalytic cycle can provide significant insight into catalyst behavior and thus become helpful in rational catalyst design. A series of ^{1}H NMR monitoring experiments were conducted to gain structural insights into the mechanism of FA dehydrogenation using Ru catalyst **C10**, specifically the decarboxylation step en route to forming the Ru-hydride species. No formation of Ru-hydride species was observed when catalyst **C10** was dissolved in DMSO-d_6 at room temperature. Similarly, no hydride signals were observed from the reaction of **C10** with HCOOK i.e. catalyst to formate = 1:1 in DMSO-d_6 at room temperature. The reaction solution inside a high-pressure J-Young NMR tube was heated to 90 °C in a water bath and NMR spectra were collected at selected time intervals using the reaction conditions shown in **Figure 4.14**. Under these non-catalytic reaction conditions, the presence of several ^{1}H NMR signals in the region δ = -11 to -14.5 ppm indicative of Ru-hydride species was noted. The presence of several hydride species is likely due to competing equilibria under these reaction conditions. The signal at δ = -14.5 ppm was assigned to a Ru(II)-(η^2-CO_2) hydride complex, consistent with literature precedent, which is related to a [Ru(tppts)$_2$H(η^2-CO_2)(H_2O)$_2$] complex.[24] **Figure 4.25** in **Section 4.8.3** of this chapter illustrates the structural variations in the catalyst during hydride formation under these reaction conditions.

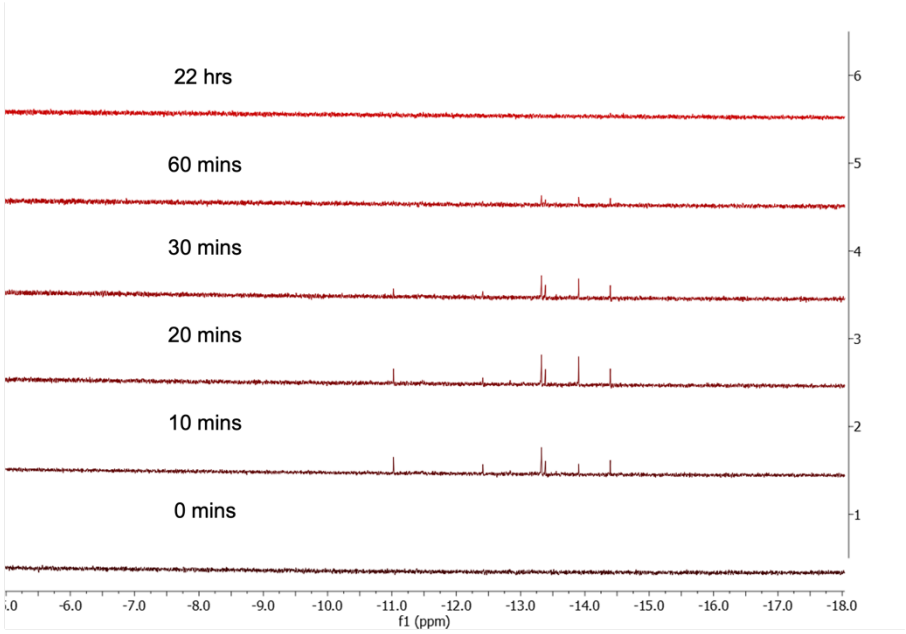

Figure 4.14: Stacked ^{1}H NMR spectra (hydride region) of **C10** in DMSO-d_6 at various time intervals. **Conditions**: **C10** (10.7 mg), HCOOK (1.8 mg), DMSO-d_6 (0.7 mL), MeOD (0.3 mL), probe temperature = 300 K, spectral width = 150 ppm.

Next, the catalyst-to-formate ratio was increased to catalytically relevant ratios i.e. 1:50 and the reaction was monitored at the time intervals shown in **Figure 4.15**. An intense ^{1}H NMR signal was observed at δ = -11 ppm as the major Ru-hydride species during the reaction of **C10** with HCOOK in DMSO-d_6 at 90 °C and identified as the key Ru-monohydride species involved in the catalytic cycle for the dehydrogenation of FA. A similar observation was made by the independent research groups of Huang and Laurenczy.[24,25] **Figure 4.26** in **Section 4.8.3** of this chapter outlines the structural variations in the catalyst during hydride generation under these reaction conditions.

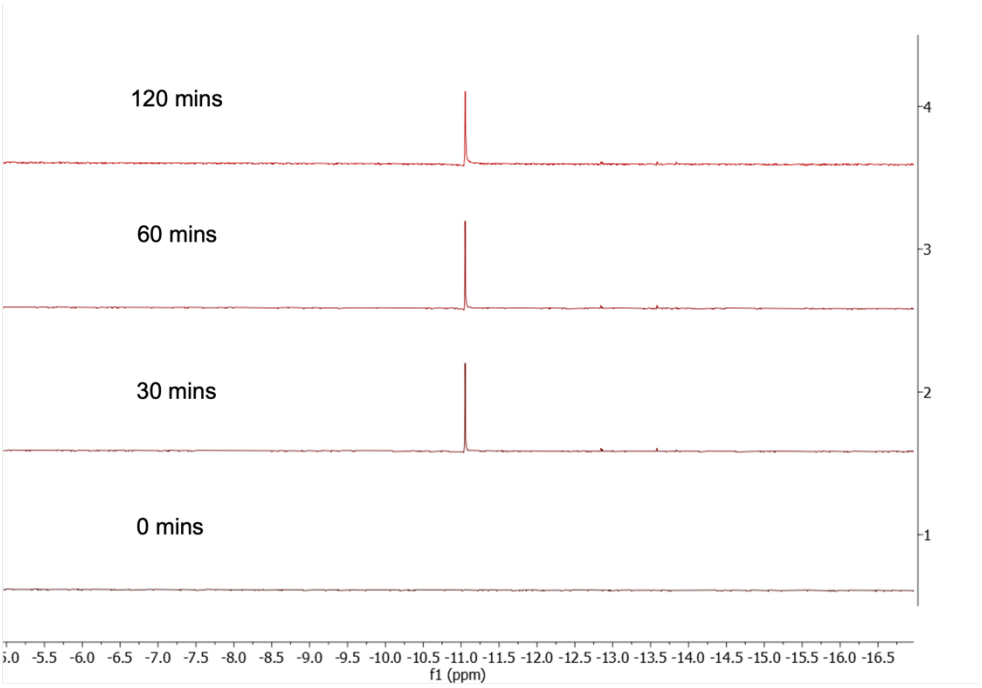

Figure 4.15: Stacked ^{1}H NMR spectra (hydride region) of **C10** in DMSO-d_6 at various time intervals. **Conditions**: **C10** (10.1 mg), HCOOK (86.9 mg), DMSO-d_6 (0.7 mL), MeOD (0.3 mL), probe temperature = 300 K, spectral width = 150 ppm.

Further, kinetic isotope effect (KIE) studies were conducted to gain deeper insight into the catalytic process of FA dehydrogenation over complex **C10** (**Table 4.2)**. Triethylamine (NEt_3) was employed as the additive to avoid deuterium scrambling. Replacing HCOOH with DCOOH had a minimal effect on the reaction rate with KIE = 1.2 (**Table 4.2**, entry 2). Employing DCOOD as the substrate led to a more pronounced decrease in the reaction rate with KIE = 2.1 (**Table 4.2**, entry 3). These results inferred that the rate-determining step likely involves the cleavage of the formyl C-H bond with decarboxylation of the Ru-formato species and the generation of Ru-hydrido species. The observed trend corroborates well with the literature precedent for reactions performed in DMSO.[10]

Table 4.2: KIE in the dehydrogenation of FA over catalyst **C10** in DMSO.[a]

Entry	Catalyst	Substrate	Solvent	TOF (hr^{-1})[b]	KIE[c]
1	**C10**	HCOOH	DMSO	115	-
2	**C10**	DCOOH	DMSO	100	1.2
3	**C10**	DCOOD	DMSO	54	2.1

[a] **Conditions**: FA (1.33 mmol, 0.05 mL), **C10** (0.2 mol%, 0.00266 mmol), NEt_3 (1 mmol), DMSO (1 mL), temperature (80 °C). [b] TOF measured at 30 mins. [c] Kinetic isotope effect = $TOF_{HCOOH}/TOF_{isotopologue}$).

Based on these observations, a tenable reaction pathway for the dehydrogenation of FA is proposed (**Scheme 4.3**). The formate-coordinated ruthenium complex **IN2** is generated from the chlorinated ruthenium complex **IN1**. The decarboxylation of formate in the Ru-formato complex **IN2** affords the key proposed Ru-hydrido complex **IN3** which is the catalyst resting state. H_2 is generated upon the interaction of a molecule of FA with **IN3** which completes the catalytic cycle.

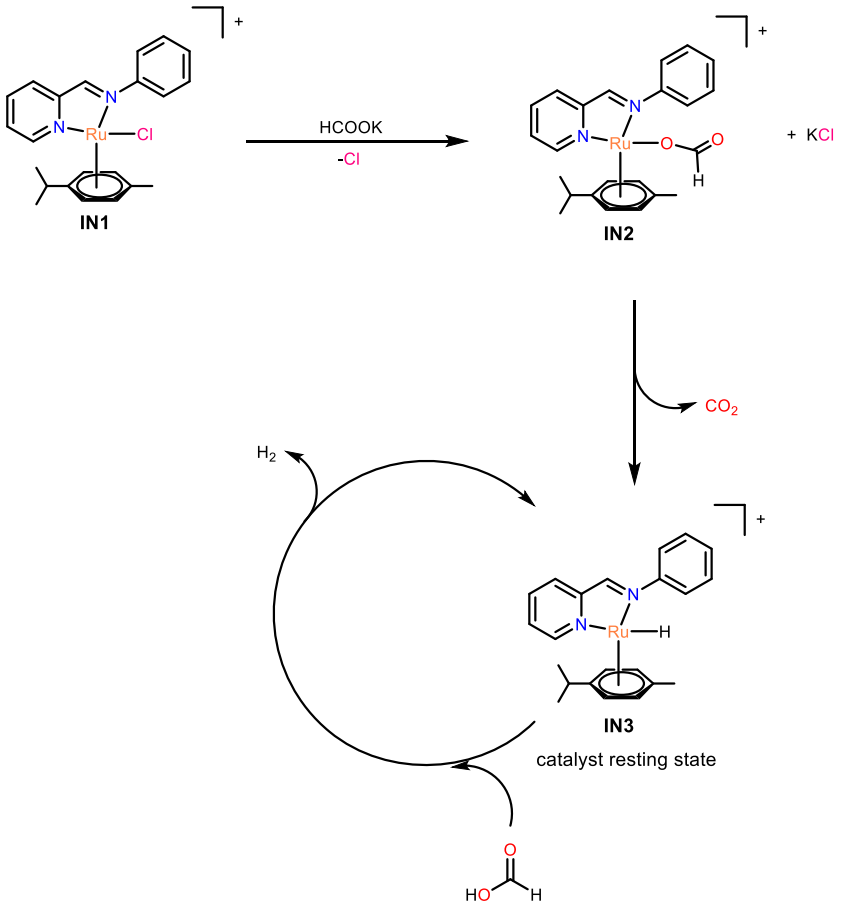

Scheme 4.3: Proposed reaction mechanism for FA dehydrogenation over **C10** in DMSO.

4.5 Insights into FA dehydrogenation in water

As shown in **Section 4.2.3, Figure 4.3**, catalyst **C10** displayed good solubility and activity toward FA dehydrogenation using water as a solvent, reaching TON = 530 after 2 hours. Prompted by these findings and the lack of literature reports detailing the use of water-soluble pyridylimine Ru(II) complexes for FA dehydrogenation, we further evaluated the performance of **C10** using water as a solvent medium. Several reaction parameters such as temperature, catalyst loading, and substrate concentration were varied, and key kinetic data such as the activation parameters (E_A, $\Delta H^{\ddagger}$, and $\Delta S^{\ddagger}$) and reaction order with respect to catalyst and substrate concentration, were ascertained. Moreover, the performance and reusability of **C10** over extended reaction times under these conditions were determined.

The influence of temperature on FA dehydrogenation was studied by varying the reaction temperature from 70 – 100 °C under the reaction conditions shown in **Figure 4.16**. Each temperature increment was accompanied by an increase in the catalytic activity of **C10** i.e. TOFs measured after 20 minutes of gas evolution increased to 34 hr^{-1} at 70 °C and increased to 67 hr^{-1}, 163 hr^{-1}, and 362 hr^{-1} for the reactions conducted at 80 °C, 90 °C, and 100 °C, respectively. For the catalytic reaction performed at 100 °C, the experimental setup was fitted with a condenser to avoid the evaporation of H_2O. As in the experiments performed in DMSO, the system was not heated beyond 100 °C to avoid favoring the pathway of FA dehydration which leads to the formation of H_2O and unwanted CO.

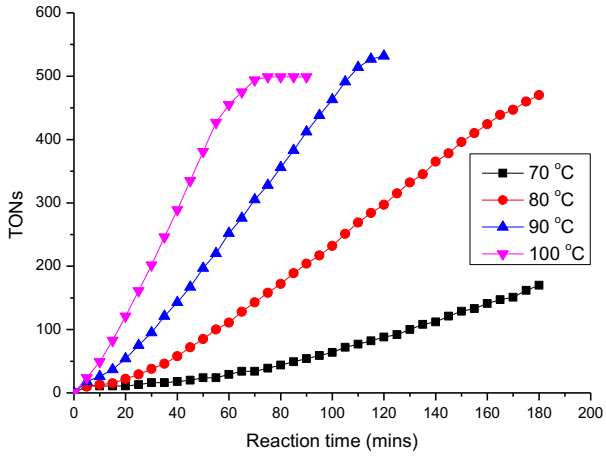

Figure 4.16: Influence of reaction temperature on the activity of **C10** in FA dehydrogenation. **Conditions**: FA (5 mmol, 0.2 mL), **C10** (0.2 mol%, 0.01 mmol), HCOOK (3 mmol), H_2O (2 mL), temperature (as indicated), total reaction volume (2.2 mL).

The activation energy (E_A) was calculated by taking the slope between the initial rates of FA consumption and the varied reaction temperatures (70 – 100 °C). A plot of the initial rates of FA consumption under these reaction conditions is provided in **Section 4.8.4**, **Figure S6**. The estimated apparent E_A by the Arrhenius plot (**Figure 4.17** (a)) was 108 kJ/mol. The attained activation energy for the reaction performed in water is approximately 24 kJ/mol higher than the E_A calculated from the reaction performed using DMSO as the solvent. This result further corroborates an earlier observation of solvent-dependent catalytic FA dehydrogenation, in which DMSO outperforms water (**Figure 4.3**). From the Eyring analyses (**Figure 4.17** (b)), the activation parameters $\Delta H^{\ddagger}$ = 105 kJ/mol and $\Delta S^{\ddagger}$ = -75 J/K/mol were calculated using the slope and the y-intercept, respectively. As highlighted earlier, a negative $\Delta S^{\ddagger}$ value indicates an associative rate-determining step such as the interaction of a molecule of FA and a reaction intermediate.

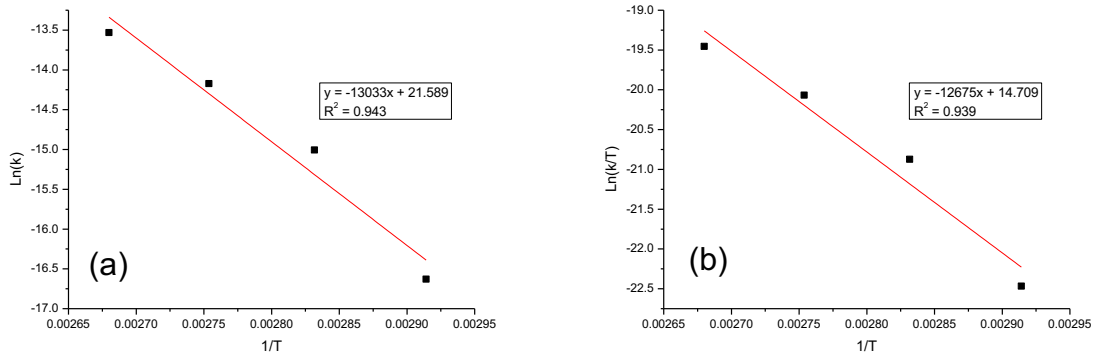

Figure 4.17: (a) Arrhenius plot and (b) Eyring plot based on FA consumption during the first 60 minutes of the reaction using **C10**.

The influence of catalyst loading on FA dehydrogenation in a water medium was evaluated by varying the concentration of **C10** as illustrated in **Figure 4.18**. As in the reactions performed in DMSO, the catalyst concentration varied from 0.025 to 0.2 mol% and was accompanied by an increase in the generation of the gas mixture. Unlike in DMSO, rate saturation was not observed at higher catalyst concentrations under these reaction conditions. Similarly, the increase in reaction rate is attributed to the presence of more catalyst molecules per unit volume that are involved in effective collisions with FA thus enhancing gas evolution.

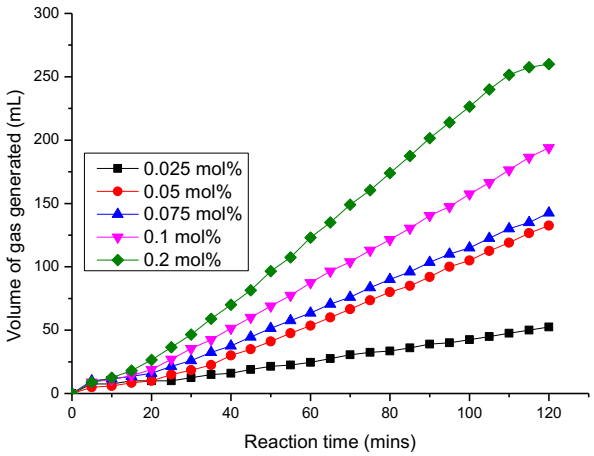

Figure 4.18: Influence of catalyst **C10** concentration on FA dehydrogenation. **Conditions**: FA (5 mmol, 0.2 mL), **C10** (as indicated), HCOOK (3 mmol), H_2O (2 mL), temperature (90 °C), total reaction volume (2.2 mL).

Figure 4.19 illustrates the double logarithmic plot of the initial rates of FA consumption with the concentration of catalyst **C10** (0.025 – 0.1 mol%). A plot of the initial rates of FA dehydrogenation under these reaction conditions is provided in **Section 4.8.4**, **S7**. A linear dependence (reaction order = 0.92) can be deduced and illustrates the generation of the monomeric species of **C10** during the initial reaction period as the most active catalytic species and the absence of dimeric species during the catalytic dehydrogenation of aqueous FA.[20] Moreover, it agrees with the involvement of Ru-formato species in the catalytic cycle for FA dehydrogenation.[21]

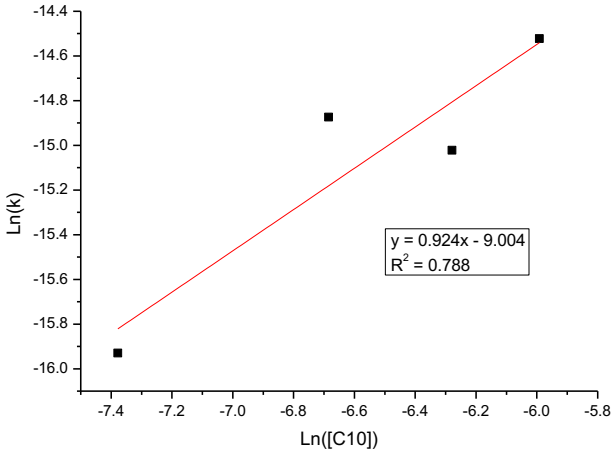

Figure 4.19: Rate order determination from the plot of Ln(k) vs Ln([**C10**]). **Conditions**: FA (5 mmol, 0.2 mL), **C10** (0.025 – 0.1 mol%), HCOOK (3 mmol), H_2O (2 mL), temperature (90 °C), total reaction volume (2.2 mL).

The influence of FA concentration on FA dehydrogenation was evaluated by varying the volume of FA injected into the reaction solution as shown in **Figure 4.20**. Increasing the volume of FA added led to significantly longer reaction times and this result was attributed to dilution effects at higher volumes that effectively decrease the concentration in the reaction solution. As in DMSO, increasing the concentration of FA in water-mediated FA dehydrogenation led to improved gas evolution rates.

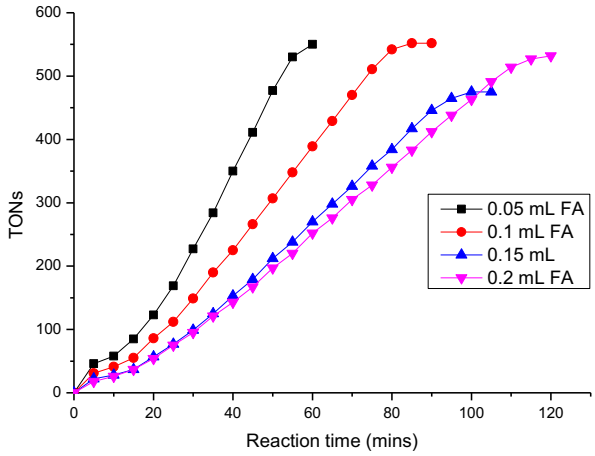

Figure 4.20: Influence of FA concentration on the activity of **C10** in FA dehydrogenation. **Conditions**: FA (as indicated), **C10** (0.2 mol%), HCOOK (3 mmol), H_2O (2 mL), temperature (90 °C), total reaction volume (2.05 – 2.2 mL).

From the double logarithmic plot of the initial rates of FA consumption with the concentration of FA (0.05 – 0.2 mL), a positive reaction order of 0.306 was obtained (**Figure 4.21**). A plot of the initial rates of FA dehydrogenation under these reaction conditions is provided in **Section 4.8.4**, **Figure S8**. Interestingly, performing the catalytic reaction using water as a solvent medium leads to the existence of a preequilibrium between the Ru catalyst and FA as well as the interaction of FA or formate ions with the Ru metal center. Usually, half-order reaction kinetics with respect to FA concentration indicate equimolar interaction of the FA substrate with the Ru complex.[12,21] This difference in Ru-FA interactions is also reflected in the more positive $\Delta S^{\ddagger}$ value in water ($\Delta S^{\ddagger}$ = -134 J/K/mol in DMSO) and implies divergent species participating in the hydrogen-formation step. Our data suggests that FA is involved in the hydrogen formation step in DMSO[10] whereas hydronium (H_3O^+) ions are involved when generating H_2 in water.[25]

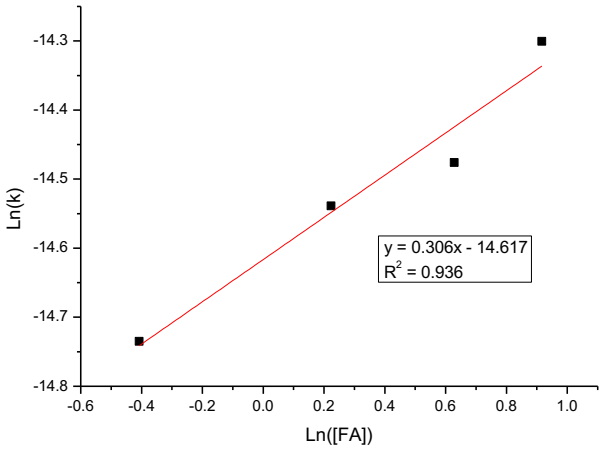

Figure 4.21: Rate order determination from the plot of Ln(k) vs Ln([FA]). **Conditions**: FA (0.05 – 0.2 mL), **C10** (0.2 mol%), HCOOK (3 mmol), H_2O (2 mL), temperature (90 °C), total reaction volume (2.05 – 2.2 mL).

KIE studies were conducted to better understand the role of formate activation versus hydrogen evolution on the rate of FA dehydrogenation (**Table 4.3**). The observed trend in KIE measurements indicated that d_2-formic acid (DCOOD) was more influential than D_2O on the reaction rate for FA dehydrogenation over **C10** under the reaction conditions in **Table 4.3**. These results inferred that the rate-determining step involved the decarboxylation of the Ru-formato species to yield the Ru-hydrido species, rather than the proton (H^+) assisted hydrogen gas evolution.[26,27] The dehydrogenation of FA in the presence of DCOOD and/or D_2O may involve a complex combination of reaction kinetics, equilibria, and isotope exchange processes, leading to the slightly low KIE values shown in **Table 4.3**. Nonetheless, the obtained data followed the literature precedent and indicated the cleavage of the formyl C-H bond with decarboxylation. For instance, Himeda and coworkers reported a KIE of 1.6 when D_2O replaced H_2O and a KIE of 2.3 when DCOOD replaced HCOOH.[28]

Table 4.3: KIE in the dehydrogenation of FA over catalyst **C10** in H_2O.[a]

Entry	Catalyst	Substrate	Solvent	TOF[b]	KIE[c]
1	**C10**	HCOOH	H_2O	375	-
2	**C10**	HCOOH	D_2O	329	1.1
3	**C10**	DCOOD	H_2O	231	1.6
4	**C10**	DCOOD	D_2O	202	1.9

Conditions: substrate (1.33 mmol, 0.05 mL), **C10** (0.2 mol%, 0.00266 mmol), NEt_3 (1 mmol), solvent (1 mL), temperature (80 °C). [b] TOF measured at 40 minutes. [c] Kinetic isotope effect = $TOF_{HCOOH}/TOF_{isotopologue}$).

Based on these observations, a probable reaction mechanism for the dehydrogenation of FA is proposed (**Scheme 4.4**). The catalytic cycle starts from the water-coordinated ruthenium complex **IN2A**, which is generated from the chlorinated complex **IN1A** in the aqueous FA solution. Next, the coordination of a formate anion at the Ru metal center displaces the H_2O ligand to afford the Ru-formato intermediate species **IN3A**. The decarboxylation of formate in **IN3A** leads to the generation of the key proposed Ru-hydride intermediate **IN4A**. Lastly, the ruthenium aqua complex **IN2A** is regenerated with the production of H_2 in the presence of hydronium ions (H_3O^+), which completes the catalytic cycle.

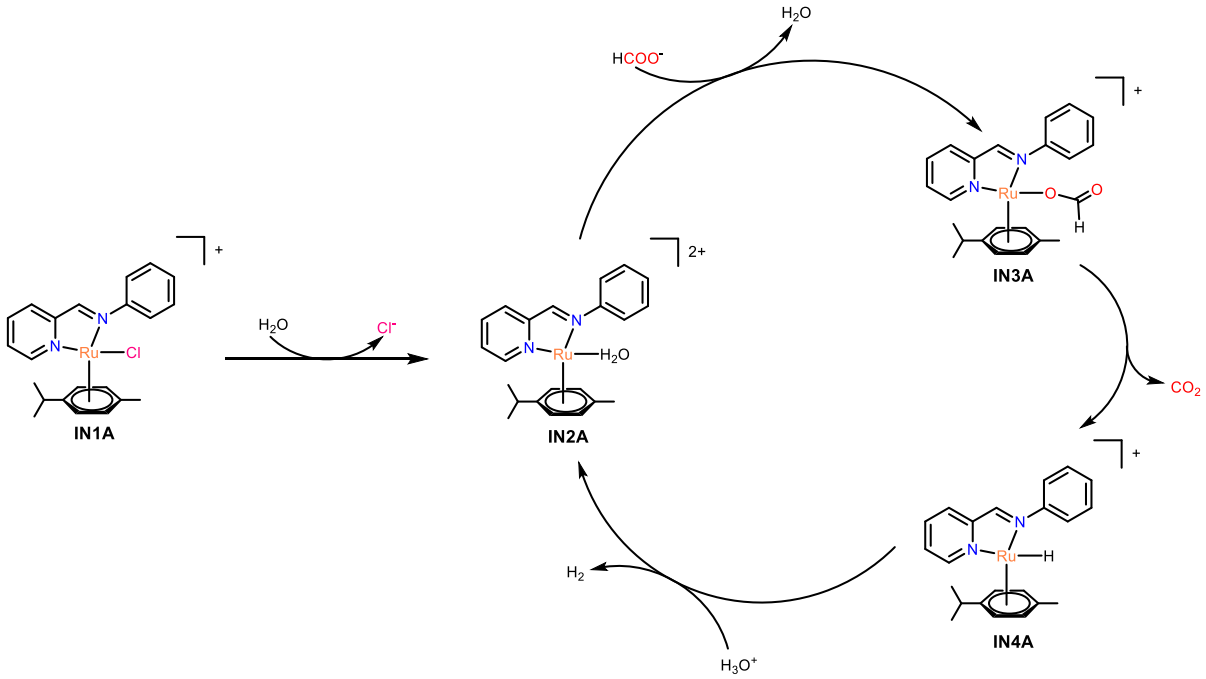

Scheme 4.4: A plausible reaction pathway for the dehydrogenation of FA over **C10** in water.

To determine the reusability of catalyst **C10** for long-term and large-scale FA dehydrogenation, the catalyst was subjected to repeated 0.1 mL FA injections every 80 minutes under the reaction conditions shown in **Figure 4.22**. To our delight, **C10** could dehydrogenate 0.1 mL batches of FA for six cycles without losing activity, achieving TONs = 6748 at the end of refill 6. TOFs of 682 hr^{-1} were obtained after complete dehydrogenation of the initial FA addition and amounted to 698 hr^{-1} at the end of the sixth refill of FA, illustrating the retained activity of **C10** with each FA injection. This sustained catalytic activity can be attributed to the ability of **C10** to withstand rigorous pH changes associated with the addition and/or consumption of the FA substrate in a water solvent medium. **Figure 4.22** (b) demonstrates the repeated addition of FA as a plot of TONs over the evaluated total reaction time. The plot shows a linear increase in the TONs with increasing reaction time without a plateau of the reaction rate.

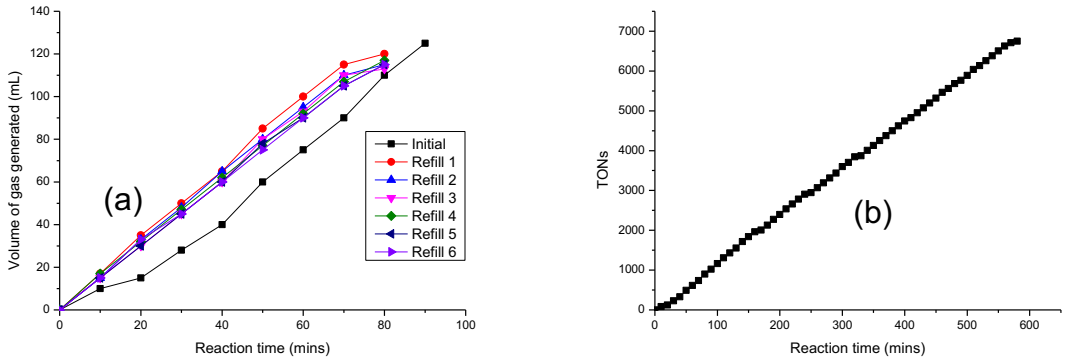

Figure 4.22: (a) Stacked plots of the gas evolution upon repetitive FA addition with t = 0 mins for each addition. (b) Influence of repeated FA injections on FA dehydrogenation. **Conditions**: FA (2.5 mmol, 0.1 mL), **C10** (0.1 mol%, 0.0025 mmol), HCOOK (3 mmol), H_2O (2 mL), temperature (90 °C), total reaction volume (2.1 mL).

The suitability of catalyst **C10** for long-term applications was evaluated by injecting FA at a constant rate (0.005 mL/min) equal to its consumption rate in the reaction. Under the optimized reaction conditions shown in **Figure 4.23**, catalyst **C10** was able, although with diminished catalytic activity (TOF = 36 hr^{-1}), to catalyze the dehydrogenation of FA for over 31 hours. These results further reinforce the increased stability of the catalytic species of **C10** in water. The decreased catalytic activity under these conditions is likely due to the reaction not proceeding at the desired pH range i.e. highly basic conditions due to the presence of excess HCOOK.

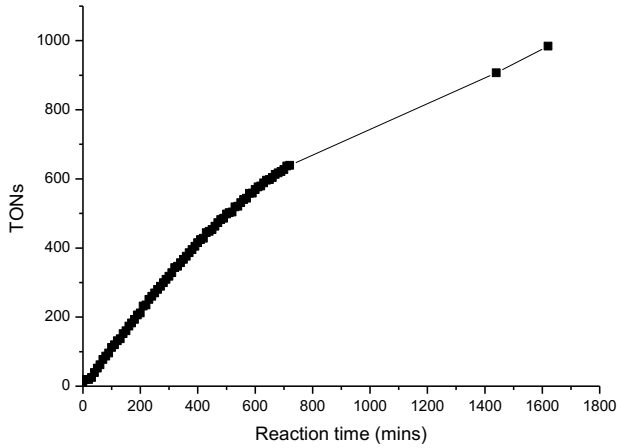

Figure 4.23: FA dehydrogenation with **C10** (0.1 mol%, 0.0106 mmol) in H_2O (8 mL) starting from a mixture of FA (10 mmol) and HCOOK (12 mmol) at 90 °C under continuous FA addition conditions. FA addition at 0.005 mL/min.

4.6 Comparing catalyst performance with reported catalytic systems

In this section, the performance of Ru catalyst **C10** toward FA dehydrogenation is compared with reported ruthenium complexes operated under similar reaction conditions. **Table 4.4** summarizes the catalytic performance of the existing literature work and compares it to the work presented in this study. Huang and coworkers reported on a highly effective Ru complex **LXXIII** that achieved maximum TONs of 1 100 000 in DMSO after 150 hours (**Table 4.4**, entry 3).[29] Ru(II) catalyst **C10** indicated promising catalytic activity (TOF = 1636 hr^{-1}) in DMSO but was prone to deactivation over time (**Table 4.4**, entry 1). The results obtained with **LXXIII** indicate the importance of tridentate ligands in stabilizing catalyst systems which in turn leads to high catalytic activity and stability over longer reaction times. Catalyst **C10** was reasonably active (TOF = 698 hr^{-1}) in H_2O reaching TONs of about 6748 after 10 hours (**Table 4.4**, entry 2). However, **C10** still lags behind some of the reported catalyst systems that are soluble and active for FA dehydrogenation in water. For instance, Singh and coworkers reported a Ru complex **LXXIV** that attained similar TONs (6050) in only 15 minutes (**Table 4.4**, entry 4).[12] In another report, Singh and coworkers illustrated a Ru catalyst system **LXXV** that reached 2248 turnover numbers in 15 minutes with reasonably high TOF = 940 hr^{-1} (**Table 4.4**, entry 5).[30] The current state-of-the-art Ru catalyst **LXXVI** (TON = 350 000 and TOF = 12 000 hr^{-1}) concerning the dehydrogenation of FA in water was reported by Huang and coworkers (**Table 4.4**, entry 6).[25] **Figure 4.24** shows the molecular structures of the reported catalyst systems.

Table 4.4: Comparing previous literature work with current work for FA dehydrogenation.

Entry	Catalyst	Substrate	Solvent	Time (hr)	TON	TOF (hr^{-1})
1	**C10**	FA/HCOOK	DMSO	3	3000	1636
2	**C10**	FA/HCOOK	H_2O	10	6748	698
3	**LXXIII**	FA/NEt_3	DMSO	150	1100000	7300
4	**LXXIV**	FA/HCOONa	H_2O	0.25	6050	1548
5	**LXXV**	FA/HCOONa	H_2O	0.25	2248	940
6	**LXXVI**	FA/HCOONa	H_2O	29	350000	12000

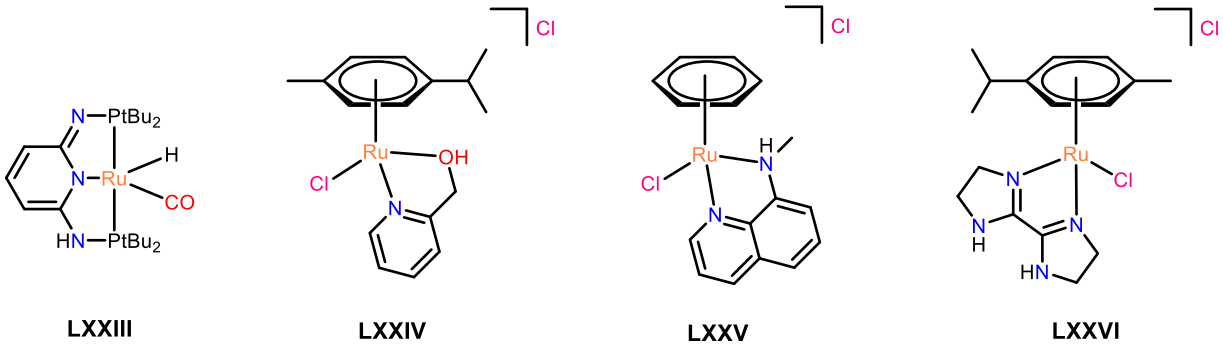

LXXIII **LXXIV** **LXXV** **LXXVI**

Figure 4.24: Reported ruthenium complexes for FA dehydrogenation.

4.7 Conclusions

A panel of cationic, half-sandwich pyridylimine ruthenium(II) complexes (**C10** – **C20**) were evaluated and found to be prolific catalyst precursors for the base or formate-assisted dehydrogenation of FA. The ligand framework had a marked influence on the reactivity of the precatalysts. Mainly, catalysts bearing an aromatic substituent on the imine nitrogen displayed good catalytic activity compared to catalysts with aliphatic substituents. Parameters such as the nature and amount of formate as well as the solvent type and its amount were found to affect the efficiency of FA dehydrogenation and optimized accordingly. Varying the counterion on the cationic complexes had no apparent effect on the rate and extent of FA dehydrogenation. Complex **C10** was soluble and active for FA dehydrogenation using water as the solvent medium. Extensive kinetic studies with a focus on temperature variation, catalyst loading, and FA concentration variation were carried out in DMSO and water. A solvent-dependent H_2 generation step was elucidated, with FA and H_3O^+ ions acting as proton sources for the reactions performed using DMSO and water, respectively. A Ru-monohydride species was detected by ^{1}H NMR spectroscopy and identified as the key intermediate species in the dehydrogenation of FA. A series of KIE experiments identified the decarboxylation of CO_2 as the rate-determining step in both DMSO and water. Plausible reaction pathways for the dehydrogenation of FA were proposed for both catalytic systems. Catalyst recyclability studies pointed toward the increased stability of **C10** in water compared to DMSO with TONs of 6748 being reached after seven catalytic cycles compared to TON ~ 3000 for the reaction performed in DMSO. Continuous FA addition experiments further reinforced the higher stability of **C10** in water compared to DMSO with catalytic activity, although to a lesser extent compared to step-wise FA addition, being retained for over 31 hours when water was used as a solvent medium.

4.8 Experimental Methods

4.8.1 General catalytic procedure for FA dehydrogenation

A stock solution of the complex in DMSO or H_2O was prepared. From the stock solution, the desired quantity of complex was added to a Schlenk flask followed by the addition of HCOOM (where M = Li, Na, K). The flask was sealed with a rubber septum and the atmosphere exchanged for N_2. The reaction solution was stirred at 800 rpm for 5 minutes at room temperature. Then, FA was added, and the mixture was stirred for an additional minute. Lastly, the reaction mixture was heated at the desired temperature using a pre-heated oil bath and the gas evolution was monitored using an inverted graduated measuring cylinder. For the continuous FA addition experiment, a similar approach was used, and an NE-300 Just Infusion™ Syringe Pump was used to inject FA from a Hamilton syringe fitted with a long metallic needle directly after the immersion of the reaction flask in the oil bath. **Figure 4.24** below shows the apparatus used to carry out the FA dehydrogenation experiments.

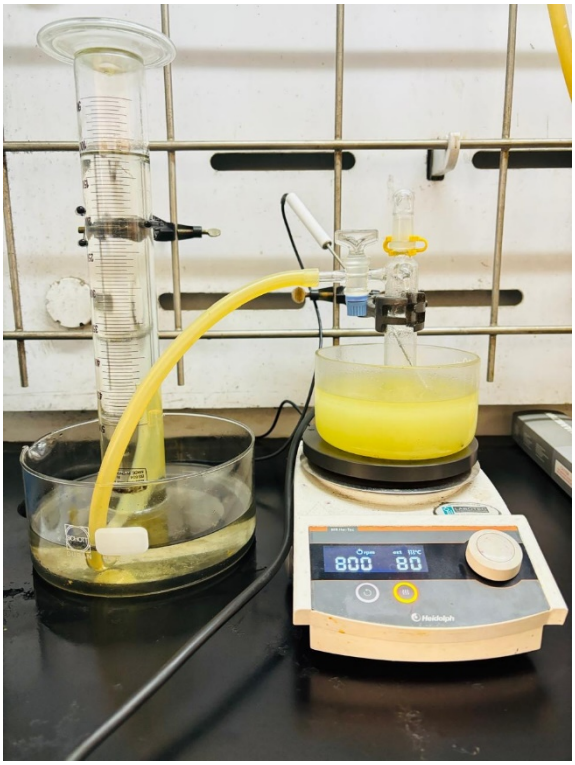

Figure 4.25: Reaction apparatus employed for FA dehydrogenation experiments.

4.8.2 Calculation of TON and TOF

In a blank experiment with FA without any catalyst, no gas was collected in the measuring cylinder. Hence, the corrected gas volume was calculated as $V_{corrected} = V_{recorded}$. The standard

molar gas volumes of CO_2 and H_2 at room temperature (25 °C) were taken as 24.42 L/mol and 24.49 L/mol, respectively.[21] The moles of FA dehydrogenated were calculated from the recorded gas volume using the following formula: $N_{FA} = (V_{recorded})/(24.49 + 24.41)$ mol. The turnover number (TON) was calculated as $TON = N_{FA}/n_{cat}$ and turnover frequency (TOF) was calculated as TOF = TON/time (hr) hr^{-1}.

4.8.3 Procedure for ^{1}H NMR mechanistic investigations

The desired amounts of ruthenium catalyst **C10** and HCOOK were dissolved in 0.7 mL DMSO-d_6 and 0.3 mL MeOD in a J-Young NMR tube and heated to 90 °C using a water bath. NMR spectra were recorded at specified time intervals on a 500 MHz instrument at a probe temperature of 300 K and spectral width of 150 ppm. Upon adding the HCOOK, the initial yellow catalyst solution changed to a red-orange solution consistent throughout the measurements. **Figures 4.25** and **4.26** indicate the positive region of the ^{1}H NMR spectra to illustrate the structural variations on the catalyst during hydride species formation.

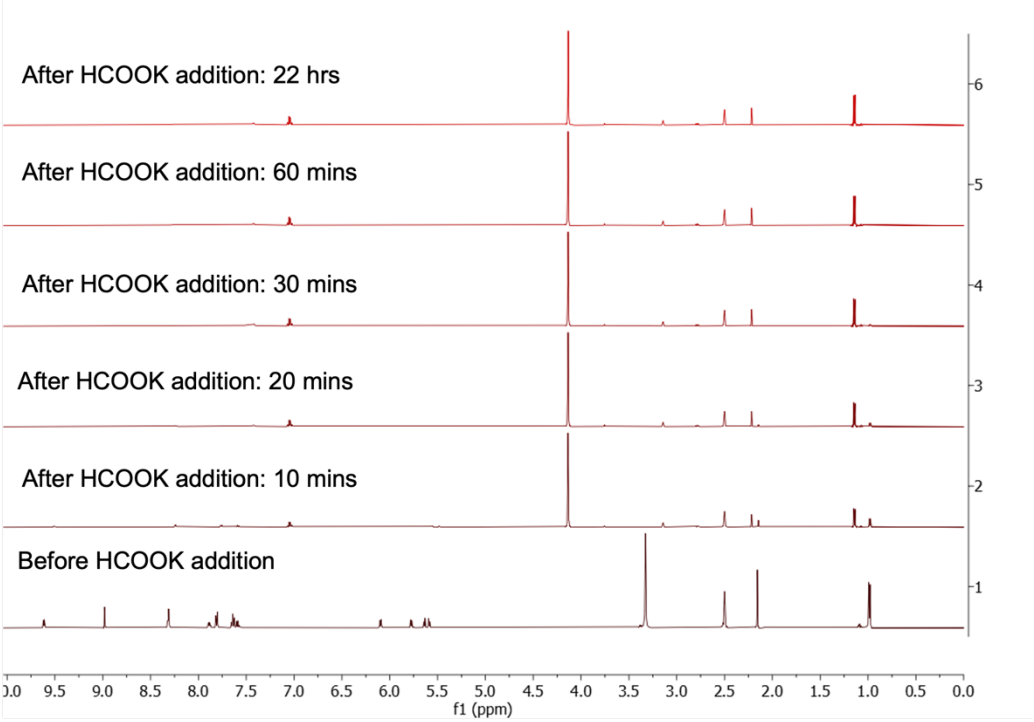

Figure 4.26: Stacked ^{1}H NMR spectra of **C10** in DMSO-d_6 at various time intervals. **Conditions**: **C10** (10.7 mg), HCOOK (1.8 mg), DMSO-d_6 (0.7 mL), MeOD (0.3 mL), probe temperature = 300 K, spectral width = 150 ppm.

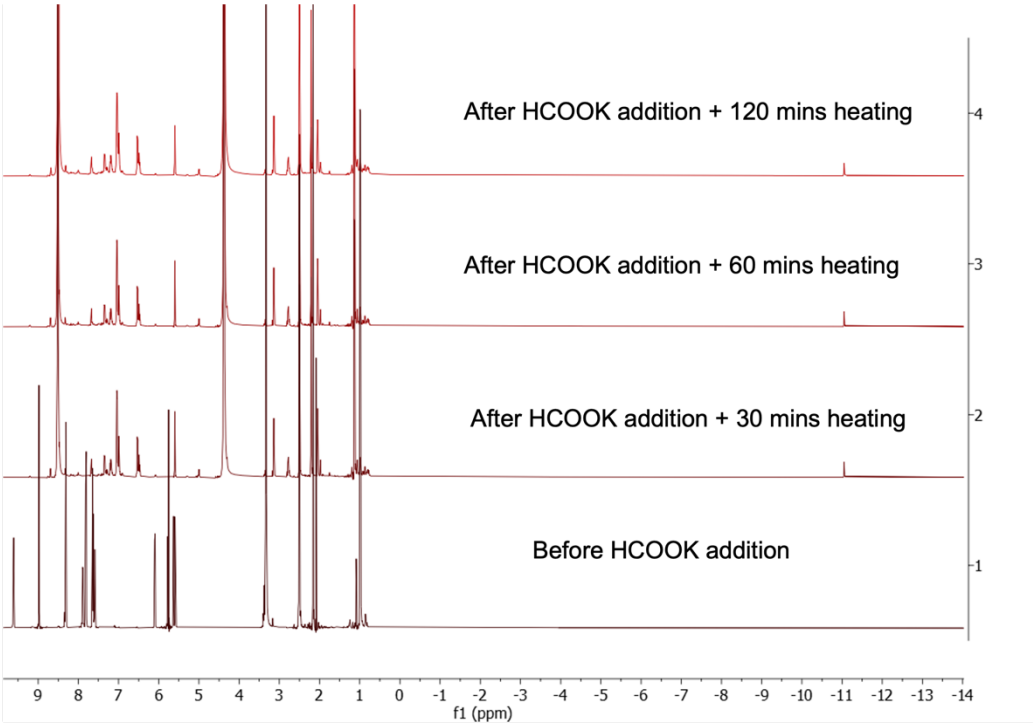

Figure 4.27: Stacked ^{1}H NMR spectra of **C10** in DMSO-d_6 at various time intervals. **Conditions**: **C10** (10.1 mg), HCOOK (86.9 mg), DMSO-d_6 (0.7 mL), MeOD (0.3 mL), probe temperature = 300 K, spectral width = 150 ppm.

4.8.4. Supplementary Information

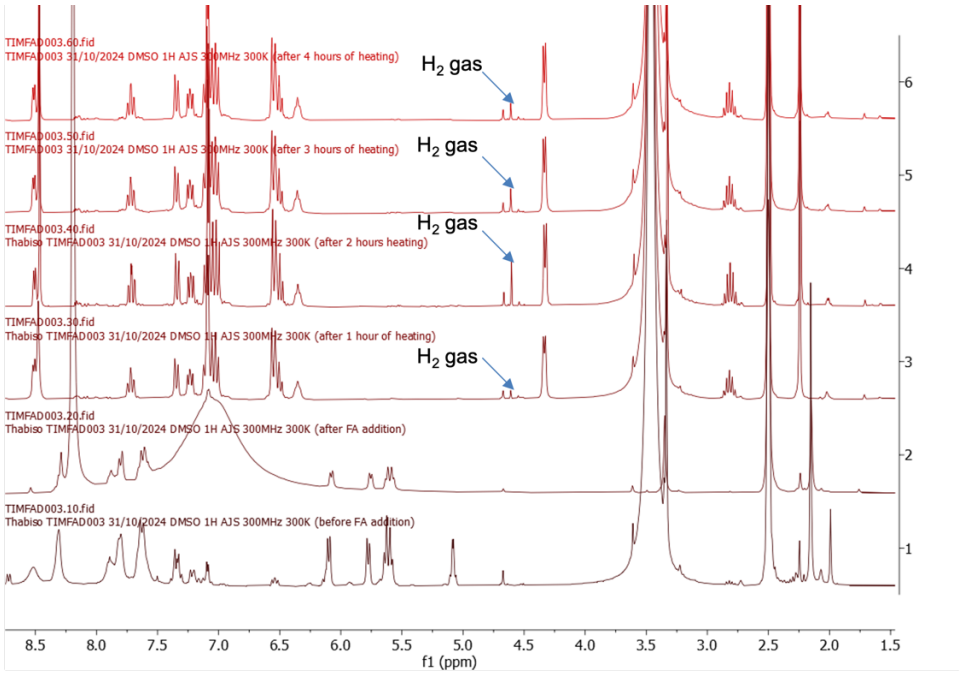

Figure S1: Stacked ^{1}H NMR (300 MHz, DMSO-d_6) spectra of the reaction mixture for FA dehydrogenation with FA (47.4 mg), **C10** (10.1 mg), and HCOOK (86.9 mg) dissolved in DMSO-d_6 (0.7 mL).

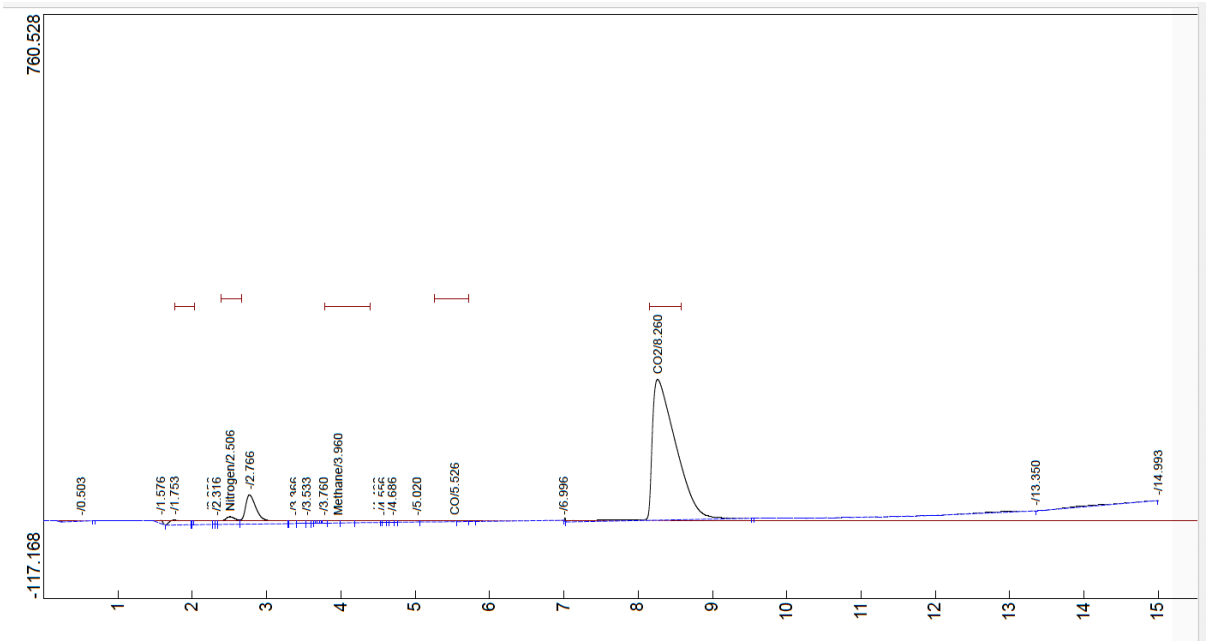

Figure S2: GC trace of the product mixture of a typical catalytic run. **Conditions**: FA (5 mmol, 0.2 mL), **C10** (0.2 mol%, 0.01 mmol), HCOONa (1 mmol), DMSO (2 mL), temperature (90 °C), total reaction volume (2.2 mL).

The initial rates of FA dehydrogenation under the reaction conditions shown in **Figures S3** – **S5** were calculated by fitting a linear model through the data points.

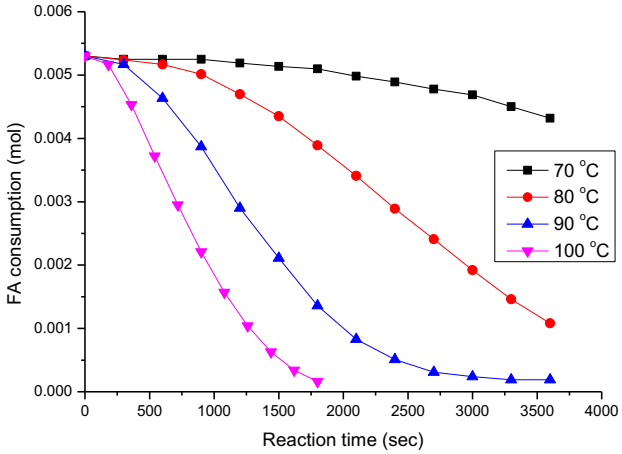

Figure S3: Initial FA consumption at different reaction temperatures. **Conditions**: FA (5 mmol, 0.2 mL), **C10** (0.2 mol%, 0.01 mmol), HCOOK (3 mmol), DMSO (2 mL), temperature (as indicated), total reaction volume (2.2 mL). 70 °C: Rate = 2.57 x 10^{-7} mol/s (R^2 = 0.90); 80 °C: Rate = 1.27 x 10^{-6} mol/s (R^2 = 0.96); 90 °C: Rate = 1.65 x 10^{-6} mol/s (R^2 = 0.92); 100 °C: Rate = 3.20 x 10^{-6} mol/s (R^2 = 0.98).

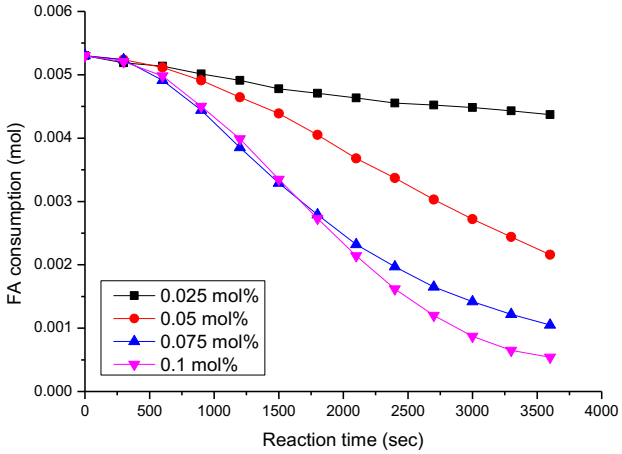

Figure S4: Initial FA consumption at different catalyst loadings. **Conditions**: FA (5 mmol, 0.2 mL), **C10** (as indicated), HCOOK (3 mmol), DMSO (2 mL), temperature (90 °C), total reaction volume (2.2 mL). 0.025 mol%: Rate = 2.62 x 10^{-7} mol/s (R^2 = 0.97); 0.05 mol%: Rate = 9.40 x 10^{-7} mol/s (R^2 = 0.98); 0.075 mol%: Rate = 1.33 x 10^{-6} mol/s (R^2 = 0.98); 0.1 mol%: Rate = 1.53 x 10^{-6} mol/s (R^2 = 0.98).

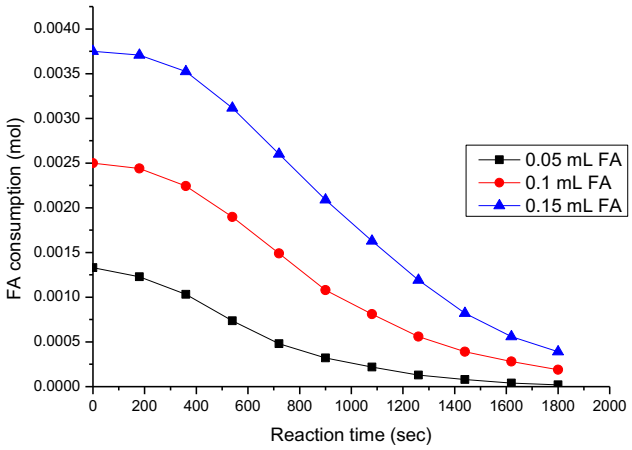

Figure S5: Initial FA consumption at different FA concentrations. **Conditions**: FA (as indicated), **C10** (0.2 mol%), HCOOK (3 mmol), DMSO (2 mL), temperature (90 °C), total reaction volume (2.05 – 2.2 mL). 0.05 mL FA: Rate = 7.90 x 10^{-7} mol/s (R^2 = 0.92); 0.1 mL FA: Rate = 1.47 x 10^{-6} mol/s (R^2 = 0.97); 0.15 mL FA: Rate = 2.14 x 10^{-6} mol/s (R^2 = 0.98).

The initial rates of FA dehydrogenation under the reaction conditions shown in **Figures S6** – **S8** were calculated by fitting a linear model through the data points.

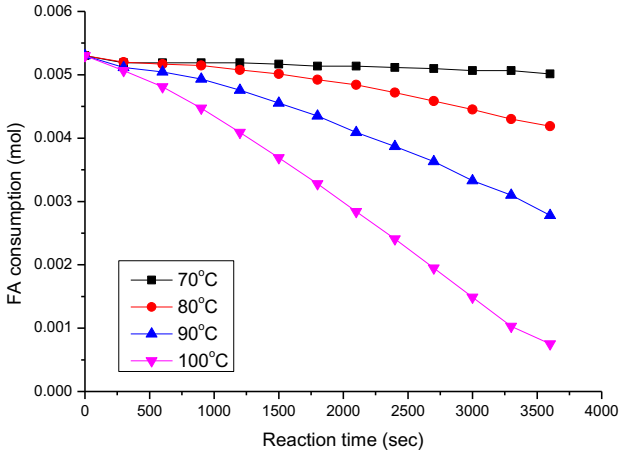

Figure S6: Initial FA consumption at different reaction temperatures. **Conditions**: FA (5 mmol, 0.2 mL), **C10** (0.2 mol%, 0.01 mmol), HCOOK (3 mmol), H_2O (2 mL), temperature (as indicated), total reaction volume (2.2 mL). 70 °C: Rate = 5.99 x 10^{-8} mol/s (R^2 = 0.90); 80 °C: Rate = 3.04 x 10^{-7} mol/s (R^2 = 0.96); 90 °C: Rate = 7.00 x 10^{-7} mol/s (R^2 = 0.98); 100 °C: Rate = 1.33 x 10^{-6} mol/s (R^2 = 0.99).

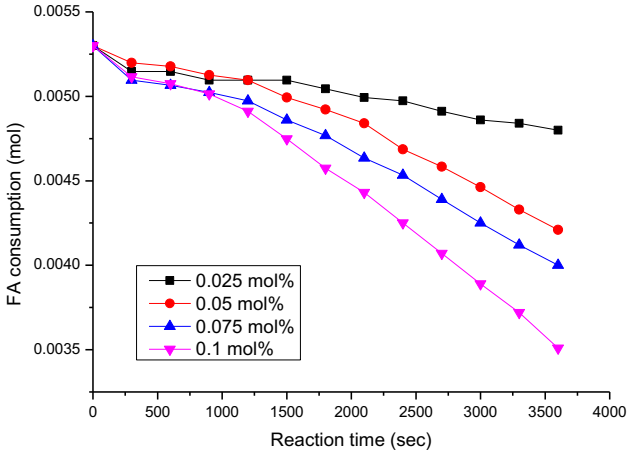

Figure S7: Initial FA consumption at different catalyst loadings. **Conditions**: FA (5 mmol, 0.2 mL), **C10** (as indicated), HCOOK (3 mmol), H_2O (2 mL), temperature (90 °C), total reaction volume (2.2 mL). 0.025 mol%: Rate = 1.21 x 10^{-7} mol/s (R^2 = 0.96); 0.05 mol%: Rate = 3.47 x 10^{-7} mol/s (R^2 = 0.98); 0.075 mol%: Rate = 2.99 x 10^{-7} mol/s (R^2 = 0.96); 0.1 mol%: Rate = 4.93 x 10^{-7} mol/s (R^2 = 0.98).

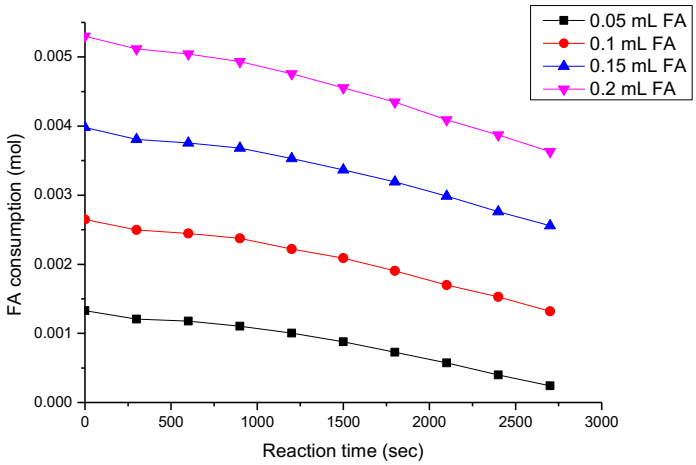

Figure S8: Initial FA consumption at different FA concentrations. **Conditions**: FA (as indicated), **C10** (0.2 mol%), HCOOK (3 mmol), H_2O (2 mL), temperature (90 °C), total reaction volume (2.05 – 2.2 mL). 0.05 mL FA: Rate = 3.99 x 10^{-7} mol/s (R^2 = 0.97); 0.1 mL FA: Rate = 4.85 x 10^{-5} mol/s (R^2 = 0.97); 0.15 mL FA: Rate = 5.17 x 10^{-7} mol/s (R^2 = 0.97); 0.2 mL FA: Rate = 6.16 x 10^{-7} mol/s (R^2 = 0.97).

4.9 References

1. Coffey, R. S. *Chem. Commun.,* **1967**, 923 – 924.
2. Ge, S., Liu, J-H., Gong, L., Mo, X-F., Liu, C., Yi, W-Y., He, P. *Eur. J. Inorg. Chem.*, **2024**, *27*, e202300509.
3. Wang, W-H., Himeda, Y., Muckerman, J. T., Manbeck, G. F., Fujita, E. *Chem. Rev.,* **2015**, *115*, 12936 – 12973.
4. Kar, S., Rauch, M., Leitus, G., Ben-David, Y., Milstein, D. *Nature Catal.,* **2021**, *4*, 193 - 201.
5. Mellone, I., Peruzzini, M., Rosi, L., Mellmann, D., Junge, H., Beller, M., Gonsalvi, L. *Dalton Trans.,* **2013**, *42,* 2495.
6. Müller, K., Brooks, K., Autrey, T. *Energ. Fuel.*, **2017**, *31*, 12603 – 12611.
7. Celaje, J. J. A., Lu, Z., Kedzie, E. A., Terrile, N. J., Lo, J. N., Williams, T. J. *Nature Commun.,* **2016**, *7*, 11308.
8. Wang, S., Huang, H., Roisnel, T., Bruneau, C., Fischmeister, C. *ChemSusChem,* **2019**, *12*, 179 – 184.
9. Himeda, Y. *Green Chem.,* **2009**, *11*, 2018 – 2022.
10. Lentz, N., Albrecht, M. *ACS Catal.,* **2022**, *12*, 12627 – 12631.
11. Wang, Z., Lu, S-H., Li, J., Wang, J., Li, C. *Chem. Eur. J.,* **2015**, *21*, 12592 – 12595.
12. Patra, S., Singh, S. K. *Inorg. Chem.,* **2020**, *59*, 4234 – 4243.

13. Xin, Z., Zhang, J., Sordakis, K., Beller, M., Du, C-X., Laurenczy, G., Li, Y. *ChemSusChem*, **2018**, *11*, 2077 – 2082.
14. Bielinski, E. A., Lagaditis, P. O., Zhang, Y., Mercado, B. Q., Würtele, C., Bernskoetter, W. H., Hazari, N., Schneider, S. *J. Am. Chem. Soc.,* **2014**, *136*, 10234 – 10237.
15. Curley, J. B., Bernskoetter, W. H., Hazari, N. *ChemCatChem*, **2020**, *12*, 1934 – 1938.
16. Anderson, N. H., Boncella, J., Tondreau, A. M. *Chem. Eur. J.,* **2019**, *25*, 10557 – 10560.
17. Léval, A., Agapova, A., Steinlechner, C., Alberico, E., Junge, H., Beller, M. *Green Chem.,* **2020**, *22*, 913 – 920.
18. Fulmer, G. R., Miller, A. J. M., Sherden, N. H., Gottlieb, H. E., Nudelman, A., Stoltz, B. M., Bercaw, J. E., Goldberg, K. I. *Organometallics*, **2010**, *29*, 2176 – 2179.
19. Iguchi, M., Guan, C., Huang, K. -W., Kawanami, H. *Int. J. Hydrogen Energy*, **2019**, *44*, 28507 – 28513.
20. Upadhyay, S. Temperature Effect on Reaction Rate. In *Chemical Kinetics and Reaction Dynamics;* Springer Netherlands: **2006**; pp 46 – 54. DOI: 10.1007/978-1-4020-4547-9_2.
21. Boddien, A., Mellmann, D., Gärtner, F., Jackstell, R., Junge, H., Dyson, P. J., Laurenczy, G., Ludwig, R., Beller, M. *Science*, **2011**, *333*, 1733.
22. Kushwaha, S., Awasthi, M. K., Das, A., Pathak, B., Singh, S. K. *Inorg. Chem.,* **2023**, *62*, 8080 – 8092.
23. Joseph, M. C., Kotzé, I. A., Nnaji, N. J., Swarts, A. J., Mapolie, S. F. *Organometallics*, **2022**, *41*, 3546 – 3556.
24. Fellay, C., Yan, N., Dyson, P. J., Laurenczy, G. *Chem. Eur. J.,* **2009**, *15*, 3752 – 3760.
25. Guan, C., Zhang, D. -D., Pan, Y. P., Iguchi, M., Ajitha, M. J., Hu, J., Li, H., Yao, C., Huang, M. -H., Min, S., Zheng, J., Himeda, Y., Kawanami, H., Huang, K. -W. *Inorg. Chem.,* **2017**, *56*, 438 – 445.
26. Wang, Z. J., Lu, S. M., Li, J., Wang, J. J., Li. C. *Chem. Eur. J.*, **2015**, *21*, 12592 – 12595.
27. Wang, W. H., Hull, J. F., Muckerman, J. T., Fujita, E., Hirose, T., Himeda, Y. *Chem. Eur. J.*, **2012**, *18*, 9397 – 9404.
28. Wang, W. H., Xu, S., Manaka, Y., Suna, Y., Kambayashi, H., Muckerman, J. T., Fujita, E., Himeda, Y. *ChemSusChem,* **2014**, *7*, 1976 – 1983.
29. Pan, Y., Pan, C. L., Zhang, Y., Li, H., Min, S., Guo, X., Zheng, B., Chen, H., Anders, A., Lai, Z., Zheng, J., Huang, K.-W. *Chem. Asian J.,* **2016**, *11*, 1357 – 1360.
30. Patra, S., Awasthi, M. K., Rai, R. K., Deka, H., Mobin, S. M., Singh, S. K. *Eur. J. Inorg. Chem.,* **2019**, 1046 – 1053.

Chapter 5: Dissertation Summary and Future Prospects

5.1 Summary and General Conclusions

This dissertation probed the synthesis, characterization, and catalytic evaluation of a series of manganese(I) and ruthenium(II) complexes ligated by pyridylimine ligands for application as catalyst precursors in formic acid (FA) dehydrogenation. It was anticipated that the steric and electronic effects induced by the pyridylimine ligands could influence both the activity and selectivity of the prepared homogeneous catalysts toward the production of hydrogen and carbon dioxide.

Chapter 2 detailed the synthesis and spectroscopic characterization of a series of known pyridylimine ligands **L1** – **L9**. Moreover, the preparation of new, neutral pyridylimine-ligated manganese(I) complexes **C1** – **C9** is discussed. Several alterations such as the introduction of aromatic and aliphatic substituents on the imine nitrogen and electron donating or withdrawing moieties on the carbon α to the pyridine nitrogen were made to study the electronic and steric influences of these substituents on the catalytic activity and selectivity of the Mn(I) complexes toward FA dehydrogenation. SCXRD analyses unambiguously confirmed the molecular geometry of the Mn(I) complexes as possessing a distorted octahedral geometry with the pyridylimine ligand occupying an equatorial position. The coordination sphere around manganese is completed by a bromide ligand and three carbonyl ligands and adopts a *fac* configuration. Notable peak broadening in the ^{1}H NMR spectra of the complexes pointed toward possible Mn-CO bond dissociation. A combination of FT-IR and SCXRD analyses presented evidence of light-induced Mn-CO dissociation resulting in the formation of Mn(II) species. Attempts to dehydrogenate FA over Mn complexes **C1** – **C9** were unsuccessful due to the light-sensitive nature of the complexes in solution and the possible formation of unproductive Mn(II) species during the reaction.

This led to the development of cationic, half-sandwich ruthenium(II) complexes **C10** – **C20** ligated by the pyridylimine ligands discussed in **Chapter 2**. The synthesis and characterization of these Ru(II) complexes by a suite of spectroscopic and analytical techniques is described in **Chapter 3**. SCXRD analyses confirmed the pseudo-octahedral molecular geometry of the Ru complexes with the p-cymene moiety adopting the usual piano-stool conformation. The anions (Cl, BPh_4, and PF_6) were located below the aromatic ring of the cation. Unlike their

Mn(I) analogues, the Ru(II) complexes were not light sensitive and displayed good stability in solution i.e. no visible colour changes were observed when the solution was left at room temperature over extended periods. **Chapter 4** details the application of cationic ruthenium complexes as catalyst precursors in FA dehydrogenation. In general, Ru complexes bearing an aromatic substituent on the imine nitrogen performed markedly better than the complexes containing an aliphatic substituent in the same position, except for **C14** bearing a benzyl substituent. Further, introducing electron-donating substituents on the aromatic ring bound to the imine nitrogen led to decreased catalytic activity compared to their unsubstituted analogue **C10**. Complexes **C19** and **C20** containing bulky BPh_4 and PF_6 counterions exhibited catalytic activities similar to their Cl analogue **C10**. Optimization of catalytic reaction conditions led to the discovery of good solubility and activity of complex **C10** in DMSO and water. By varying reaction parameters such as temperature, catalyst loading, and substrate concentration, activation parameters such as activation energy, enthalpy-, and entropy of activation as well as deeper insights into the mechanism of FA dehydrogenation in both DMSO and water were elucidated. Based on the detection of the Ru monohydride species using ^1H NMR experiments and a series of kinetic isotope effect (KIE) experiments, a plausible pathway for the dehydrogenation of FA in DMSO and water was proposed. Complex **C10** displayed better reusability and long-term stability in a water medium than DMSO.

5.2 Future Prospects

The study presented in this dissertation has the potential for future exploration and development to better understand the catalytic behaviour of pyridylimine-ligated manganese and ruthenium complexes. Our spectroscopic and crystallographic data suggest that the manganese(I) complexes are sensitive to light when in solution, which inhibits their activity towards FA dehydrogenation. For ruthenium(II) complexes, the substituents on the imine nitrogen as well as the α carbon on the pyridine ring of the pyridylimine ligands influenced the activity of the catalysts toward FA dehydrogenation.

5.2.1 Manganese-catalyzed FA dehydrogenation

The prepared Mn(I) complexes were found to be unstable in solution and overall poor catalyst precursors for the dehydrogenation of FA. The light-induced dissociation of the Mn-CO bond can be evaded by the utilization of tridentate ligand systems that increase the π back-donation from the manganese metal centre. It is anticipated that this ligand framework will increase the electron density around the manganese metal centre thus decreasing the lability of the Mn-

CO bond. Additionally, electron-withdrawing substituents on the phenyl ring bound to the imine nitrogen can be introduced to gain further insight into the electronic effects. Moreover, the prepared Mn(I) complexes could be immobilized on various support materials such as Chitosan among others to improve their stability, reusability, and recovery. Some examples of the envisaged catalytic systems are shown in **Figure 5.1**.

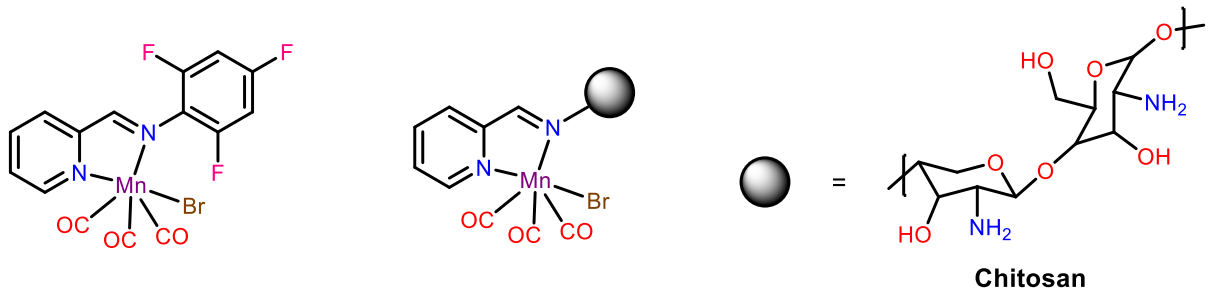

Figure 5.1: Proposed pyridylimine manganese(I) complexes.

5.2.2 Ruthenium-catalyzed FA dehydrogenation

The synthesized Ru(II) complexes displayed excellent catalytic activity toward FA dehydrogenation. For reactions performed in DMSO, complex **C10** exhibited a degree of deactivation with each addition of fresh FA into the catalytic system. The immobilization of the ruthenium complex on silica support such as SBA-15 could enhance the reusability and recovery of **C10** in DMSO. The dehydrogenation of various grades of FA i.e. 90%, 95%, and, 99% could be carried out to gain deeper insights into the role of water in the catalytic system. Measuring the pH of the reaction solutions during formate amount variation experiments could point out the exact optimal pH for efficient FA dehydrogenation. The prepared catalysts could be evaluated for the generation of high-pressure gases by conducting the dehydrogenation of FA in an autoclave. Moreover, density functional theory (DFT) simulations can be incorporated to support the experimental mechanistic observations further.

As mentioned in the introductory chapter of this dissertation, the study aimed to prepare a series of manganese(I) and ruthenium(II) complexes based on pyridylimine ligands and demonstrate their usefulness in the dehydrogenation of FA. The manganese complexes had little to no activity for the targeted organic transformation while the ruthenium complexes proved to be very efficient for this process. It is envisaged that the complexes have the potential to be further explored in other catalytic transformations. The manganese complexes can be applied to direct or indirect hydrogenation reactions of substrates such as CO_2 and ketones. The ruthenium complexes could also be useful in CO_2 hydrogenation which would

render them effective catalysts for both hydrogenation and dehydrogenation reactions. The activity of the ruthenium complexes for these organic transformations could demonstrate their ability to operate as an efficient catalyst in a LOHC system.

Appendix (NMR, IR, and MS)

NMR Spectra

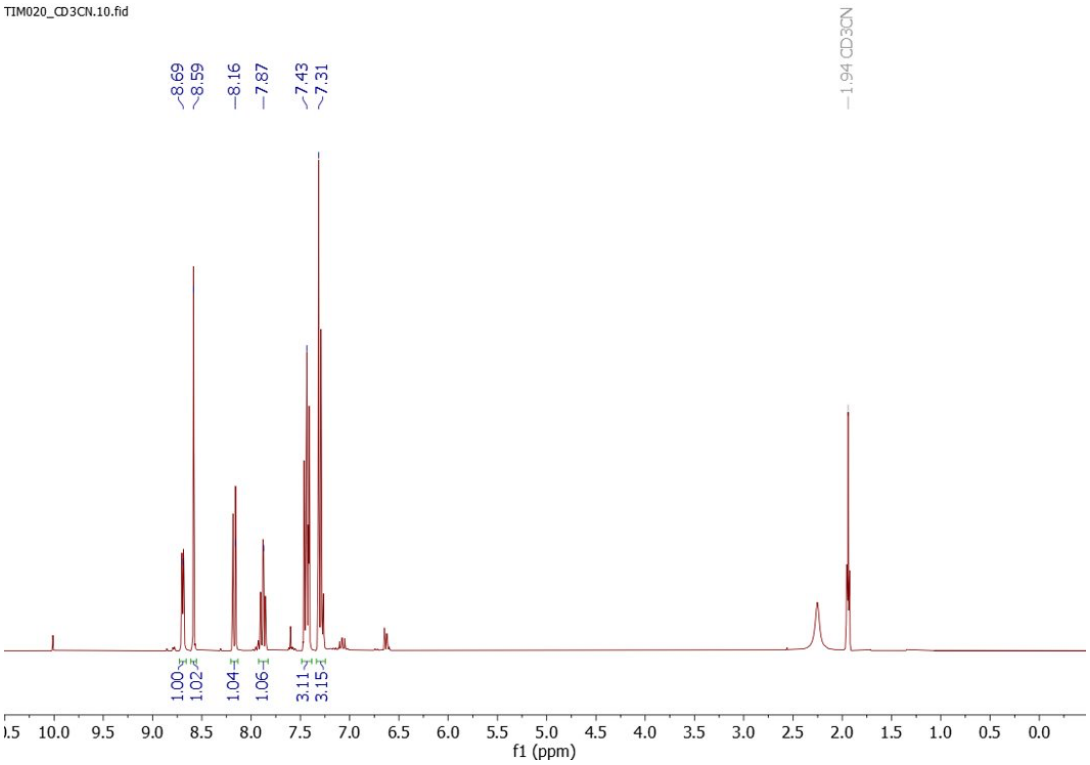

Figure 1: ^{1}H NMR spectrum of pyridylimine ligand **L1** recorded at 300 K.

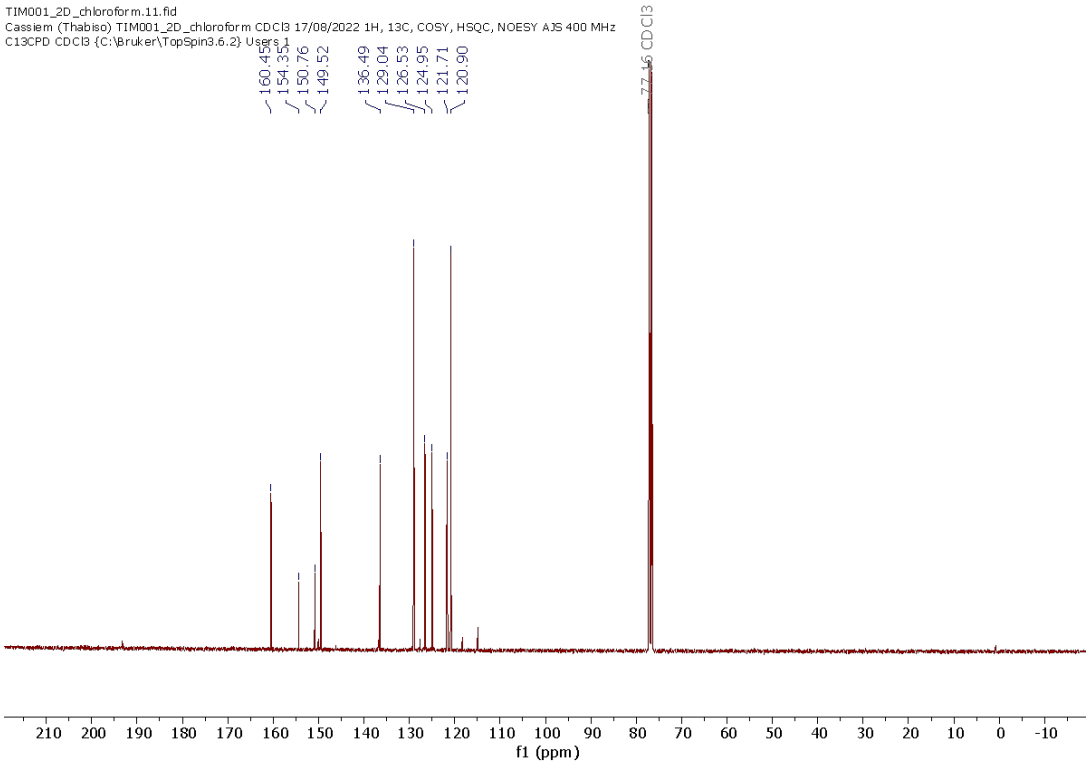

Figure 2: ^{13}C NMR spectrum of pyridylimine ligand **L1** recorded at 300 K.

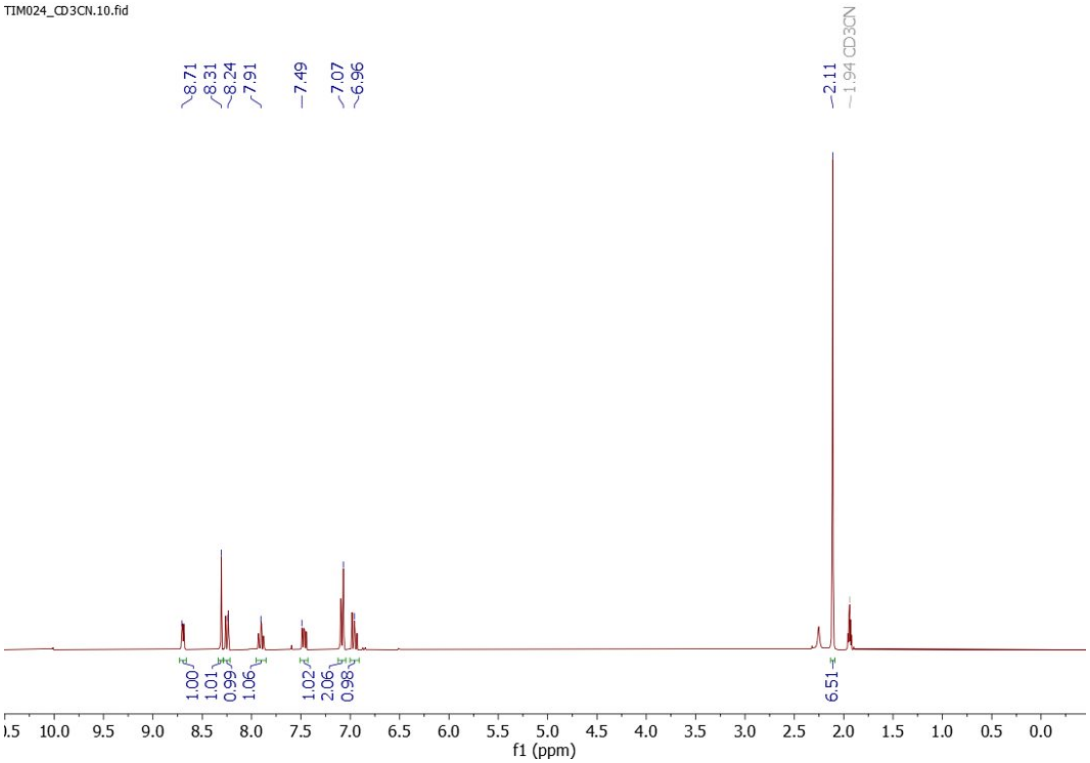

Figure 3: ^{1}H NMR spectrum of pyridylimine ligand **L2** recorded at 300 K.

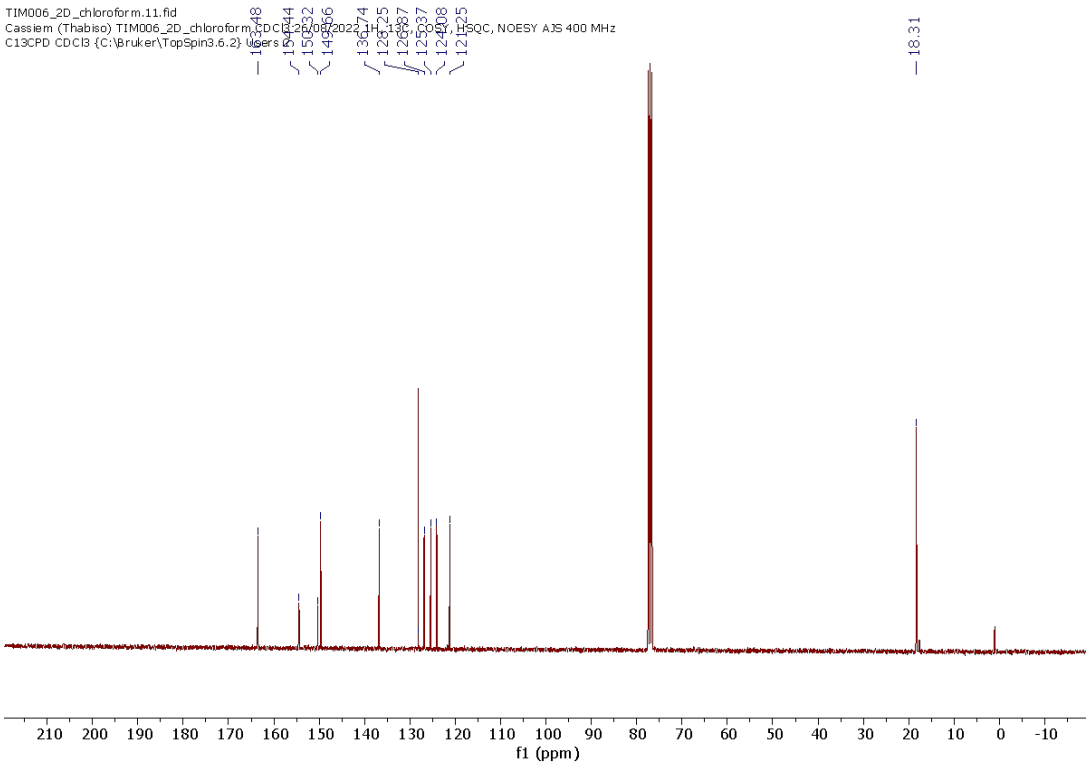

Figure 4: ^{13}C NMR spectrum of pyridylimine ligand **L2** recorded at 300 K.

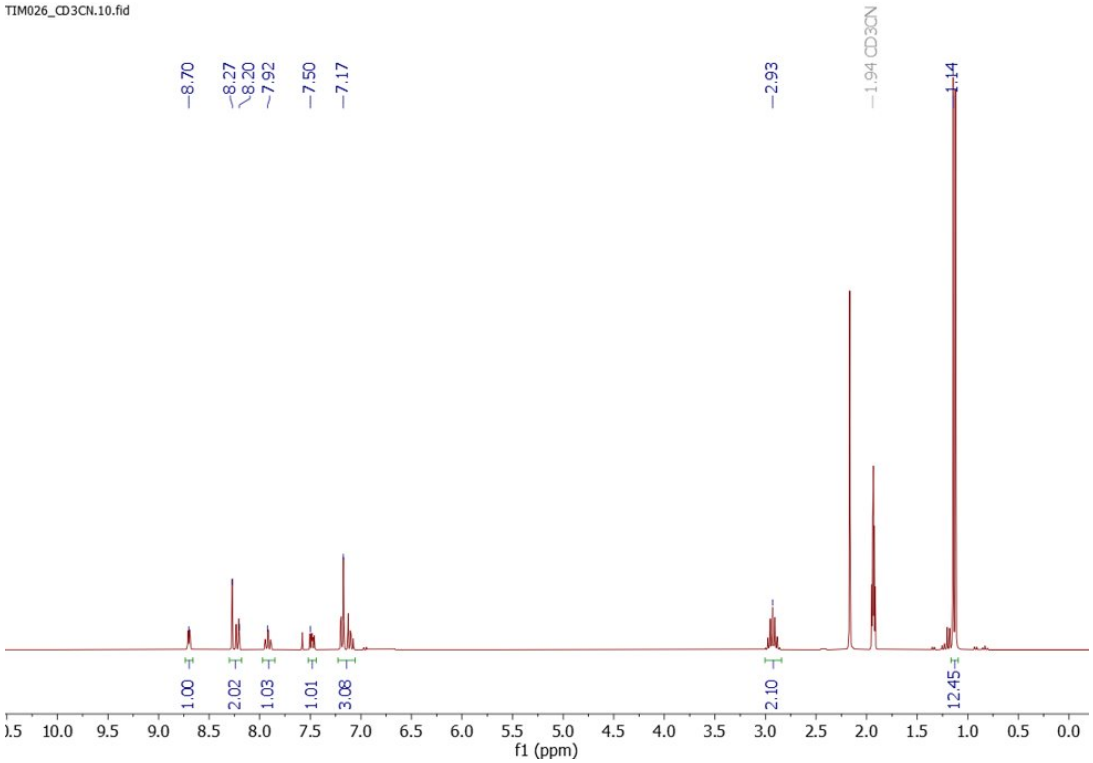

Figure 5: ^{1}H NMR spectrum of pyridylimine ligand **L3** recorded at 300 K.

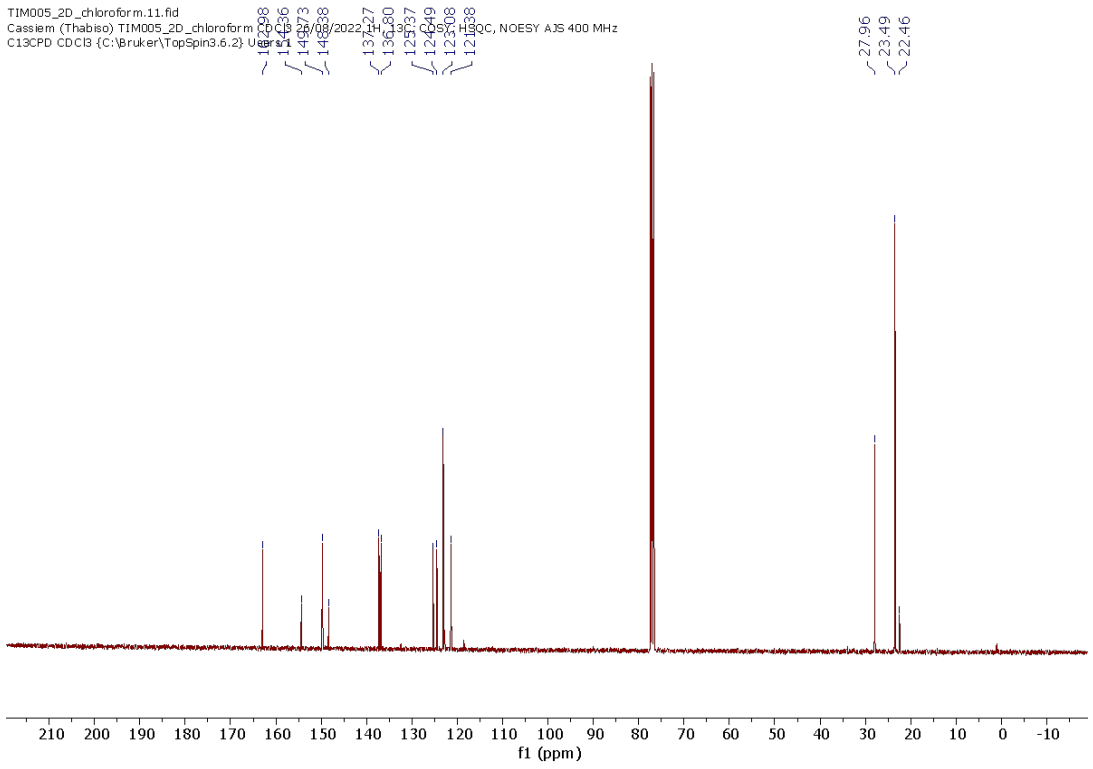

Figure 6: ^{13}C NMR spectrum of pyridylimine ligand **L3** recorded at 300 K.

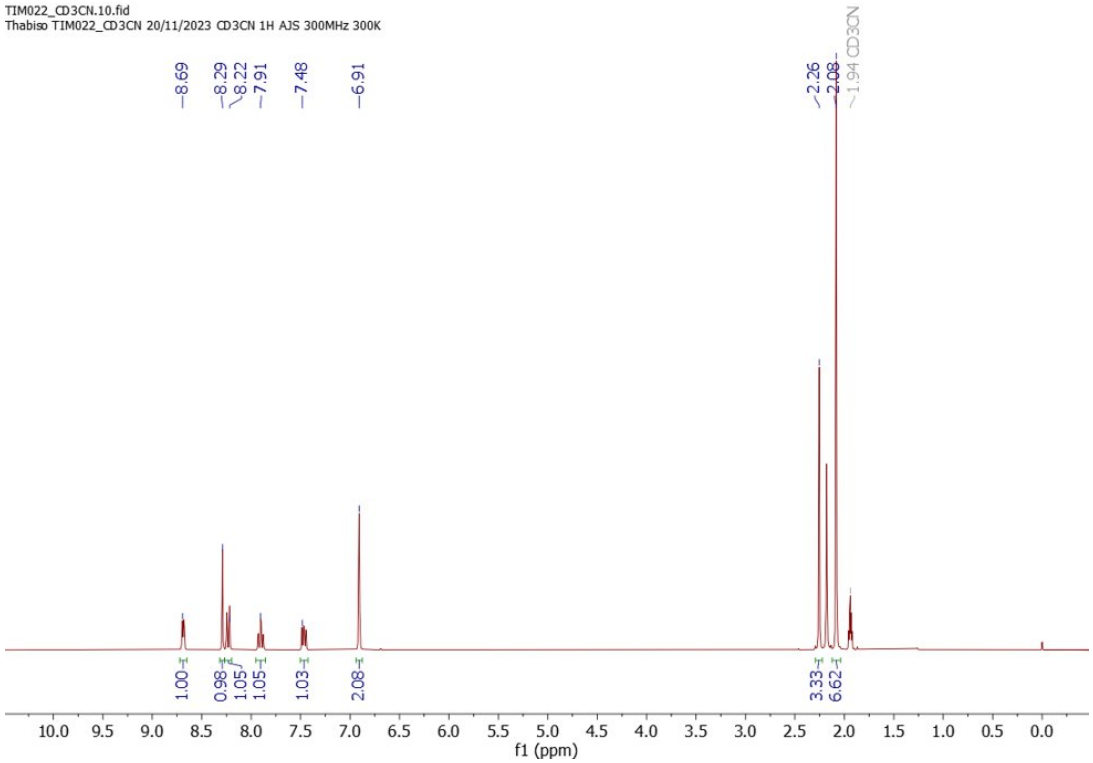

Figure 7: ^{1}H NMR spectrum of pyridylimine ligand **L4** recorded at 300 K.

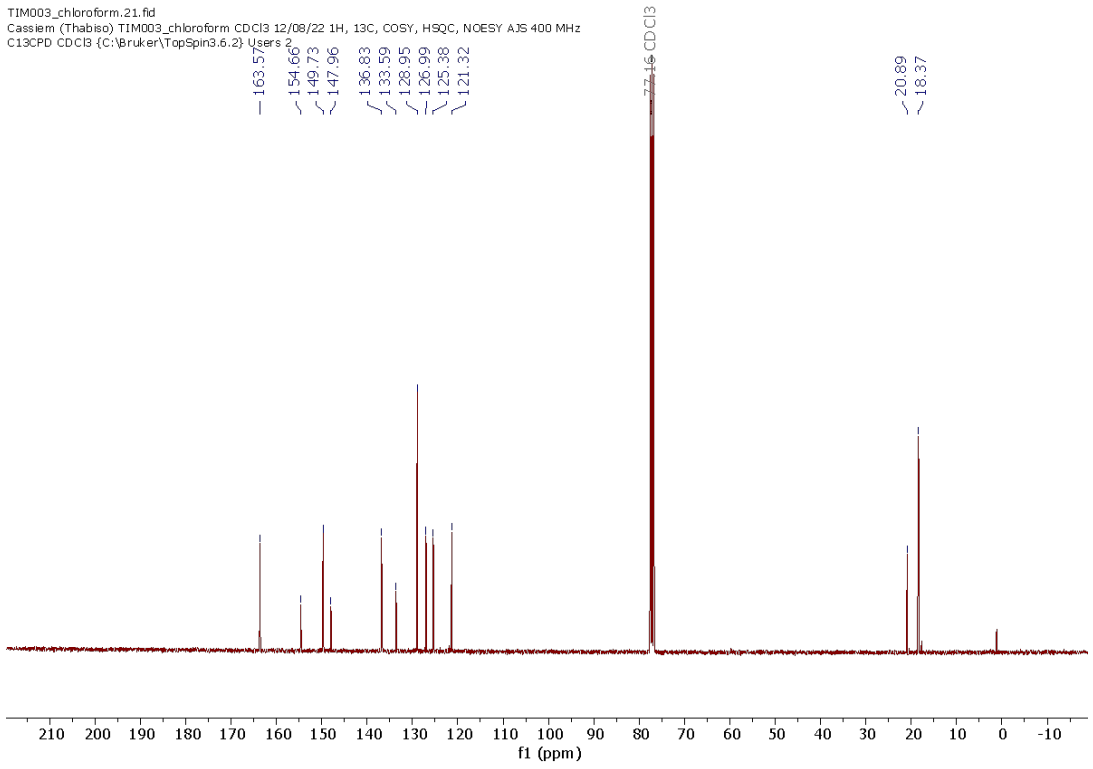

Figure 8: ^{13}C NMR spectrum of pyridylimine ligand **L4** recorded at 300 K.

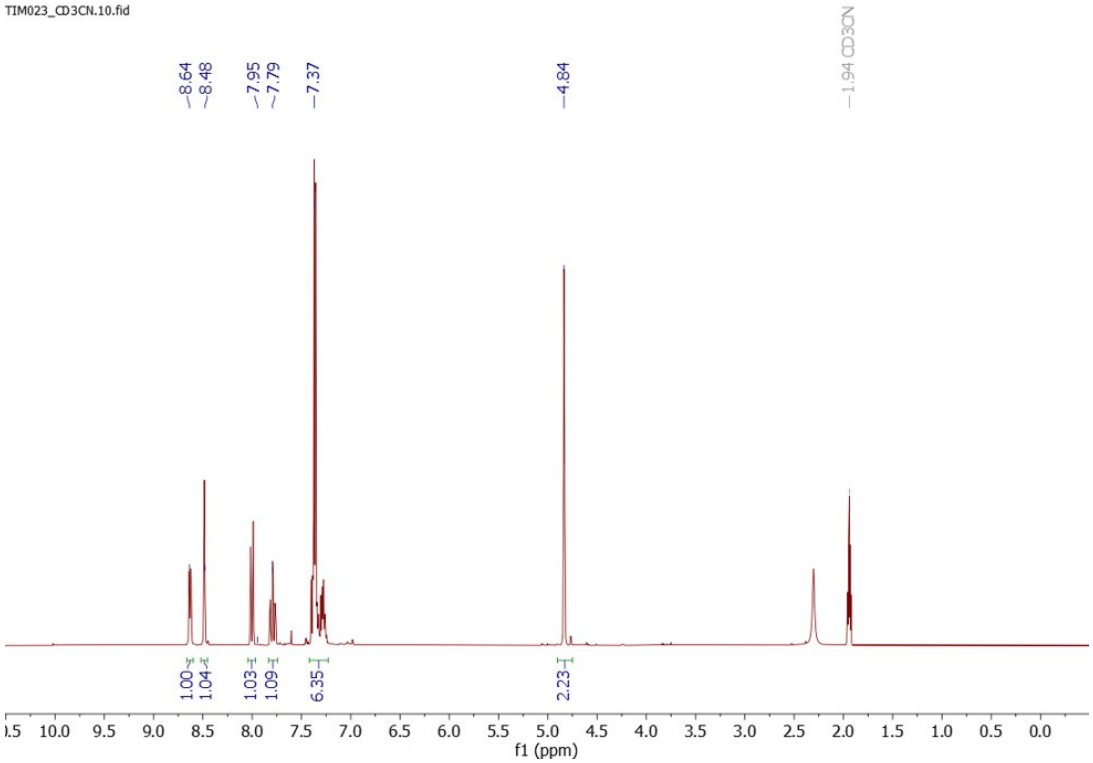

Figure 9: ^{1}H NMR spectrum of pyridylimine ligand **L5** recorded at 300 K.

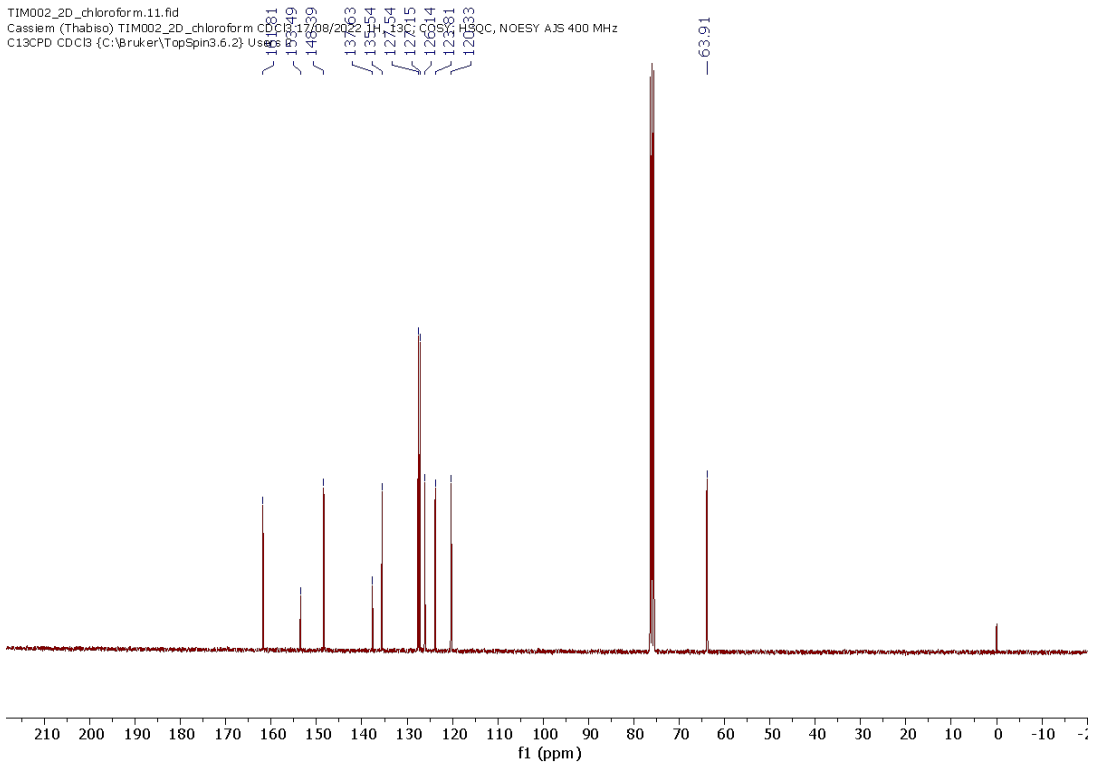

Figure 10: ^{13}C NMR spectrum of pyridylimine ligand **L5** recorded at 300 K.

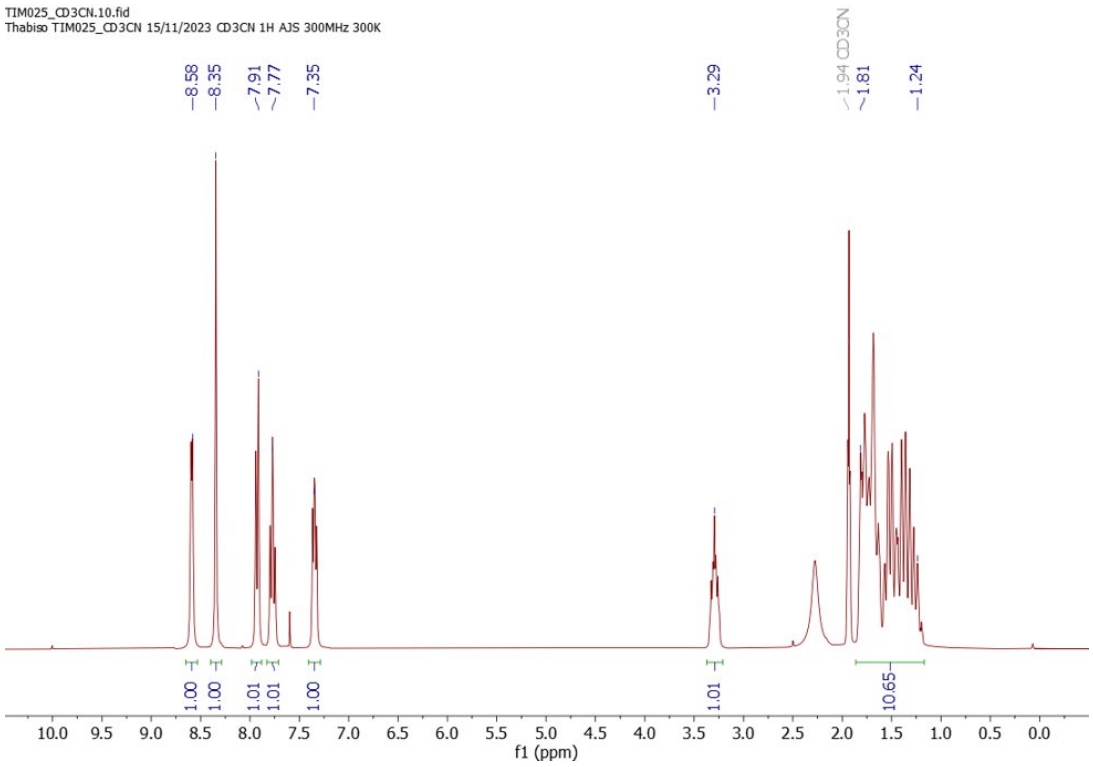

Figure 11: ^{1}H NMR spectrum of pyridylimine ligand **L6** recorded at 300 K.

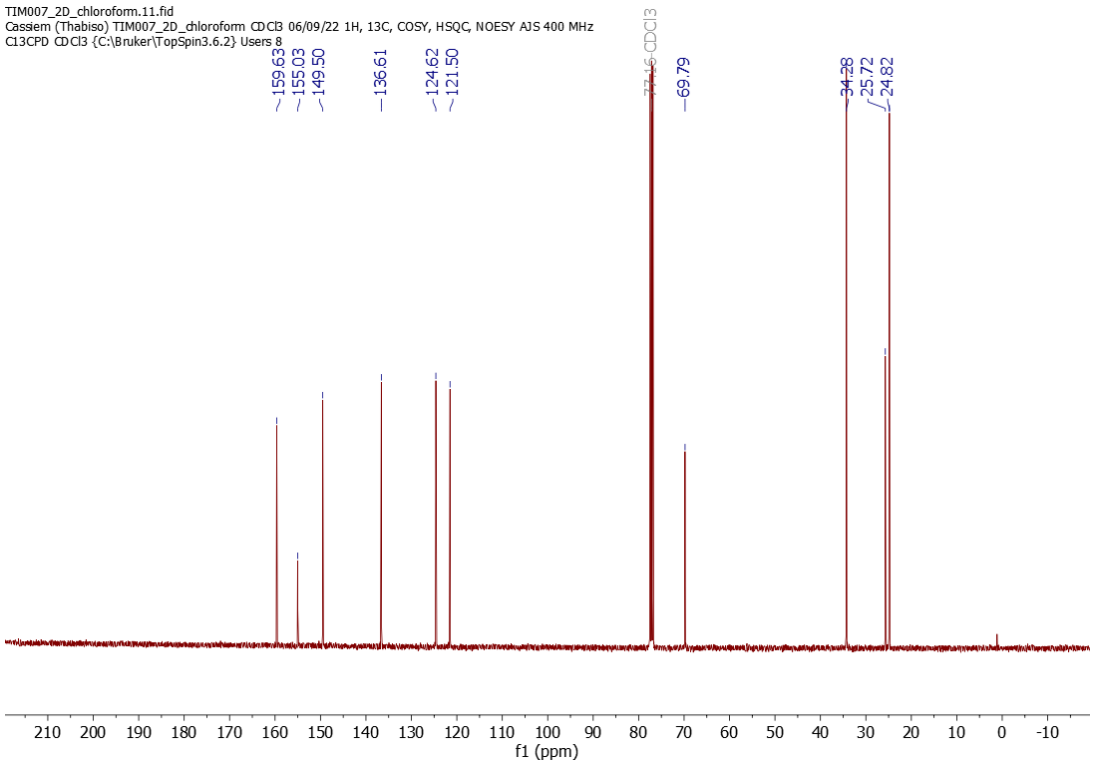

Figure 12: ^{13}C NMR spectrum of pyridylimine ligand **L6** recorded at 300 K.

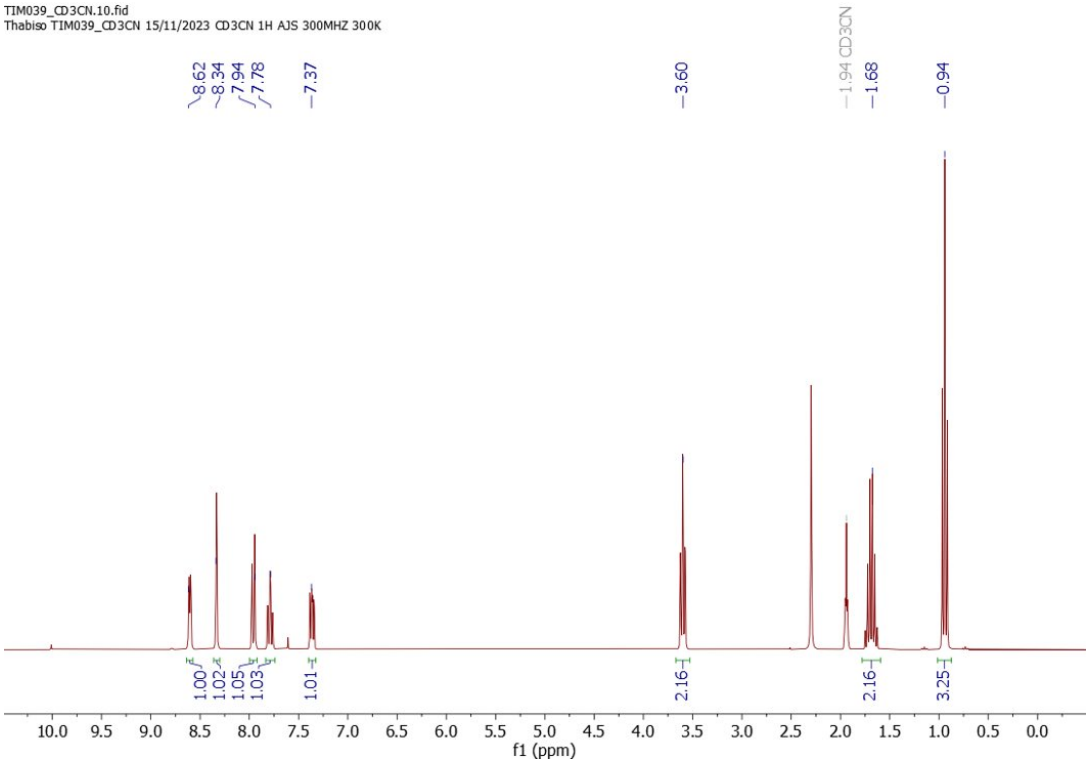

Figure 13: ^{1}H NMR spectrum of pyridylimine ligand **L7** recorded at 300 K.

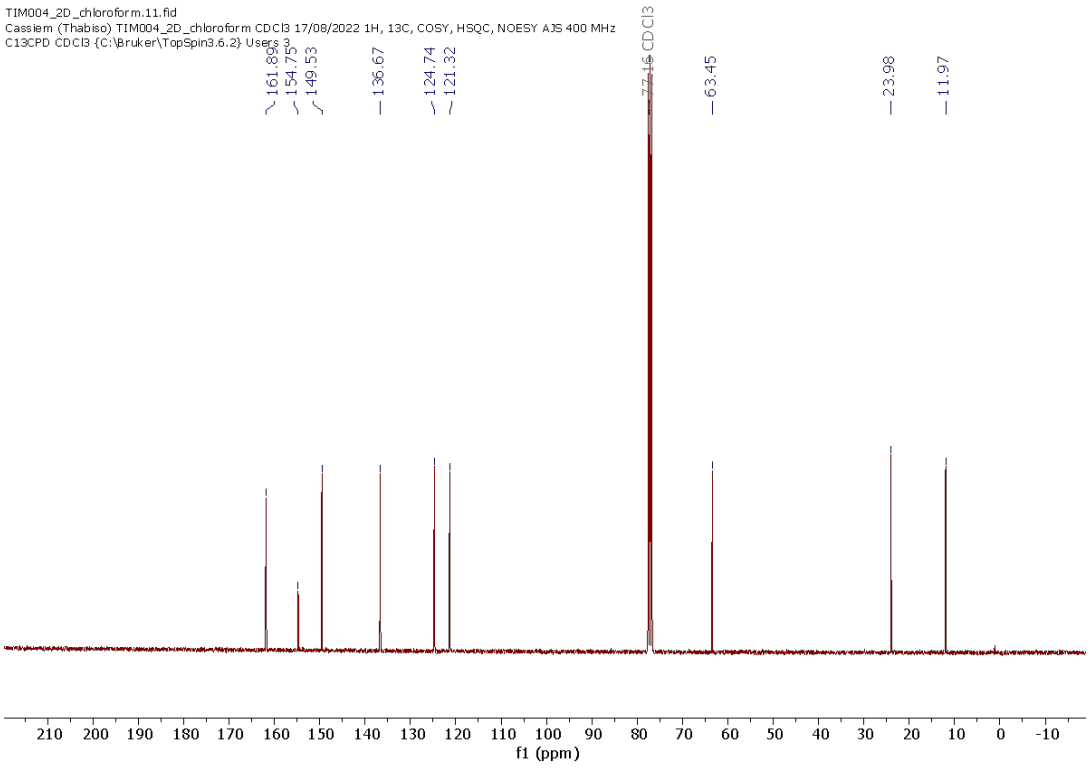

Figure 14: ^{13}C NMR spectrum of pyridylimine ligand **L7** recorded at 300 K.

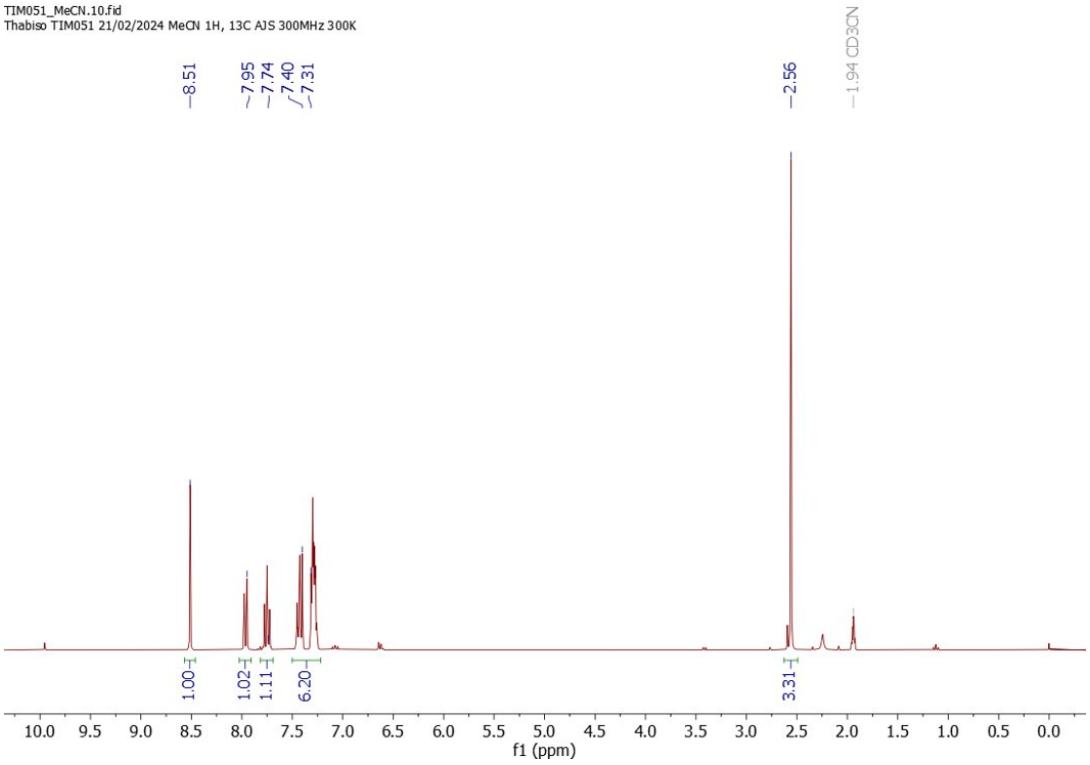

Figure 15: ^{1}H NMR spectrum of pyridylimine ligand **L8** recorded at 300 K.

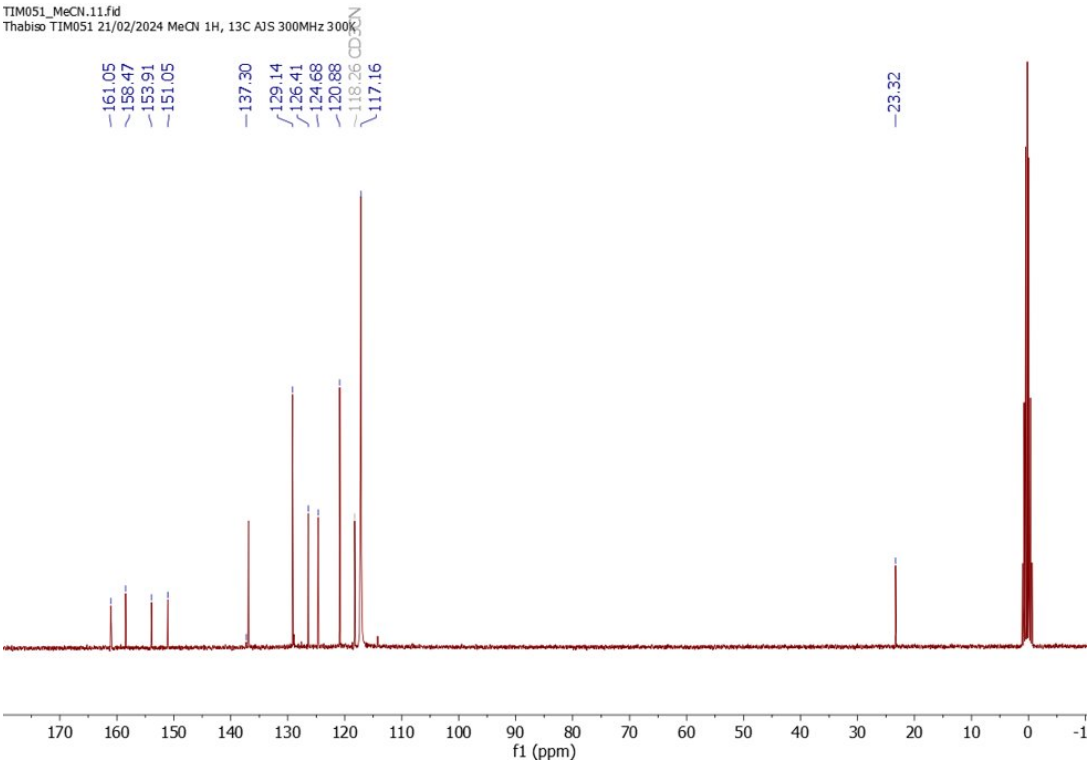

Figure 16: ^{13}C NMR spectrum of pyridylimine ligand **L8** recorded at 300 K.

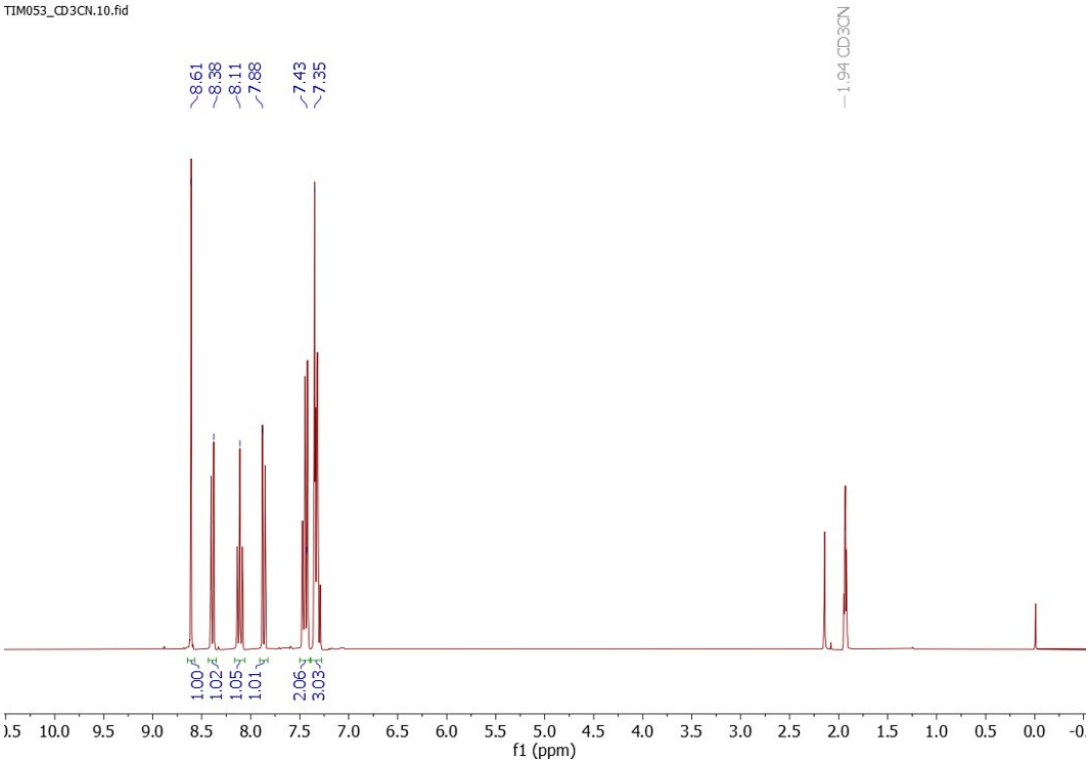

Figure 17: ^{1}H NMR spectrum of pyridylimine ligand **L9** recorded at 300 K.

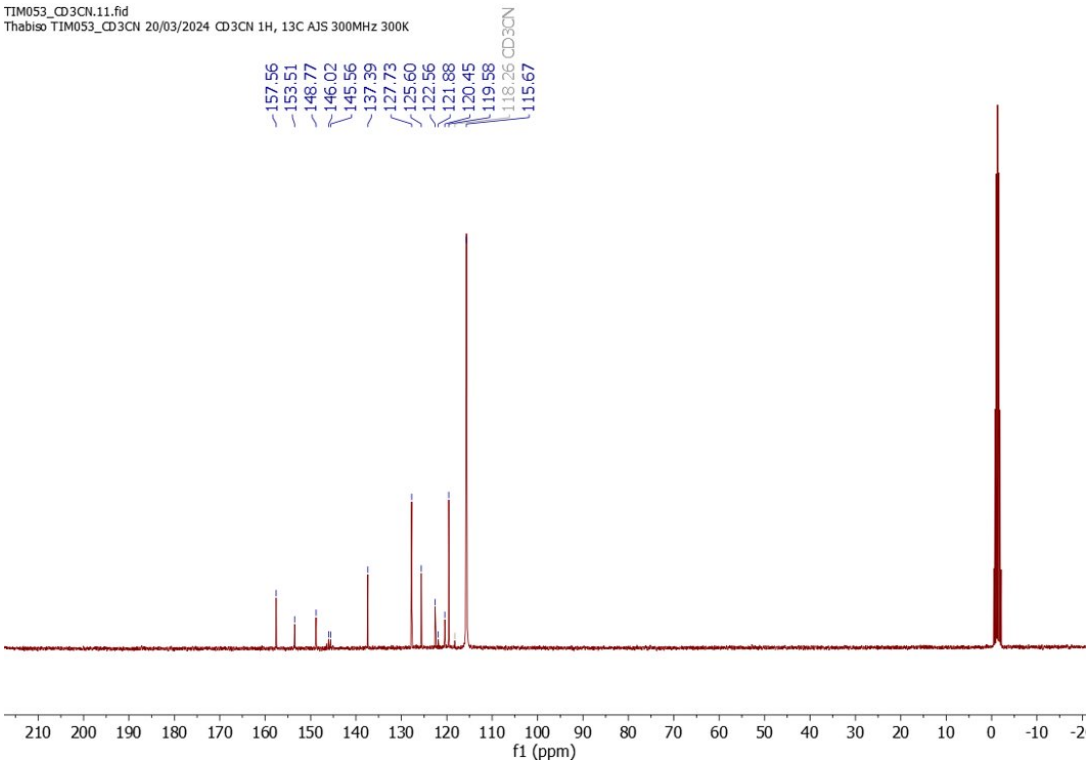

Figure 18: ^{13}C NMR spectrum of pyridylimine ligand **L9** recorded at 300 K.

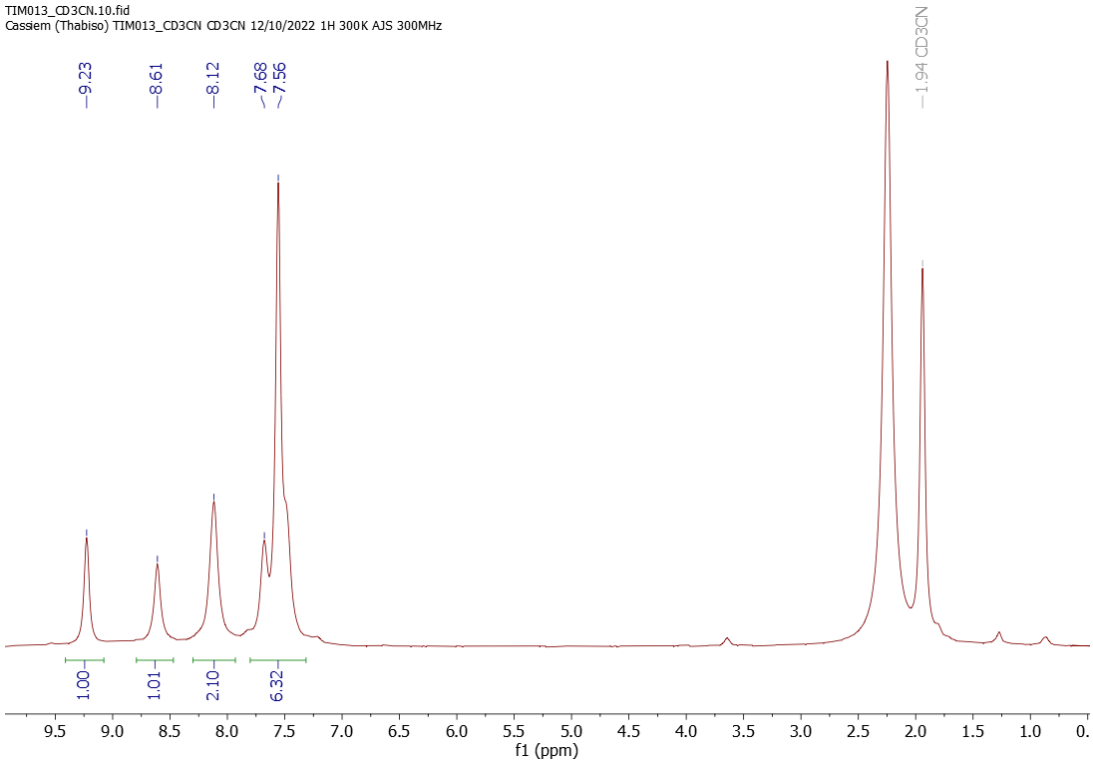

Figure 19: ^{1}H NMR spectrum of pyridylimine manganese complex **C1** recorded at 300 K.

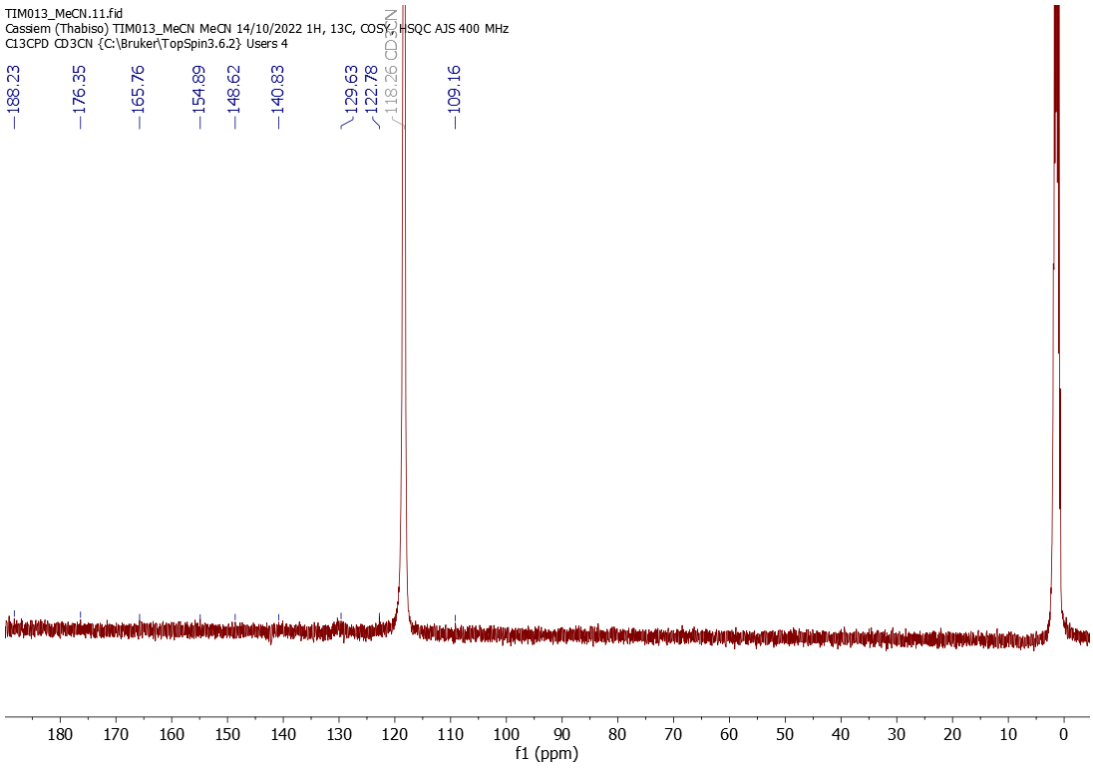

Figure 20: ^{13}C NMR spectrum of pyridylimine manganese complex **C1** recorded at 300 K.

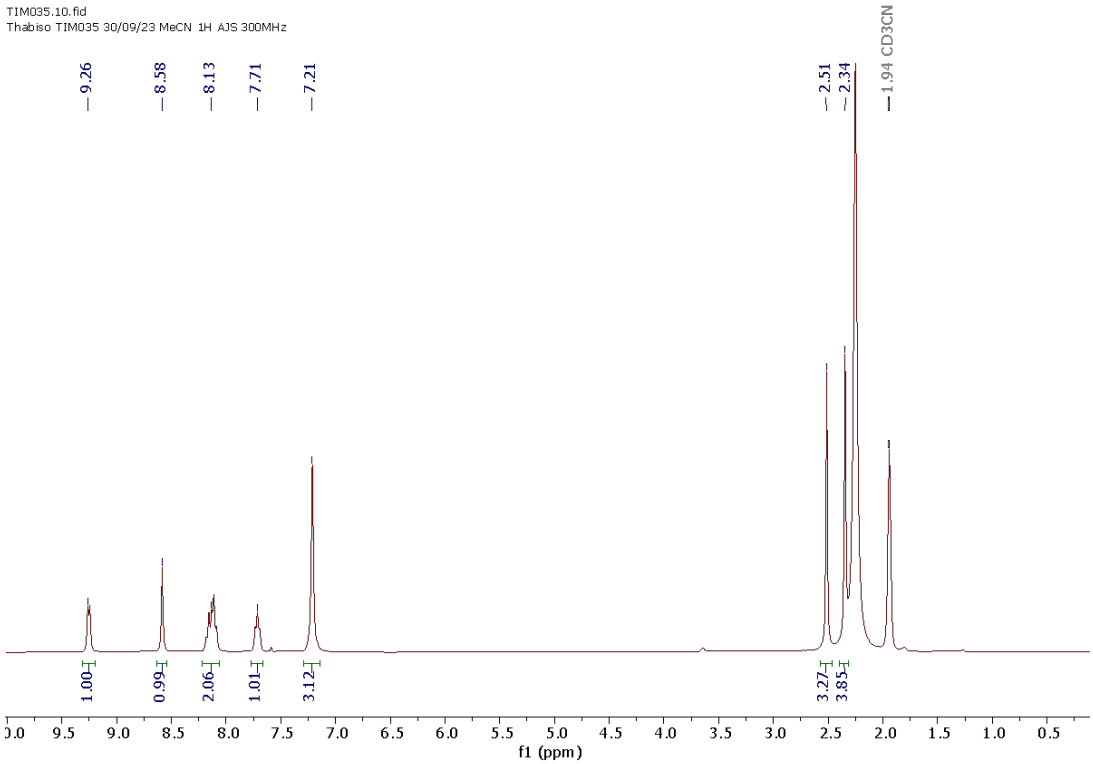

Figure 21: ^{1}H NMR spectrum of pyridylimine manganese complex **C2** recorded at 300 K.

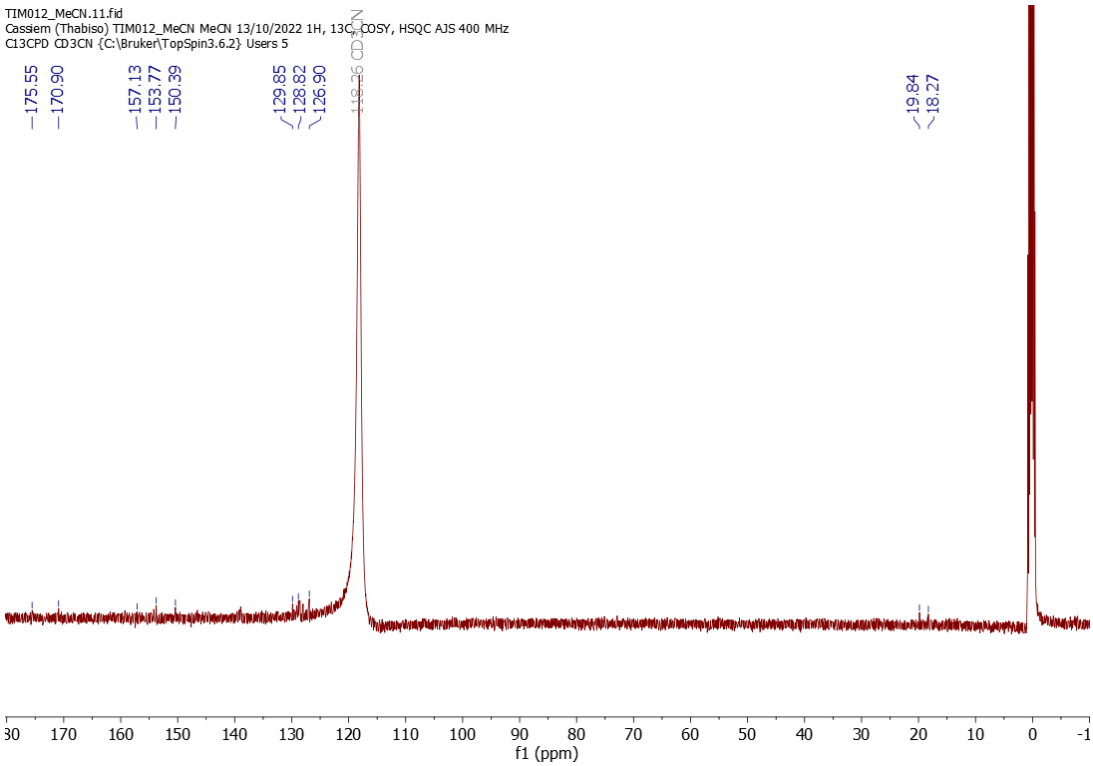

Figure 22: ^{13}C NMR spectrum of pyridylimine manganese complex **C2** recorded at 300 K.

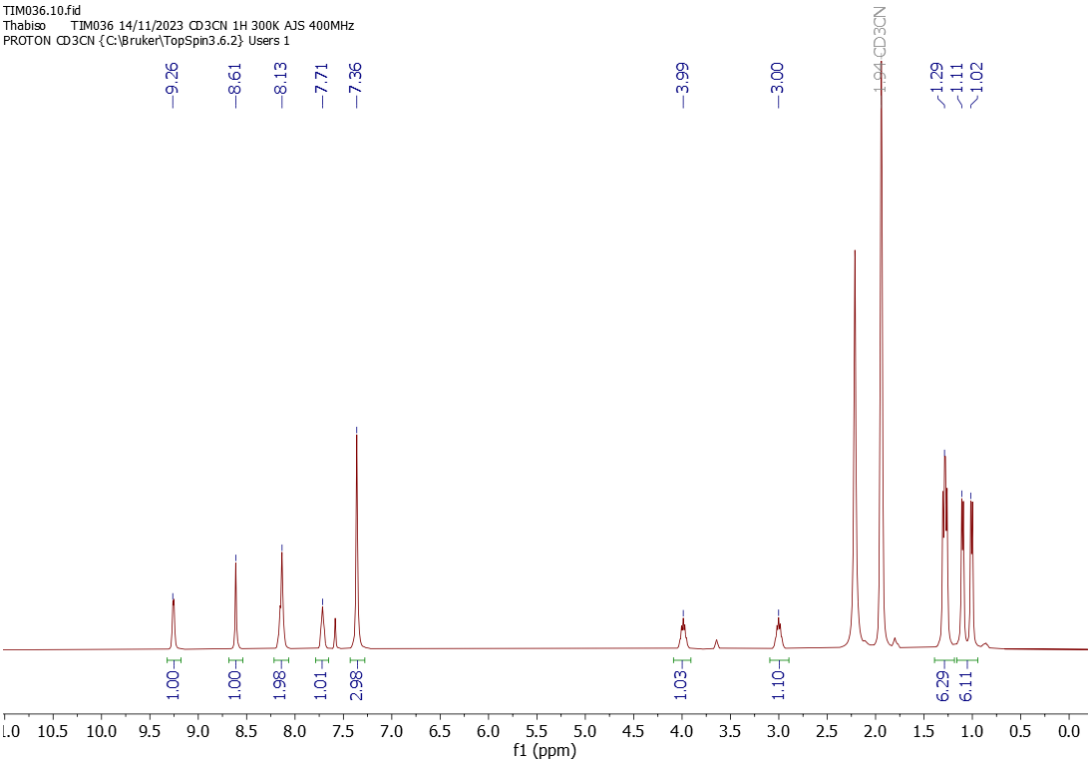

Figure 23: ^{1}H NMR spectrum of pyridylimine manganese complex **C3** recorded at 300 K.

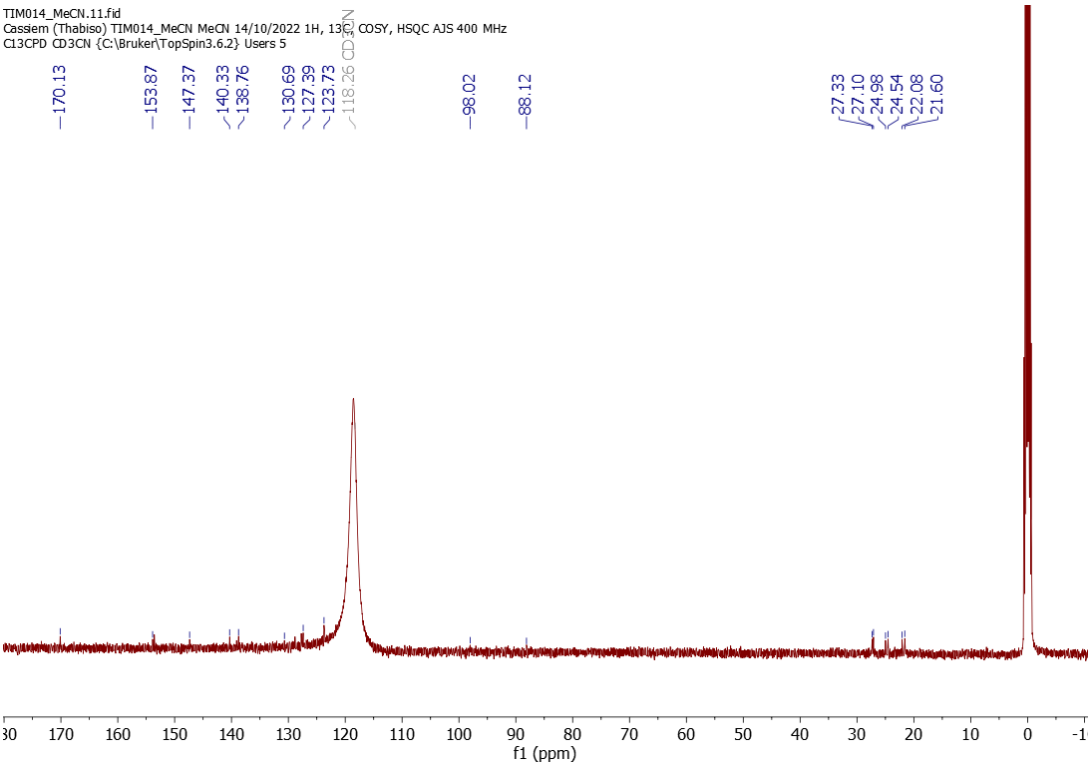

Figure 24: ^{13}C NMR spectrum of pyridylimine manganese complex **C3** recorded at 300 K.

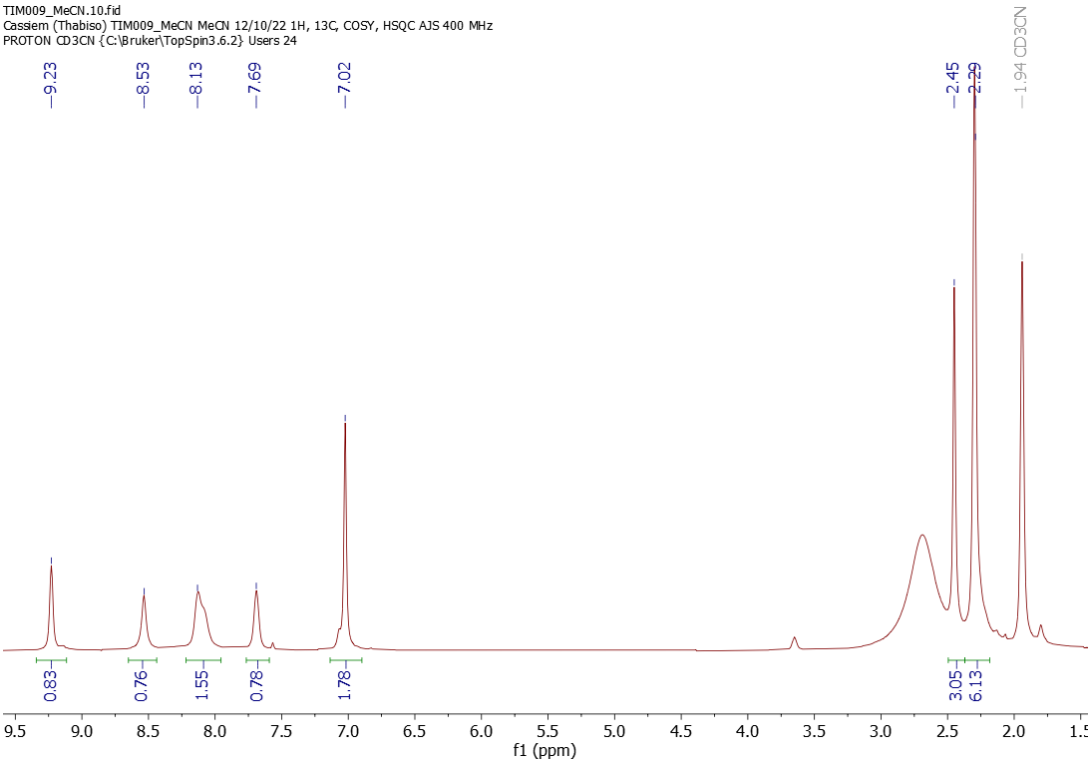

Figure 25: ^{1}H NMR spectrum of pyridylimine manganese complex **C4** recorded at 300 K.

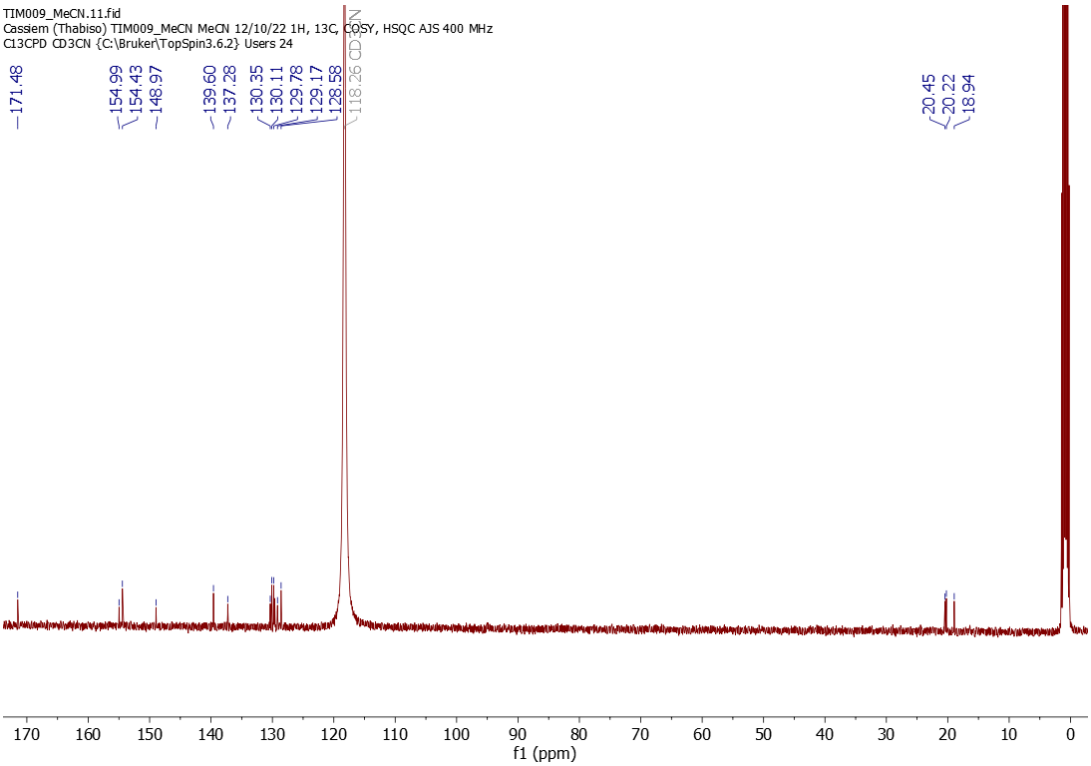

Figure 26: ^{13}C NMR spectrum of pyridylimine manganese complex **C4** recorded at 300 K.

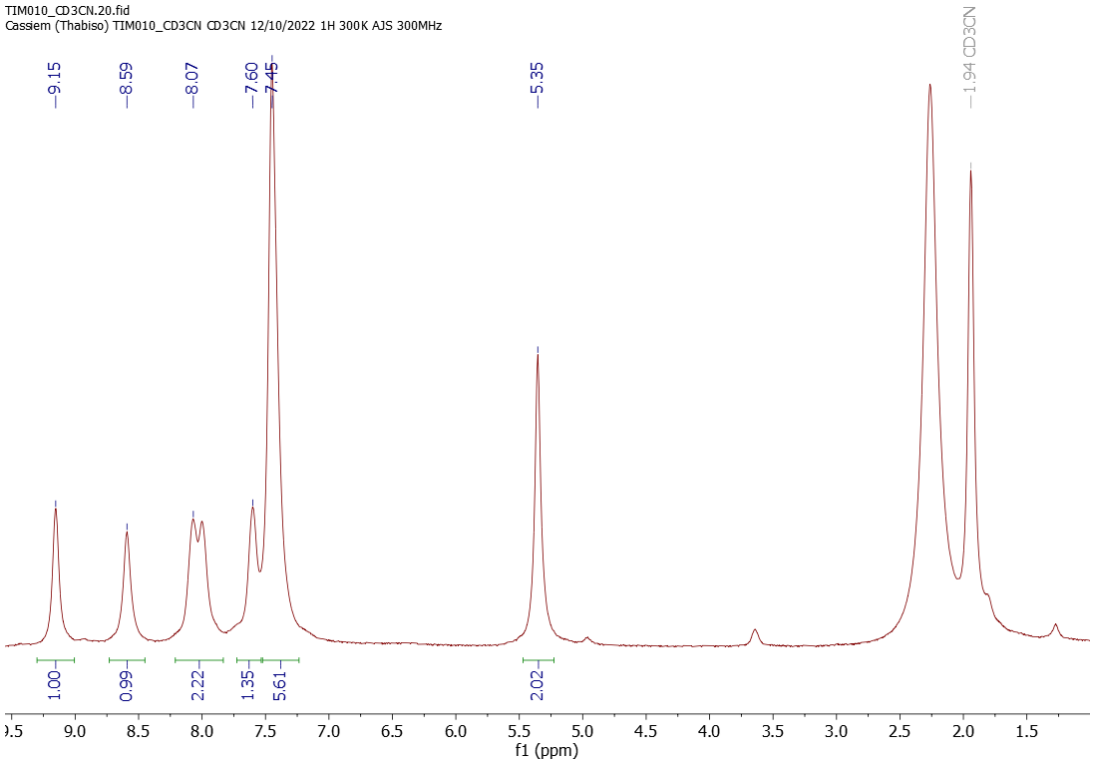

Figure 27: ^{1}H NMR spectrum of pyridylimine manganese complex **C5** recorded at 300 K.

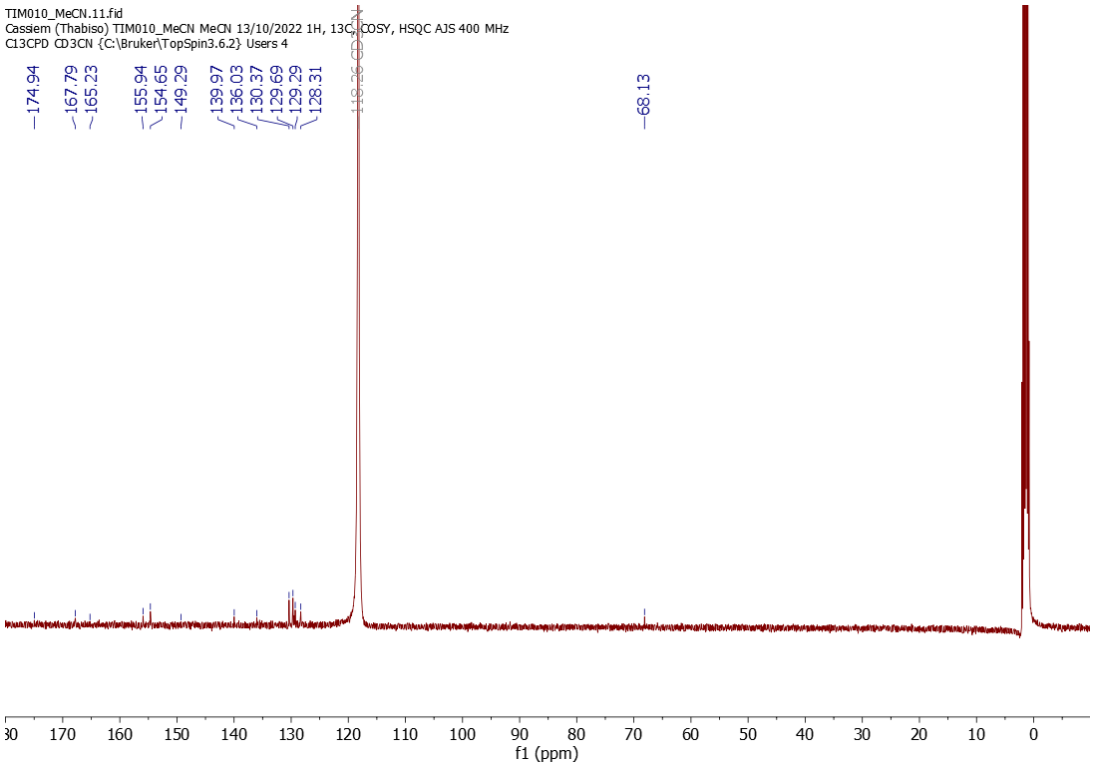

Figure 28: ^{13}C NMR spectrum of pyridylimine manganese complex **C5** recorded at 300 K.

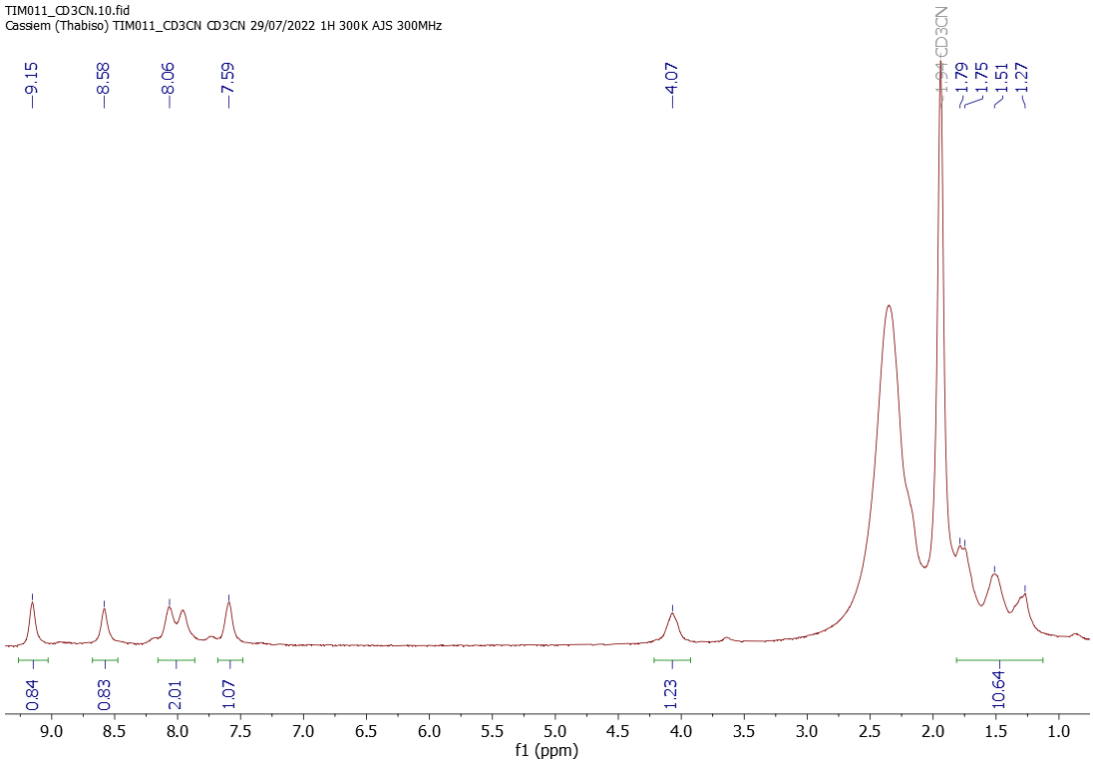

Figure 29: ^{1}H NMR spectrum of pyridylimine manganese complex **C6** recorded at 300 K.

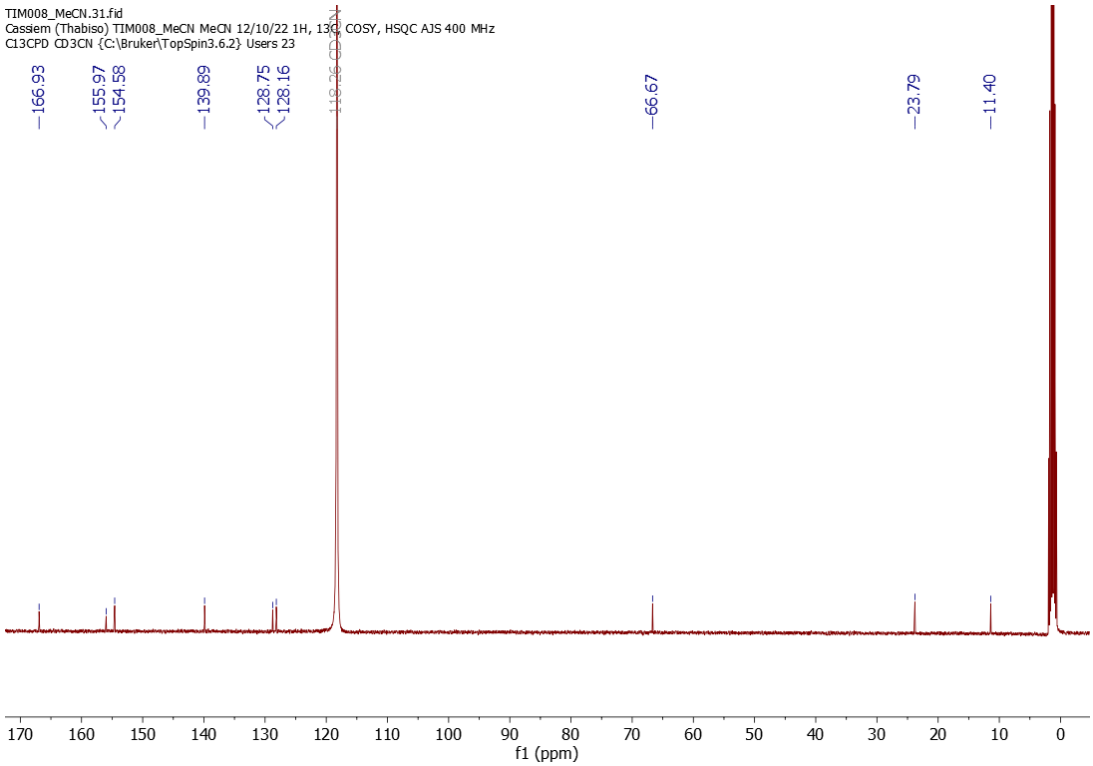

Figure 30: ^{13}C NMR spectrum of pyridylimine manganese complex **C6** recorded at 300 K.

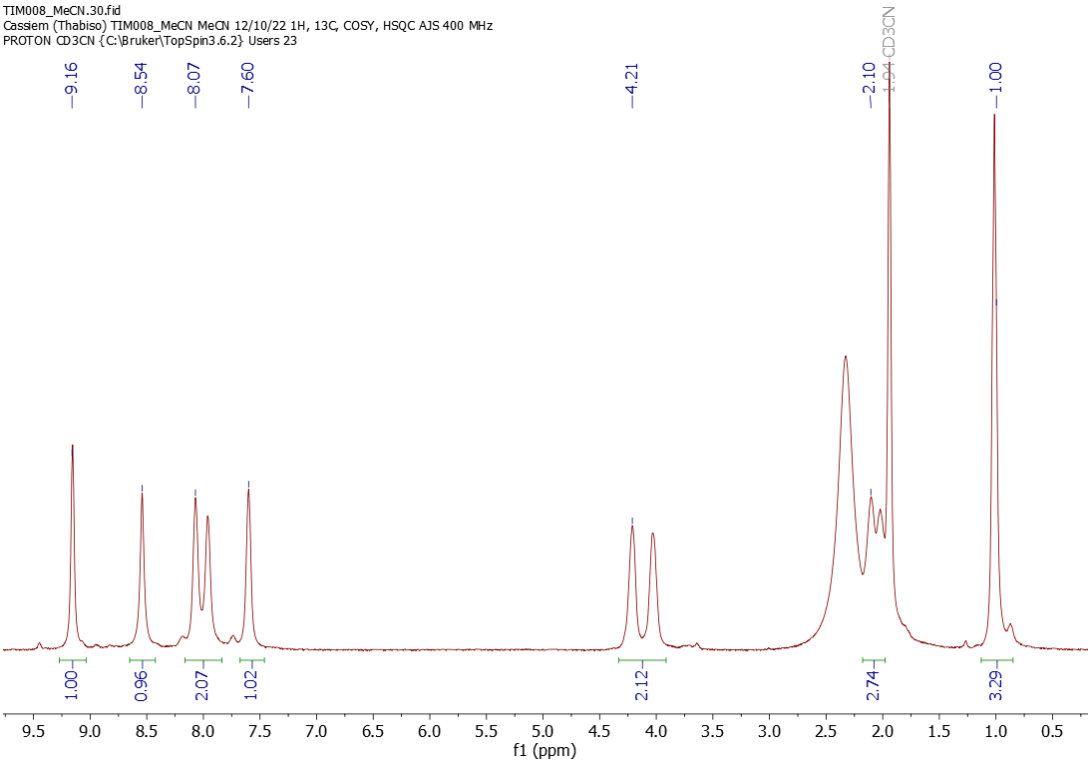

Figure 31: ^{1}H NMR spectrum of pyridylimine manganese complex **C7** recorded at 300 K.

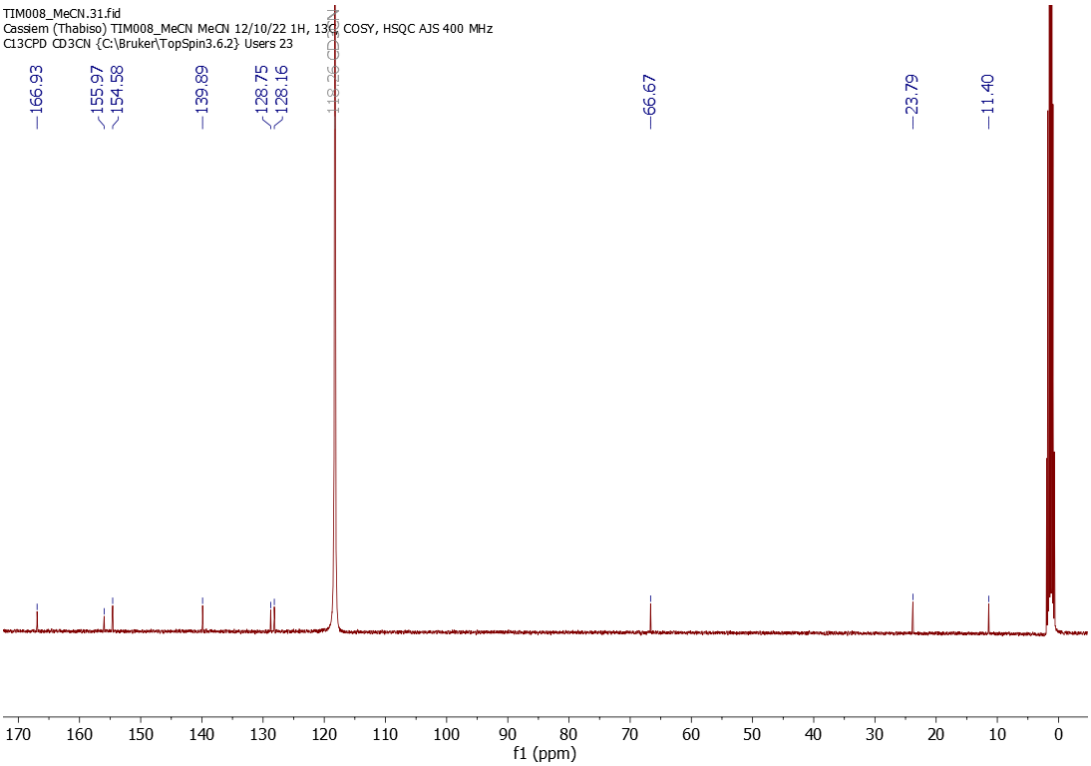

Figure 32: ^{13}C NMR spectrum of pyridylimine manganese complex **C7** recorded at 300 K.

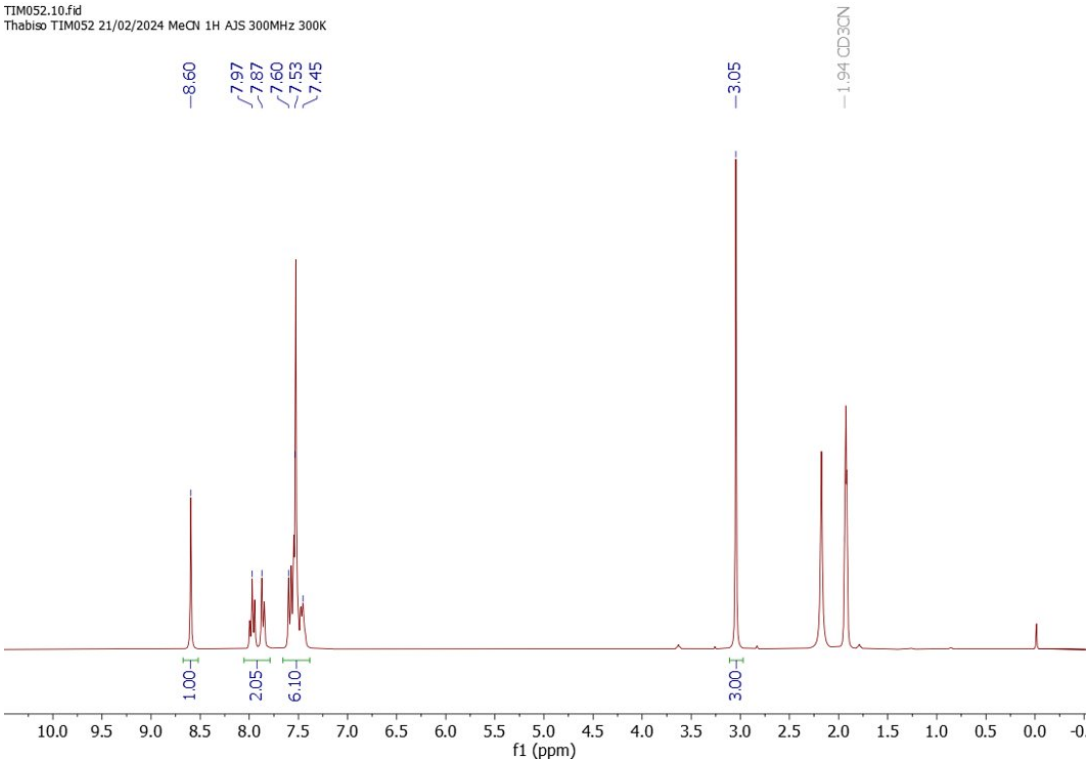

Figure 33: ^{1}H NMR spectrum of pyridylimine manganese complex **C8** recorded at 300 K.

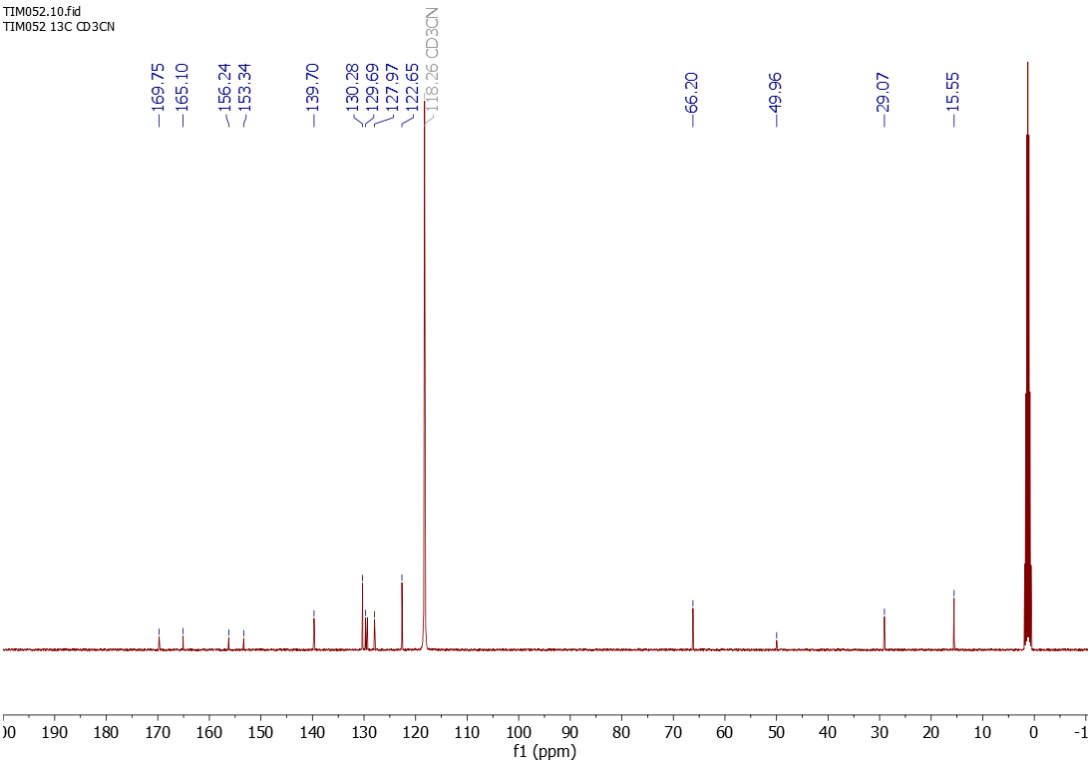

Figure 34: ^{13}C NMR spectrum of pyridylimine manganese complex **C8** recorded at 300 K.

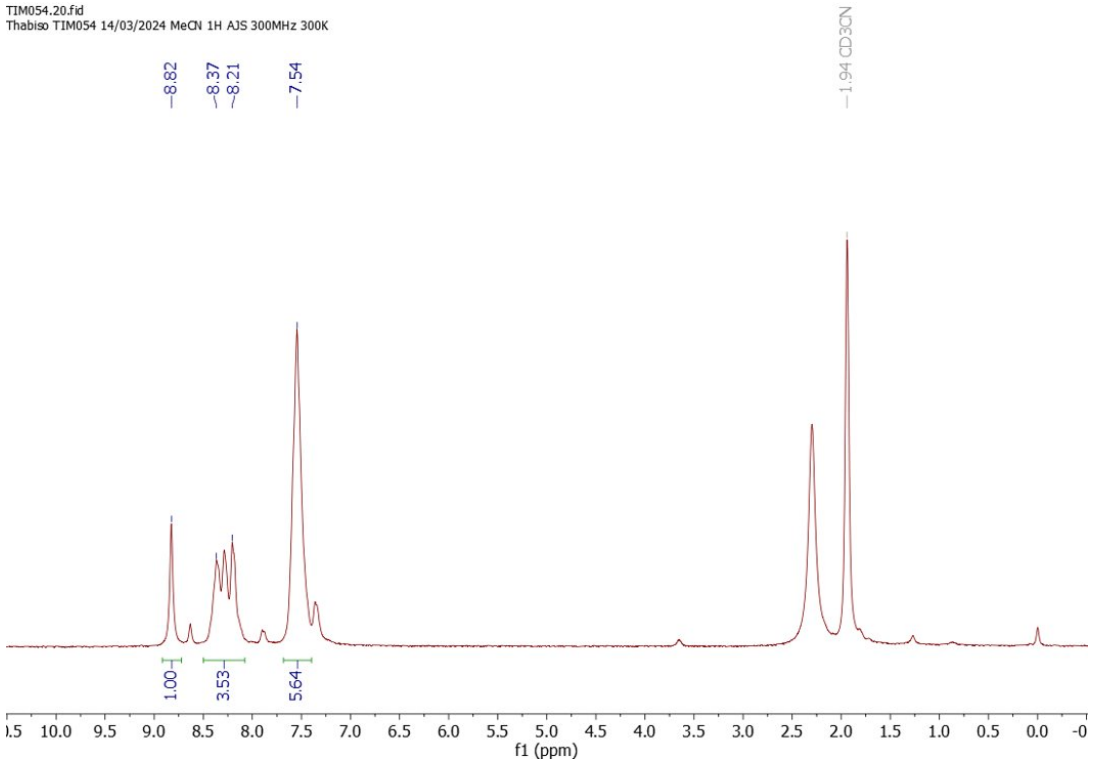

Figure 35: ^{1}H NMR spectrum of pyridylimine manganese complex **C9** recorded at 300 K.

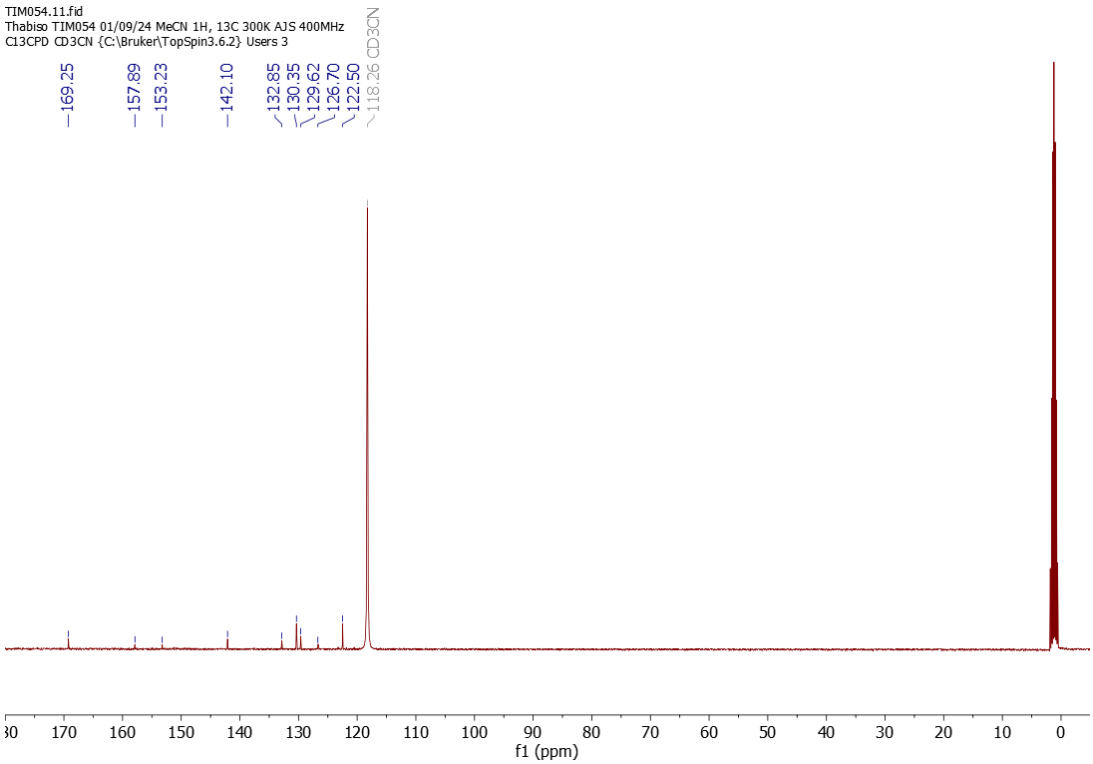

Figure 36: ^{13}C NMR spectrum of pyridylimine manganese complex **C9** recorded at 300 K.

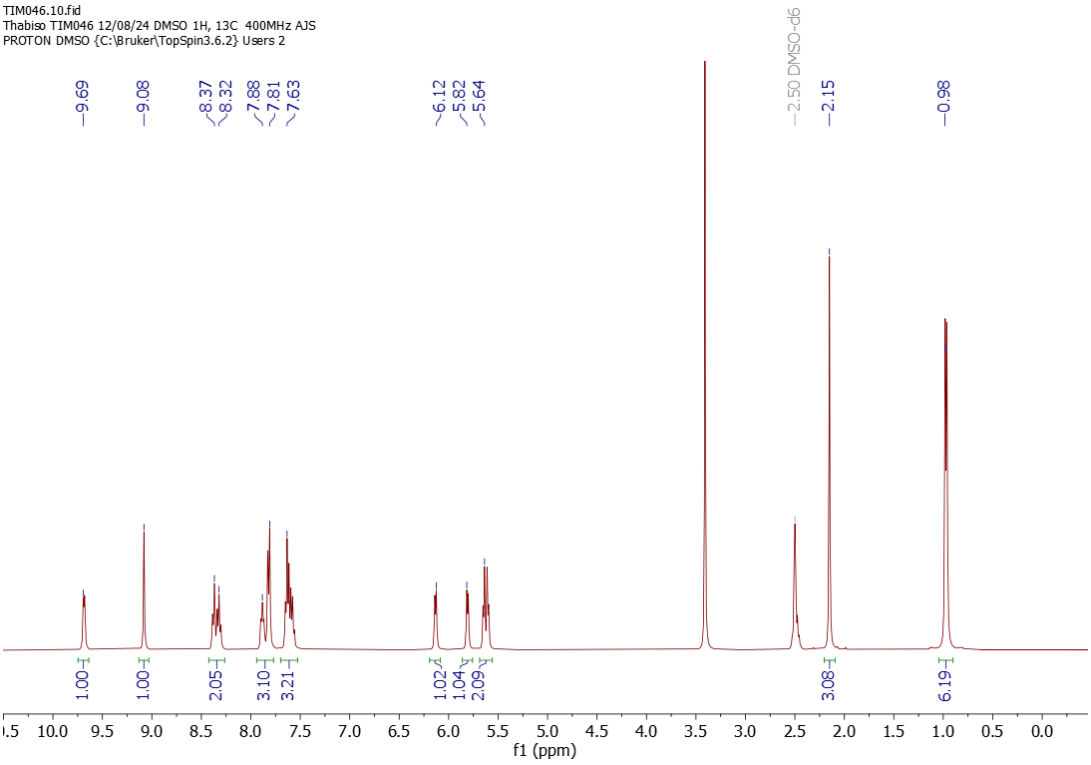

Figure 37: ^{1}H NMR spectrum of pyridylimine ruthenium complex **C10** recorded at 300 K.

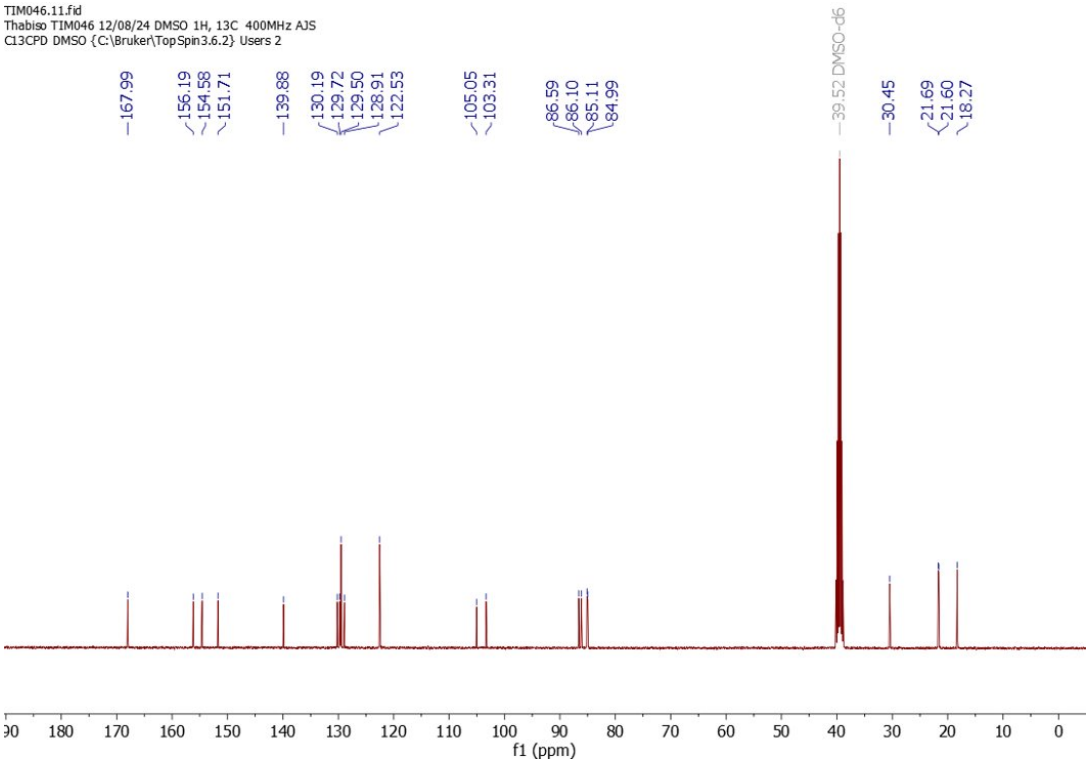

Figure 38: ^{13}C NMR spectrum of pyridylimine ruthenium complex **C10** recorded at 300 K.

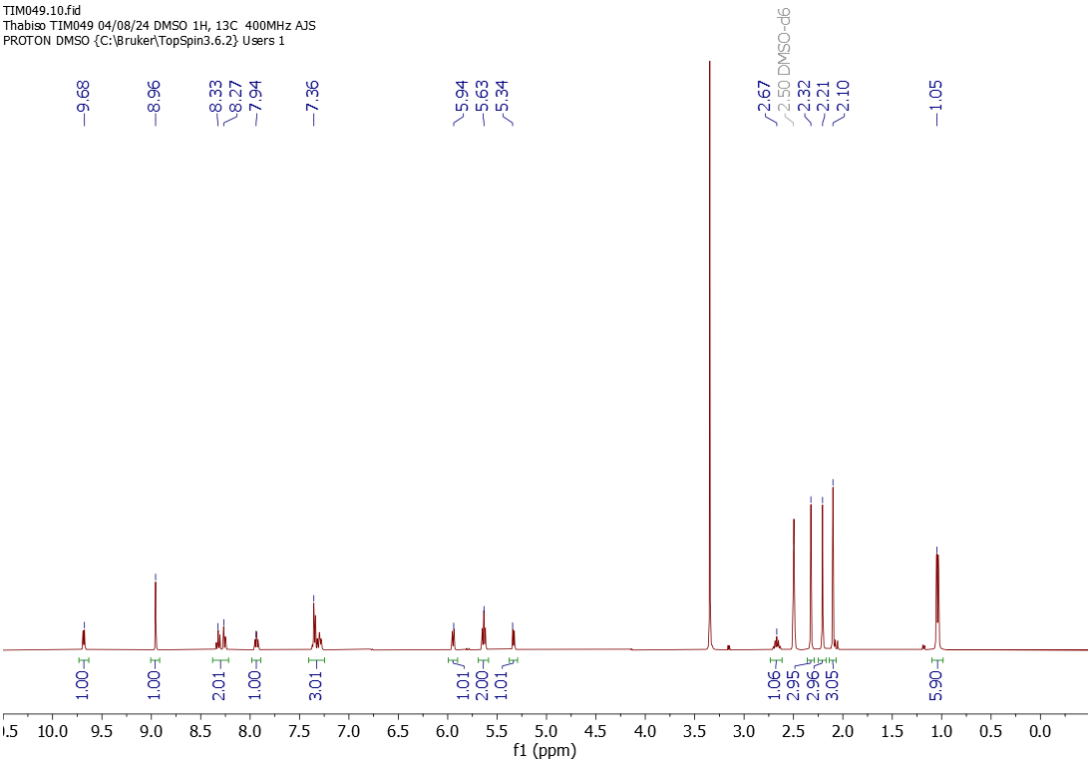

Figure 39: ^{1}H NMR spectrum of pyridylimine ruthenium complex **C11** recorded at 300 K.

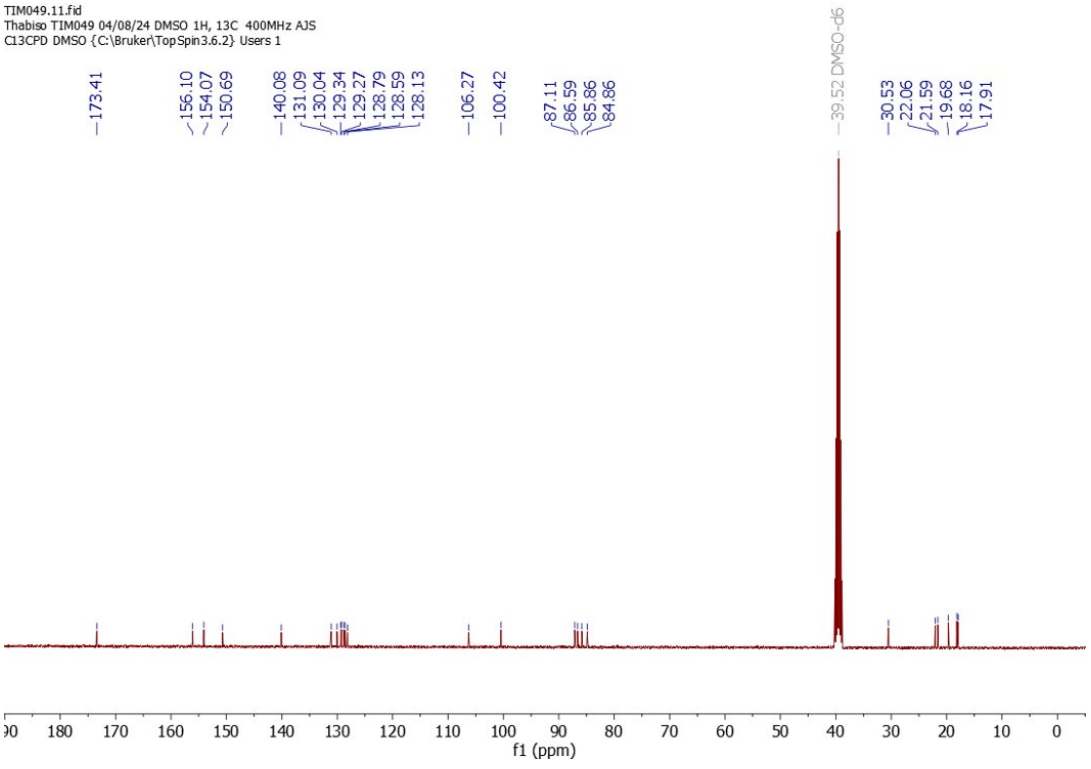

Figure 40: ^{13}C NMR spectrum of pyridylimine ruthenium complex **C11** recorded at 300 K.

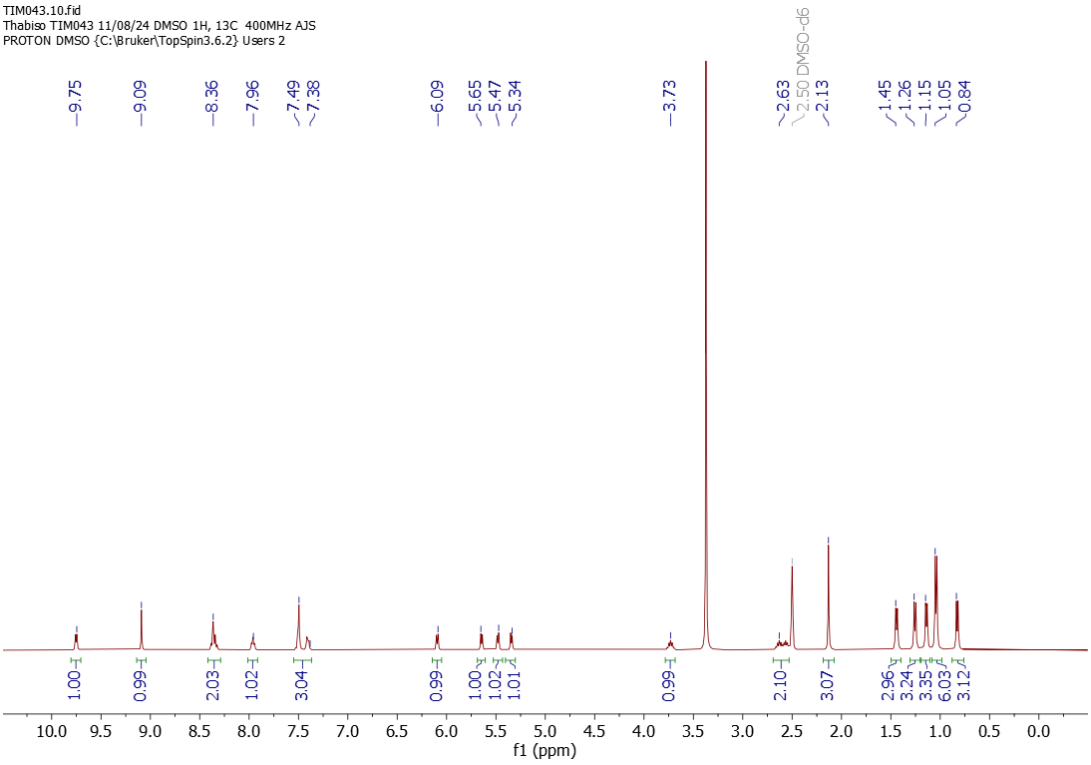

Figure 41: ^{1}H NMR spectrum of pyridylimine ruthenium complex **C12** recorded at 300 K.

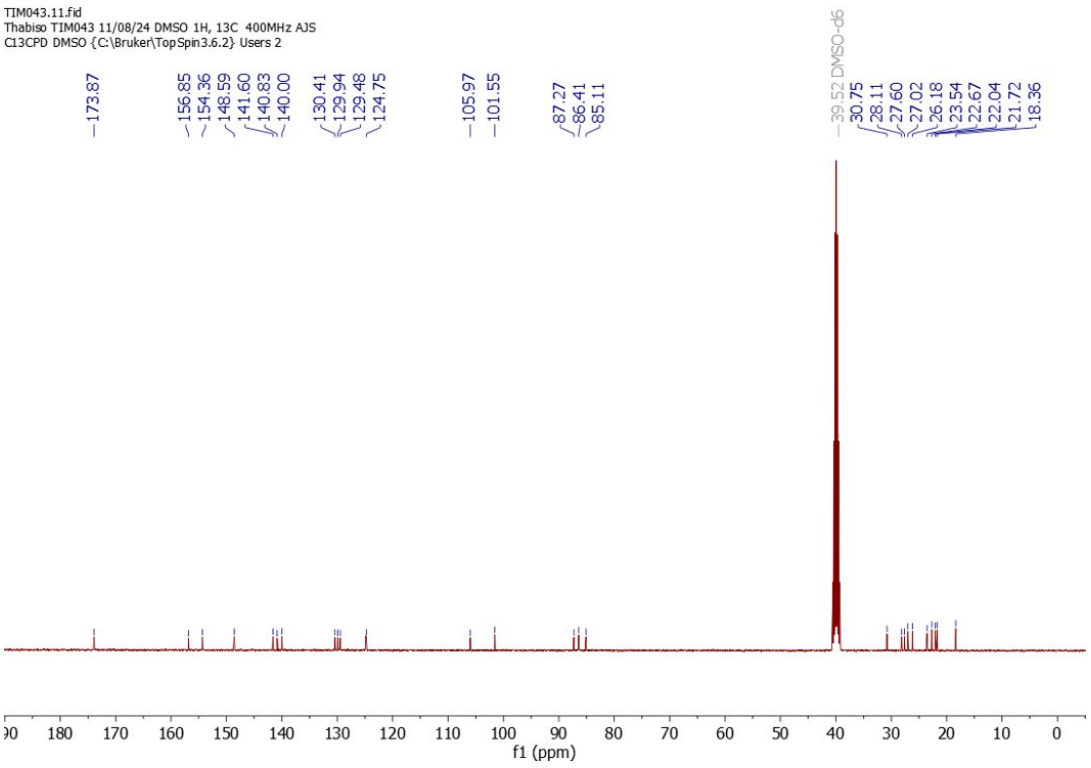

Figure 42: ^{13}C NMR spectrum of pyridylimine ruthenium complex **C12** recorded at 300 K.

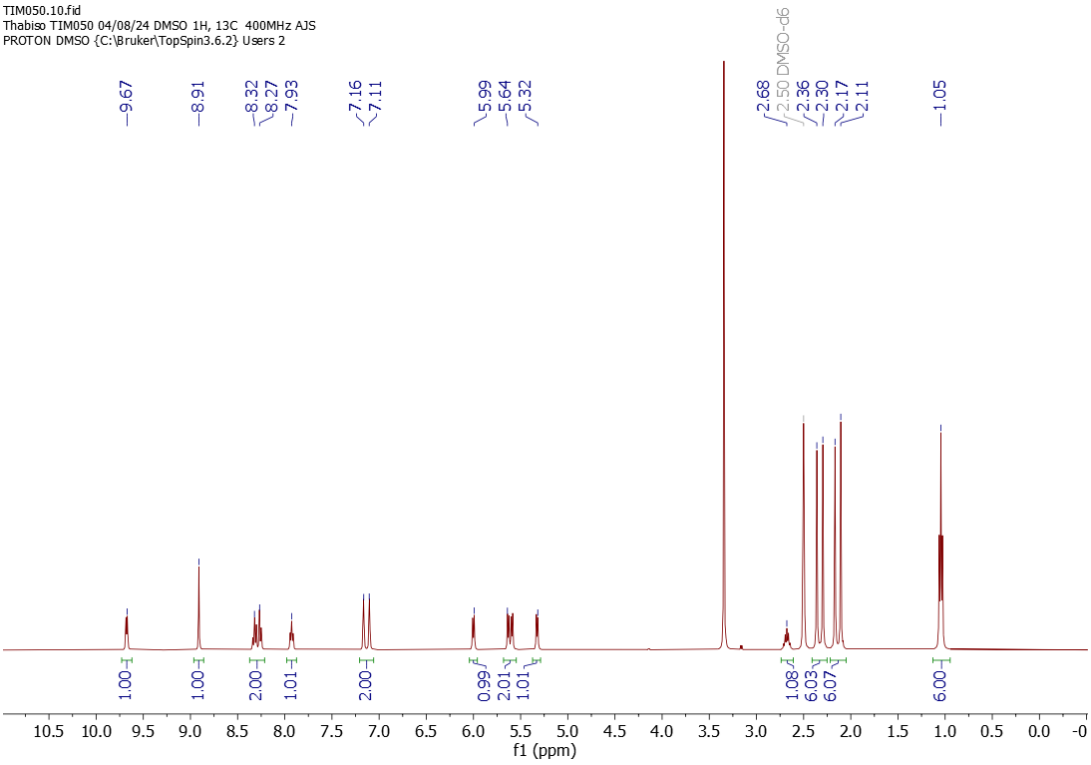

Figure 43: ^{1}H NMR spectrum of pyridylimine ruthenium complex **C13** recorded at 300 K.

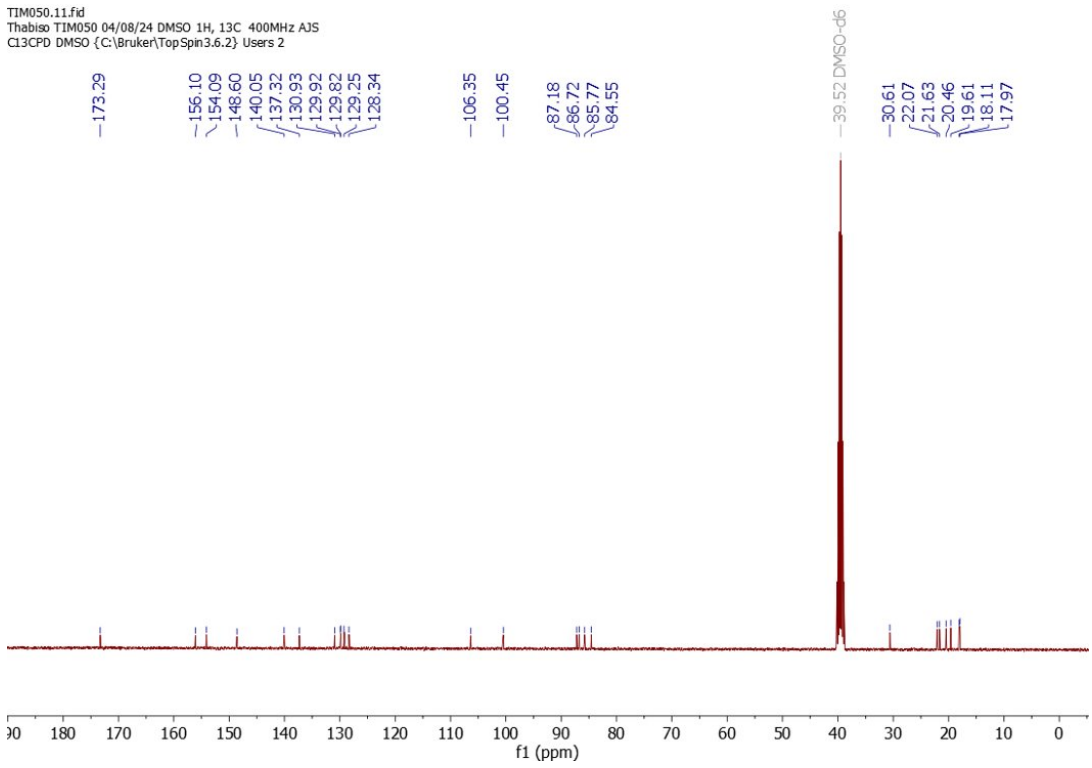

Figure 44: ^{13}C NMR spectrum of pyridylimine ruthenium complex **C13** recorded at 300 K.

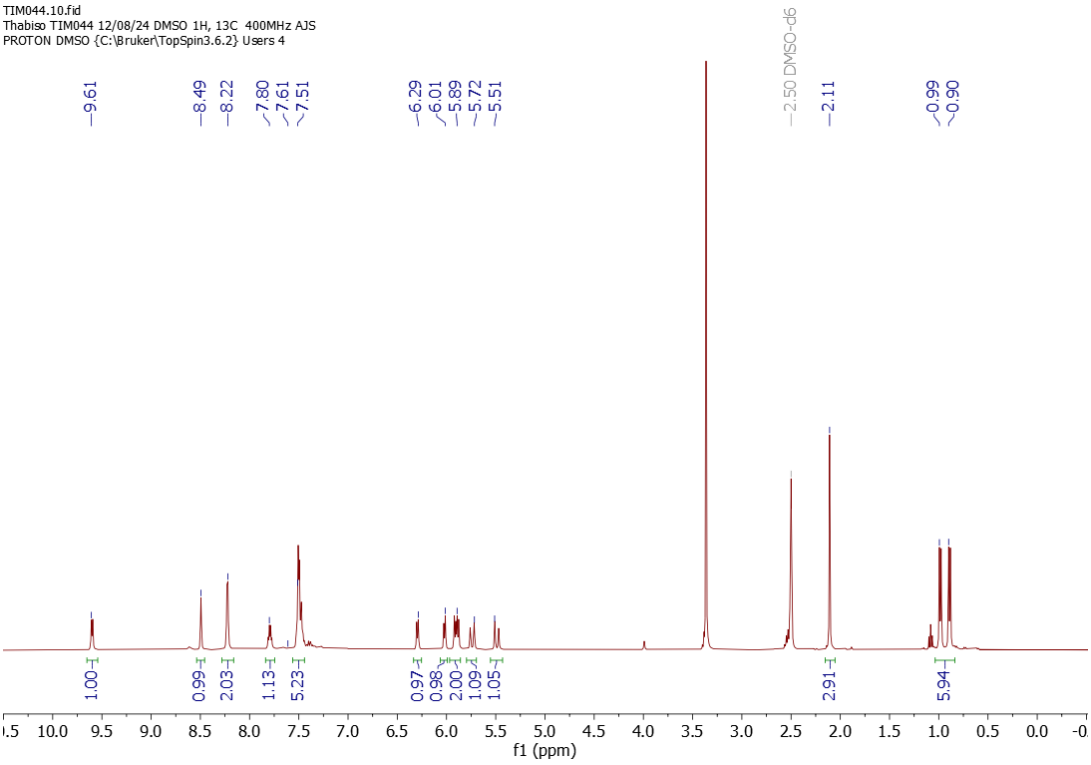

Figure 45: ^{1}H NMR spectrum of pyridylimine ruthenium complex **C14** recorded at 300 K.

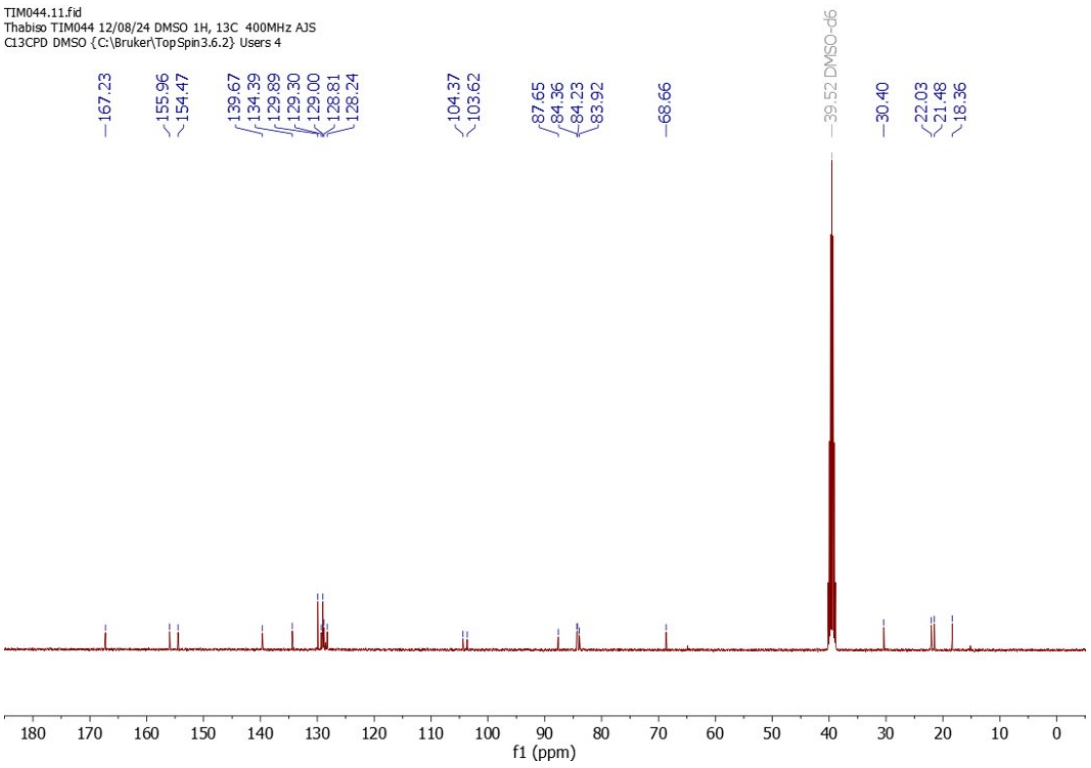

Figure 46: ^{13}C NMR spectrum of pyridylimine ruthenium complex **C14** recorded at 300 K.

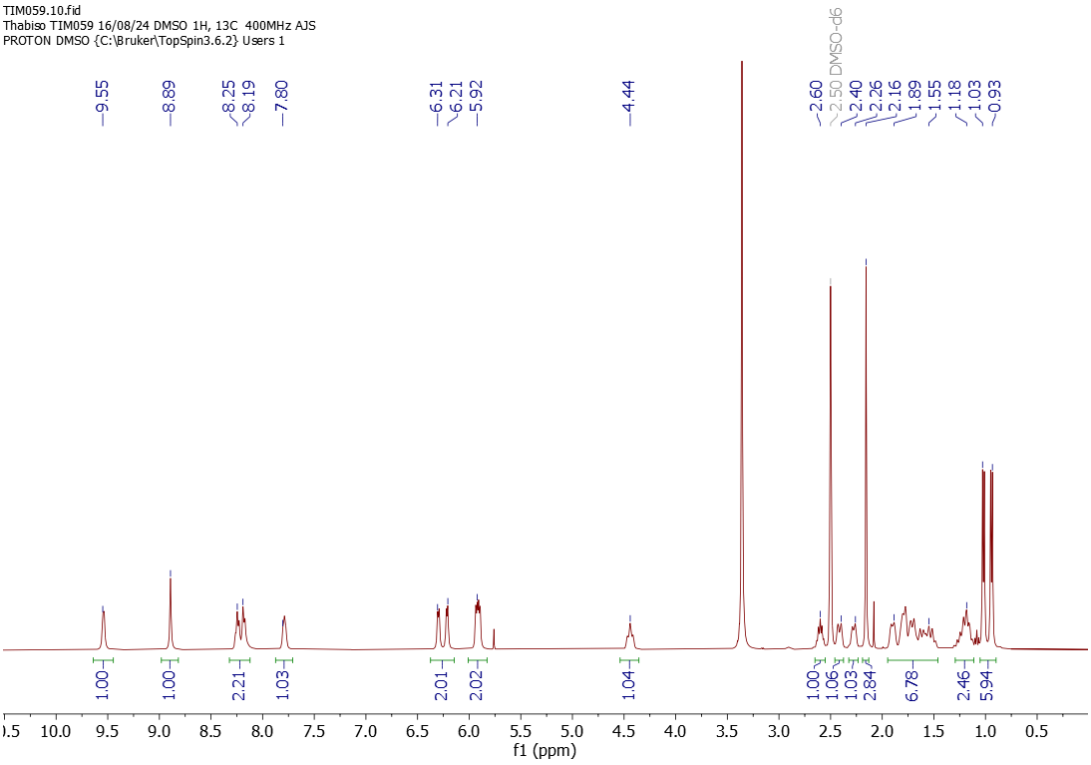

Figure 47: ^{1}H NMR spectrum of pyridylimine ruthenium complex **C15** recorded at 300 K.

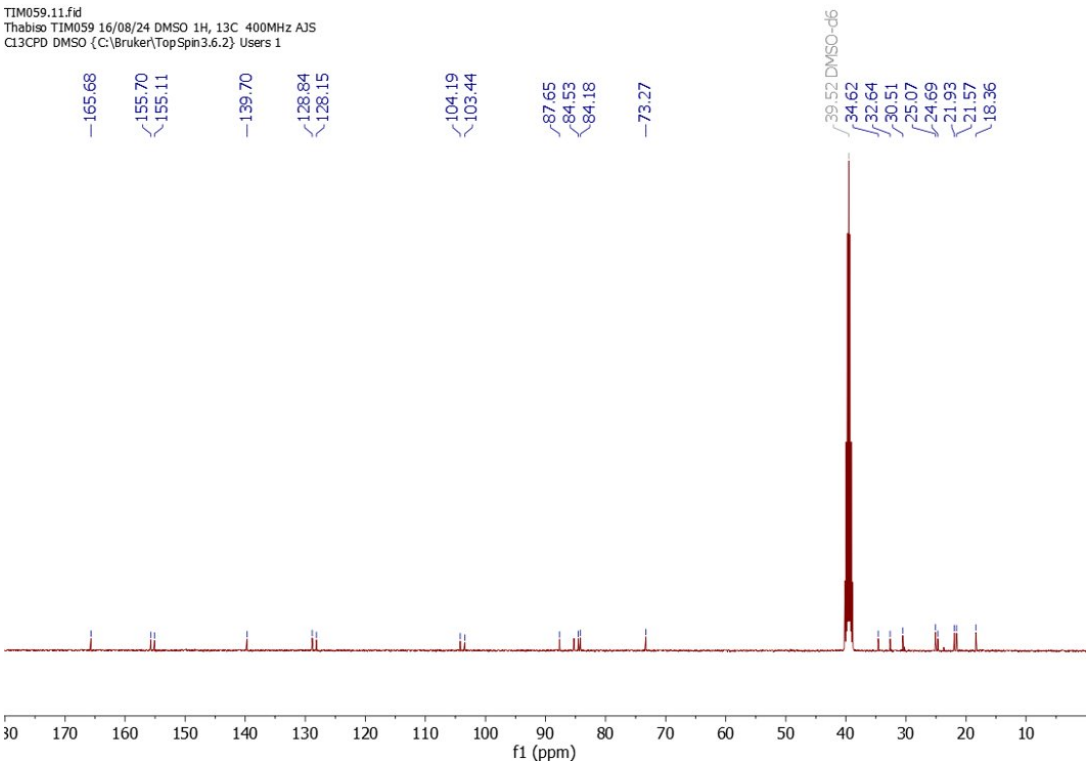

Figure 48: ^{13}C NMR spectrum of pyridylimine ruthenium complex **C15** recorded at 300 K.

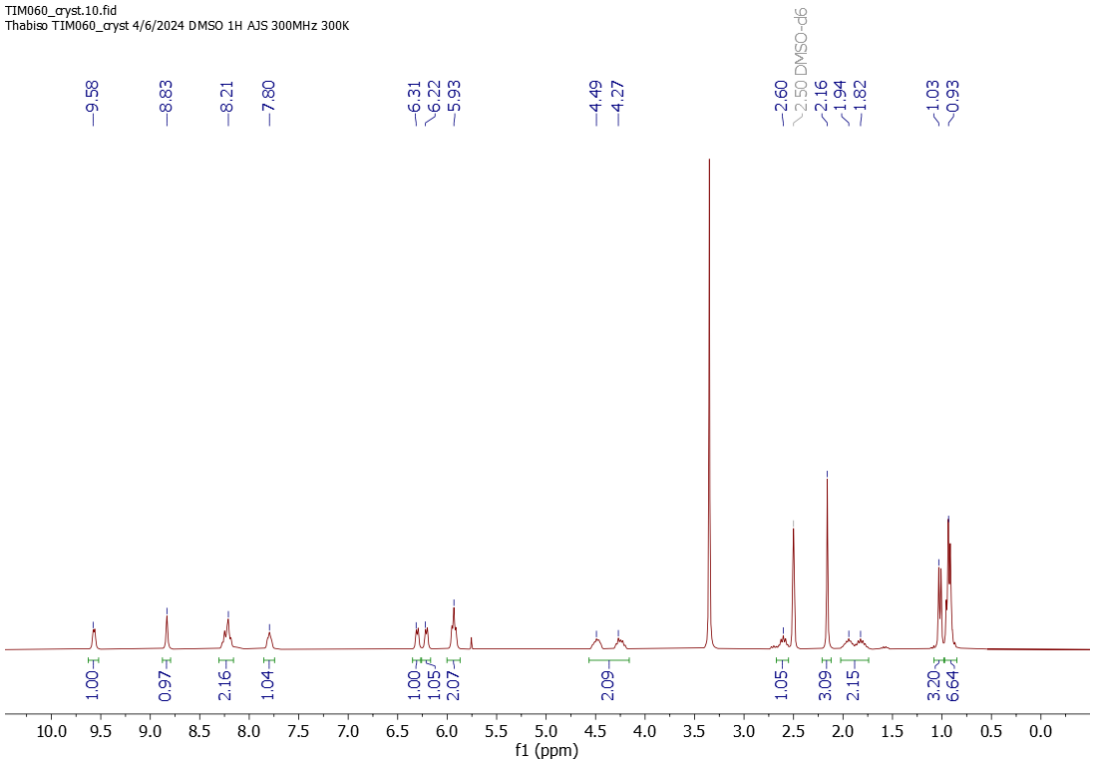

Figure 49: ^{1}H NMR spectrum of pyridylimine ruthenium complex **C16** recorded at 300 K.

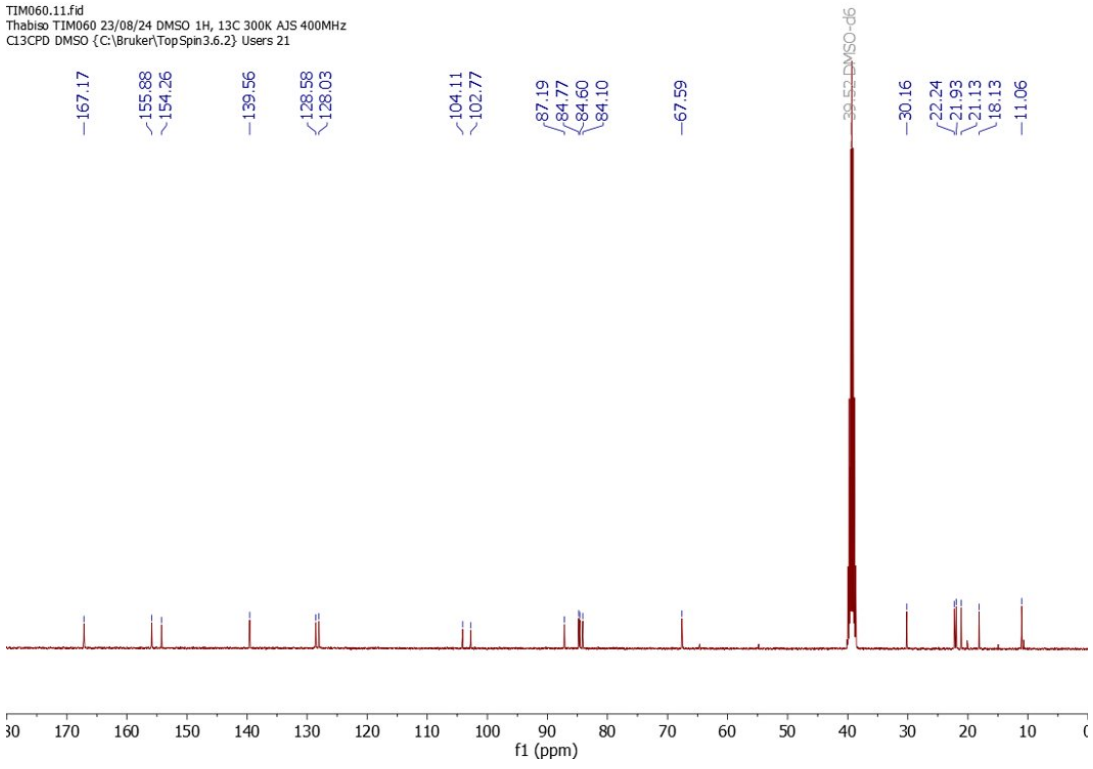

Figure 50: ^{13}C NMR spectrum of pyridylimine ruthenium complex **C16** recorded at 300 K.

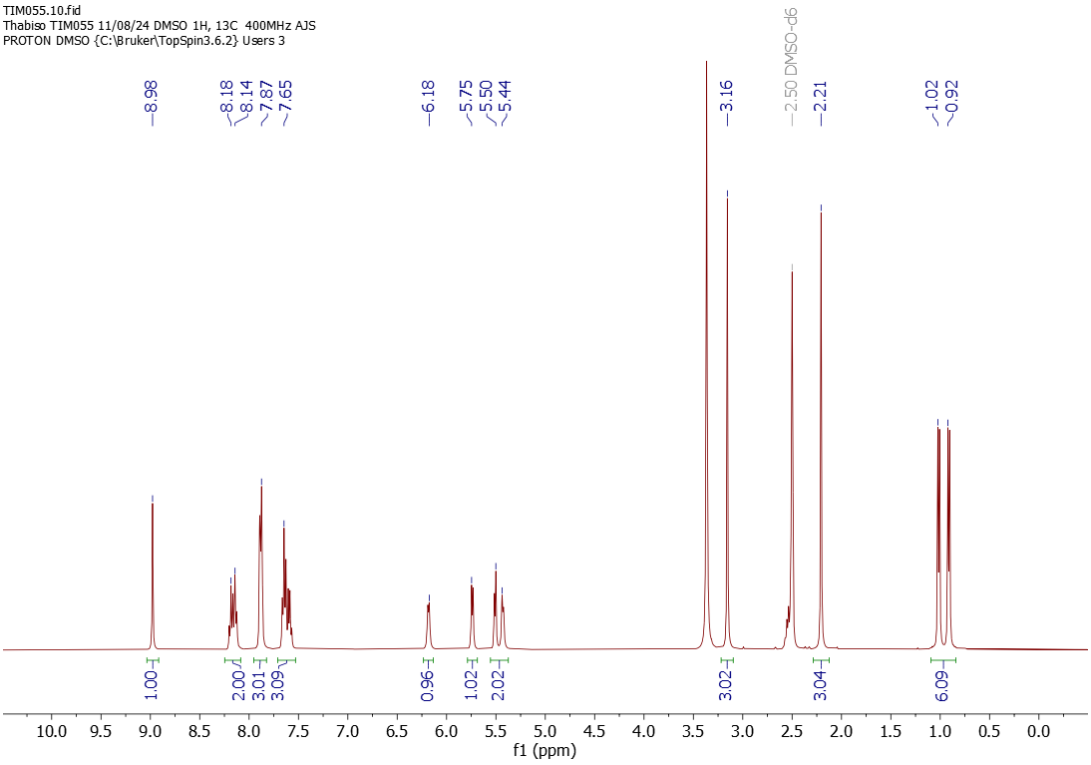

Figure 51: ^{1}H NMR spectrum of pyridylimine ruthenium complex **C17** recorded at 300 K.

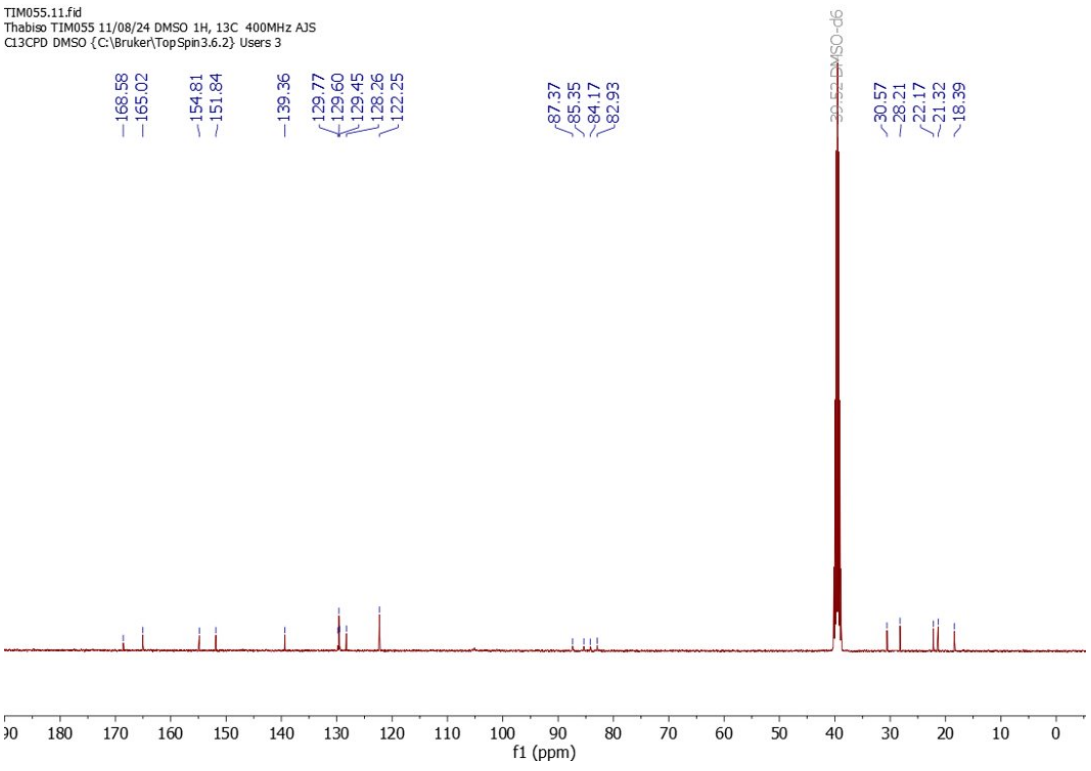

Figure 52: ^{13}C NMR spectrum of pyridylimine ruthenium complex **C17** recorded at 300 K.

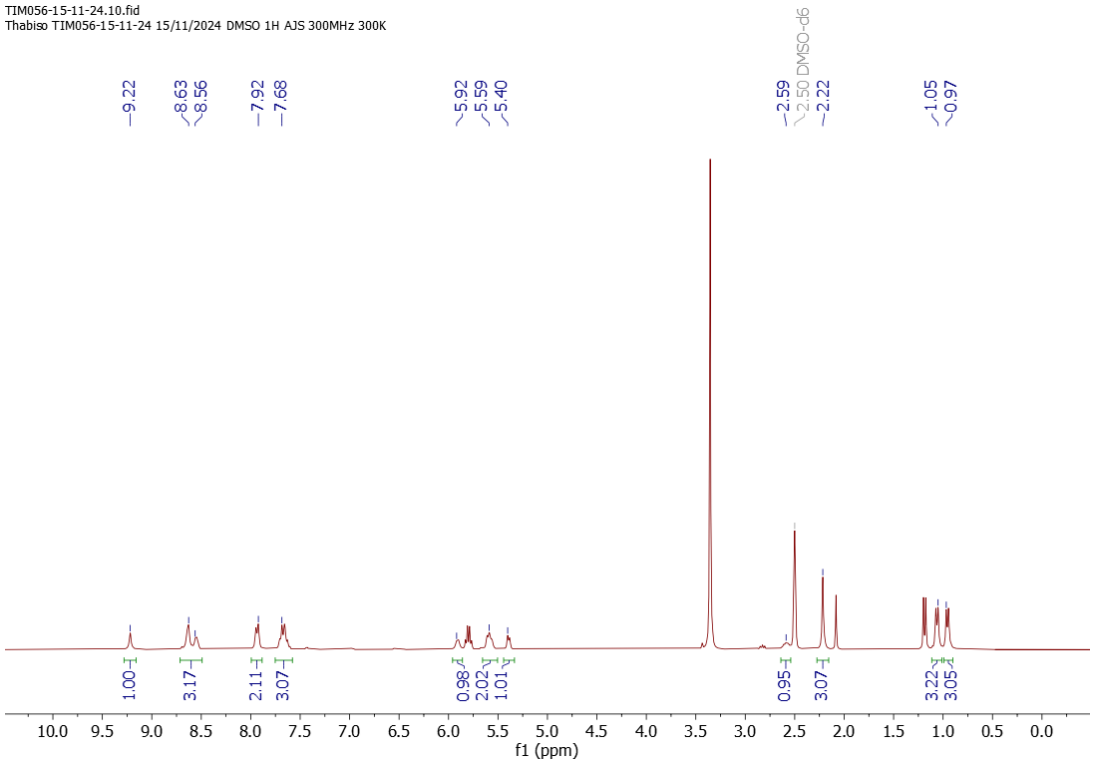

Figure 53: ^{1}H NMR spectrum of pyridylimine ruthenium complex **C18** recorded at 300 K.

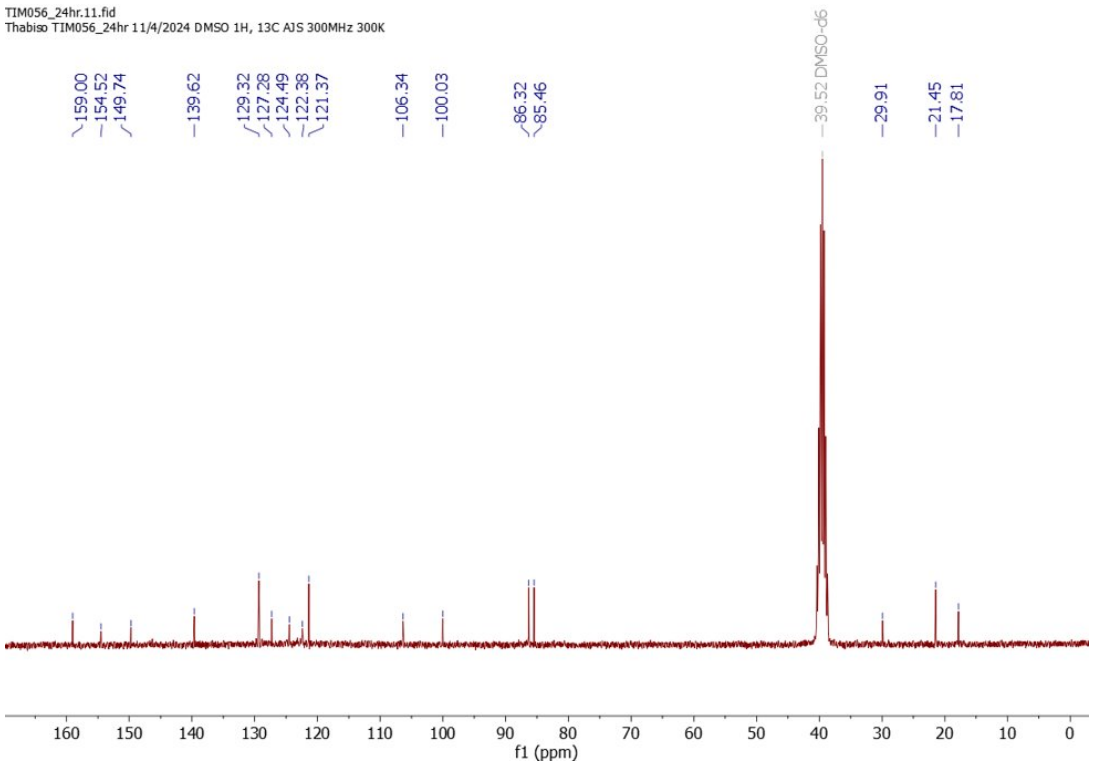

Figure 54: ^{13}C NMR spectrum of pyridylimine ruthenium complex **C18** recorded at 300 K.

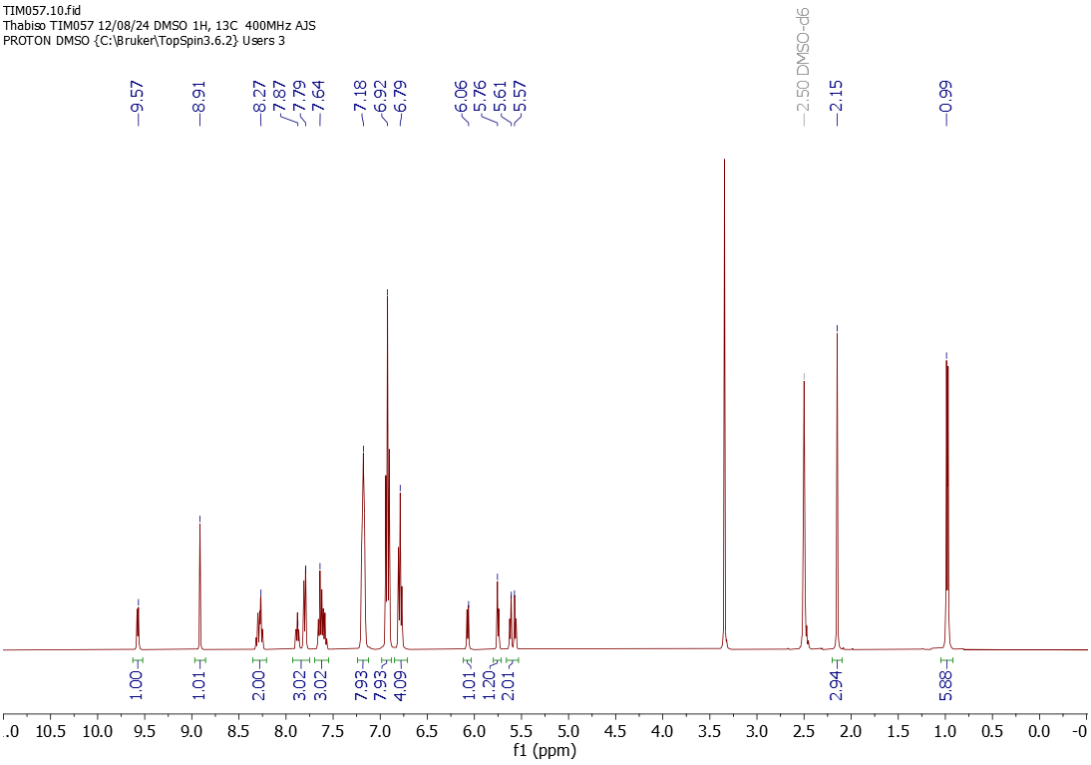

Figure 55: ^{1}H NMR spectrum of pyridylimine ruthenium complex **C19** recorded at 300 K.

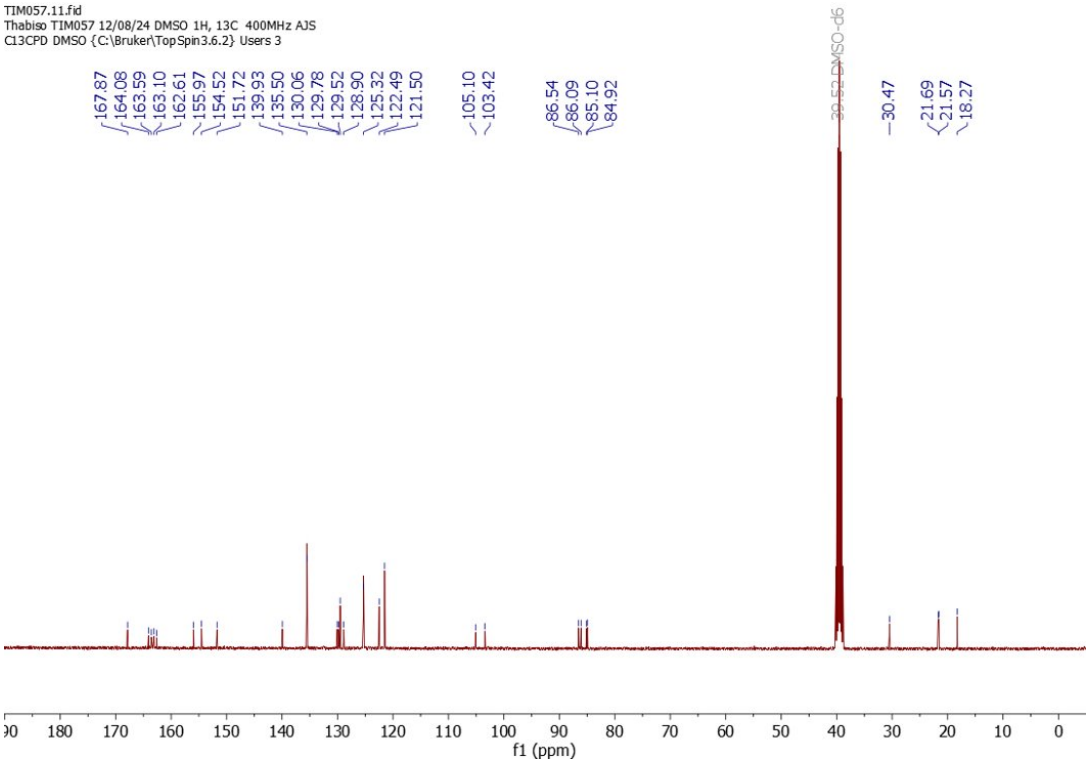

Figure 56: ^{13}C NMR spectrum of pyridylimine ruthenium complex **C19** recorded at 300 K.

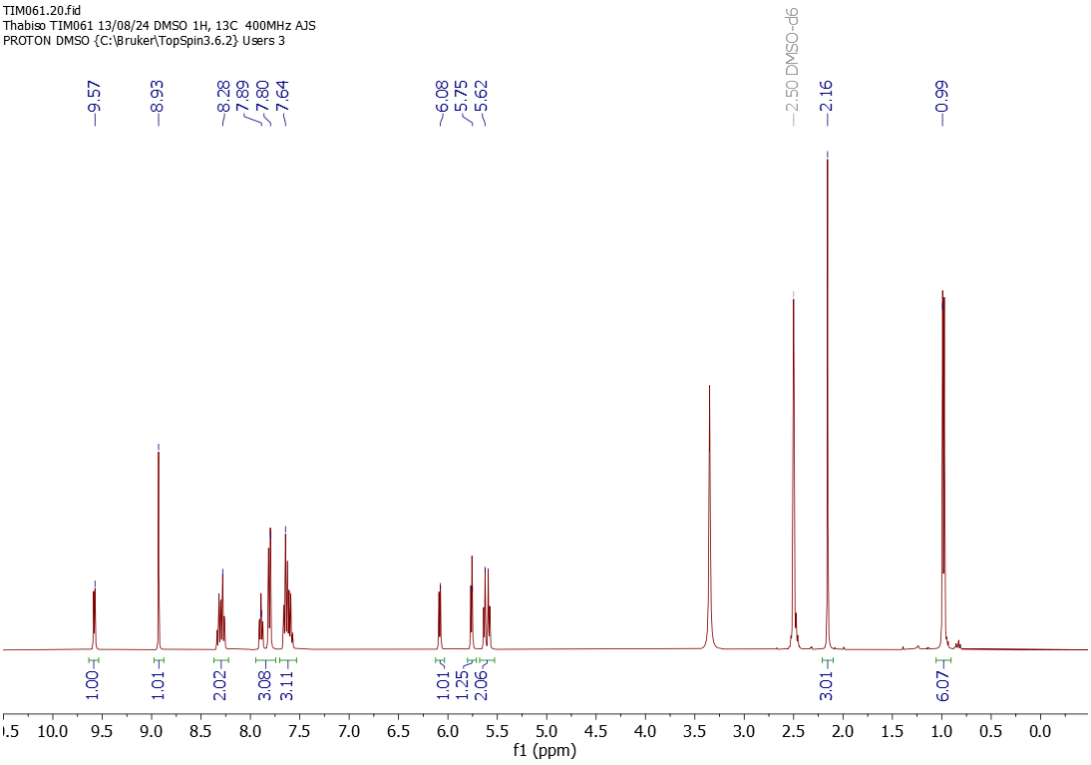

Figure 57: ^{1}H NMR spectrum of pyridylimine ruthenium complex **C20** recorded at 300 K.

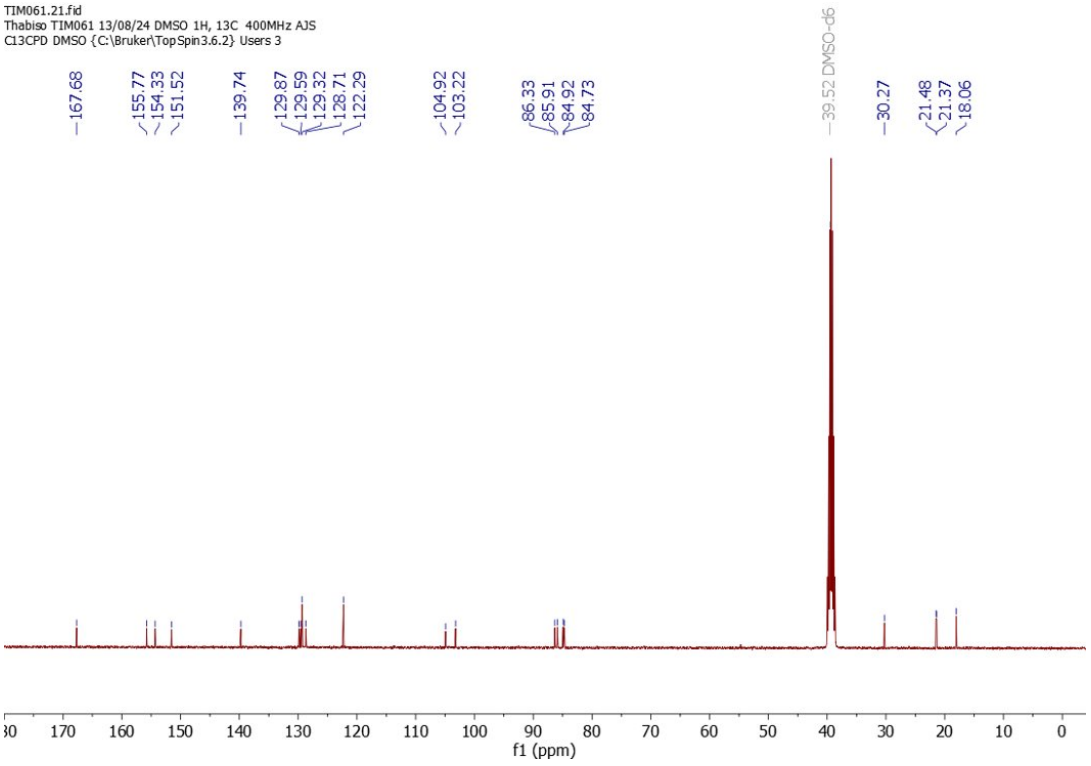

Figure 58: ^{13}C NMR spectrum of pyridylimine ruthenium complex **C20** recorded at 300 K.

FT-IR Spectra (Ligands and Complexes)

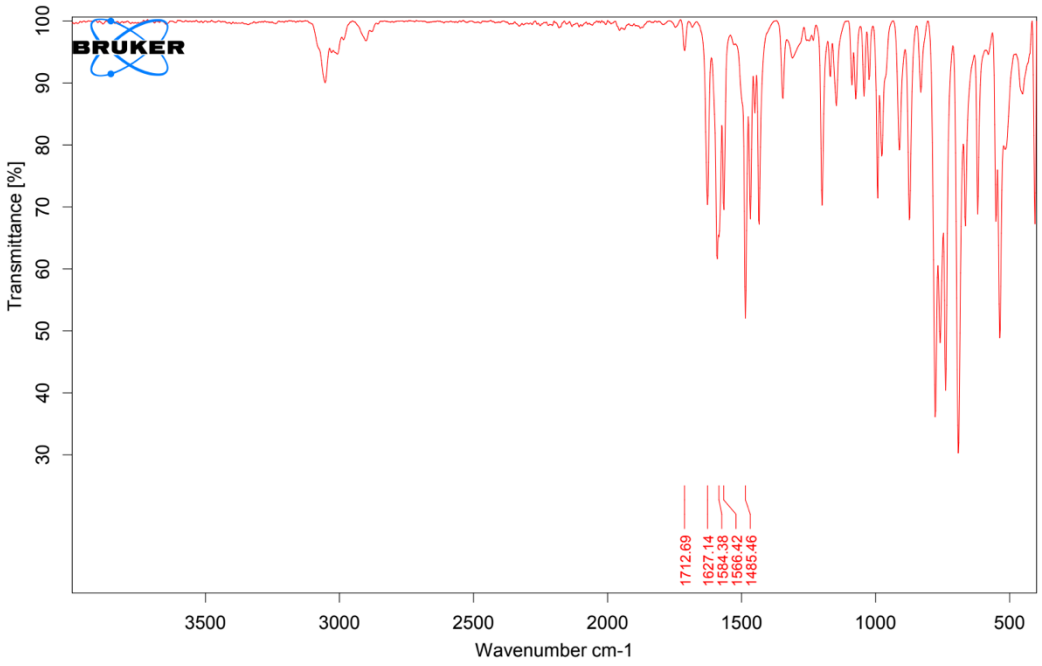

Figure 59: FT-IR spectrum of pyridylimine ligand **L1**.

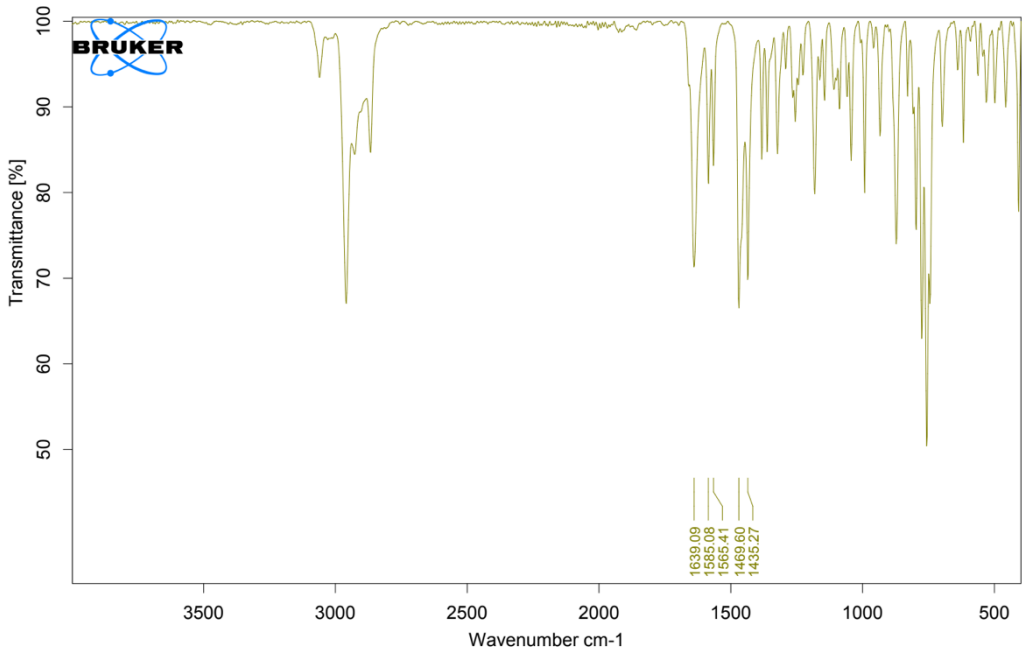

Figure 60: FT-IR spectrum of pyridylimine ligand **L2**.

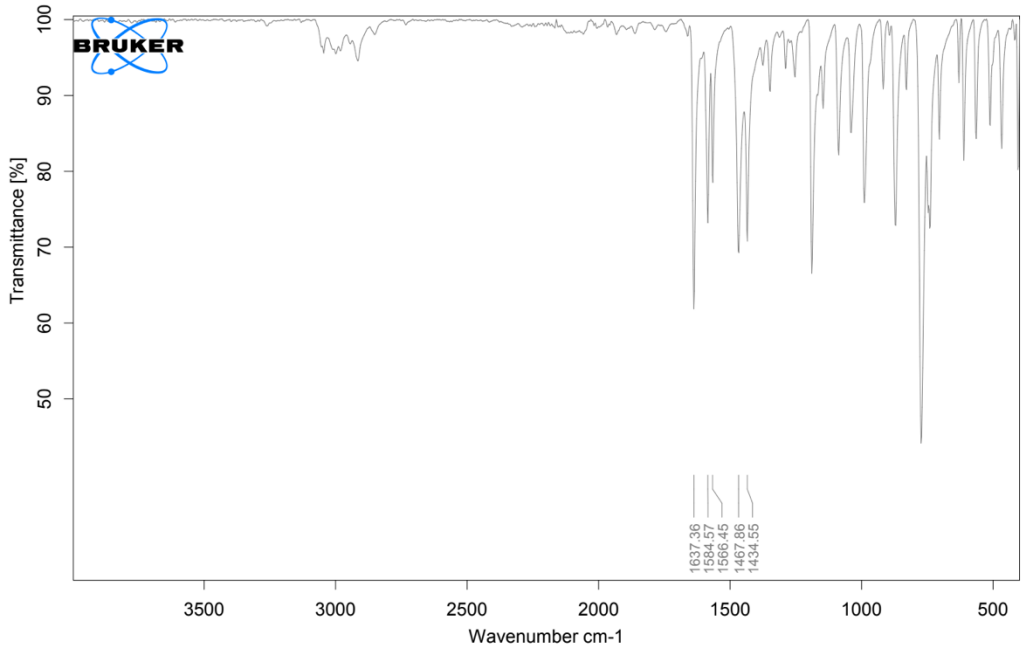

Figure 61: FT-IR spectrum of pyridylimine ligand **L3**.

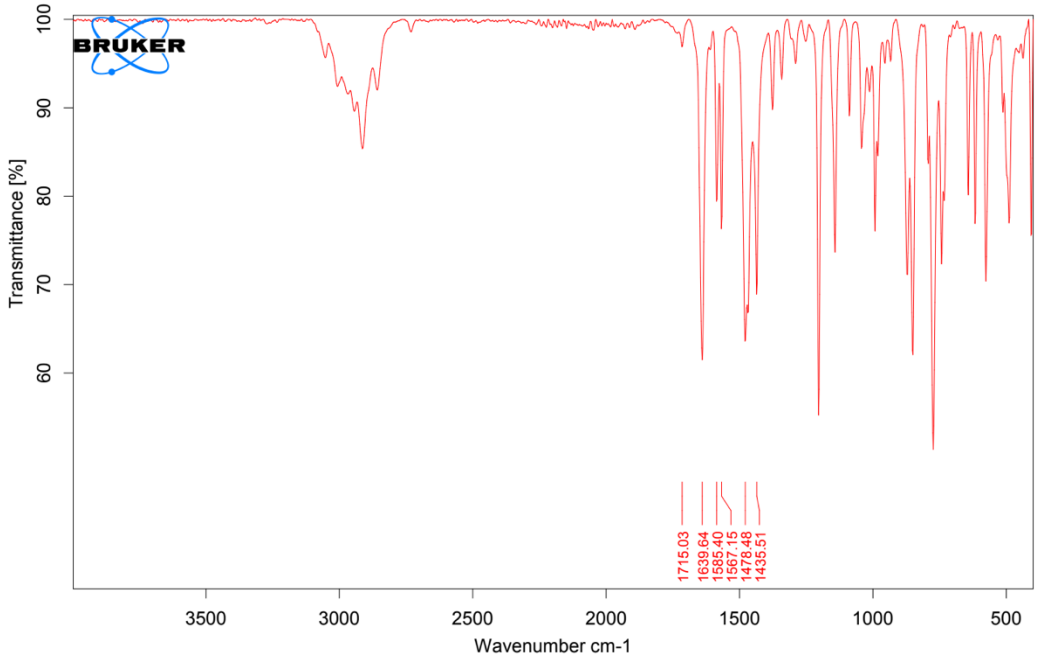

Figure 62: FT-IR spectrum of pyridylimine ligand **L4**.

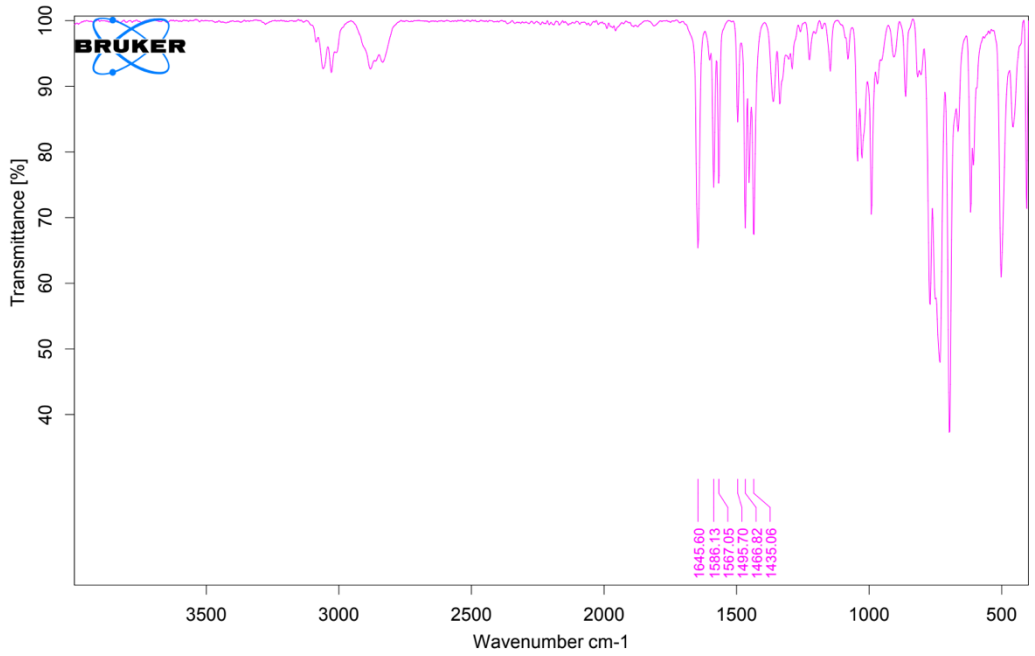

Figure 63: FT-IR spectrum of pyridylimine ligand **L5**.

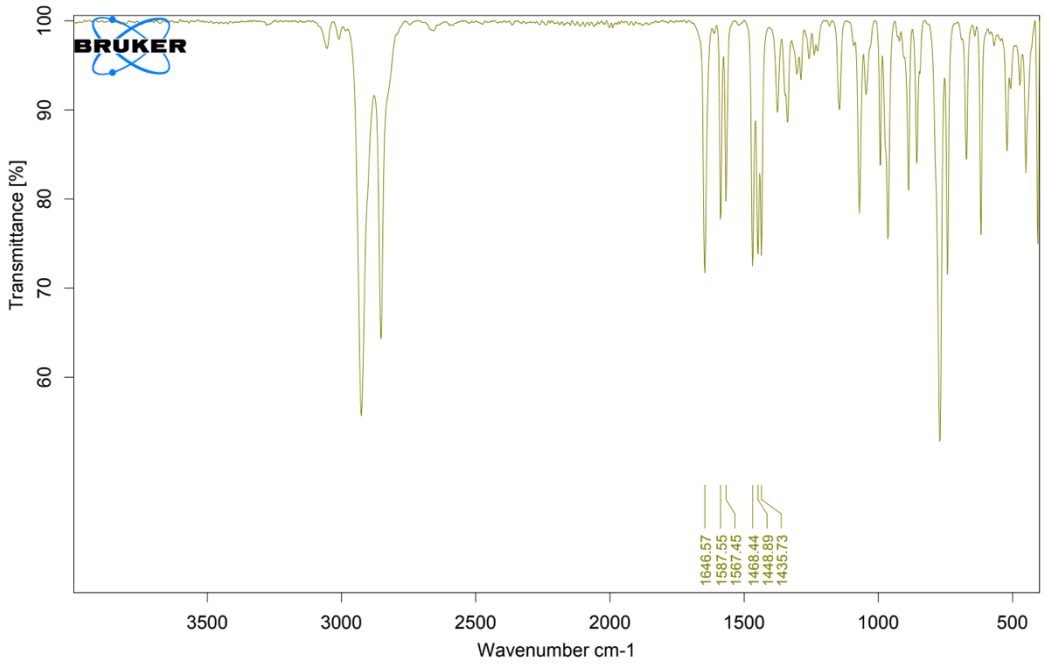

Figure 64: FT-IR spectrum of pyridylimine ligand **L6**.

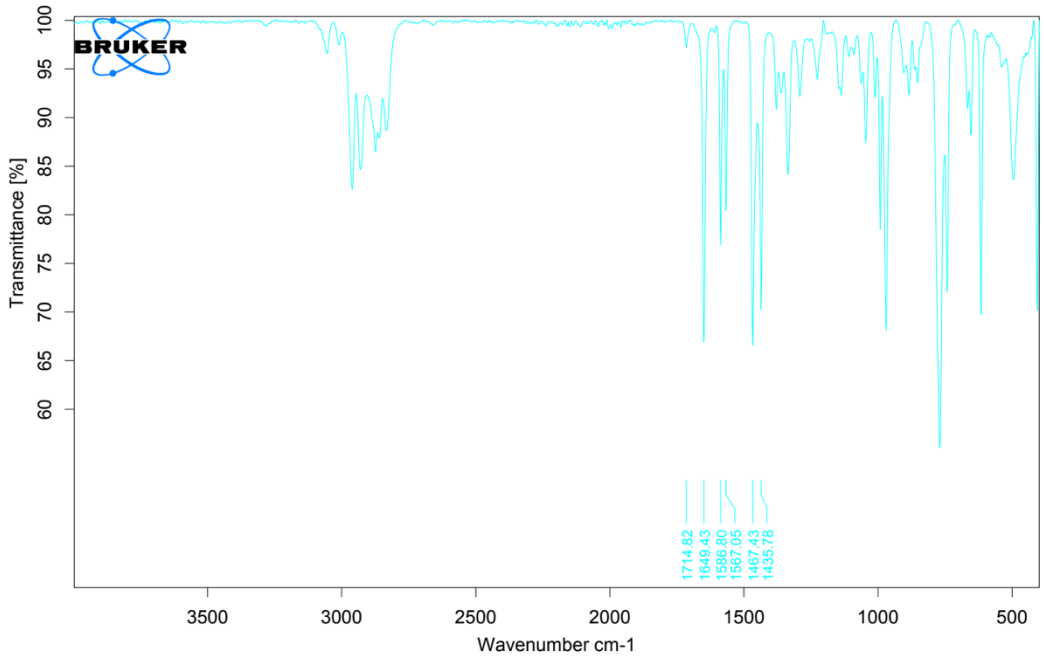

Figure 65: FT-IR spectrum of pyridylimine ligand **L7**.

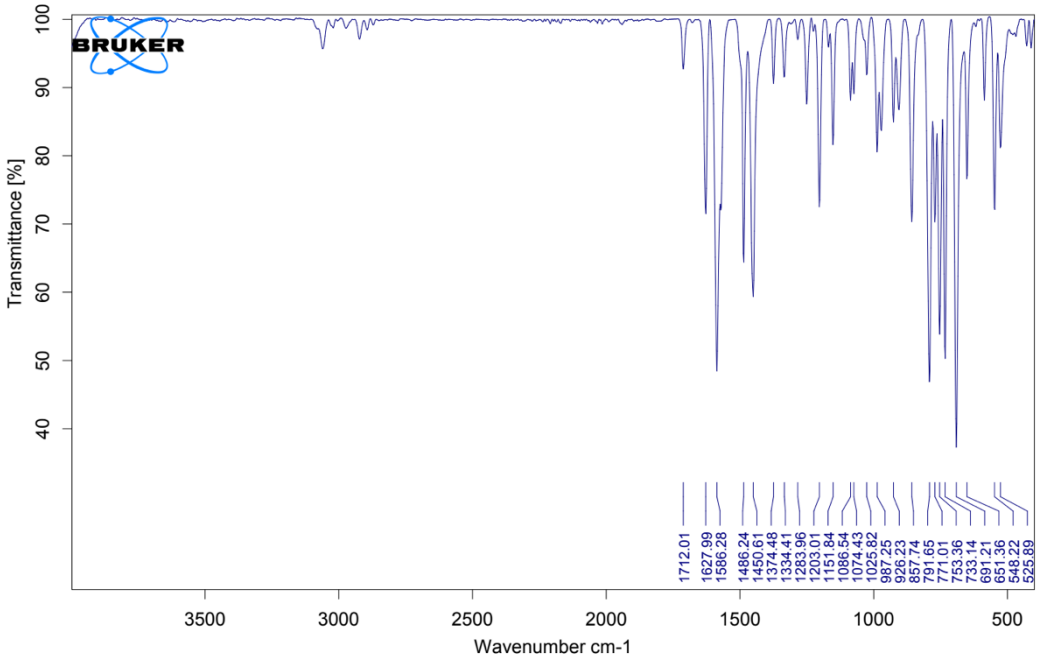

Figure 66: FT-IR spectrum of pyridylimine ligand **L8**.

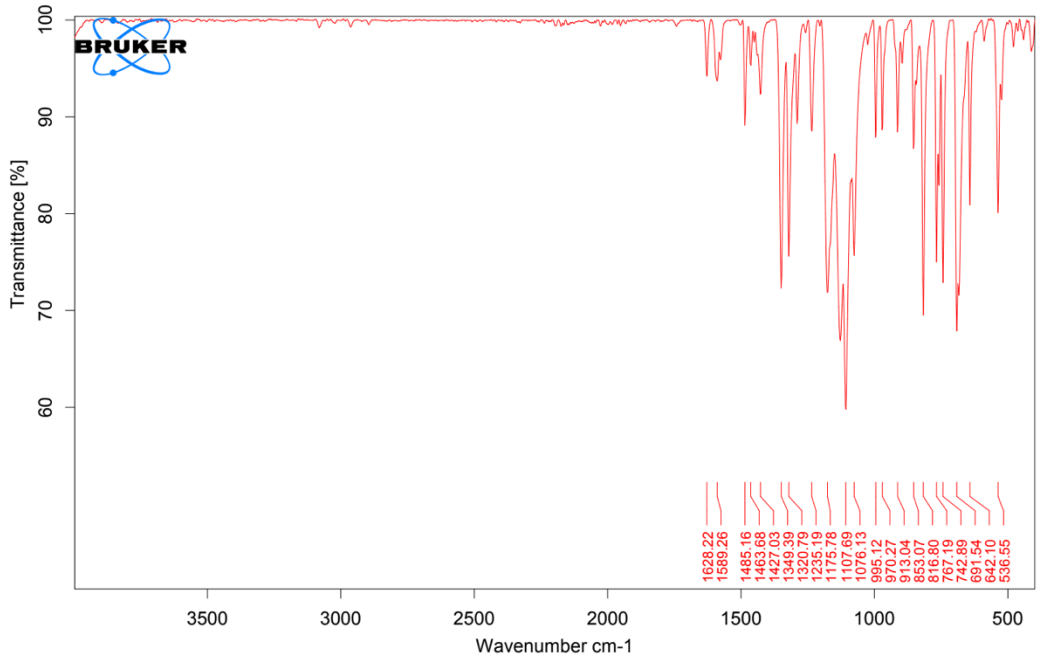

Figure 67: FT-IR spectrum of pyridylimine ligand **L9**.

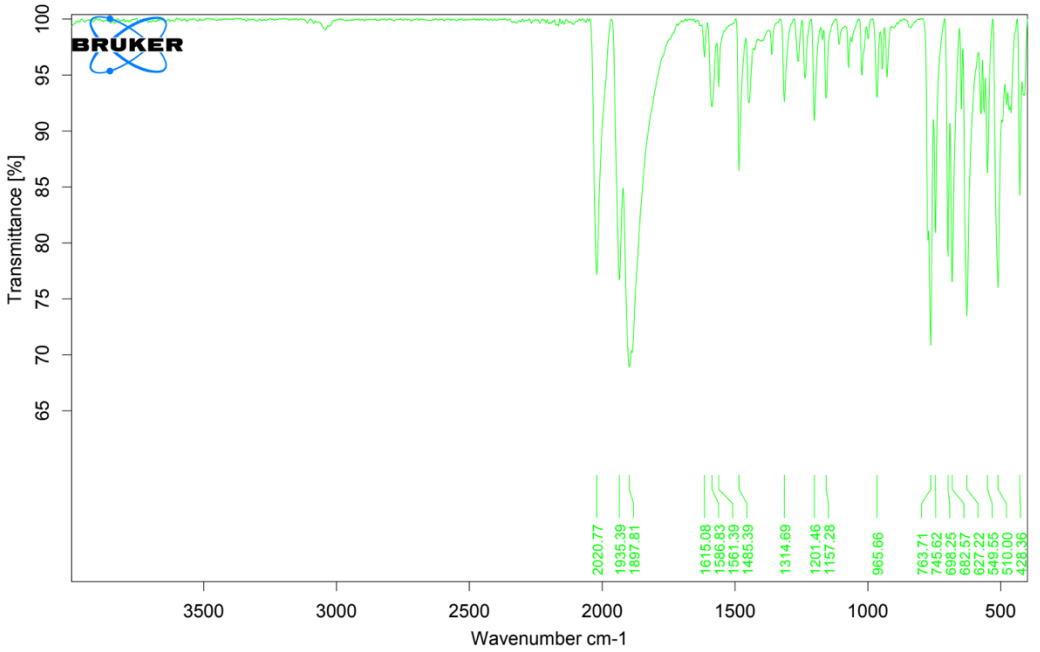

Figure 68: FT-IR spectrum of pyridylimine manganese complex **C1**.

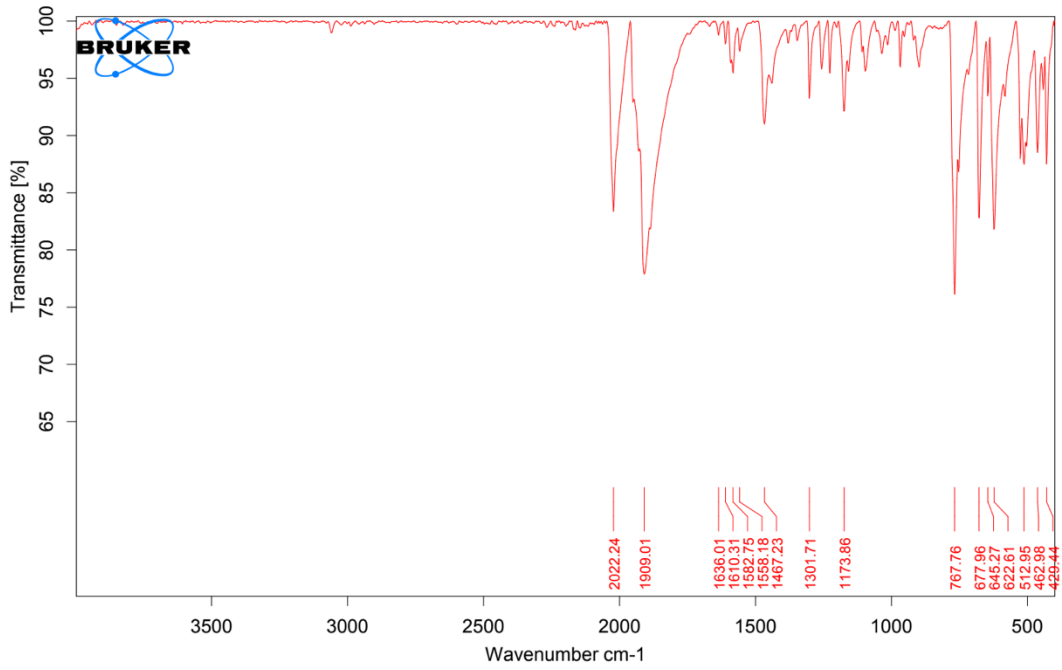

Figure 69: FT-IR spectrum of pyridylimine manganese complex **C2**.

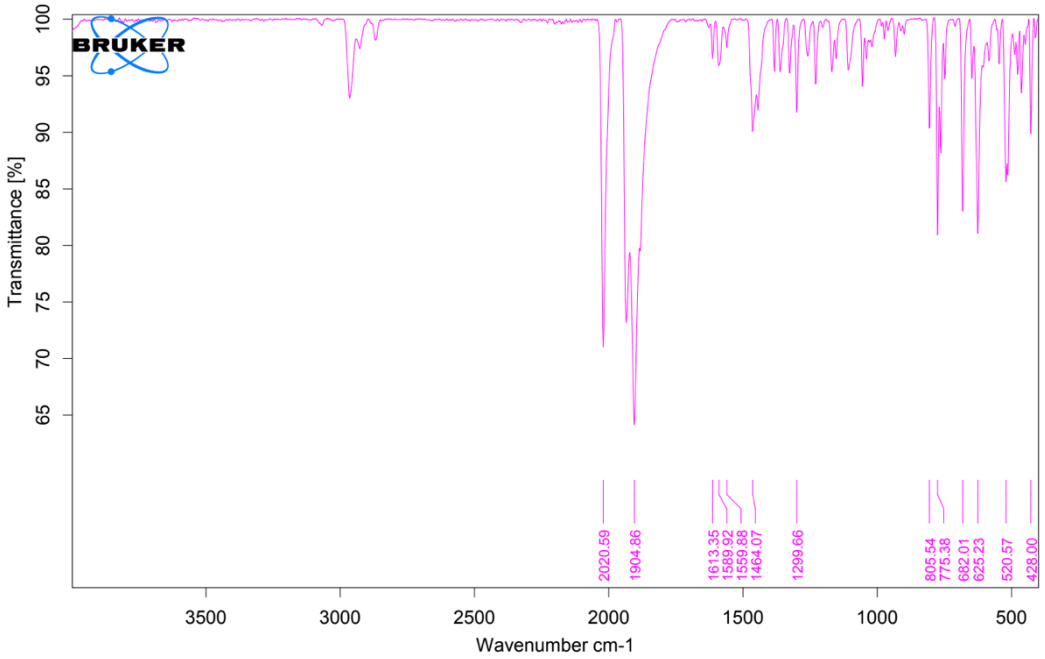

Figure 70: FT-IR spectrum of pyridylimine manganese complex **C3**.

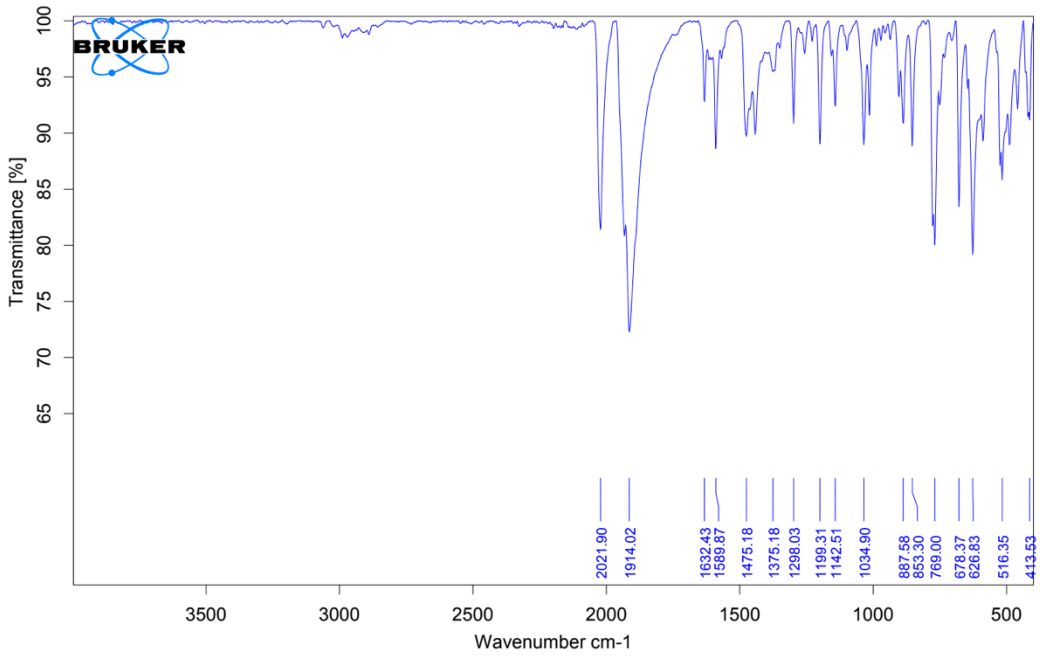

Figure 71: FT-IR spectrum of pyridylimine manganese complex **C4**.

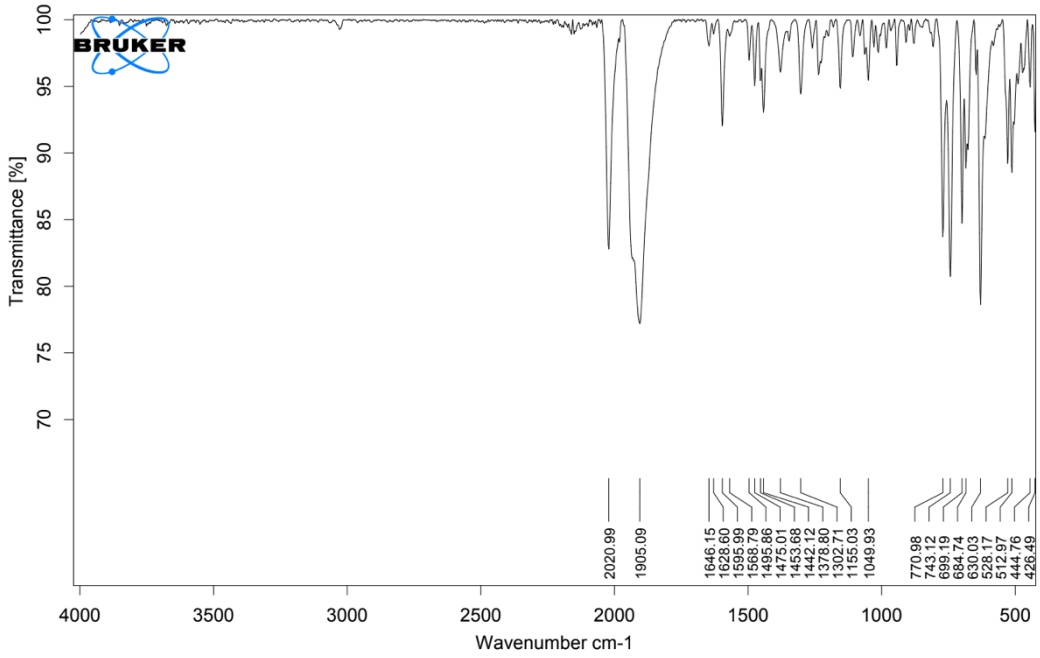

Figure 72: FT-IR spectrum of pyridylimine manganese complex **C5**.

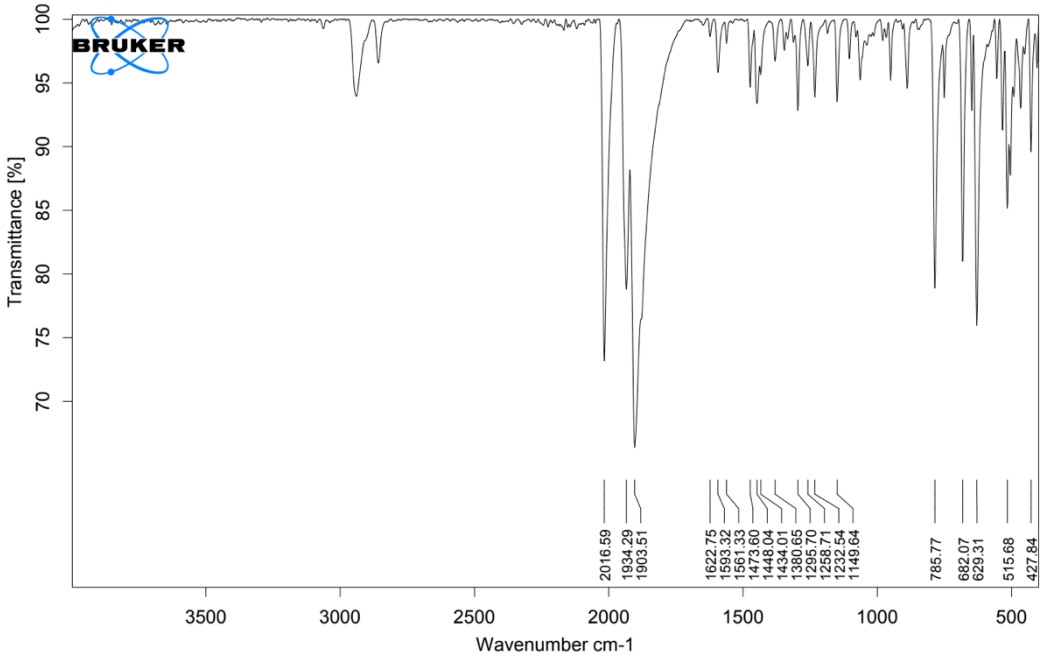

Figure 73: FT-IR spectrum of pyridylimine manganese complex **C6**.

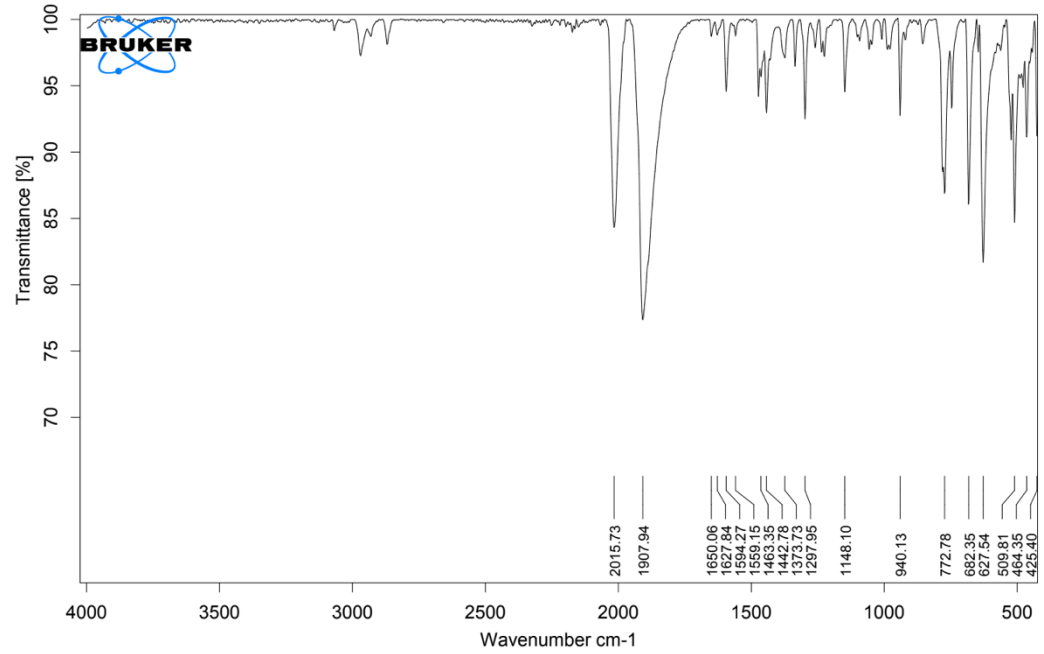

Figure 74: FT-IR spectrum of pyridylimine manganese complex **C7**.

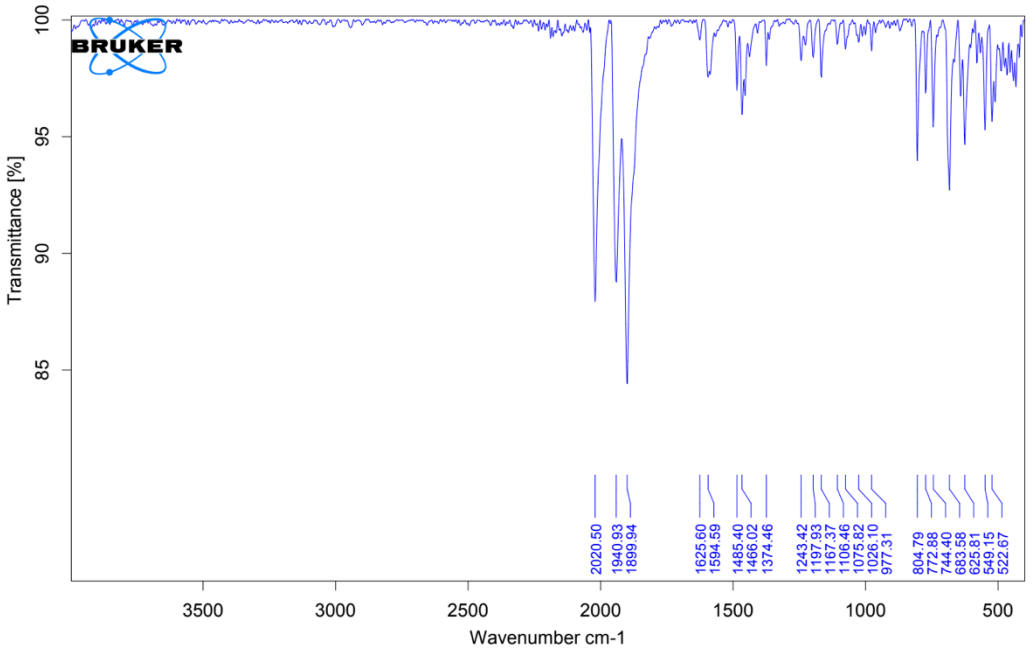

Figure 75: FT-IR spectrum of pyridylimine manganese complex **C8**.

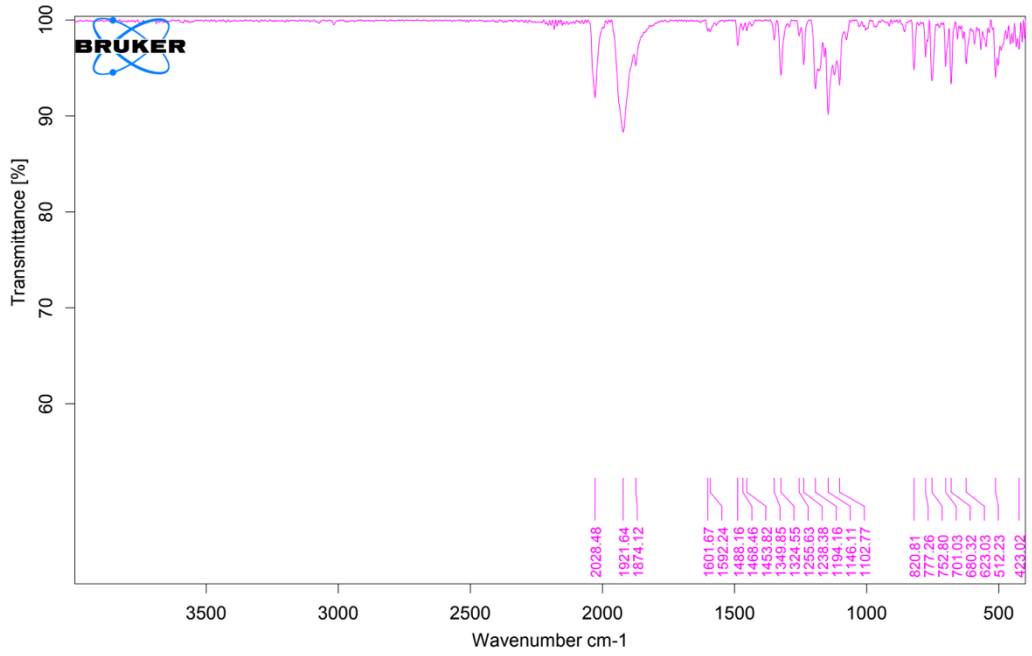

Figure 76: FT-IR spectrum of pyridylimine manganese complex **C9**.

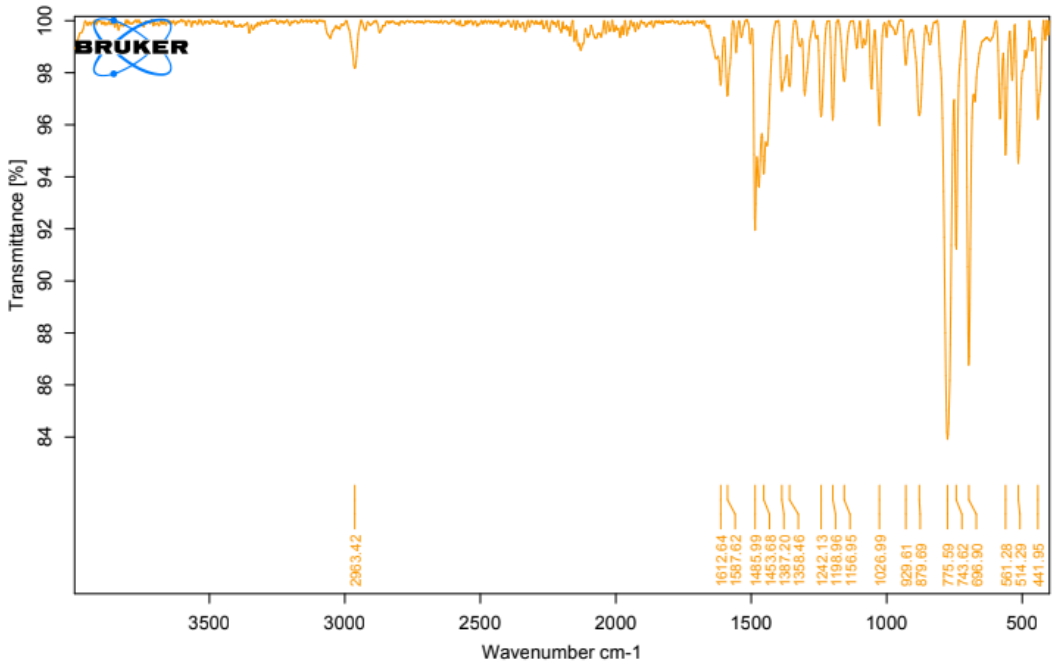

Figure 77: FT-IR spectrum of pyridylimine ruthenium complex **C10**.

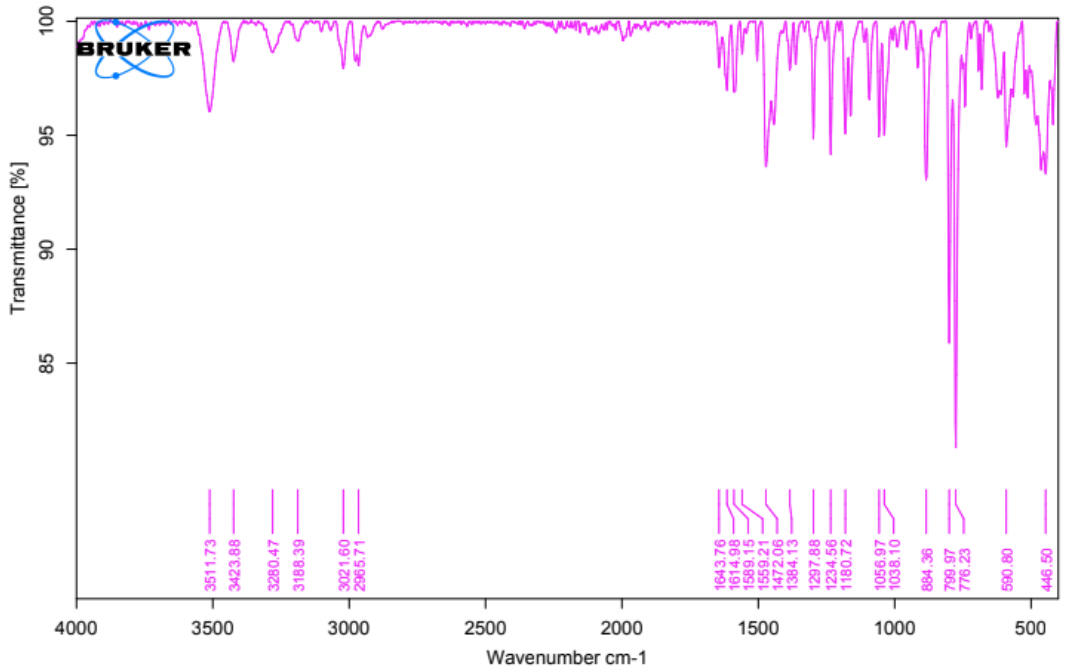

Figure 78: FT-IR spectrum of pyridylimine ruthenium complex **C11**.

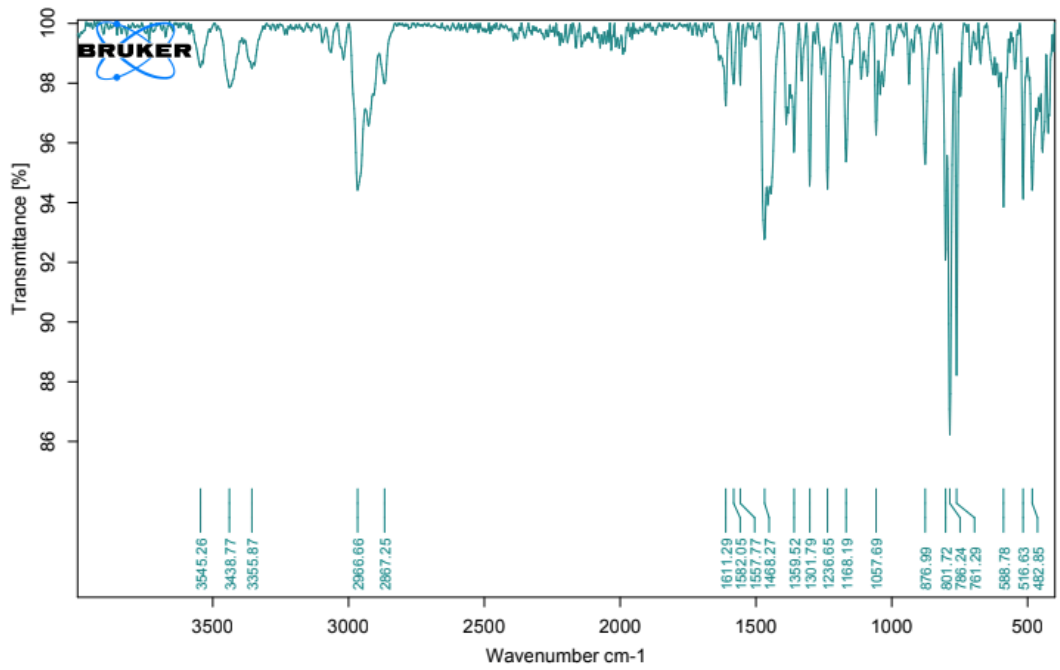

Figure 79: FT-IR spectrum of pyridylimine ruthenium complex **C12**.

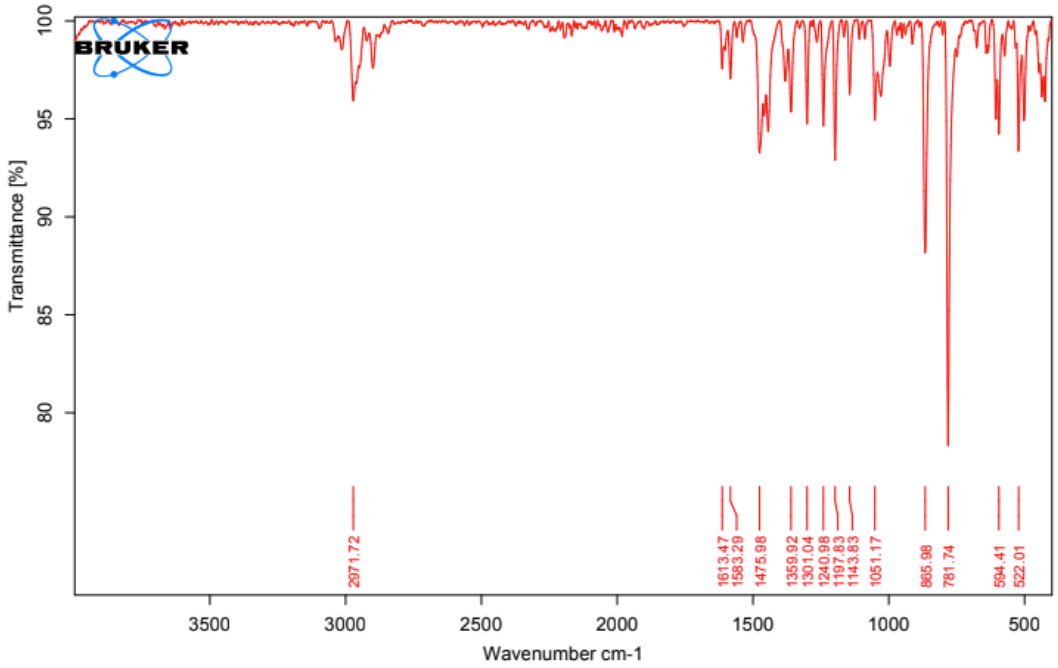

Figure 80: FT-IR spectrum of pyridylimine ruthenium complex **C13**.

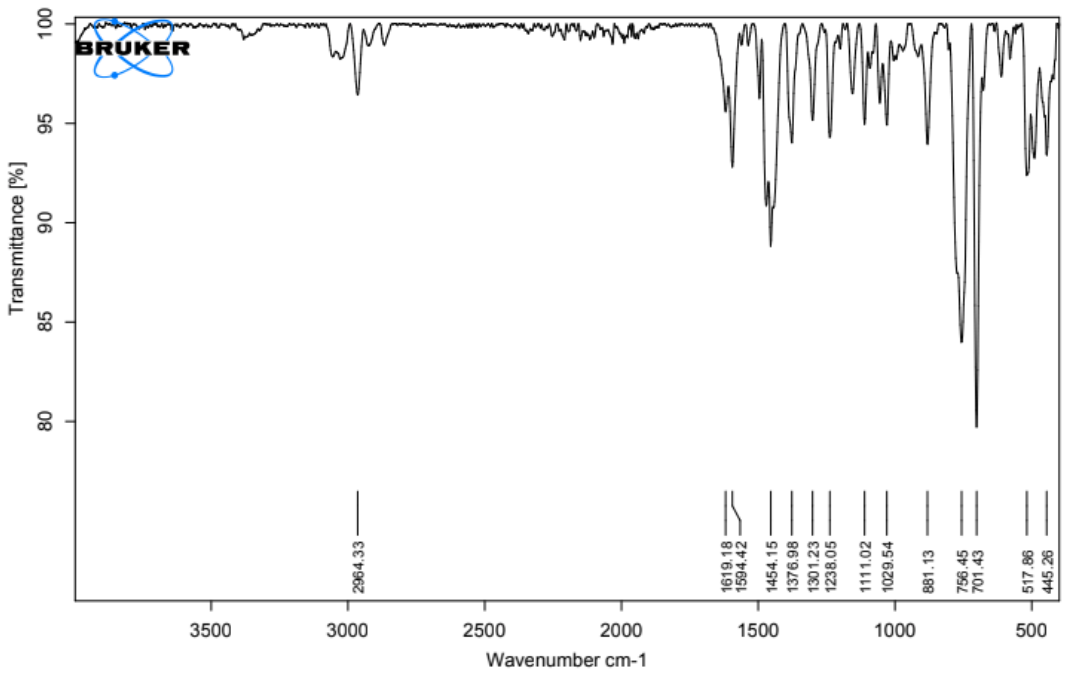

Figure 81: FT-IR spectrum of pyridylimine ruthenium complex **C14**.

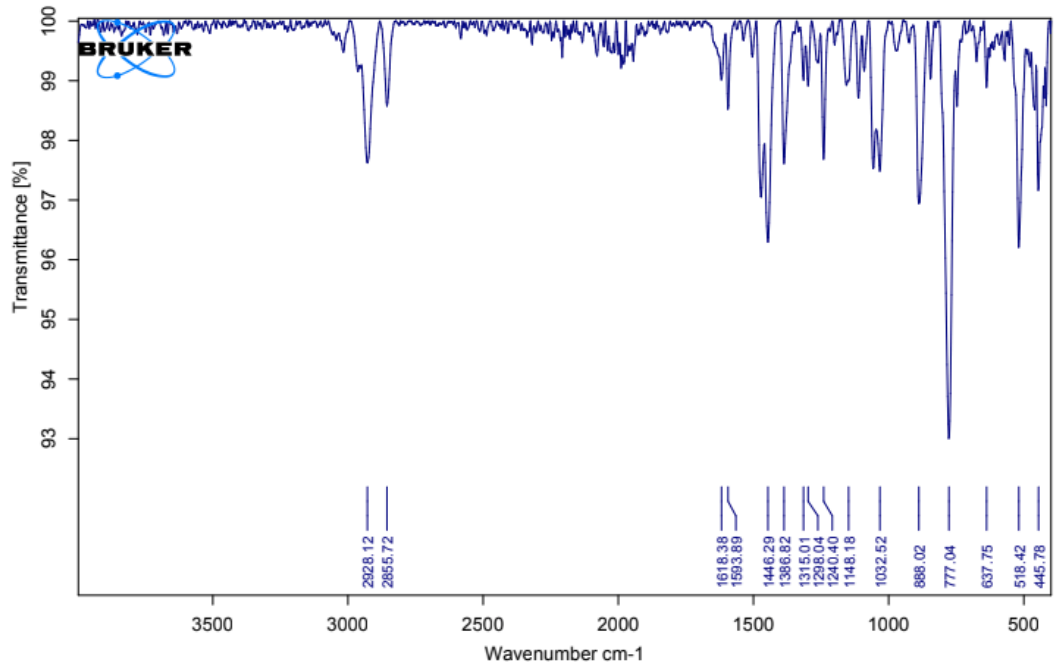

Figure 82: FT-IR spectrum of pyridylimine ruthenium complex **C15**.

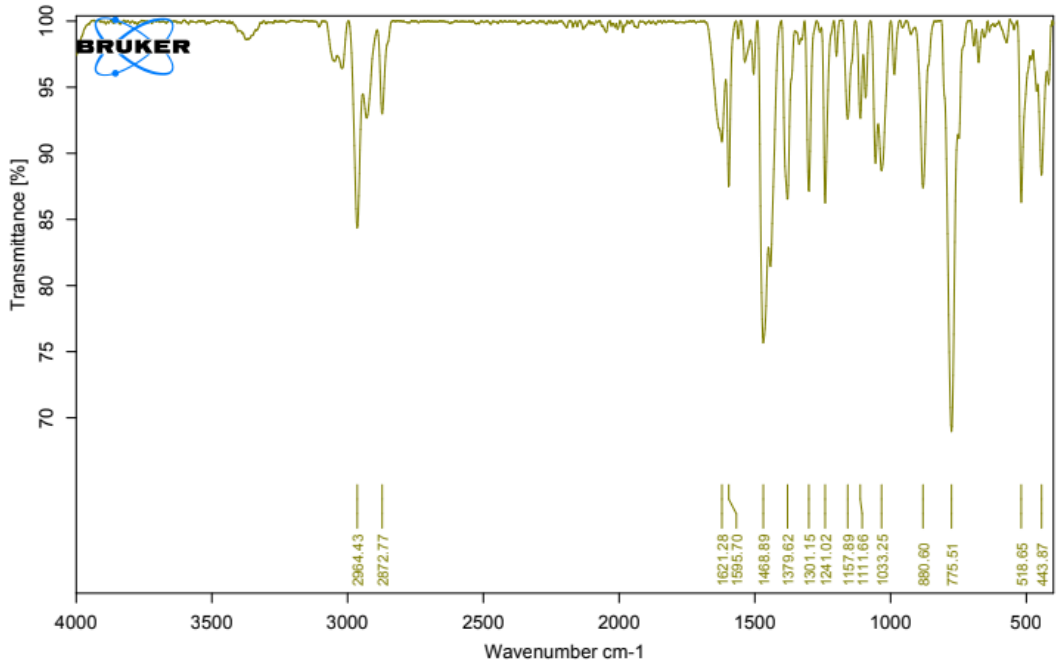

Figure 83: FT-IR spectrum of pyridylimine ruthenium complex **C16**.

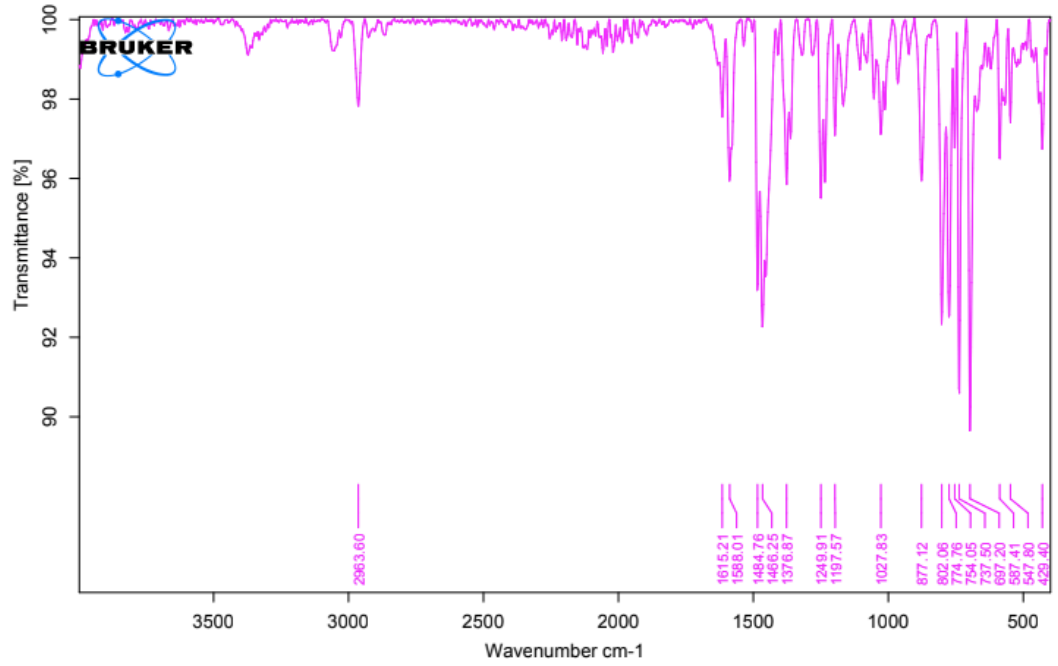

Figure 84: FT-IR spectrum of pyridylimine ruthenium complex **C17**.

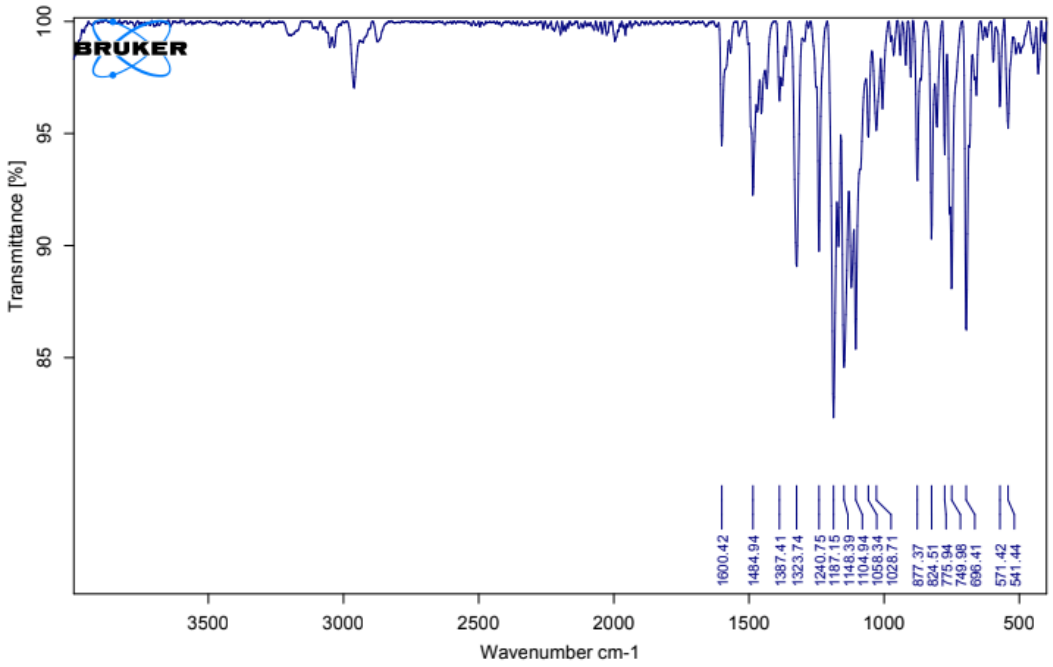

Figure 85: FT-IR spectrum of pyridylimine ruthenium complex **C18**.

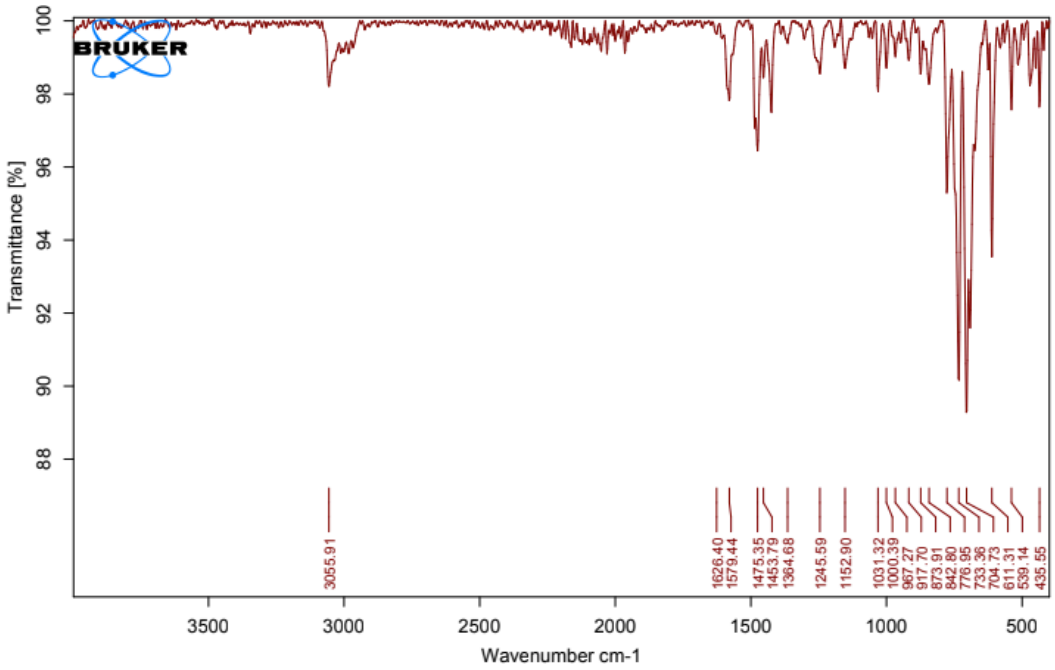

Figure 86: FT-IR spectrum of pyridylimine ruthenium complex **C19**.

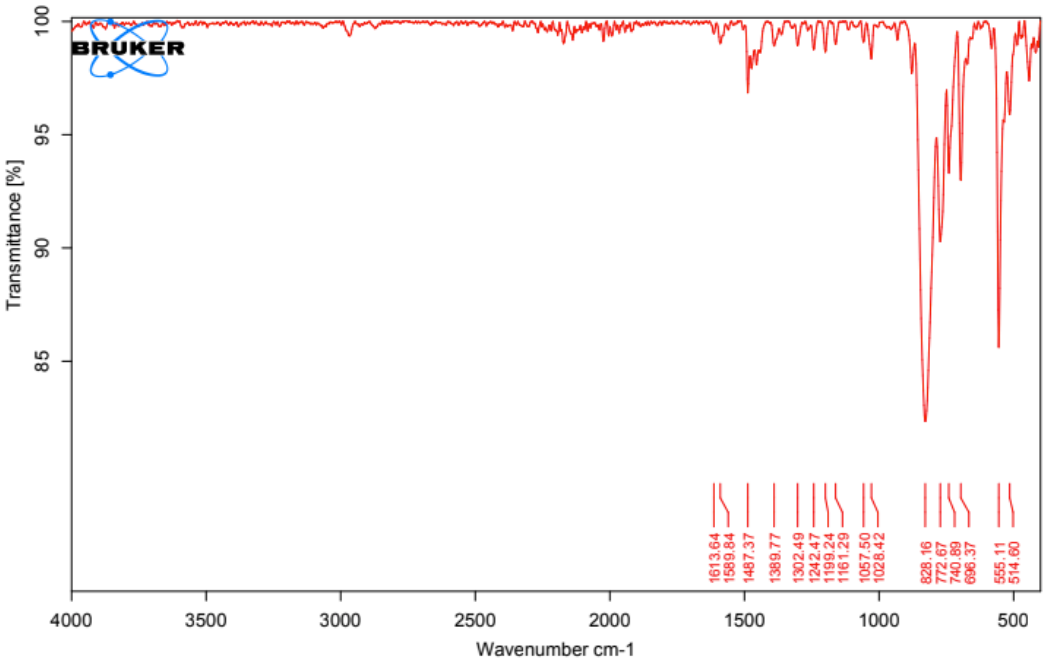

Figure 87: FT-IR spectrum of pyridylimine ruthenium complex **C20**.

Mass Spectra (Ligands and Complexes)

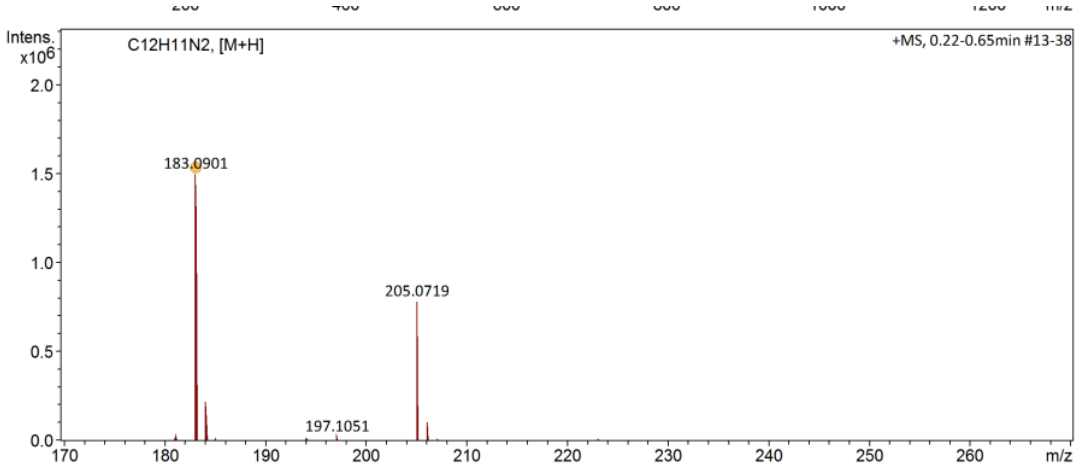

Figure 88: Mass spectrum of pyridylimine ligand **L1** recorded in the positive mode.

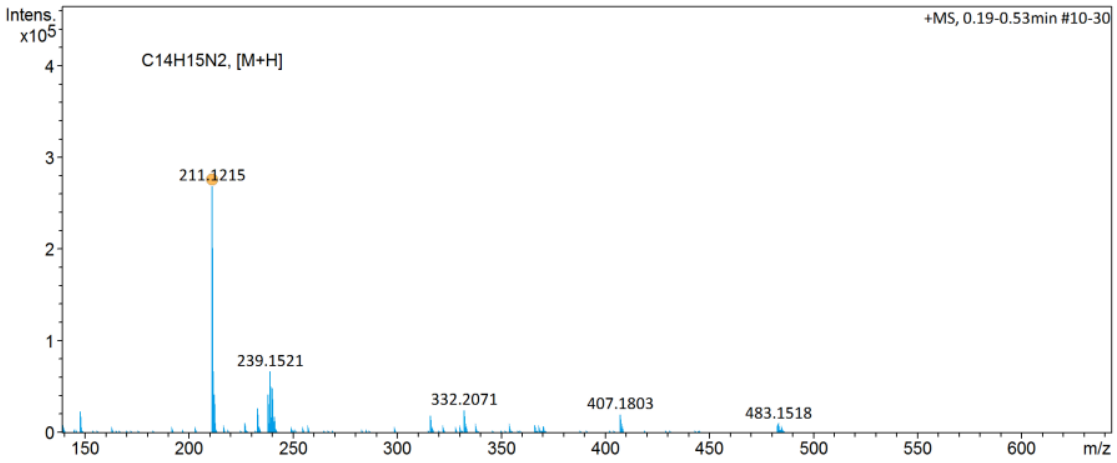

Figure 89: Mass spectrum of pyridylimine ligand **L2** recorded in the positive mode.

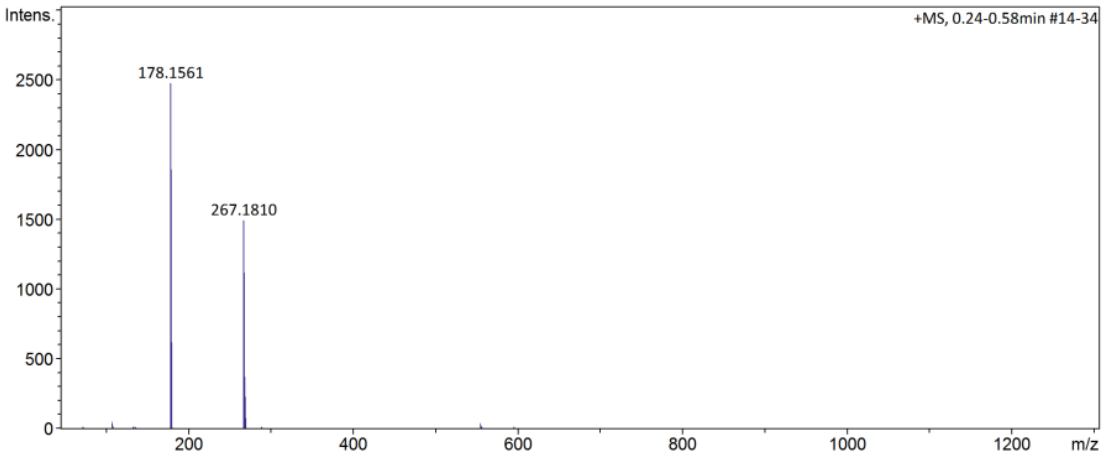

Figure 90: Mass spectrum of pyridylimine ligand **L3** recorded in the positive mode.

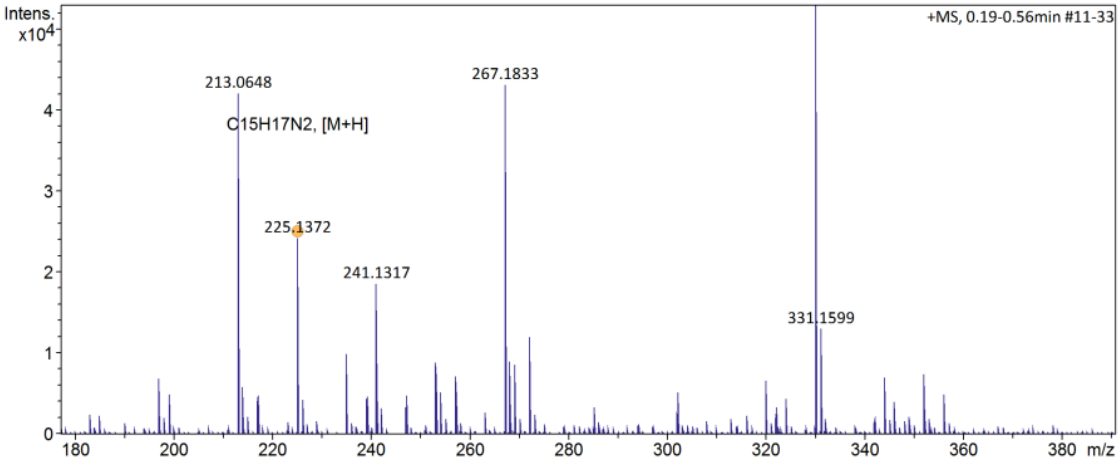

Figure 91: Mass spectrum of pyridylimine ligand **L4** recorded in the positive mode.

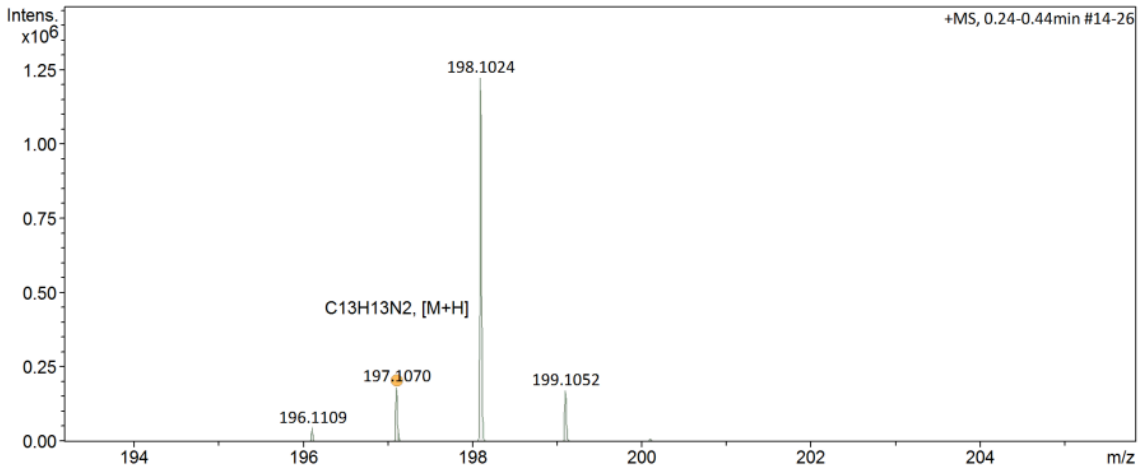

Figure 92: Mass spectrum of pyridylimine ligand **L5** recorded in the positive mode.

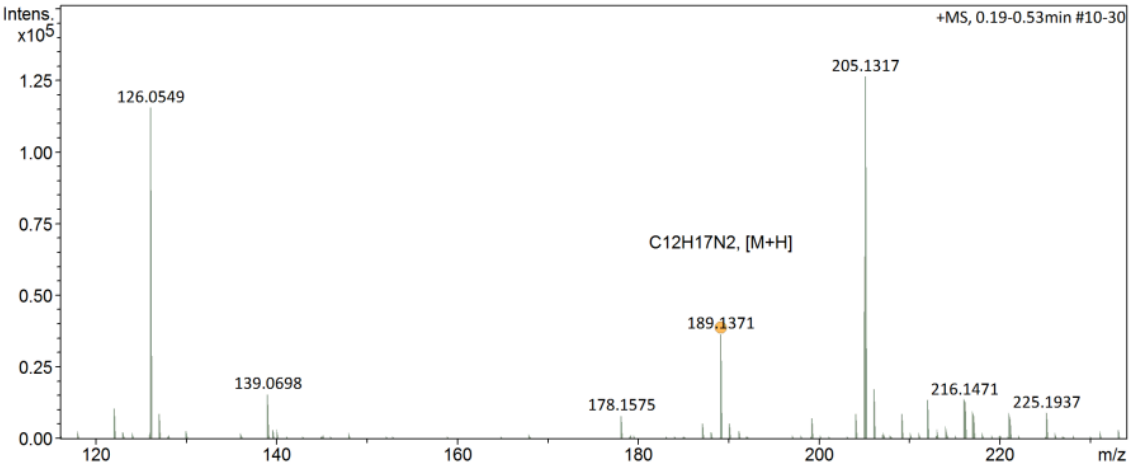

Figure 93: Mass spectrum of pyridylimine ligand **L6** recorded in the positive mode.

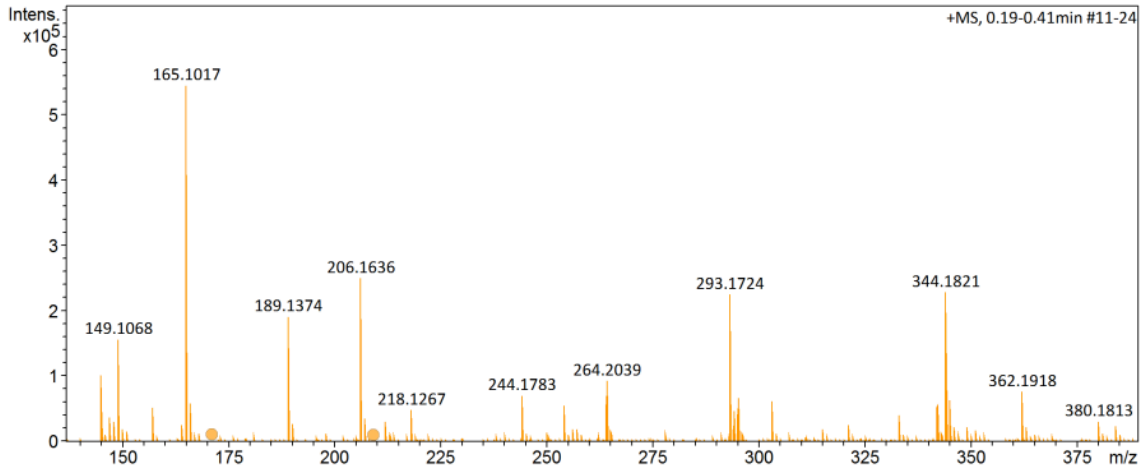

Figure 94: Mass spectrum of pyridylimine ligand **L7** recorded in the positive mode.

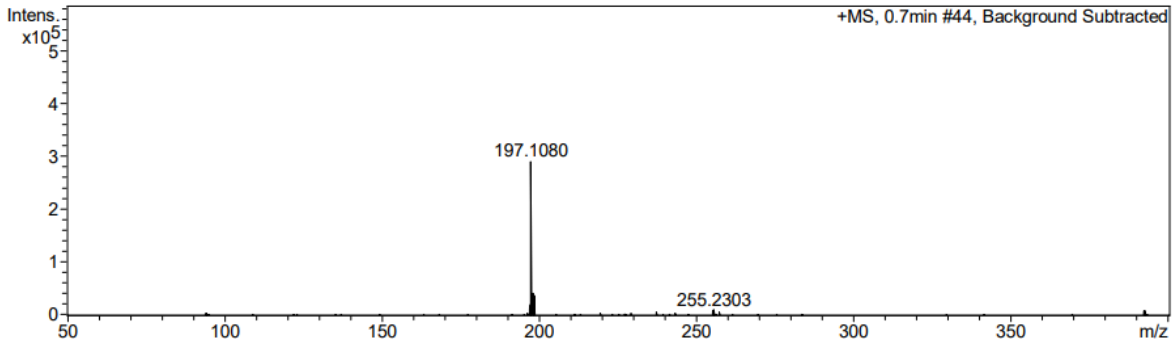

Figure 95: Mass spectrum of pyridylimine ligand **L8** recorded in the positive mode.

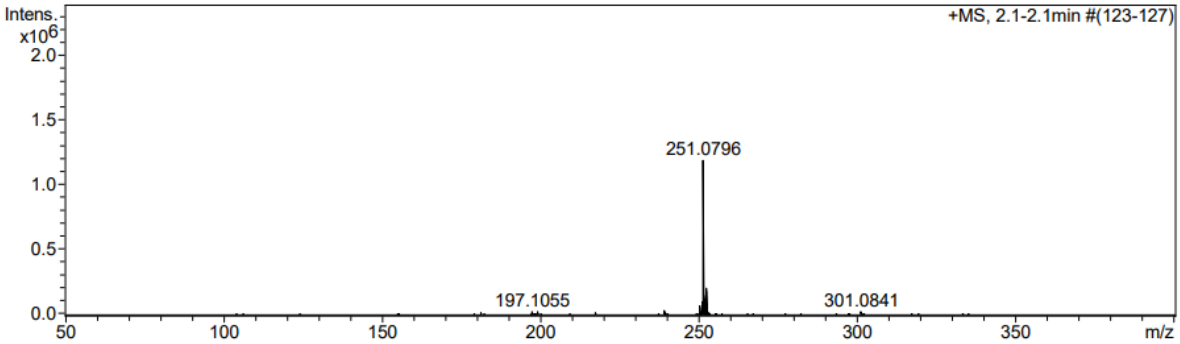

Figure 96: Mass spectrum of pyridylimine ligand **L9** recorded in the positive mode.

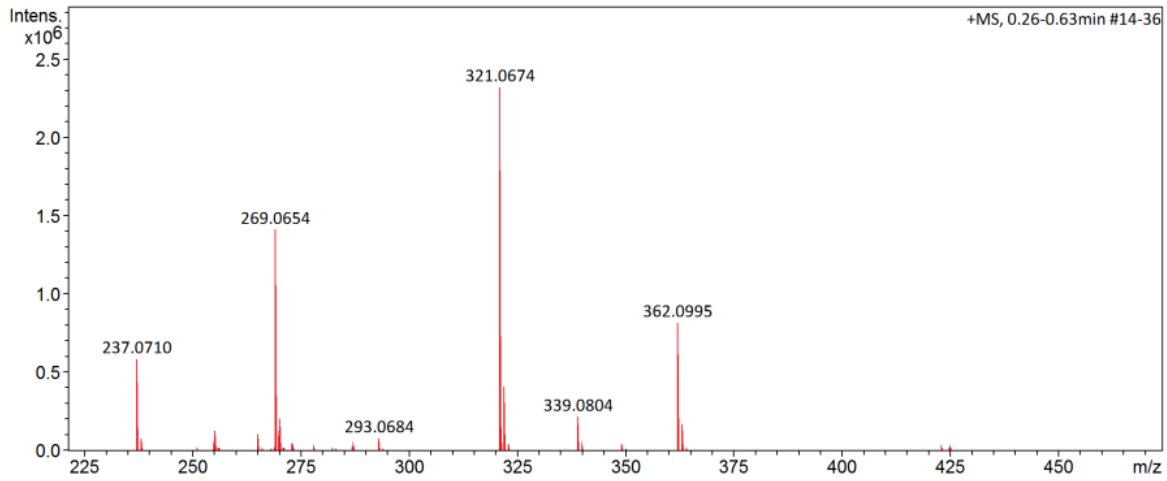

Figure 97: Mass spectrum of manganese complex **C1** recorded in the positive mode.

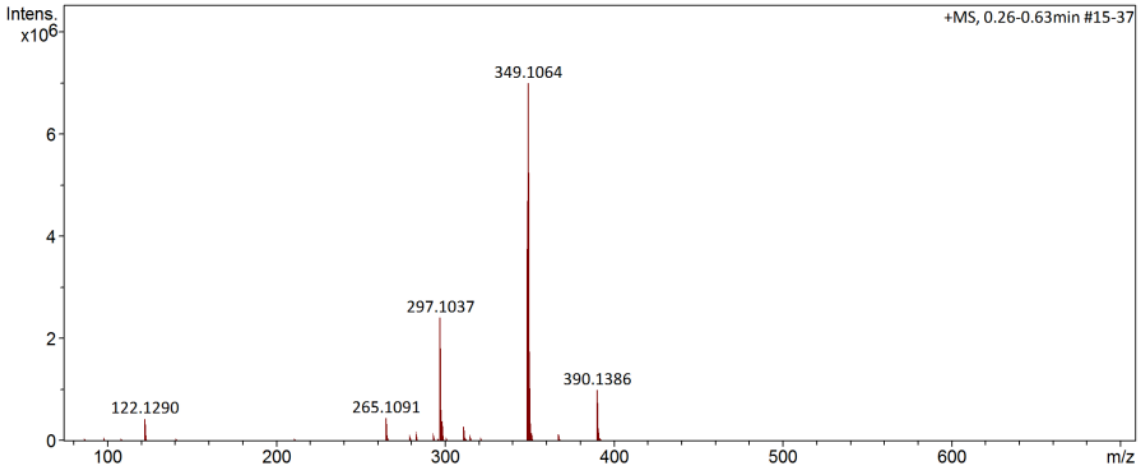

Figure 98: Mass spectrum of manganese complex **C2** recorded in the positive mode.

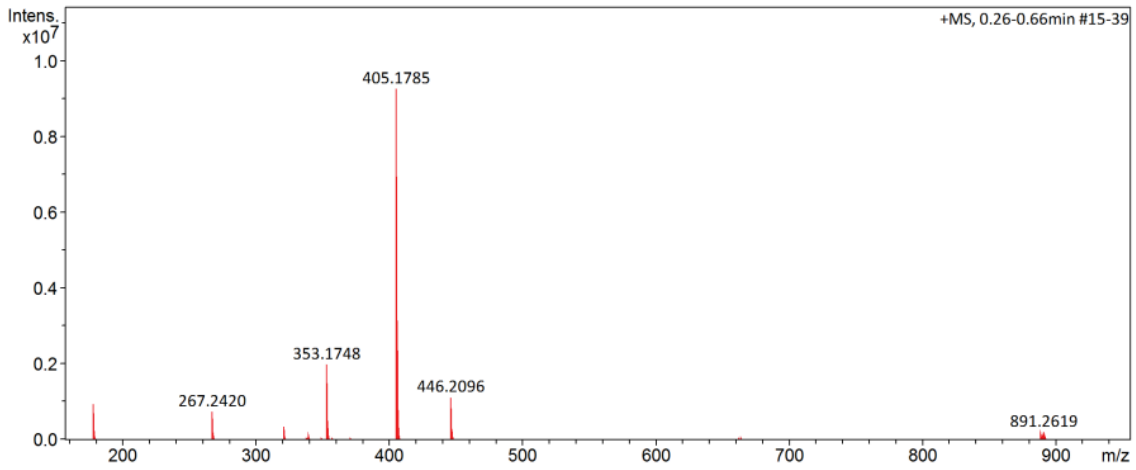

Figure 99: Mass spectrum of manganese complex **C3** recorded in the positive mode.

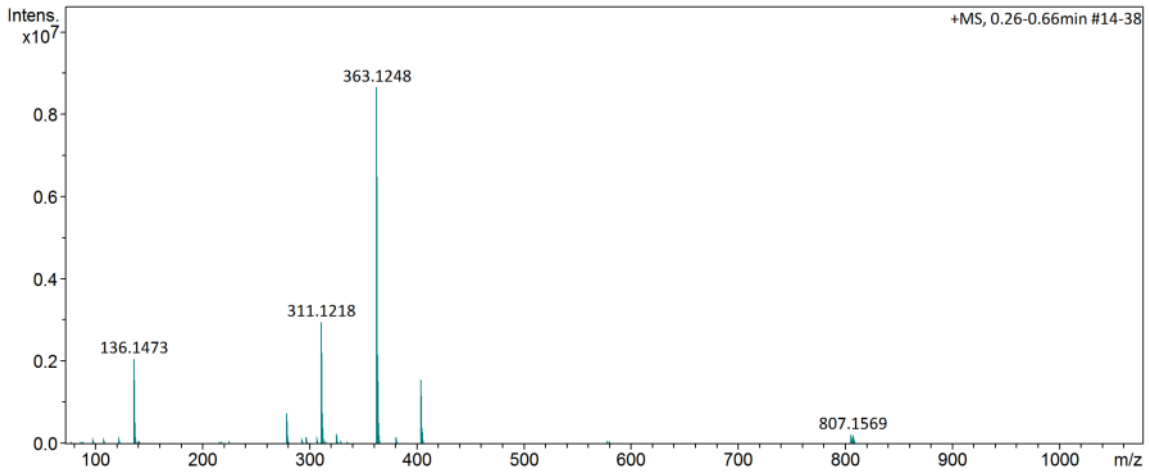

Figure 100: Mass spectrum of manganese complex **C4** recorded in the positive mode.

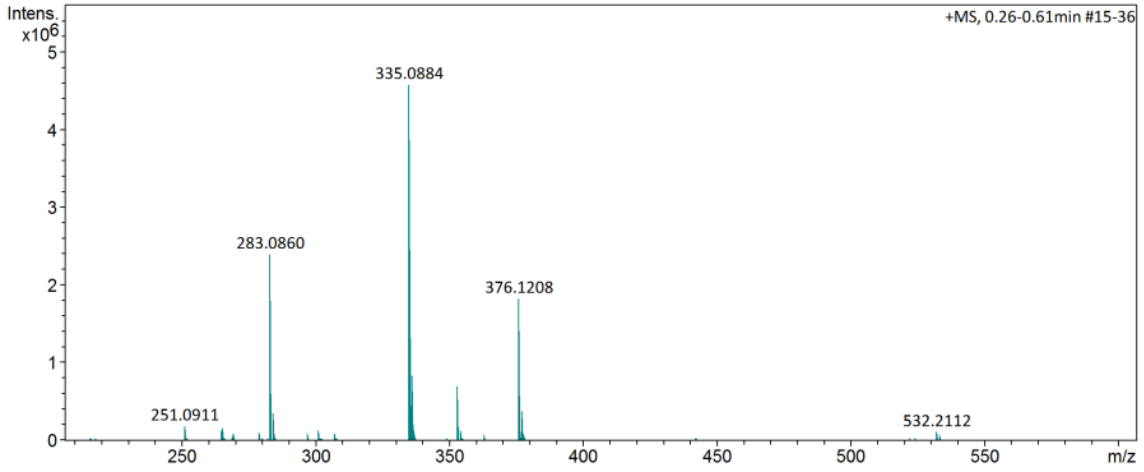

Figure 101: Mass spectrum of manganese complex **C5** recorded in the positive mode.

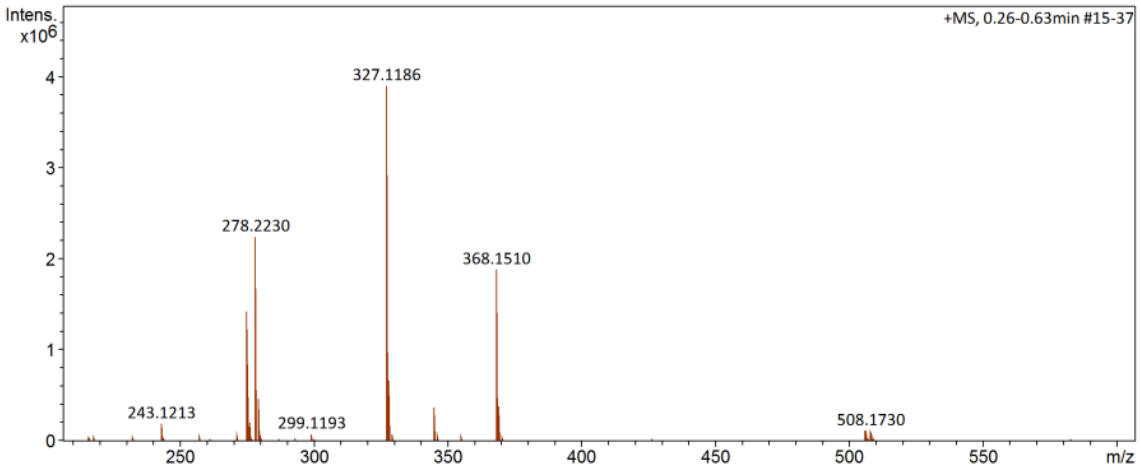

Figure 102: Mass spectrum of manganese complex **C6** recorded in the positive mode.

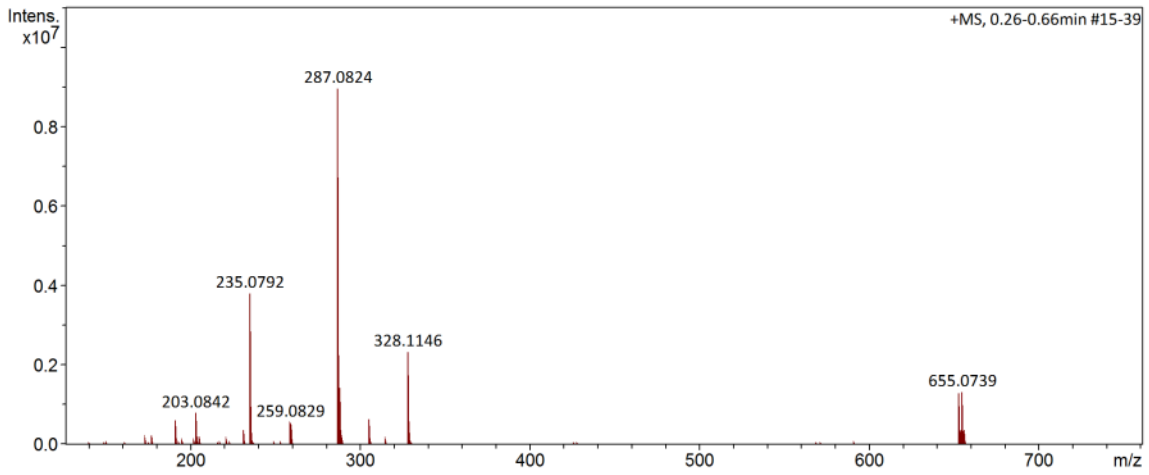

Figure 103: Mass spectrum of manganese complex **C7** recorded in the positive mode.

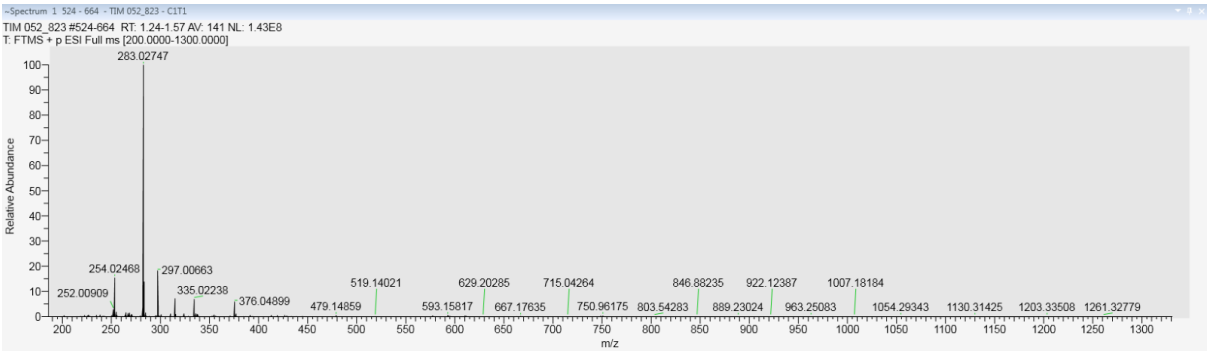

Figure 104: Mass spectrum of manganese complex **C8** recorded in the positive mode.

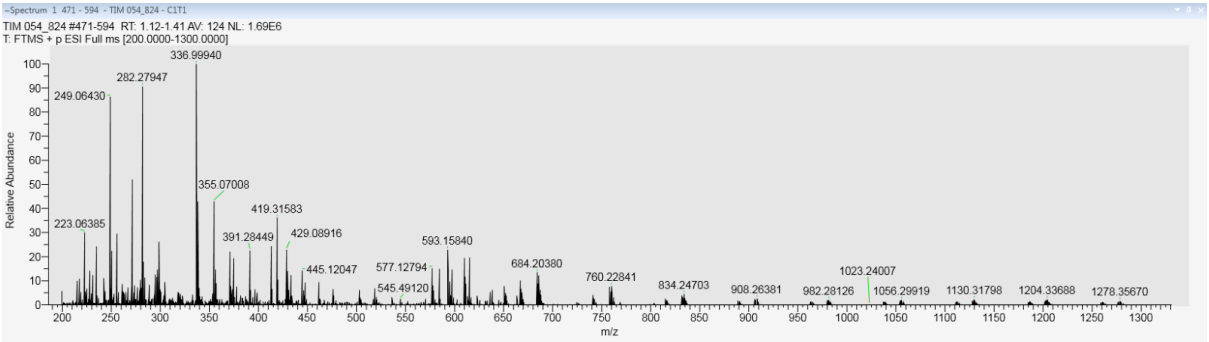

Figure 105: Mass spectrum of manganese complex **C9** recorded in the positive mode.

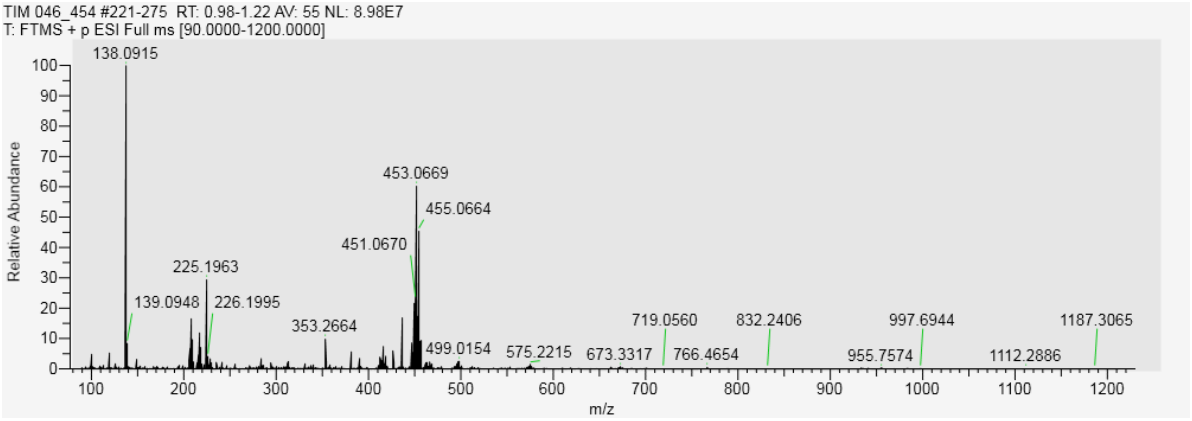

Figure 106: Mass spectrum of ruthenium complex **C10** recorded in the positive mode.

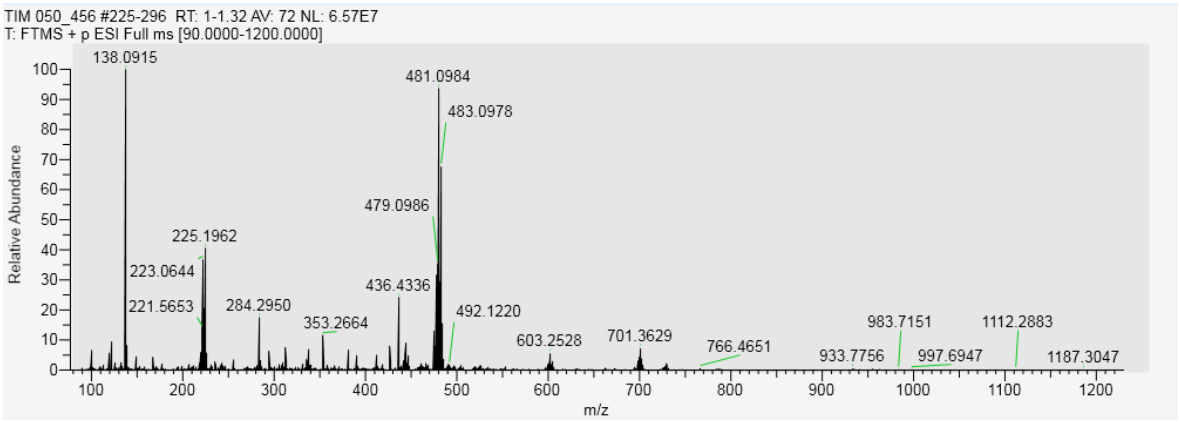

Figure 107: Mass spectrum of ruthenium complex **C11** recorded in the positive mode.

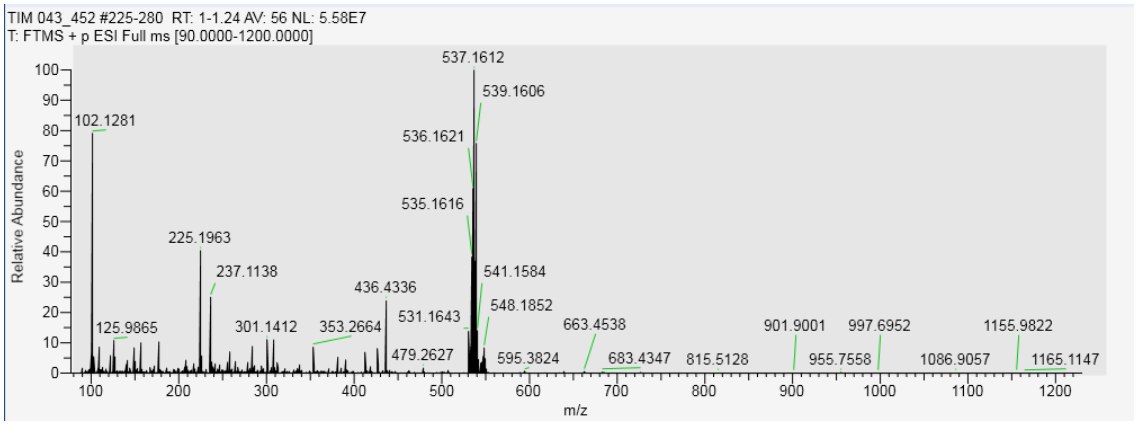

Figure 108: Mass spectrum of ruthenium complex **C12** recorded in the positive mode.

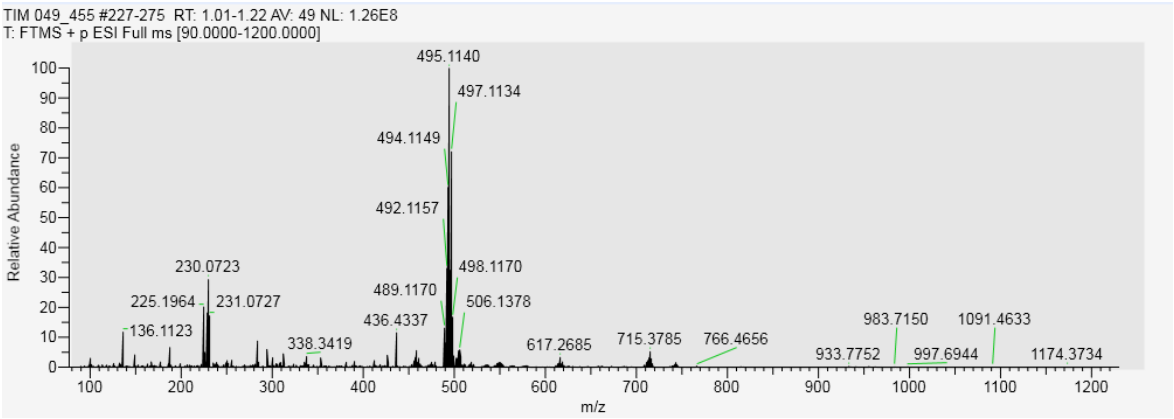

Figure 109: Mass spectrum of ruthenium complex **C13** recorded in the positive mode**.**

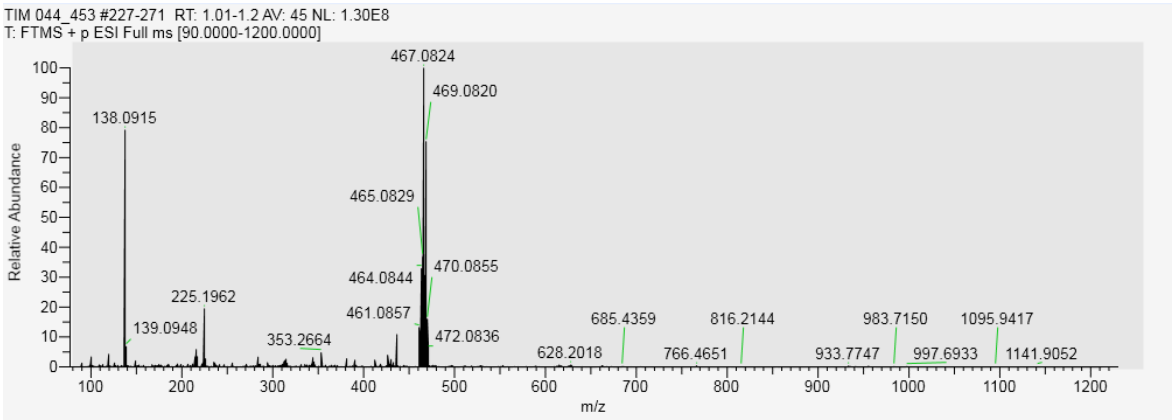

Figure 110: Mass spectrum of ruthenium complex **C14** recorded in the positive mode.

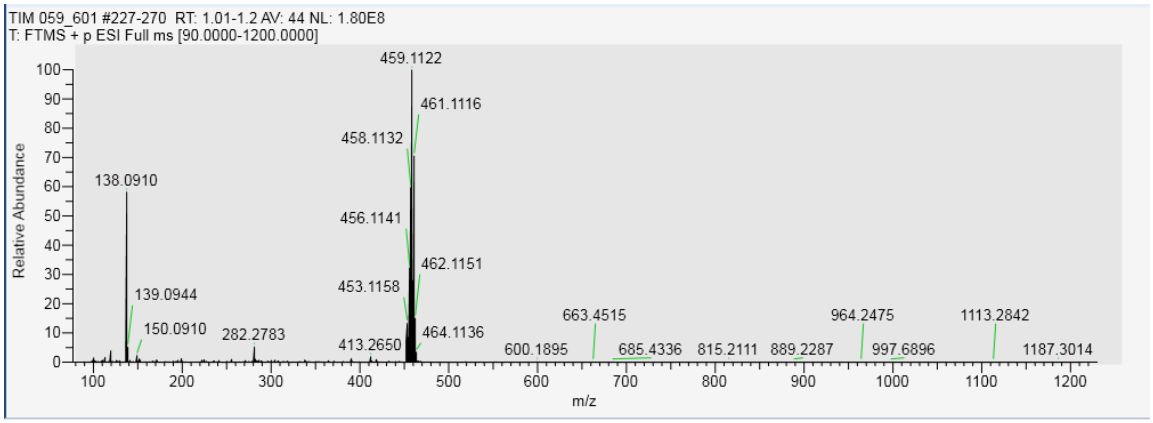

Figure 111: Mass spectrum of ruthenium complex **C15** recorded in the positive mode.

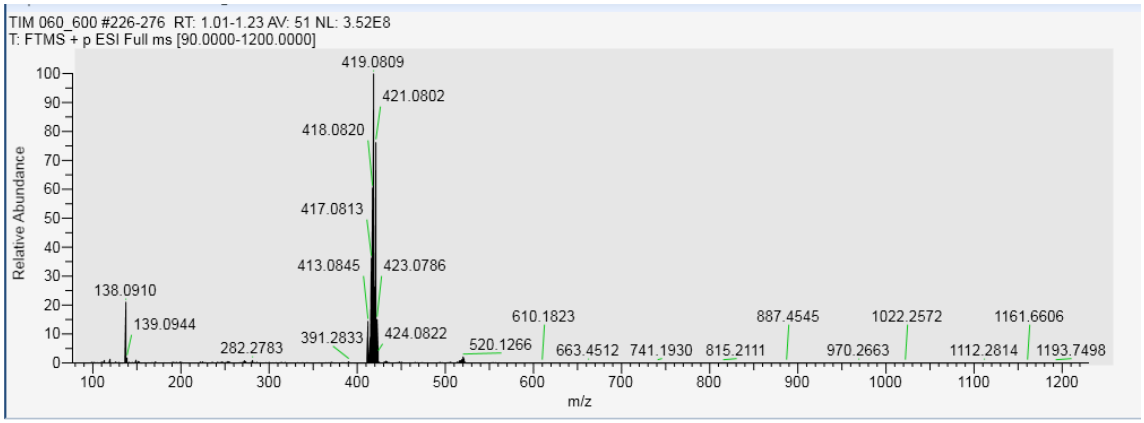

Figure 112: Mass spectrum of ruthenium complex **C16** recorded in the positive mode.

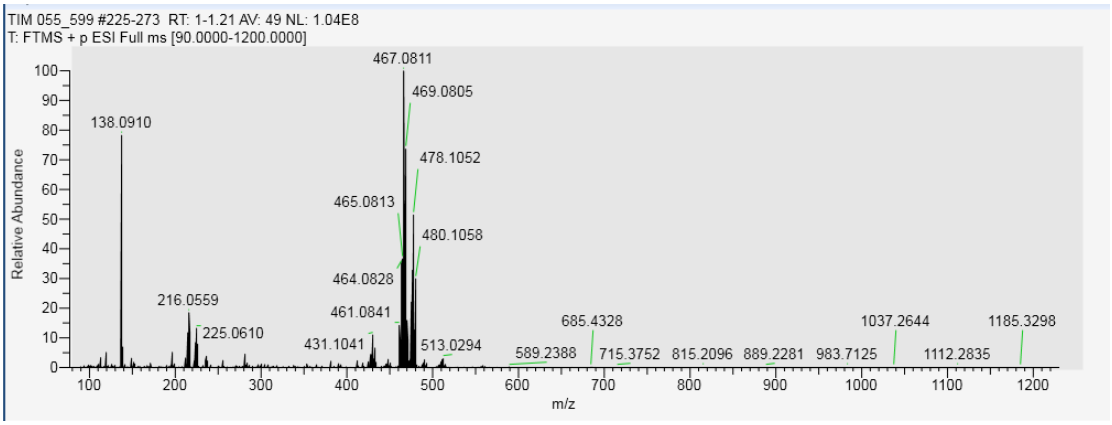

Figure 113: Mass spectrum of ruthenium complex **C17** recorded in the positive mode.

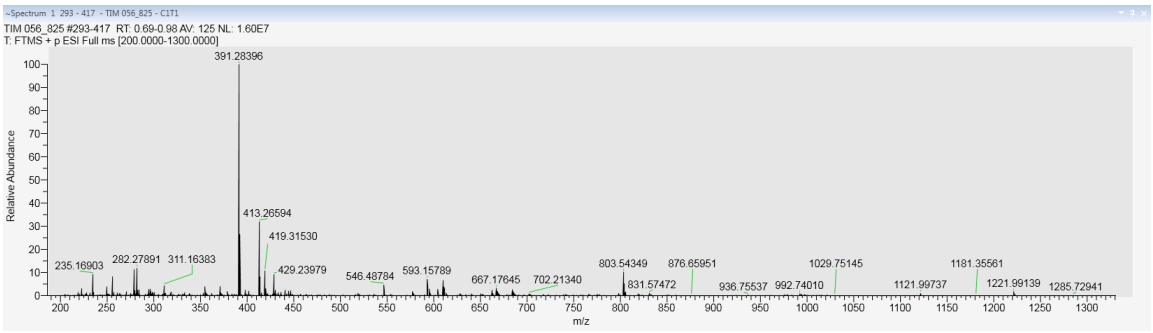

Figure 114: Mass spectrum of ruthenium complex **C18** recorded in the positive mode.

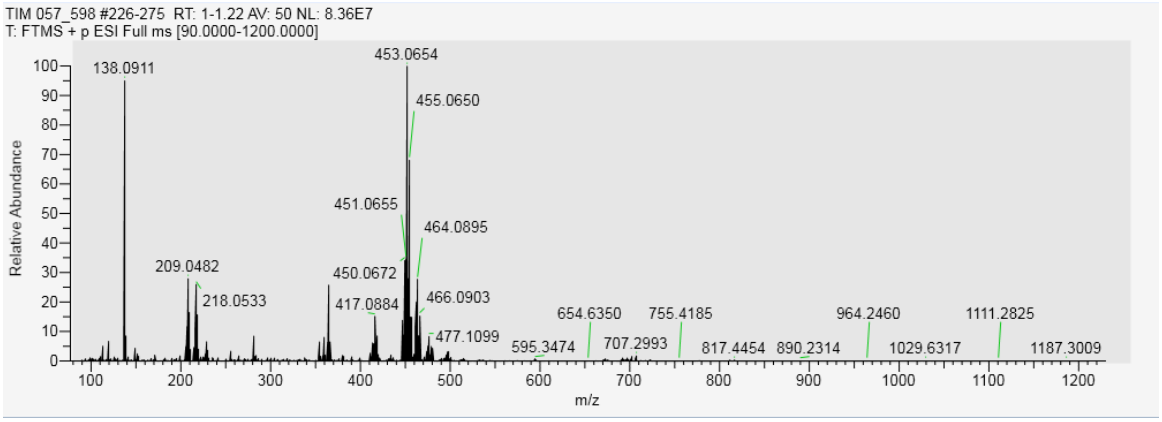

Figure 115: Mass spectrum of ruthenium complex **C19** recorded in the positive mode.

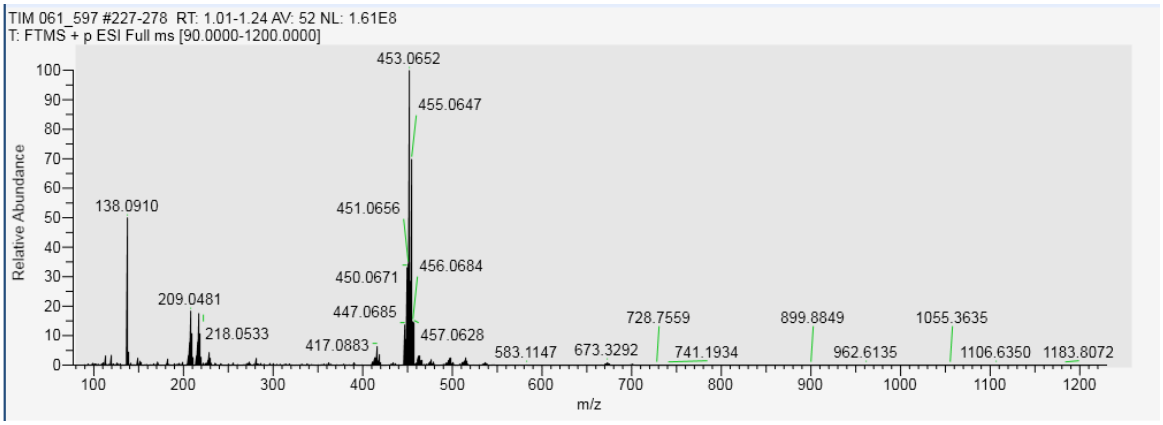

Figure 116: Mass spectrum of ruthenium complex **C20** recorded in the positive mode.

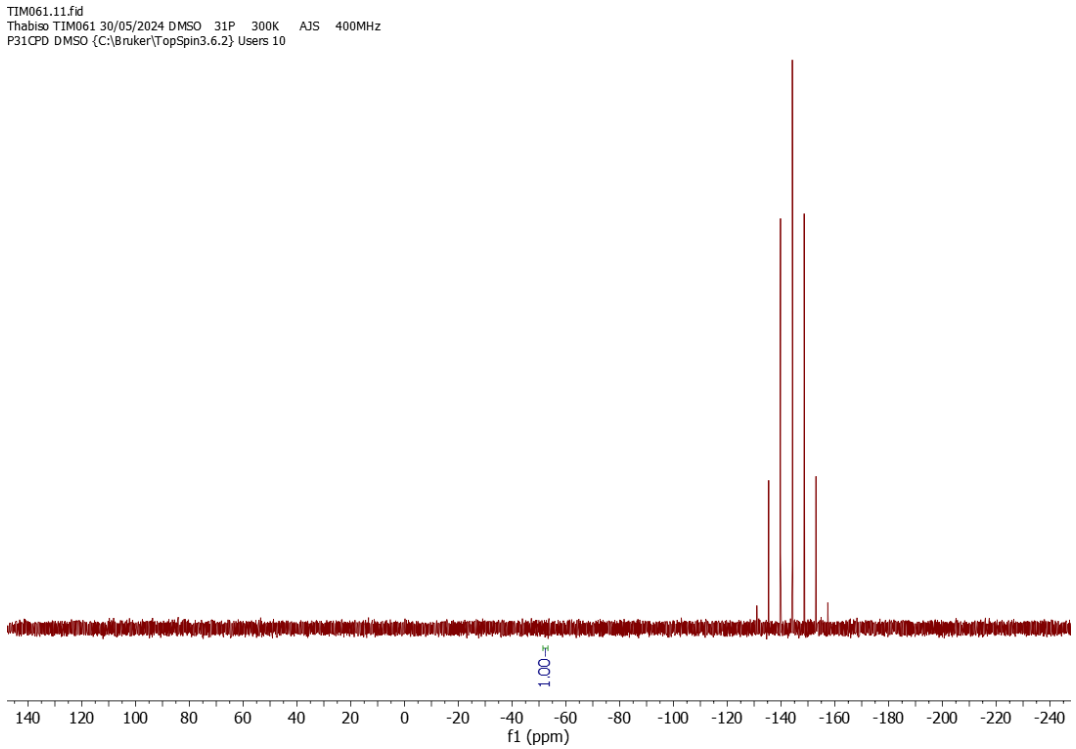

Figure 117: ^{31}P NMR spectrum of ruthenium complex **C20**.